TITLE NEUTRON SCATTERING STUDIES OF MAGNETIC PROPERTIES OF SUPERCONDUCTORS.

AUTHOR Mark Philip
NUTLEY

DEGREE Ph.D

AWARDING BODY Warwick University

DATE 1994

THESIS NUMBER DX182698

NEUTRON SCATTERING STUDIES OF MAGNETIC PROPERTIES OF SUPERCONDUCTORS.

Being submitted for the Degree of Doctor of Philosophy

at the University of Warwick by

Mark Philip Nutley. B.Sc. (Warwick).

The Department of Physics, University of Warwick, U.K.

The Institut Max Von Laue - Paul Langevin, Grenoble, France.

March 1994.

VARIABLE PRINT QUALITY

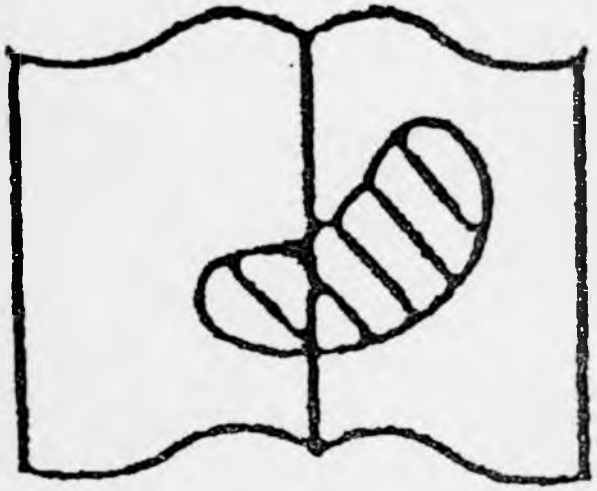

Abstract

The magnetic properties of conventional and high-temperature superconductors have been investigated using several neutron scattering techniques.

Elastic-neutron diffraction measurements have been performed upon a single crystal of $PrBa_2Cu_3O_{7-\delta}$ to explore the nature of the magnetic order. At T_{N1}, which is above room temperature for all δ, the Cu spins in the CuO_2 planes order in a simple antiferromagnetic arrangement with the spins lying within the **a-b** plane. At a lower temperature, at T_{N2}, the chainer Cu spins also order antiferromagnetically in the **a-b** plane forcing an overall non-collinear configuration of Cu spins. T_{N2} was found to be strongly dependent on the oxygen concentration of the crystal. No long-range magnetic ordering of the Pr spins was observed down to 1.9K, although strong two-dimensional short-range correlations of the Pr spins were observed at temperatures up to 20K, with the Pr spins aligning antiferromagnetically along the **c** direction. The failure of the onset of long-range magnetic order is attributed to frustration in the crystal caused by impurities and substitutional defects. These strong two-dimensional short-range correlations, at uncharacteristically high temperatures, provide possible evidence of the hybridisation of the Pr 4f electrons with the conduction electrons of the CuO_2 planes.

The magnetisation density induced by an applied field in $PrBa_2Cu_3O_{7-\delta}$ has been measured by polarised-neutron diffraction. The magnetisation density distribution at the Pr site is found to differ strongly from a spherical free-ion distribution with the magnetisation density extending towards the Cu sites in the CuO_2 planes. This distortion from a free-ion density distribution again supports the hypothesis of the hybridisation of the Pr 4f electrons with the conduction electrons of the CuO_2 planes.

Polarised-neutron reflectrometry has been used to study the evolution of the magnetic induction profile at the surface of a superconducting Pb film with increasing applied field. In the bulk superconducting state the spin-dependent reflectivity profiles are consistent with a pure exponential decay of the magnetic induction with a penetration depth of (390 ± 10) Å. In the surface superconducting region the reflectivity profiles are accurately described over the whole range of applied fields by the Ginsburg-Landau theory if the Ginsburg-Landau parameter, κ, is allowed to vary.

Declaration.

The work contained in this thesis is my own, except where specifically stated as otherwise, and was based at the Department of Physics at the University of Warwick and the Institut Max Von Laue - Paul Langevin, Grenoble.

No part of this work has previously been submitted to this or any other academic institution for admission to a higher degree. Some of the work has already appeared in the form of publications which are listed at the end of the reference section.

CONTENTS

CHAPTER THREE

Instrument and experimental techniques.

CHAPTER FOUR

Magnetic ordering in $PrBa_2Cu_3O_{7-\delta}$.

CHAPTER FIVE

Magnetisation density in $PrBa_2Cu_3O_{7-\delta}$.

CHAPTER SIX

The penetration of a magnetic field into superconducting lead.

Acknowledgements.

I would like to express my sincere thanks to all my friends and colleagues who have contributed in one way or another to the realisation of this thesis. In particular, special thanks are due to Dr Andrew Boothroyd, (Clarendon Lab, Oxford), who as well as instigating and actively participating in this research provided support and friendship throughout the last three years. I would also like to thank my two supervisors, Dr Garry McIntyre (Institut Laue-Langevin) and Prof Stuart Palmer (University of Warwick), for their advice and encouragement over a turbulent and eventful three years.

The experimental results contained within this thesis have been gathered from neutron sources around Europe and I would like to thank collectively the individual research institutions, technicians and our collaborators within them. Special thanks are due to Niels Hessel-Andersen and Hélène Casalta at RisØ, Béatrice Gillon, Phillipe Raison and Robert Dufour at Saclay, Jeff Penfold, John Webster and Peter Philips at ISIS and Patrick Feder at the ILL.

Additionally thanks must also go to Bernard Barbara, (CNRS, Grenoble), for his hospitality and help during the difficulties encountered with the shut-down of the ILL, and Steve Bramwell (ILL) for fruitful discussions.

I would like to acknowledge the Institut Laue Langevin and the former SERC for their financial support.

Finally ,and by no means least, I would like to thank my friends in Warwick and Grenoble who have help make the last three years so enjoyable, especially the ILL guys, the former SSB, Adrian, Ade, Mieke, Karin, all my old flatmates, Saxo, Nick, Deep, Roger, Nancy and Spike the dinosaur ... and finally I dedicate this thesis to my family, especially my Grandfather.

INTRODUCTION

A clear understanding of the magnetic properties of superconducting materials could yield valuable insight into the phenomenon of superconductivity as well as being of great interest for our general understanding of magnetism. Neutron scattering provides an excellent tool for the examination of the magnetic properties of materials due to the neutron possessing no net charge and a magnetic moment. The neutron is therefore able to penetrate deep into the bulk of materials and is able to interact with the magnetic moments of unpaired electrons. In this thesis several magnetic properties of conventional and high temperature (high-T_c) superconductors are examined using various neutron scattering techniques.

In high-T_c superconductivity when Pr is doped into the $YBa_2Cu_3O_{7-\delta}$ superconductor the superconducting transition, T_c, decreases as the amount of Pr increases until superconductivity is entirely suppressed at a composition of $Y_{0.5}Pr_{0.5}Ba_2Cu_3O_{7-\delta}$, (Liang et al. 1987). In contrast, the doping of the other rare-earth ions into $YBa_2Cu_3O_{7-\delta}$, has very little effect on the T_c of ~90K, (Hor et al. 1987). In addition there is also evidence that the Pr member of the $ReBa_2Cu_3O_{7-\delta}$ family of materials, where Re is a rare-earth ion, also has an anomalous magnetic behaviour. The Re^{3+} ion spins, within the superconducting compounds, all order antiferromagnetically below 2.5K while the Pr spins appear to order at the surprisingly high temperature of 17K, (Li et al. 1989). The mechanism for this anomalous behaviour of $PrBa_2Cu_3O_{7-\delta}$ is still a matter of debate and its explanation could aid the general understanding of the origins of high-T_c superconductivity. There is considerable experimental and theoretical evidence that this behaviour may be due to a magnetic interaction between the magnetic moments on the Pr sites and the conduction electrons of the CuO_2 planes. Such an interaction

might localise the current-carrying holes and hence inhibit superconductivity and provide a super-exchange interaction for the Pr spins.

In an attempt to correlate the mechanism of magnetic exchange and high-T_c superconductivity we made a detailed study of the magnetic structure of $PrBa_2Cu_3O_{7-\delta}$. Up to the present, experiments on the magnetic order of Pr in $PrBa_2Cu_3O_{7-\delta}$ have only been performed using polycrystalline samples. We have performed several single-crystal neutron diffraction studies, upon a $PrBa_2Cu_3O_{7-\delta}$ crystal in various oxygenation states, in order to determine accurately the various ordered magnetic states of the Cu and Pr magnetic moments and to study the dependence of these ordered states on temperature.

Additionally, we have attempted to observe directly the possible hydridisation of the Pr 4f electrons with the conduction electrons of the CuO_2 planes using polarised-neutron diffraction. We have performed a polarised-neutron diffraction experiment upon a single crystal of $PrBa_2Cu_3O_{7-\delta}$ in order to accurately determine the magnetisation density distribution within the crystal unit cell.

From the Ginsburg-Landau model of conventional superconductivity, superconductivity was predicted to persist in a narrow surface region of a material above the critical applied magnetic field for the bulk superconducting state, (Saint-James and de Gennes. 1963), a phenomenon known as surface superconductivity. The detailed investigation of the surface superconducting region has proved difficult since only a small fraction of the sample is in the superconducting state. Polarised-neutron reflectrometry (Felcher. 1981), a surface sensitive technique, has been used to investigate this region within Pb films. The existence of a surface superconducting layer produces a variation in the magnetic induction profile as a function of depth in the sample and hence a contrast mechanism for the scattering of neutrons. The aim of this series of experiments was to study the evolution of the surface

superconducting region with applied field and to determine the validity of the Ginsburg-Landau theory in both the bulk and superconducting regions.

CHAPTER ONE

ASPECTS OF SUPERCONDUCTIVITY.

1.1 Introduction.

In the early part of this century Kammerlingh Onnes discovered that the dc resistivity of mercury fell to zero below 4.2 K, and thus first observed the phenomenon which would be known as superconductivity, (Kammerlingh Onnes. 1911). Materials which were considered as superconductors exhibited two distinct characteristics, zero resistivity and zero magnetic induction within the bulk of the material, in a weak external field. Throughout the next 75 years, wide interest in superconductivity developed, although it remained a low-temperature phenomenon, with a reasonable number of elements and materials found to be superconducting below 25 K. By the late sixties a complete microscopic theory, BCS theory, had been developed which provided an accurate explanation of the observed physical properties of superconductors, (Bardeen et al 1957). The basis of this theory was an attractive interaction, mediated by phonons, between electrons near the Fermi surface. Pairs of electrons, known as 'Cooper pairs', condense into a lower energy state in which each electron has an opposite momentum and spin to its pair. As these 'Cooper pairs' all move with a single coherent motion local perturbations cannot scatter an individual pair and hence the collective group of 'Cooper pairs' may flow without a dissipation of energy.

In 1986 an important breakthrough in the field of superconductivity occurred when Bednorz and Muller, 1986, discovered superconductivity in cuprate oxides at 30K. This led to a revolution in the field and shortly after, superconducting materials were discovered which were superconducting above liquid nitrogen temperatures. The discovery of these high-temperature superconductors, which could not be satisfactorily explained using the

conventional BCS theory, opened up the field of high-Tc superconductivity, (for a general overview of the historical developments see e.g Cyrot and Pavuna. 1992)

1.2 The field penetration into a bulk superconductor.

The principal magnetic property, and basic characteristic, of all superconducting materials is the exclusion of a magnetic field from the bulk of the superconductor, an effect known as the Meissner effect (Meissner and Oschenfeld. 1933). The vanishing magnetic induction in the interior of the material is due to induced surface currents whose magnitude and distribution are such that they create an opposing internal field cancelling out the applied field. The magnetic induction, B(x), does not drop to zero discontinuously at the surface but decays over a characteristic length, λ_p, known as the penetration depth and defined by

$$\lambda_p = \frac{1}{B_a}\int_0^{\infty} B(z)\, dz \qquad (1.1)$$

where $B_a = \mu_0 H_a$, H_a is the applied field and z is the distance measured normal to the surface. (*Note: The penetration depth is conventionally denoted simply by λ in order to avoid confusion with the neutron wavelength, also conventionally denoted by λ, we denote the penetration depth by λ_p and the London penetration depth by λ_L throughout this thesis.)

Shortly after the discovery of the Meissner effect, London and London (1935) developed a macroscopic model for the electromagnetic behaviour of a superconductor based upon a local relationship between the current density, J(r), and the vector potential associated with the magnetic field, A(r). This relationship can be written as

$$J(r) = -\frac{ne^2}{m} A(r) \qquad (1.2)$$

where n is the density of the superconducting particles, of charge e and mass m. The application of Maxwell's equations, within the London theory, leads to an exponential decay of the magnetic induction with increasing depth into the superconductor, characterised by a London penetration depth, λ_L where

$$B(z) = B(0) \exp(- z/\lambda_L) \tag{1.3}$$

Experimental values obtained for the penetration depth were generally several times larger than predicted and also showed a purity and sample size dependence not permitted within the London theory.

The failure of the London theory was explained by Pippard (1953) who proposed that the London equation was the limiting form of a more general non-local relationship, between the current density and vector potential, described by

$$J(\mathbf{r}) = -\frac{3ne^2}{4\pi\xi_0 m} \int \frac{\mathbf{R}(\mathbf{R} \cdot \mathbf{A}(\mathbf{r}'))}{R^4} \exp(- R/\xi)\, d^3\mathbf{r}' \tag{1.4}$$

where ξ is a coherence distance over which order extends in the superconductor, $\mathbf{r}$ and $\mathbf{r}'$ are the positions of the electrons of each Cooper pair and $\mathbf{R} = \mathbf{r} - \mathbf{r}'$. In the limit where $\mathbf{A}(\mathbf{r}')$ varies very little over length scales of the order ξ then equation 1.4 is the same as equation 1.2. The range of coherence, commonly known as the coherence length, is dependent on the mean free path, l, of superconducting electrons and is related to the coherence length of a pure superconductor, ξ_0 ($\xi \rightarrow \xi_0$ as $l \rightarrow \infty$), by

$$\frac{1}{\xi(l)} = \frac{1}{\xi_0} + \frac{1}{\alpha l} \tag{1.5}$$

where α is a constant of order unity. The validity of the non-local Pippard equation is strongly supported by BCS theory (Bardeen et al. 1957) and an entirely equivalent non-local relationship follows directly from BCS theory.

From the non-local relationship the penetration depth can be evaluated explicitly in two limiting cases :

$$\lambda_p = \left(\frac{\xi_0 \lambda_L}{\xi}\right)^{\frac{1}{2}} \qquad \text{for } \xi >> l, \quad \text{(London limit)} \qquad (1.6)$$

and

$$\lambda_p = \left(\frac{\sqrt{3}}{2\pi} \xi_0 \lambda_L^2\right)^{\frac{1}{3}} \qquad \text{for } \xi << l, \quad \text{(Pippard limit)} \qquad (1.7)$$

The application of the non-local relationship within BCS theory leads to small deviations from an exponential decay and, in some cases, even a reversal in the sign of the magnetic induction within the superconductor is possible (Drangeid and Sommerhalder. 1962).

1.3 Ginsburg-Landau theory.

In 1950, Ginsburg and Landau introduced a phenomenological approach to superconductivity based upon Landau's work on second-order phase transitions (for a detailed description of Ginsburg-Landau theory and its application to superconductivity see Lynton. 1964, Parks. 1969, Tilley and Tilley. 1986). This approach modified the London theory, as did later Pippard (1953), by breaking the rigidity of the superconducting wave function and introducing an order parameter, Ψ, which was the measure of the order in the superconducting state. It can also be assumed that the order parameter is equivalent to an 'effective' wave function of the superconducting electrons. The important consequence of this assumption is that Ψ is complex and varies in space. Ψ is defined to be zero in the non-superconducting phase and unity in the superconducting phase at zero temperature, in a zero applied field.

The Ginsburg-Landau theory expresses the free energy density of a superconductor, G_s, in terms of Ψ and the vector potential, $\mathbf{A}$, that describes an applied magnetic field, $\mathbf{H}$, :

$$G_s(H) = G_n(0) + \alpha|\psi|^2 + \frac{\beta}{2}|\psi|^4 + \frac{h}{2m^*}\psi^*\left|\left(i\nabla + \frac{e^*\mathbf{A}}{c}\right)\right|^2\psi + \int_0^B H\,dB \qquad (1.8)$$

where G_n is the free energy of the normal paramagnetic state in zero field, α and β are Landau parameters, m^* and e^* are the effective mass and charge of the superconducting pairs, and B is the local internal magnetic induction. Minimisation of the total free energy with respect to Ψ and $\mathbf{A}$ leads to two equilibrium equations, known as the Ginsburg-Landau equations and commonly written as

$$\frac{h}{2m^*}\left|\left(i\nabla + \frac{e^*\mathbf{A}}{c}\right)\right|^2\psi + \frac{\partial G_s(0)}{\partial\psi^*} = 0 \qquad (1.9)$$

$$\nabla^2\mathbf{A} = -\frac{4\pi}{c}\mathbf{J}_s = \frac{2\pi i e^{*2}h}{m^*c}\left[\psi^*\nabla\psi - \psi\nabla\psi^*\right] + \frac{4\pi e^{*2}}{m^*c^2}|\psi|^2\mathbf{A} \qquad (1.10)$$

where $\mathbf{J}_s$ is the superconducting current. In a very weak field, $H \approx 0$, Ψ remains practically constant, and equation 1.10 reduces to

$$-\frac{4\pi}{c}\mathbf{J}_s = \frac{4\pi e^{*2}}{m^*c^2}|\psi|^2\mathbf{A} \qquad (1.11)$$

These coupled non-linear Ginsburg-Landau equations have been solved for a number of simple one-dimensional problems. Important successes of this theory include the prediction of the correct dependence with temperature of the critical field for a superconducting region, close to the transition temperature, and an explanation of the large positive energy needed to explain the Meissner effect. Other calculations have also showed a change of sign of the surface energy for $\kappa = 0.707$, where $\kappa = \lambda_p/\xi$, the Ginsburg-Landau parameter which helped define the difference in behaviour between type I and II superconductors. (For type II superconductors, an additional phase exists in which superconducting regions coexist with normal regions between two critical fields, H_{c1} and H_{c2}, e.g. see Parks. 1969).

Ginsburg-Landau theory represents a generalisation of London's theory and therefore is effectively a local theory and distinct from the non-local theories of Pippard (1953) and BCS (1957). However, a full examination of BCS theory reveals the essentially correct nature of Ginsburg-Landau theory, and as the Ginsburg-Landau equations are much simpler than BCS theory they are often used to provide a valuable insight into the general aspects of superconductivity. An additional problem is that Ginsburg-Landau theory is valid only near the transition between the normal metallic state and the superconducting state because the free energy, equation 1.8, is actually a power series in $|\Psi|^2$ and so only applies when $|\Psi|^2 << 1$. The domain of validity of these equations may be increased by relaxing several of the restrictions on the free energy while remaining within the scope of the microscopic theories. Ginsburg-Landau theory can be particular useful in the domain of surface effects and in relating the two length parameters of superconductivity, the penetration depth, λ_p, and the coherence length, ξ.

1.3.1 Surface superconductivity.

In 1963, theoretical calculations by Saint-James and de Gennes, based upon Ginsburg-Landau theory, predicted an additional superconducting phase which extended to a depth of the order of the coherence length from the surface of a material above an applied field which was sufficient to drive the bulk material normal, (Saint-James and de Gennes. 1963). The existence of this surface superconducting region explained the puzzling discrepancies between the critical fields, for the transition from the superconducting to the normal state, obtained separately from resistive and magnetic techniques.

Saint-James and de Gennes linearised the Ginsburg-Landau equations and applied the boundary conditions for a planar superconductor-insulator interface. These calculations predicted a surface superconducting region, with an upper critical field, H_{c3}, for materials with a $\kappa > 0.42$. The value of H_{c3}

depends upon the angle the applied field makes with the interface and is a maximum when the applied field is parallel to the surface. For a field perpendicular to the interface no surface superconducting region is predicted. The solutions of the Ginsburg-Landau equations are strongly effected by their boundary conditions and as a result a surface superconducting region cannot occur for a superconductor-normal metal interface.

For the particular case of an applied field parallel to the interface H_{c3} can be expressed as

$$H_{c3} = 2.392\ \kappa\ H_{c1}\ , \qquad (1.12)$$

and for type II materials this may be simplified to

$$H_{c3} = 1.695\ H_{c2} \qquad (1.13)$$

The predicted variation of H_{c3} on the value of κ, along with the critical fields H_{c1} and H_{c2}, can be seen more clearly in figure 1.1, (Tinkham. 1975).

The work of Saint-James and de Gennes (1963) stimulated much interest and experimental activity in the phenomenon of surface superconductivity. Shortly after their work the existence of a surface superconducting region was confirmed, for both type I and type II superconductors, by various experimental techniques, including magnetisation measurements (Tomasch and Joseph. 1964), resistivity measurements (Hempstead and Kim. 1964) and ac susceptibility measurements (Strongin et al. 1964). Due to the dependence of H_{c3} on κ (equation 1.12) surface superconductivity investigations also provided an accurate technique for determining κ for type I superconductors, (Rosenblum and Carbona. 1964b, Seidel and Meissner. 1965).

The linearised Ginsburg-Landau equations, used by Saint-James and de Gennes, are only strictly valid near H_{c3}, where Ψ is much smaller than its value in a zero field, Ψ_0. For arbitrary fields the full non-linear Ginsburg-Landau equations must be considered. These non-linear equations have been

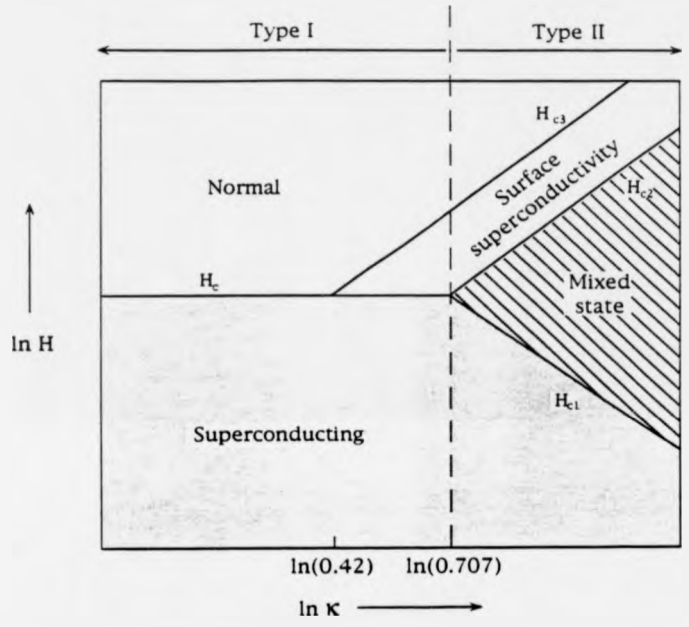

Figure 1.1: Dependence of the characteristic critical fields of superconductors on the value of the Ginsburg-Landau constant, κ. H_{c3} is the value of the limiting field strength for surface superconductivity when the applied field is parallel to the surface, (figure 13.12, Tinkham. 1975).

solved using an iterative numerical calculation. (Felici and Gray. 1984), and have enabled the variation of the magnetic induction and order parameter, with respect to the distance from the surface, to be calculated explicitly. These calculations have shown a maximum diamagnetism for $\kappa \sim 0.707$ in an applied field slightly greater than H_{c2}. The variation of the magnetic induction profile and the behaviour of Ψ with applied field, for $\kappa = 0.5$, is shown in figure 1.2.

1.4 The $ReBa_2Cu_3O_{7-\delta}$ class of superconductors.

After the discovery of superconductivity above 90K in $YBa_2Cu_3O_{7-\delta}$ (Wu et al. 1987), further investigations revealed an entirely new class of superconductors of the form $ReBa_2Cu_3O_{7-\delta}$, where Re is a rare earth element, (e.g. Yang et al 1987 and Hor et al. 1987). Surprisingly the substitution of the trivalent rare earth ion for Y was found not to change the superconducting properties significantly, even though most of the rare earth ions have partially filled 4f electron shells and an associated magnetic moment. This is in contrast to the situation for conventional superconductors where small concentrations of paramagnetic ions are found to suppress strongly the transition temperature, T_c, (Maple. 1973) The only known exception within this class of materials is where the rare earth element is Pr. (Attempts to prepare the compounds $CeBa_2Cu_3O_{7-\delta}$ and $TbBa_2Cu_3O_{7-\delta}$, with the same structure as $YBa_2Cu_3O_{7-\delta}$, have failed (Yang et al. 1988), and $PmBa_2Cu_3O_{7-\delta}$ has not been prepared because of the short half life of the radioactively unstable Pm nucleus. Therefore the only truly non-superconducting member of this series is $PrBa_2Cu_3O_{7-\delta}$.)

The superconducting properties of $ReBa_2Cu_3O_{7-\delta}$ show little variation with the choice of Re^{3+} ion, with the exception of Pr. The transition temperatures, for $\delta = 0$, are typically between 90K and 94K, and decrease with increasing δ until $\delta = 0.6$ where superconductivity is destroyed and the material becomes

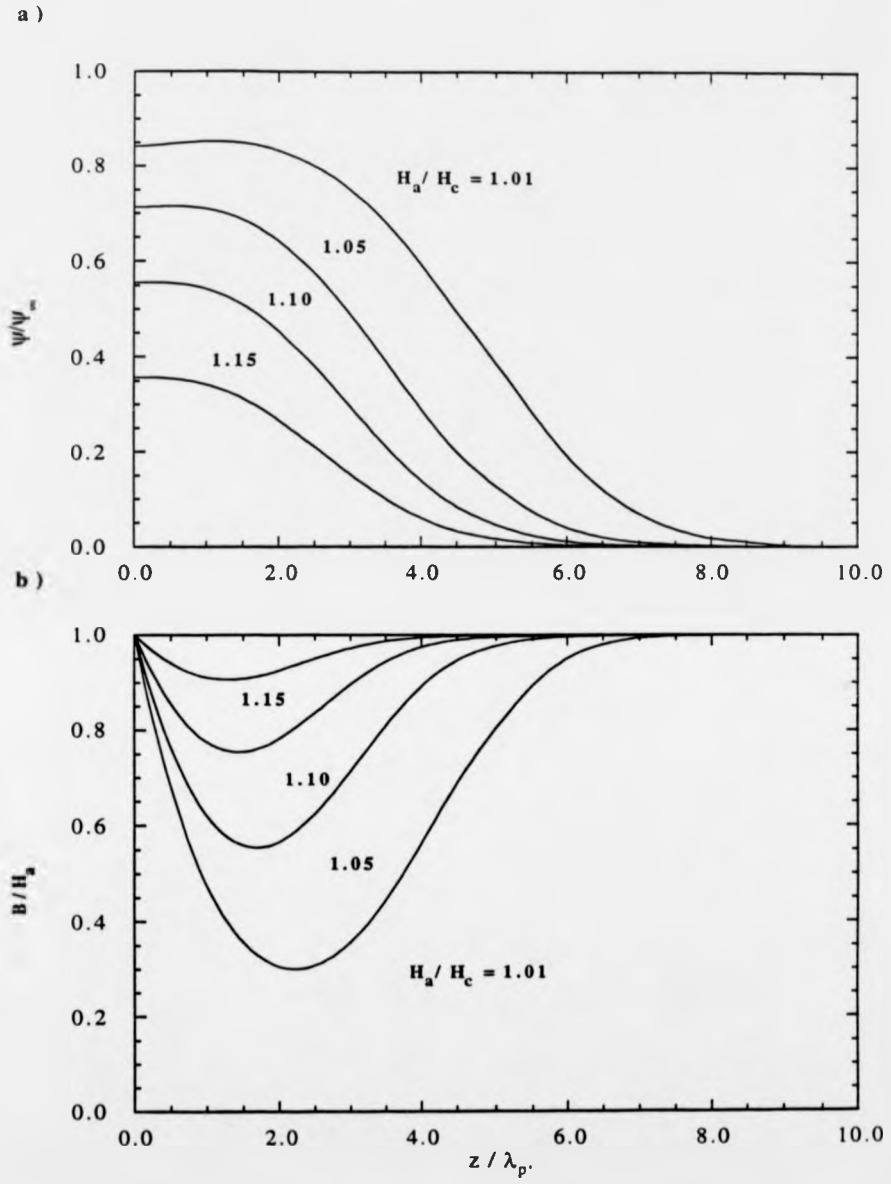

Figure 1.2: The magnetic induction, (a), and the superconducting order parameter, (b), are plotted as a function of distance from the surface of a superconductor for κ = 0.5 and for various indicated values of the reduced applied field H_a/H_c, (calculated upon the same basis as figure 3, Felici and Gray. 1984.).

insulating, (e.g. Hor et al. 1987 and Cava et al. 1987). In addition to these high values of T_c, the $ReBa_2Cu_3O_{7-\delta}$ compounds have very large values of the upper critical magnetic fields $H_{c2}(T)$ (Orlando et al. 1987). Measurements of the initial slopes of H_{c2}, $\left(\frac{dH_{c2}}{dT}\right)_{T_c}$, on polycrystalline samples, have also revealed no systematic dependence on the ionic radii. For all the $ReBa_2Cu_3O_{7-\delta}$ compounds, direct resistance measurements on epitaxially grown films, (Chaudhari et al. 1987), and indirect magnetisation techniques, (Ferriera et al. 1987), have found critical currents of 10^6-10^7 Acm^{-2} for current flow in the **a - b** planes, at liquid helium temperatures. (For a more detailed examination of the superconducting properties of the $ReBa_2Cu_3O_{7-\delta}$ compounds see Markert et al. 1989.)

The structure of these compounds has been well established using neutron powder and single-crystal diffraction. It is a layered, orthorhombic, perovskite-like structure, with space group Pmmm, (eg Jorgensen et al. 1987 and McIntyre et al. 1988). The main features of the structure are two nearly-square-planar $Cu\text{-}O_2$ layers, separated by the Re^{3+} ion, weakly bonded through Cu-O-Cu bonds to one-dimensional Cu-O chains, see figure 1.3. The charge carriers involved in the superconductivity are generally believed to be holes in the $Cu\text{-}O_2$ planes whose concentration is governed by the concentration of oxygen vacancies in the Cu-O chains. The variation of this structure with the different sized rare-earth ions has been systematically examined and the lattice parameters and interionic distances have been found to vary linearly with the ionic radius, see figure 1.4 (e.g Guillaume et al. 1993).

1.5 The anomalous behaviour of $PrBa_2Cu_3O_{7-\delta}$.

In contrast to the other rare earths the substitution of Pr for Y in $YBa_2Cu_3O_{7-\delta}$ suppresses T_c while maintaining the same crystal structure.

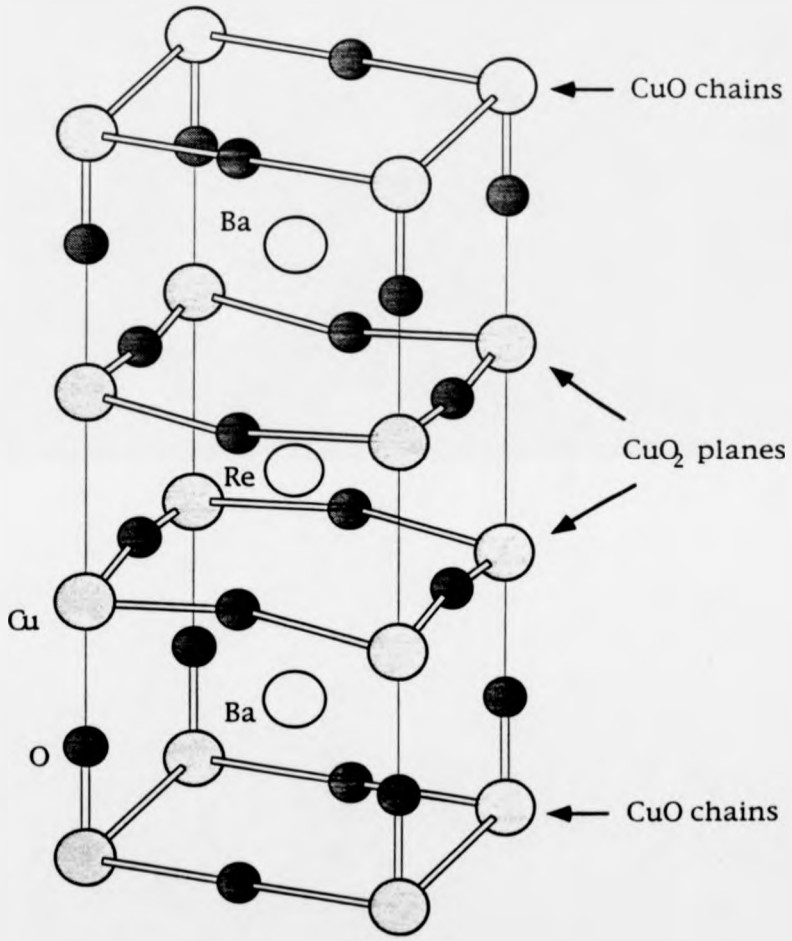

Figure 1.3: The unit cell of the orthorhombic $ReBa_2Cu_3O_{7-\delta}$, where Re is a rare-earth element.

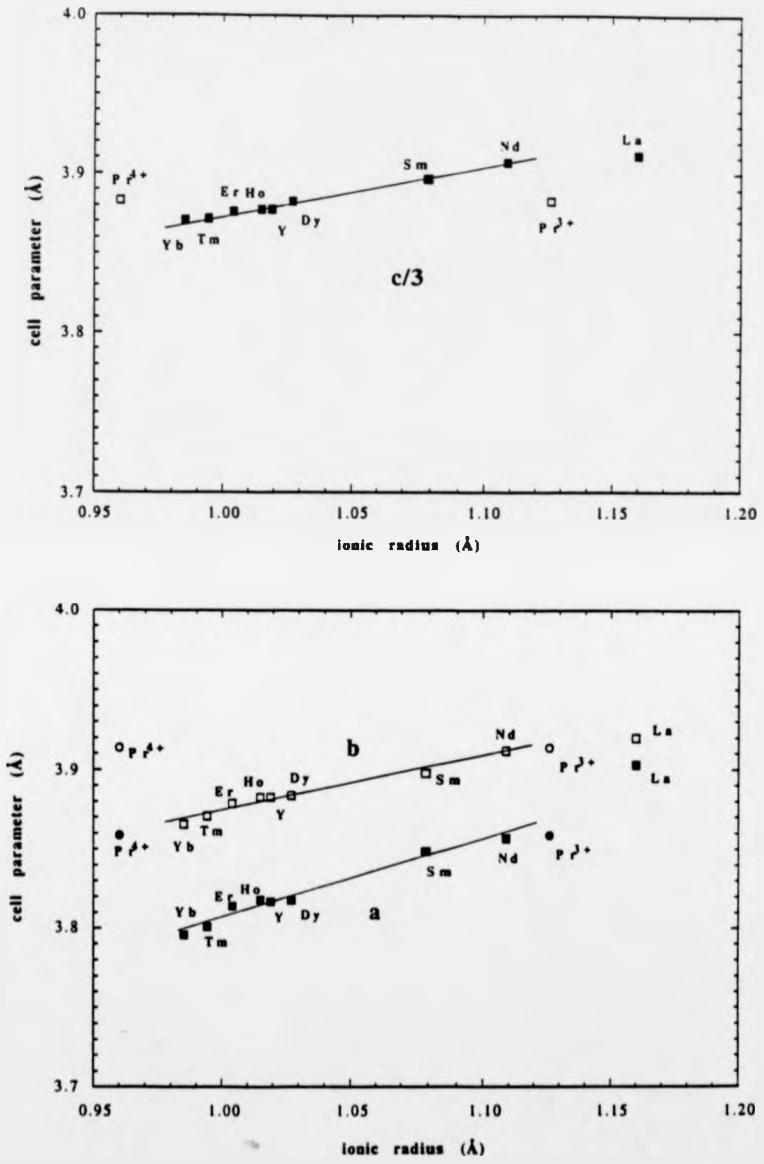

Figure 1.4: The Lattice parameters a, b and c/3 of $ReBa_2Cu_3O_7$ versus the radius of the trivalent Re ions, (see figure 3, Guillaume et al. 1993).

Studies of $Y_{1-x}Pr_xBa_2Cu_3O_{7-\delta}$ have shown that T_c decreases monotonically with x, with superconductivity completely destroyed between x = 0.5 and 0.6, see figure 1.5 (Soderholm et al. 1988, Liang et al. 1987, Neumeier and Maple. 1992). Additionally a unique transition from a metallic to a semiconducting behaviour of the normal state resistivity is observed at x = 0.4 (Dalichaouch et al. 1988). As well as its non-superconducting nature, $PrBa_2Cu_3O_{7-\delta}$ differs significantly from the other $ReBa_2Cu_3O_{7-\delta}$ materials in that the Pr moments are believed to order antiferromagnetically at ~17K, a factor of ten higher than expected based on RKKY scaling of T_N from the other $ReBa_2Cu_3O_{7-\delta}$ compounds, (Li et al. 1989 and Kebede et al. 1989).

This anomalous behaviour has lead to a large amount of research into $PrBa_2Cu_3O_{7-\delta}$ with the goal of identifying and understanding the reason for its non-metallic nature, and the absence of superconductivity. Identifying the correct mechanism might also help in the general understanding of high-T_c superconductivity. In spite of this wide interest the mechanism for the suppression of superconductivity remains unresolved. Two basically different mechanisms have been proposed to account for the behaviour of $PrBa_2Cu_3O_{7-\delta}$. One attributes the behaviour to a Pr valence state greater than +3 which results in the filling of holes in the CuO_2 conduction band, commonly known to as 'hole filling' and the second argues that Pr is primarily +3, so no hole filling occurs, and the absence of superconductivity is based upon hybridization effects between the Pr 4f electrons and the CuO_2 conduction electrons.

1.5.1 The hole filling mechanism.

The hole-filling mechanism is based upon a valence state for Pr greater than the one which occurs for the rare-earths (+3) in the superconducting members of the $ReBa_2Cu_3O_{7-\delta}$ series. A valence state greater than +3 would explain the lack of superconductivity and the semiconductor nature of

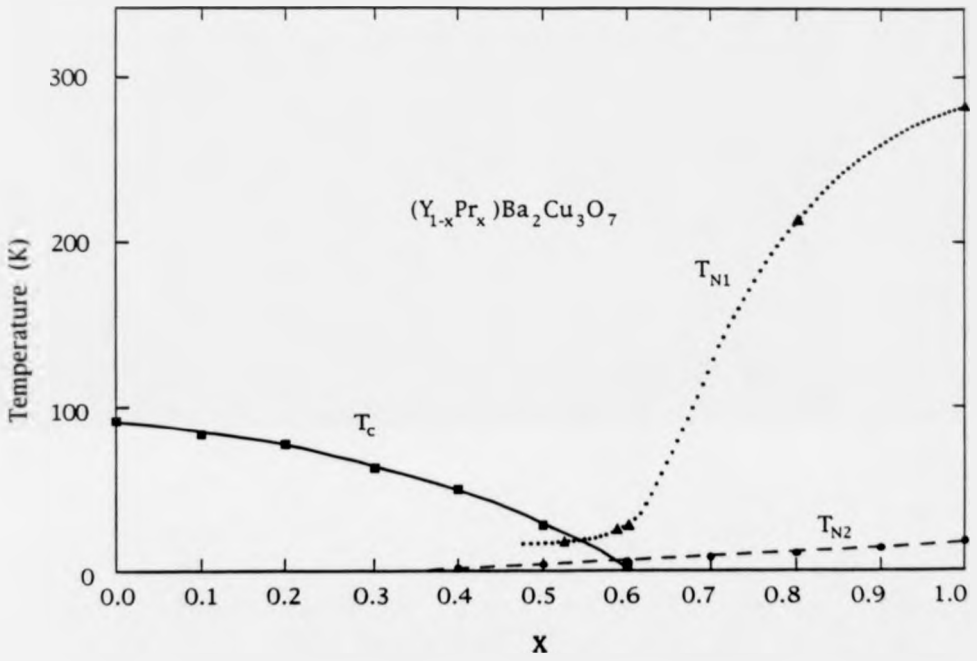

Figure 1.5: The phase diagram for $(Y_{1-x}P_x)Ba_2Cu_3O_{7-\delta}$. T_{N1} corresponds to antiferromagnetic ordering of the Cu moments within the Cu-O planes as determined by zero-field μSR measurements. T_{N2} is attributed to Pr moment ordering, (see figure 3, Cooke et al. 1990).

$PrBa_2Cu_3O_{7-\delta}$ since the additional electrons contributed by the $Pr^{>3+}$ ions would be expected to fill the mobile holes within the CuO_2 planes, effectively localising the holes on the Pr site (Wood. 1991 and Radousky. 1992). The validity of this mechanism, and the actual valency of Pr, is a point of strong debate and has not been fully resolved experimentally.

Experimental evidence of the +4 valence state can be found from studies of the superconductors $Pr_{0.5}Ca_{0.5}Ba_2Cu_3O_{7-\delta}$ and $Y_{1-x-y}Ca_yPr_xBa_2Cu_3O_{7-\delta}$ ((Norton et al. 1991 and Neumeier et al. 1989 respectively). It may be argued that the presence of superconductivity within these materials is due to the Ca^{2+} ions, which substitute on the rare-earth ion site, thereby introducing additional holes in the CuO_2 planes which compensates for the hole-filling from the Pr^{4+} ions. The fact that $Pr_{0.5}Ca_{0.5}Ba_2Cu_3O_{7-\delta}$ is superconducting with $T_c \approx 35K$, whereas $Pr_{0.5}Y_{0.5}Ba_2Cu_3O_{7-\delta}$ is only superconducting at $T_c \approx 0K$, may indicate that hole filling is an important factor in the suppression of superconductivity within $PrBa_2Cu_3O_{7-\delta}$.

Additional experimental evidence, presented in support of the valence of +4, or a 'mixed' valency state came from magnetic susceptibility measurements, (Dalichaouch et al. 1988 and Kebede et al. 1989). Analysis of the data yielded an effective moment, $\mu_{eff} \approx 2.7\mu_B$ per Pr ion by using a Curie-Weiss relationship to describe the behaviour of the magnetic susceptibility with temperature. Comparison with the effective moments for Pr^{3+} and Pr^{4+} free ions, 3.58 μ_B and 2.54 μ_B respectively, suggested a mixed valence state for the Pr ion with an average valence of ≈ 3.9. However it has been strongly counter-argued that this behaviour is in fact entirely consistent with the presence of solely Pr^{3+} ions, (Boothroyd et al. 1993, Soderholm and Goodman. 1989). The basic assumption of the susceptibility measurements, that the Pr ions behave as free ions, can only be made when the electron spins do not interact and when there are no low-lying excited crystal field states which are significantly populated. Several other examples of a non-free-ion-like

behaviour of Pr^{3+} can also be found. For example susceptibility studies of $PrScO_3$ and $BaPrO_3$, in which the valence state of Pr is known to be +3, produced similarly low values for μ_{eff}. The small μ_{eff} found in $PrBa_2Cu_3O_{7-\delta}$ may be due to crystal-field effects, or alternatively the result of hybridization of the Pr 4f electrons with the planar CuO_2 conduction electrons. It is believed that all the susceptibility measurements upon $PrBa_2Cu_3O_{7-\delta}$, can be understood in terms of crystal-field theory for a Pr^{3+} ion, (Boothroyd et al. 1993, Soderholm et al. 1991). In reality the valence state cannot be solely evaluated from susceptibility measurements alone.

Structural evidence for the valence state falls heavily in favour of a +3 valency state. Many structural studies (see for example Lopez-Morales et al. 1990 and Neumeier et al. 1989) have shown that a Pr^{3+} ion is compatible with the linear relationships found to describe accurately the behaviour of the lattice parameters and various bond distances with the varying rare-earth-ion radii, within $ReBa_2Cu_3O_{7-\delta}$. In contrast to the majority of the structural studies some works report that a 'mixed' valence state Pr ion describes the structural properties more accurately. Neumeier et al. 1990 reported that the separation of the CuO_2 planes indicates that Pr ions have an intermediate valence of ~3.3.

Similarly, no conclusive case can be drawn on the valence state from NMR measurements. Conflicting claims of the degree and importance of hole filling in the suppression of superconductivity are made by various groups (Reyes et al. 1991, 1990 and Han et al. 1991).

Photoemission studies of $Y_{1-x}Pr_xBa_2Cu_3O_{7-\delta}$ have suggested that the Pr valence is close to +3 and that the Pr 4f spectral line has a complex shape which implies extensive hybridization between the 4f electrons and the CuO_2 conduction band, (Kang et al. 1989).

The results from more conventional and direct techniques for determining the valency of an ion support the argument of a +3 valence state.

Investigations using electron energy-loss spectroscopy, EELS, have shown that the low energy-loss spectrum for $PrBa_2Cu_3O_{7-\delta}$ closely matches the equivalent spectrum for $YBa_2Cu_3O_{7-\delta}$ which leads to the conclusion that the valence states of Y and Pr are very similar, (Fink et al. 1990). X-ray absorption measurements, XANES, have also found no evidence of a +4 valence state, (Soderholm and Goodman. 1989). The L_{III} absorption edge for Pr in $PrBa_2Cu_3O_{7-\delta}$ is located closely to the position of a standard Pr^{3+} absorption edge and no evidence was found of either a shift to higher energies, as would be expected for a higher valence state, nor any splitting of the absorption peak which would occur if a 'mixed' valence Pr ion was present.

1.5.2 The hybridization mechanism.

An alternative model to explain the absence of superconductivity in $PrBa_2Cu_3O_{7-\delta}$ is based upon the more traditional magnetic pair-breaking mechanism, first proposed by Abrikosov and Gor'kov. 1961, (Peng et al. 1989). In conventional superconductors the presence of magnetic ions is usually incompatible with the superconducting state. In contrast superconductivity in the $ReBa_2Cu_3O_{7-\delta}$ series is generally unaffected by the presence of the magnetic rare-earth ions. This is believed to be due to the complete isolation of the electrons in the CuO_2 planes from the magnetic ions. The exception to this is $PrBa_2Cu_3O_{7-\delta}$ where it is proposed that the 4f electrons hybridize with those from the CuO_2 plane. The unique behaviour of the Pr member is not completely surprising as Pr is located to the far left of the lanthanide series and therefore the Pr 4f wave functions are expected to be more spatially extended than in the other lanthanides. It is speculated that the effect of this hybridization of electrons provides a mechanism that causes a localisation of the conducting holes within the CuO_2 planes resulting in the loss of the metallic and hence the superconducting properties, (Torrance and Metzger. 1989). Electron band calculations confirm that hybridization would be much

stronger in $PrBa_2Cu_3O_{7-\delta}$ than in other $ReBa_2Cu_3O_{7-\delta}$ compounds and consequently the spin splittings of the important CuO_2 conduction bands near the Fermi surface are up to ten times larger in the Pr compound, (Guo and Temmerman. 1990 and Goodman and Soderholm. 1990).

Evidence of a pair-breaking mechanism comes from the behaviour of the transition temperature, T_c, with varying Pr concentration in $Y_{1-x}Pr_xBa_2Cu_3O_{7-\delta}$ (Peng et al. 1989 and Maple et al. 1989). The depression of T_c with the introduction of the Pr magnetic impurities may be modelled well using a conventional pair-breaking approach, (Abrikosov and Gor'kov. 1961). Additionally, the pressure dependence of T_c in $Y_{1-x}Pr_xBa_2Cu_3O_{7-\delta}$ differs markedly from that in $YBa_2Cu_3O_{7-\delta}$ and has also been described well using a pair-breaking approach, (Neumeier et al. 1988).

Inelastic neutron studies have also provided evidence of hybridization, (Boothroyd et al. 1991, 1993, Soderholm et al. 1990, 1991 and Jostarndt et al. 1992). The sharp, well-defined crystal-field transitions in the inelastic neutron scattering spectra, expected for localised Pr states and measured for other $ReBa_2Cu_3O_{7-\delta}$ compounds, have not been observed. In contrast the $PrBa_2Cu_3O_{7-\delta}$ spectra exhibit only broadened transitions. This broadening is attributed to the significant interaction of the 4f states of Pr with the planar CuO_2 conduction electrons.

In comparison with the other $ReBa_2Cu_3O_{7-\delta}$ members, where the highest antiferromagnetic ordering temperature observed for the rare earths is for Gd, with $T_N \approx 2.3K$, the ordering temperature of Pr, $T_N \approx 17K$, is two orders of magnitude higher than that expected from a scaling of T_N for Gd by the respective de Gennes factor, (see section 1.6). The anomalously high value of T_N in the Pr system, in the absence of conduction electrons to mediate the RKKY interaction, can be explained by a considerable hybridization of the 4f electrons within the CuO_2 planes, which may provide an effective superexchange interaction between the Pr ions. In contrast, the Gd^{3+} ions do

not experience such exchange due to the local nature of their 4f moments, (Wortmann and Felner. 1990). This idea is further strengthened by the behaviour of T_N with oxygen concentration in $PrBa_2Cu_3O_{7-\delta}$ (Felner et al. 1989 and Kebede et al. 1991) where T_N is found to decrease below 10K, as oxygen is removed, in contrast to the independence of T_N to oxygen concentration for the other rare-earths members.

Additional evidence supporting this mechanism for the suppression of superconductivity can also be found from the behaviour of the Pauli susceptibility with Pr concentration and the behaviour of the upper critical fields in $Y_{1-x}Pr_xBa_2Cu_3O_{7-\delta}$ (Peng et al. 1989).

1.6 The magnetic properties of $ReBa_2Cu_3O_{7-\delta}$.

The high transition temperatures of the $ReBa_2Cu_3O_{7-\delta}$, series, and those of the other high-T_c materials, cannot be explained in a simple way using the traditional phonon-mediated interaction between the superconducting pairs, as invoked by BCS theory. In view of the presence of magnetism in the CuO_2 planes the possibility exists that magnetic interactions are responsible for the creation of the superconducting pairs. (Note : for a detailed discussion of the magnetic properties of the $ReBa_2Cu_3O_{7-\delta}$, series see Markert et al. 1989.)

Two types of antiferromagnetic ordering, within the $ReBa_2Cu_3O_{7-\delta}$ series, have been observed. The Cu^{2+} ions, of spin = 1/2, have been found to order three-dimensionally at surprisingly high temperatures in non-superconducting, oxygen-deficient samples, with a Néel temperature, T_N, that increases with δ and can reach ~500K at δ = 1. The systematic appearance of long-range antiferromagnetic order of the Cu^{2+} moments as superconductivity is destroyed supports the hypothesis that a mechanism of magnetic origin may be responsible for both phenomena. Similarly, within the $La_{2-x}M_xCuO_{4-\delta}$ series, where M = Ba or Sr, the destruction of antiferromagnetic order and the appearance of superconductivity also

appears to be coupled. Various theoretical models exist, based upon a magnetic interaction, ranging from the 'resonating valence band' model (Anderson. 1987), to one which assumes that the holes, on the O site, are paired or localised depending on the the degree of order of the Cu spins, (Emery. 1987 and Hirsch et al. 1987). At much lower temperatures, $T < 2.5K$, the rare earth ions have also been found to order antiferromagnetically, for all oxygen concentrations. A full understanding of the interaction responsible for rare-earth ordering in this region of coexistence of superconductivity and magnetic order, may enable a clearer picture of the underlying electronic structure to be obtained, which in turn may aid our understanding of high-T_c superconductivity.

1.6.1 The antiferromagnetic ordering of Cu.

Various neutron diffraction studies have been performed to investigate the appearance of Cu spin ordering and have shown a consistent behaviour across the $ReBa_2Cu_3O_{7-\delta}$, series, (Lynn et at. 1988 and references therein). A typical example is the behaviour of $YBa_2Cu_3O_{7-\delta}$, where superconductivity is observed up to $\delta \approx 0.6$, and at slightly larger values of δ antiferromagnetic ordering of the planar Cu^{2+} ions occurs, with a Néel temperature, T_N, that increases approximately linearly with δ and reaches ~500K at $\delta = 1$, (Burlet et al. 1988 and Tranquada et al. 1988). A second magnetic transition has been observed, at lower temperatures, which is associated with the ordering of the Cu^{2+} moments in the Cu-O chains, (Kadowaki et al. 1988). The absence of a region of overlap between the two phenomena, superconductivity and antiferromagnetic order, is a common feature of all high-T_c materials. The high three-dimensional ordering temperature however indicates that the magnetic energies are large and that strong two-dimensional magnetic correlations may be expected at even higher temperatures, or higher values of δ and hence possibly into the superconducting regions.

Single-crystal neutron-diffraction studies have provided a detailed picture of the antiferromagnetic order within several of these materials (eg Li et al. 1988). At the higher transition temperature, T_{N1}, the Cu^{2+} spins in the CuO_2 planes order antiferromagnetically with the magnetic moments aligned in the **a** - **b** plane while the Cu^{2+} ions in the chains remain disordered. The Cu^{2+} moments within the CuO_2 planes are also coupled antiferromagnetically along the **c** direction. The disordered state of the Cu moments within the chains may possibly be due to weaker coupling caused by the reduced amount of oxygen in these layers. At the lower transition temperature, T_{N2}, the Cu^{2+} spins within the Cu-O chains also begin to order antiferromagnetically. At temperatures close to 0K the full magnetic structure is a collinear antiferromagnetic arrangement of spins along the **c** axis, with the moments lying in the **a** - **b** plane, (see figure 1.6). At intermediate temperatures, $0 < T < T_{N2}$, a non-collinear spin structure exists, deduced from the the temperature dependence of several magnetic diffraction peaks (see figure 1.7), due to the competition between the two different stacking arrangements. The precise values for T_{N1} and T_{N2} are found to be highly sensitive to the oxygen concentration.

A full study of the Cu ordering as function of δ has not been made for the non-superconductor $PrBa_2Cu_3O_{7-\delta}$. In one previous investigation, on crystals of $PrBa_2Cu_3O_{7-\delta}$ that had been exposed to different oxygen treatments, differences were found from the typical $ReBa_2Cu_3O_{7-\delta}$ behaviour, (Rosov et al. 1992). The ordering of the planar Cu ions was found to be insensitive to δ, and T_N remained ~370K for all δ. By contrast the ordering along the chains was found to vary strongly with δ and fell from T_N ~370K at $\delta = 0$ to T_N ~160K for $\delta \simeq 0.6$. Additionally the spins of the Cu ions within the chains were found to have a spin component out of the basal plane, (see figure 1.6).

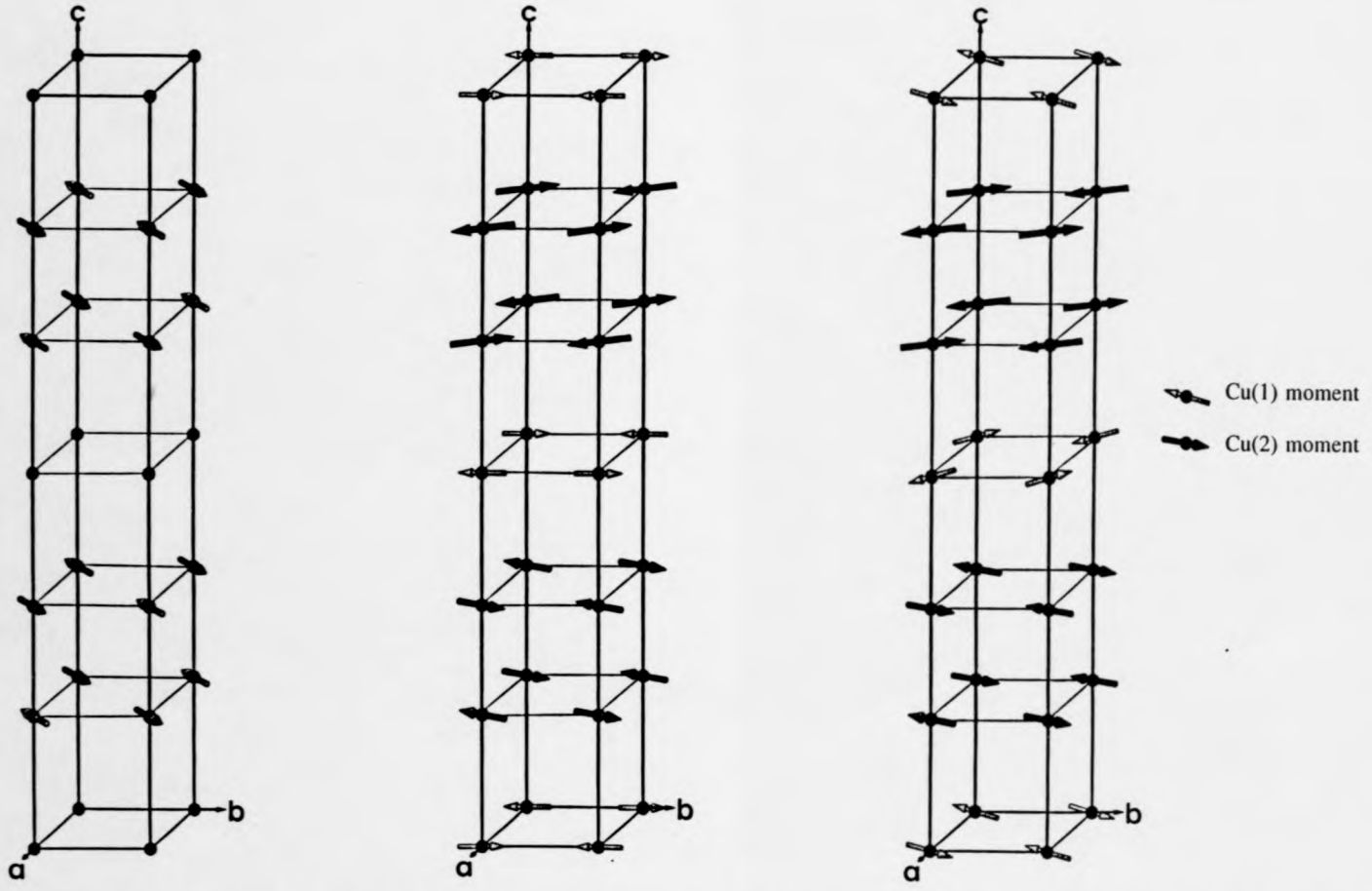

Figure 1.6: The moment directions for the magnetic structure of a) the plane-only ordered state of $PrBa_2Cu_3O_{7-\delta}$ and $ReBa_2Cu_3O_{7-\delta}$, b) the plane and chain ordered state of $ReBa_2Cu_3O_{7-\delta}$, and c) the plane and chain ordered state of $PrBa_2Cu_3O_{7-\delta}$, where the Cu chain moments have a significant component along the c-axis, (as proposed by Rosov et al. 1992, see figure 1).

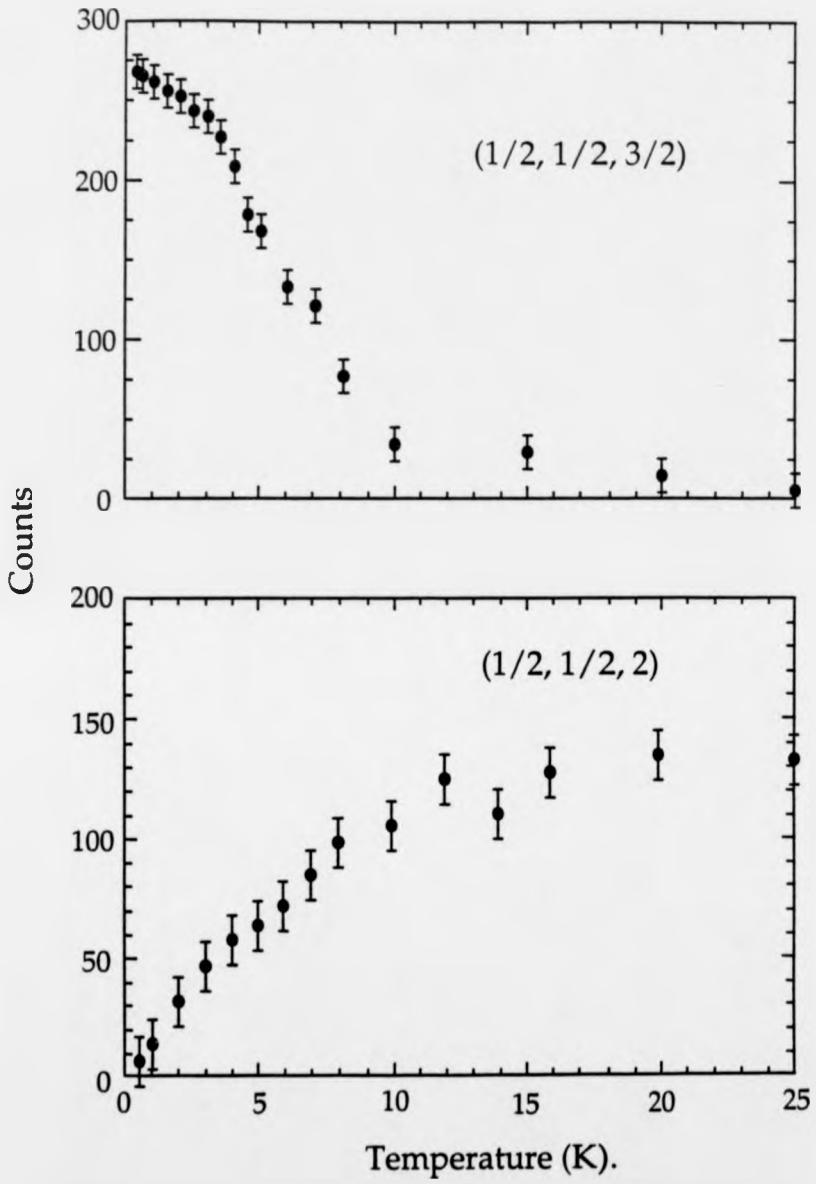

Figure 1.7: The temperature dependence of the intensities of the (1/2, 1/2, 3/2) and the (1/2, 1/2, 2) magnetic Bragg reflections, for a $NdBa_2Cu_3O_{6.35}$ crystal, (see figure 5b, Li et al. 1990).

1.6.2 The antiferromagnetic ordering of the Re^{3+} ions.

Specific heat measurements provided the first evidence of the antiferromagnetic ordering of the Re^{3+} ions, below the relatively low temperature of 2.5K, (Lee et al. 1988, Maple. 1987 and Ramerez. 1987). The measured ordering temperatures fall within the range of 0.17K, T_N for Ho, and 2.25K, T_N for Gd (see figure 1.8). Neutron diffraction is a more direct technique for probing magnetic structures and has confirmed the existence of antiferromagnetic order in several of the $ReBa_2Cu_3O_{7-\delta}$ compounds and allowed the magnetic structures to be accurately determined, (for example Paul et al. 1988 and Goldman et al. 1987). The alignment of the rare-earth magnetic moments is found to differ between compounds, as is common for many rare-earth materials due to the magnetic anisotropy from the crystalline electric field at the rare-earth site. In $NdBa_2Cu_3O_{7-\delta}$ the Nd magnetic moments are found to lie along the **c** axis, (Yang et al. 1989) while for $ErBa_2Cu_3O_{7-\delta}$ the Er moments are aligned within the **a** - **b** plane, (Lynn et al. 1987 and Maletta et al. 1990).

Further specific-heat measurements on oxygen-deficient samples have revealed that the magnetic ordering is strongly dependent on the oxygen concentration although the actual effect differs widely from compound to compound. In $NdBa_2Cu_3O_{7-\delta}$ the increase in δ from 0.1 to 0.5, destroys superconductivity, and increases the ordering temperature from 0.5K to 1.5K, (Maple et al. 1988). In contrast with this behaviour an equivalent change in δ, for $DyBa_2Cu_3O_{7-\delta}$, appears to destroy the long range antiferromagnetic order, (Lee et al. 1988).

The behaviour of C(T) for several of the $DyBa_2Cu_3O_{7-\delta}$ compounds has been accurately modelled in terms of antiferromagnetic two-dimensional and three-dimensional Ising models, (Simizi et al. 1987, Van de Berg et al. 1987 and Zhu et at. 1988). This analysis predicts weaker exchange interactions in the **c** direction than the **a** - **b** plane, as expected due to the much larger ionic

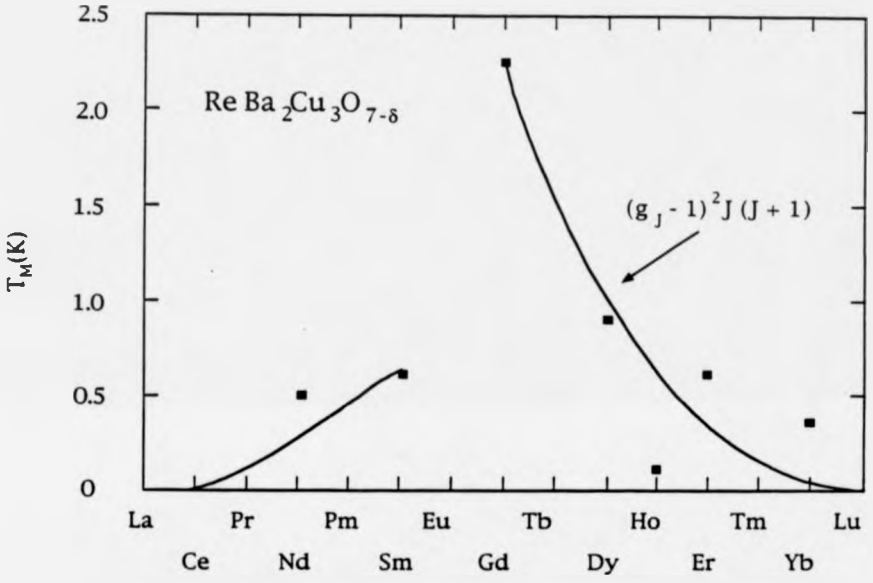

Figure 1.8: The magnetic ordering temperature T_M vs. Re for $ReBa_2Cu_3O_{7-\delta}$ compounds with Re = Nd, Sm, Gd, Dy, Ho, ER and Yb. The solid line represents the values of T_M expected from a scaling of T_M for Re = Gd by the de Gennes factor $(g_J - 1)^2 J(J+1)$, where g_J is the Landé g-factor and J is the total angular momentum of the Re^{3+} ion Hund's rules ground state, (see figure 8, Maple et al. 1987).

separation of the Re^{3+} ions in the **c** direction, and also, surprisingly, strong anisotropic exchange interactions within the **a - b** planes. As the Re^{3+} ions are positioned midway between two approximately planar CuO_2 layers where the orthorhombic distortion from the tetragonal limit is small, the exchange interactions within the **a - b** plane would be expected to be similar in both the **a** and **b** directions. One possible source of this anisotropy is the Cu-O chains which lie in the **b** direction. Although they are too far from the Re^{3+} ions to produce strong anisotropic exchange interactions they appear to play a strong role in the ordering due to the dependence of T_N on δ.

In common with other properties, the magnetic ordering of Pr^{3+} also behaves differently to that of the other rare earths of the $ReBa_2Cu_3O_{7-\delta}$ series. Specific-heat measurements and powder neutron-diffraction studies have shown the magnetic ordering temperature of Pr to be ~17K, see figure 1.9 (Li et al. 1989 and Kebede et al. 1989). This ordering temperature is two orders of magnitude higher than would be expected if one scaled T_N for the other rare earths, assuming a purely dipolar or RKKY exchange. The ordering temperature of 17K cannot be definitely assigned to the Pr ions from data from solely these two techniques alone and the possibility remains that the ordering may be associated with the Cu ions within the chains. However results from Mossbauer spectroscopy of $Pr_{0.93}Gd_{0.07}Ba_2Cu_3O_{7-\delta}$ support the assumption that the ordering is associated with the Pr sublattice, (Wortmann and Felner. 1990). Several studies have been made of $Y_{1-x}Pr_xBa_2Cu_3O_{7-\delta}$ to examined the effect of Pr concentration on the ordering temperature, (Cooke et al. 1987, Ghamaty et al. 1991). These have shown that T_N decreases steadily with decreasing x, and at $x = 0.3$ T_N falls to near 1K. Little experimental work on $PrBa_2Cu_3O_{7-\delta}$ has been performed to determine the effect of oxygen concentration on the Pr ordering temperature, although specific-heat studies of the oxygen deficient $PrBa_2Cu_3O_6$ have shown T_N has decreased to 10.5K, (Kebede et at. 1991).

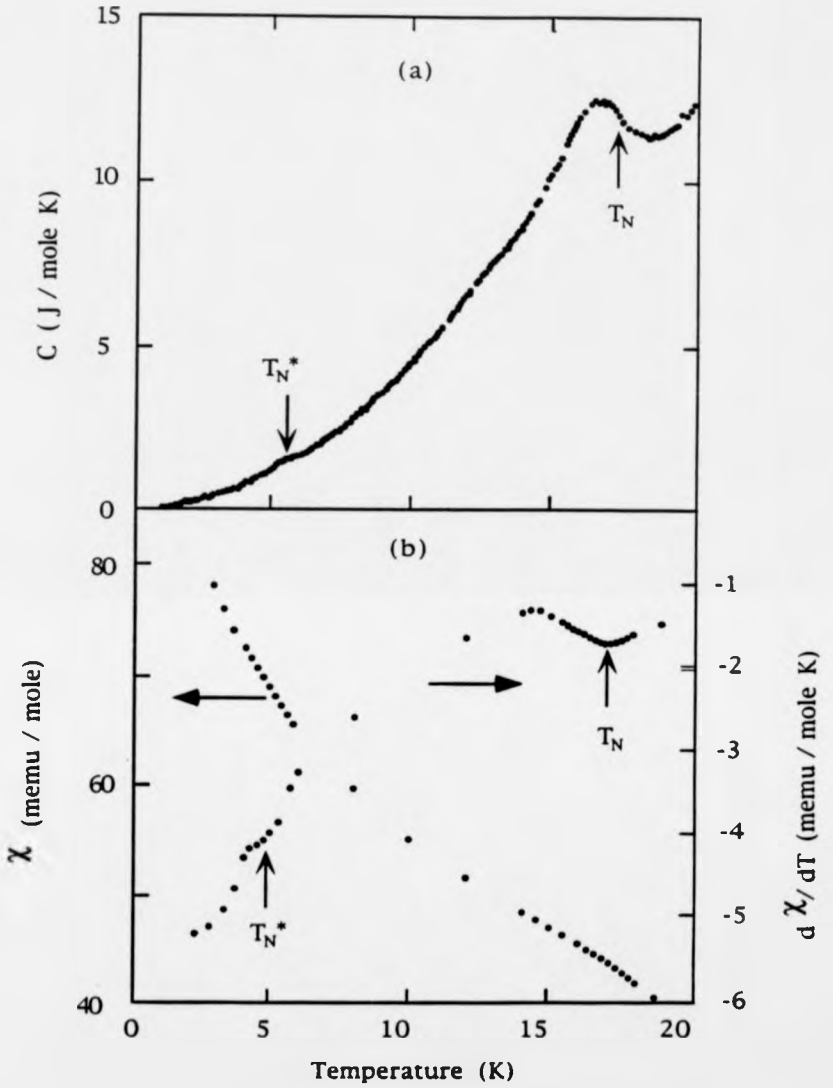

Figure 1.9: a) Measurements of the specific heat at low temperatures for $PrBa_2Cu_3O_7$ showing the magnetic transition at T_N = 17K, b) Measurements of the magnetic susceptibility $\chi(T)$ (in memu/mole) and the temperature derivative $d\chi/dT$ for $PrBa_2Cu_3O_7$,(see figure 3, Li et al. 1989).

CHAPTER TWO

THE THEORY OF NEUTRON SCATTERING.

2.1 Introduction.

Neutron scattering has developed into a versatile tool in the study of physical and chemical properties of materials across the spectrum of the sciences, from molecular biology to engineering. In the particular realm of magnetism, neutron scattering is an invaluable technique for studies ranging from magnetic ordering to magnetic excitations.

Due to its zero charge the neutron experiences no coulomb repulsion from atomic nuclei and is able to penetrate deep within a material with little attenuation, except for the few elements, such as gadolinium, which have a high absorption cross section. In the majority of cases therefore the neutron probes the bulk properties. Since thermal neutrons have a wavelength of the order of interatomic distances (1 - 3Å), interference effects between scattering from individual nuclei leads to information on the nuclear and magnetic structure of crystals. Additionally with energies of 10 - 100meV neutrons are an important probe in the investigation of thermal excitations within crystals.

Of special interest to this study is the unique probe neutron scattering provides in the investigation of magnetic properties. The neutron has a magnetic moment (μ_n = -1.043 Bohr magnetons) and interacts, via a dipole - dipole interaction, with the magnetic moments of the unpaired electrons within the material. This reveals information about the magnetic properties on a microscopic scale including the arrangement of atomic spins and the electron spin-density distribution.

The theory of neutron scattering is extensive and it is not the aim of this thesis to provide a complete theoretical discussion of this technique. A more

rigourous treatment of the theory can be found in the revelant texts (Bacon. 1975, Lovesey. 1986, Squires. 1976 and Williams. 1988). Within this chapter a concise account of the theory revelant to this study will be presented. Initially the nuclear and magnetic elastic scattering of unpolarised neutrons will be described and subsequently the determination of the magnetic order within a single crystal. This will then be extended to the polarised neutron case and its application to magnetisation-density studies and polarised-neutron reflectivity.

2.2 The neutron scattering experiment.

A typical neutron scattering experiment may be described by the geometry shown in figure 2.1. A monochromatic beam of neutrons, with wave vector **k** and energy ε, strikes the sample and is scattered. In the scattering process the momentum of the neutron changes and the wave vector becomes **k'**. In general the physically measured quantity can be described as the partial differential cross section,

$$\frac{d^2\sigma}{d\Omega d\varepsilon} = \frac{\text{(number of neutrons of energy } \varepsilon \rightarrow \varepsilon+\delta\varepsilon, \text{ scattered per sec into a solid angle } d\Omega \text{)}}{\Phi} \qquad (2.1)$$

where $\delta\varepsilon$ is the change in energy of the neutron and Φ is the incident flux of neutrons. Often no energy is transferred in the scattering event and only the total number of neutrons scattered in a solid angle $d\Omega$ is important. The cross section for this elastic scattering is known as the differential cross section,

$$\frac{d\sigma}{d\Omega} = \frac{\text{(number of neutrons scattered per sec into a solid angle } d\Omega \text{)}}{\Phi} \qquad (2.2)$$

2.3 Nuclear elastic scattering.

Intially we can consider the elastic scattering of neutrons by a general group of particles, neglecting the interaction of the neutron with the

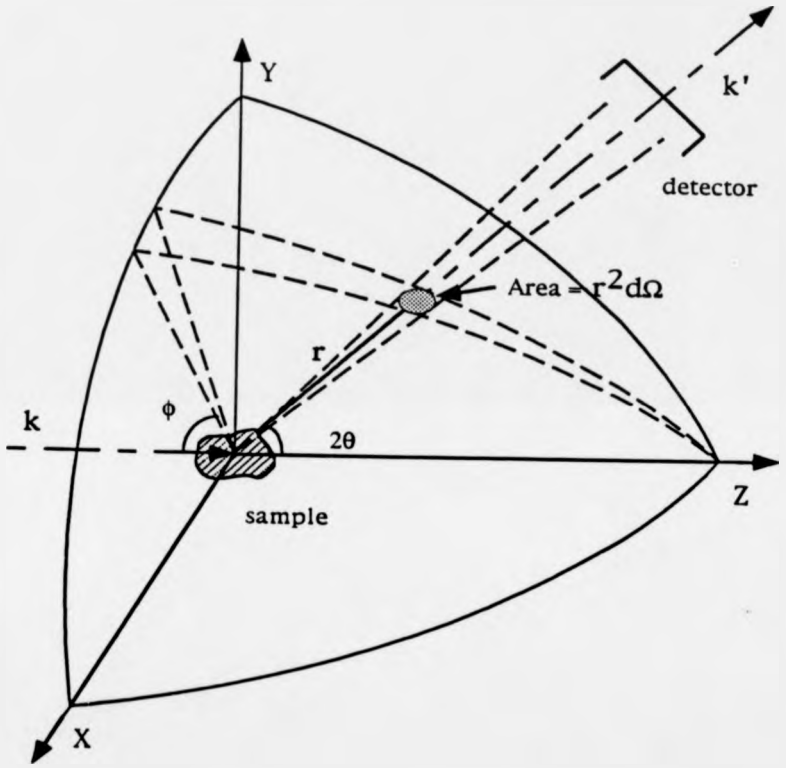

Figure 2.1: The geometry of the neutron scattering experiment.

nuclear spin. A neutron of wave vector **k** and of energy $E = \hbar^2 k^2 / 2m$, represented by the wave function Ψ_k, interacts with the scattering system and is scattered, changing its wave vector to **k'** and wave function to $\Psi_{k'}$. As the scattering event is elastic the neutron retains the same energy and hence $|k| = |k'| = k$. The probability of a transition from the wave vector state **k** to **k'** is given by Fermi's Golden Rule :-

$$W_{k \to k'} = (2\pi/h) \left| \int dr \, \Psi^*_{k'} \, \hat{V}_N \, \Psi_{k'} \right|^2 \rho_{k'}(E) \tag{2.3}$$

where $\hat{V}_N$ is the nuclear interaction potential and $\rho_{k'}(E)$ is the density of the final scattering states. It may be shown (Lovesey. 1986) that the differential cross section can be represented by

$$\frac{d\sigma}{d\Omega} = \left| \left\langle k' \left| \hat{V}_N \right| k \right\rangle \right|^2 = |f(\kappa)|^2 \tag{2.4}$$

where $f(\kappa)$ is the scattering amplitude and $\kappa = k - k'$, the change in wave vector. Due to the fact that the neutron - nucleus interaction occurs over a very short range compared to the wavelength of the neutron, λ, the scattering is assumed to be isotropic. The scattering amplitude can therefore be described by a constant b, the scattering length, independent of scattering direction. The scattering length does not vary systematically with Z but is highly dependent on the atomic type, isotope and relative neutron - nuclear spin orientations.

$$\frac{d\sigma}{d\Omega} = |b|^2 \tag{2.5}$$

If we now consider an ordered array of nuclei, with position vectors $\mathbf{R}_l$ and scattering lengths b_l, it can be shown, using the Born approximation, that the only possible form of interaction potential which can produce isotropic scattering is a delta function. By defining the interaction potential as,

$$\hat{V}_N = (2\pi\hbar^2/m)\, b\, \delta(\mathbf{r}-\mathbf{R}) \tag{2.6}$$

the matrix element is therefore

$$\left\langle \mathbf{k}' \left| \hat{V}_N \right| \mathbf{k} \right\rangle = b_j \exp(i\mathbf{K}\cdot\mathbf{R}_j) \tag{2.7}$$

and the differential cross section per atom becomes,

$$\frac{d\sigma}{d\Omega} = \sum_{jj'} \exp\left[i\mathbf{K}\cdot(\mathbf{R}_j - \mathbf{R}_{j'}) \right] \overline{b_j b_{j'}} \tag{2.8}$$

This may be written as a sum of two parts, an incoherent scattering term and a coherent scattering term,

$$\left(\frac{d\sigma}{d\Omega}\right)_{\text{total}} = \left(\frac{d\sigma}{d\Omega}\right)_{\text{incoherent}} + \left(\frac{d\sigma}{d\Omega}\right)_{\text{coherent}} \tag{2.9}$$

The incoherent term describes scattering which is completely isotropic and reveals no structural information, assuming a rigid lattice. This results in a constant background beneath the coherent cross section (Note: For a real lattice a Debye-Waller factor must be introduced to account for thermal motion of the atoms.).

$$\left(\frac{d\sigma}{d\Omega}\right)_{\text{incoherent}} = N\overline{|b - \bar{b}|^2} \tag{2.10}$$

where N is the total number of nuclei. The coherent term arises from the interference effects between the neutrons scattered from each nuclei.

$$\left(\frac{d\sigma}{d\Omega}\right)_{\text{coherent}} = |\bar{b}|^2 \left| \sum_j \exp(i\mathbf{K}\cdot\mathbf{R}_j) \right|^2 \tag{2.11}$$

The coherent scattering is highly anisotropic and only occurs for special orientations, where $\mathbf{k} - \mathbf{k}' = \tau$ a reciprocal lattice vector, (see figure 2.2). As $\mathbf{K}$ moves away from the reciprocal lattice vector the terms fall rapidly out of phase and the cross section rapidly becomes negligible. For a large crystal the differential cross section may be written as (Lovesey. 1986),

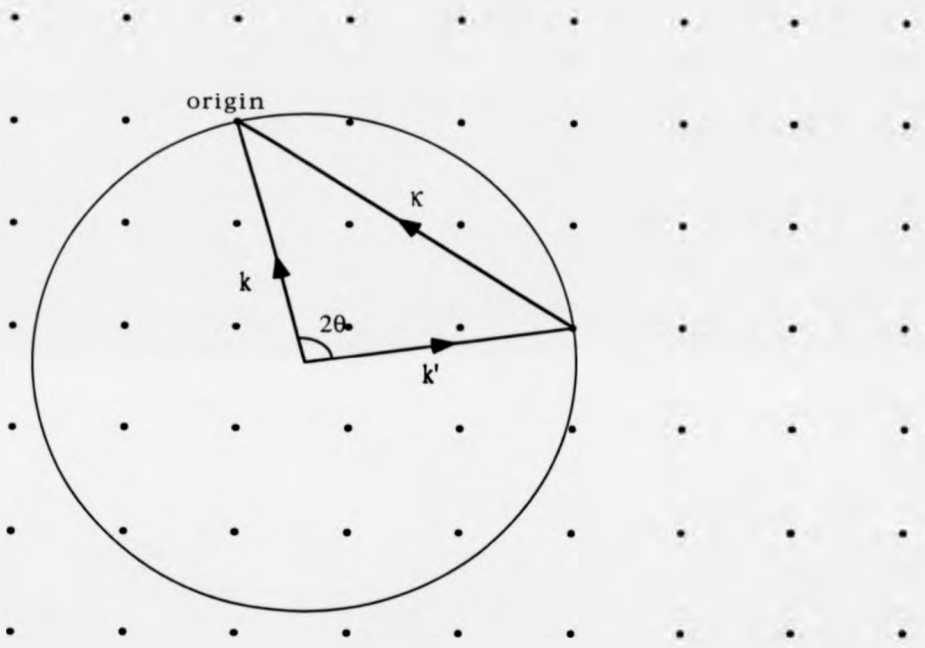

Figure 2.2: A reciprocal space representation of the condition for Bragg reflection from a crystalline lattice.

$$\left(\frac{d\sigma}{d\Omega}\right)_{coherent} = N\frac{(2\pi)^3}{v_o}\sum_{\tau}\delta(K-\tau)|F_N(K)|^2 \qquad (2.12)$$

where $F_N(K)$ is the nuclear unit-cell structure factor and v_o is the volume of the unit cell. This geometric condition is known as the Bragg condition and is satisfied by the familiar Bragg equation (Bacon. 1976), $n\lambda = 2\,d_{hkl}\sin\theta$, where $2d_{hkl}$ is the crystal plane separation. From the measurement of the nuclear scattering cross section $|F_N(K)|$ can be found which may be Fourier transformed, if the phases are known, or fitted to determine the nuclear structure of the unit cell.

Experimentally a δ function is not realised and the Bragg peaks have a finite width due to the instrument resolution and mosaic spread within the crystal. This problem is solved by measuring the intensity across the full angularly broadened peak. The most common method for measuring the integated intensity is the omega scan. The detector is fixed at twice the Bragg angle from the incident beam and the sample is rotated through the Bragg position about the axis perpendicular to the plane containing the incident and diffracted beams. The peak intensity is given by,

$$I = F\int \sigma\, d\omega \qquad (2.13)$$

where Φ is the incident neutron flux on the sample, σ the total cross section for the Bragg condition and $d\omega$ is the change in angular position of the sample. It can be shown that the intensity becomes,

$$I = \Phi\left(\frac{V}{v_o^2}\right)\frac{\lambda^3}{\sin 2\theta}|F_N(\tau)|^2 \qquad (2.14)$$

where V is the volume of the crystal, $V = Nv_o$. In real crystals the situation is not as simple as described in this approach as the intensity is altered due to extinction and absorption effects, effects which are here neglected.

2.4 Magnetic elastic scattering.

If we now take into account the spin state of the neutron, the interaction between the neutron dipole moment μ_n and the localised atomic moment produced by unpaired electrons will result in additional scattering, known as magnetic scattering. For the interaction of a neutron with a field **B**, produced by a single moving electron the magnetic interaction potential may be expressed as,

$$\hat{V}_m = \hat{\mu}_n \cdot \mathbf{B} = -\gamma \mu_N \hat{\sigma} \cdot \mathbf{B} \qquad (2.15)$$

where $\hat{\sigma}$ is the Pauli spin operator for the neutron, γ is the gyromagnetic ratio, γ=-1.913, and μ_N is the nuclear magneton. If we assume that the localised atomic moment arises solely from the electron spin, neglecting the orbital component, the potential, in terms of the distance R from the electron, becomes,

$$\hat{V}_M = \gamma \mu_N \left[2 \mu_B \hat{s} \cdot \text{curl} \left(\frac{\hat{s} \times \mathbf{R}}{|\mathbf{R}|^3} \right) \right] \qquad (2.16)$$

where $\hat{s}$ is the electron spin operator and μ_B is the Bohr magneton. This potential represents a classical dipole-dipole interaction between moments. It has been shown (Squires. 1976) by defining an interaction vector $\hat{\mathbf{Q}}$, at an arbitary angle to the scattering vector κ where

$$\hat{\mathbf{Q}} = \sum_{i \text{ electrons}} s_i \exp(i\kappa \cdot r_i)$$

that

$$\langle \mathbf{k}' | \hat{V}_M | \mathbf{k} \rangle = -r_0 \hat{\sigma} \cdot \hat{\mathbf{Q}}_\perp \qquad (2.17)$$

where r_i is the position of the electron, r_0 the classical electron radius multiplied by γ and $\hat{\mathbf{Q}}_\perp$ is the component of the interaction operator perpendicular to κ, (see figure 2.3). An important implication of this is that only the magnetic component perpendicular to the scattering vector gives rise to scattering, ie if the atomic moment lies parallel to the scattering vector

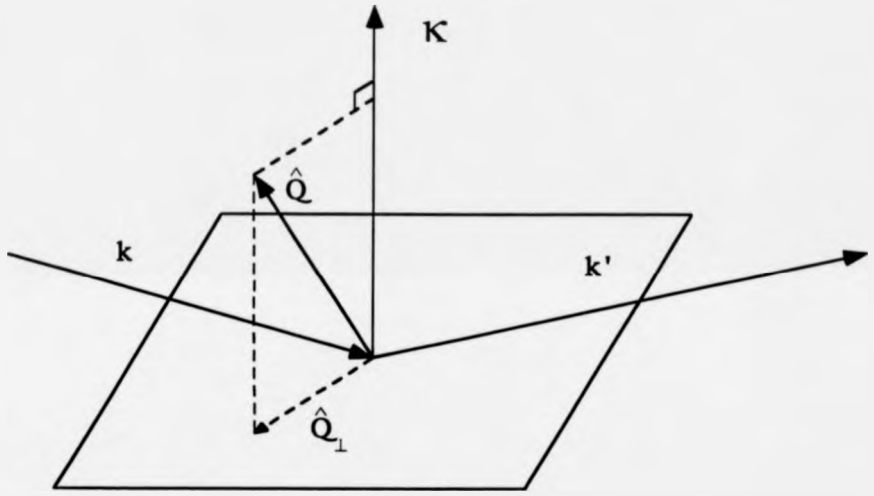

Figure 2.3: The geometric relationship between $\hat{\mathbf{Q}}$, $\hat{\mathbf{Q}}_{\perp}$ and $\mathbf{K}$.

no magnetic scattering occurs. The interaction vector $\hat{\mathbf{Q}}$ can also be defined as,

$$\hat{\mathbf{Q}} = \frac{1}{\mu_B} \int \mathbf{M}(\mathbf{r}) \exp(i\mathbf{k} \cdot \mathbf{r}) \, d\mathbf{r} \tag{2.18}$$

where $\mathbf{M}(\mathbf{r})$ is a magnetisation-density operator. Hence $\hat{\mathbf{Q}}_\perp$ and therefore the differential cross section is proportional to the Fourier transform of the magnetisation density. This is expected as the field with which the neutron interacts depends on the resultant atomic magnetisation.

Following a similar procedure to that for nuclear scattering for an ordered array of nuclei, the matrix element may be written as,

$$\left\langle \mathbf{k}' \middle| \hat{V}_M \middle| \mathbf{k} \right\rangle = -r_0 \hat{\sigma} \cdot \left[\hat{\kappa} \times (\hat{s}_j \times \hat{\kappa}) \right] \exp(i\kappa \cdot \mathbf{r}) \tag{2.19}$$

By comparing this to the matrix element for nuclear scattering (equation 2.7) a magnetic scattering length $\hat{p}$ can be defined as,

$$\hat{p} = -r_0 \hat{\sigma} \cdot \left[\hat{\kappa} \times (\hat{s}_j \times \hat{\kappa}) \right] = 2r_0 \langle \hat{s}_j \rangle \langle \hat{s'} \rangle \cdot \left[\hat{\kappa} (\hat{\eta} \cdot \hat{\kappa}) - \hat{\kappa} \right] \tag{2.20}$$

where $\langle \hat{s'} \rangle$ is the average neutron spin vector and $\hat{\eta}$ is the unit vector in the direction of the atomic spin. In contrast to the nuclear scattering situation, the dimensions of the electron cloud, responsible for the magnetic scattering, are of the same order as the neutron wavelength. To account for this spatial distribution a magnetic form factor f_m, the Fourier transform of the magnetisation density of a single atom, needs to be added to the differential cross section.

A general form of the magnetic differential cross section, for a large crystal can be written as,

$$\frac{d\sigma}{d\Omega} = r_0^2 \left| f_m(\kappa) \right|^2 \sum_{\alpha\beta} \left(\delta_{\alpha\beta} - \kappa_\alpha \kappa_\beta \right) \sum_{ij} \exp(i\kappa \cdot (\mathbf{R}_i - \mathbf{R}_j)) \langle s_i^\alpha \rangle \langle s_j^\beta \rangle \tag{2.21}$$

where α , β are the cartesian directions and $\langle s_i^\alpha \rangle$ is the average component in the direction α of nuclei i.

So far the derivation to the cross sections has been simplified by considering a rigid lattice. In practice thermal vibrations exist in the lattice and the cross sections are modified by a temperature dependent factor, the Debye-Waller factor.

2.5 Scattering from magnetically ordered crystals.

A ferromagnetic crystal, in the absence of an applied magnetic field, will consist of small domains of oriented moments. Averaging over all the domains the magnetic cross section becomes (Lovesey. 1986),

$$\left(\frac{d\sigma}{d\Omega}\right)_{coherent} = \frac{r_0^2}{3} N \frac{(2\pi)^3}{v_o} \sum_{\tau} \delta(\kappa - \tau) |f_M(\kappa)|^2 G_{hkl}^2 \langle s_\eta \rangle^2 \qquad (2.22)$$

where $\langle s_\eta \rangle$ is the average spin perpendicular to the scattering vector and G_{hkl} is a geometric structure factor (Note: In the nuclear cross section the nuclear structure factor can be written as $F_N(\kappa) = b\ G_{hkl}$). The cross section may also be represented in terms of the magnetic structure factor, $F_M(\kappa)$.

$$\left(\frac{d\sigma}{d\Omega}\right)_{coherent} = \frac{N}{3} \frac{(2\pi)^3}{v_o} \sum_{\tau} \delta(\kappa - \tau) |F_M(\kappa)|^2 \qquad (2.23)$$

By comparing the nuclear and magnetic cross sections, equations (2.12) and (2.22), strong differences are apparent, (Note: the factor of 1/3 is a result of averaging over the magnetic domains). Firstly the magnetic structure factor is temperature dependent due to the its proportionality to $\langle s_\eta \rangle$. As the temperature is increased and the Curie ordering temperature, T_c, is approached $\langle s_\eta \rangle$, and therefore the magnetic cross section, fall away to zero. In contrast the nuclear cross section is not temperature dependent if the Debye-Waller factor is neglected. Secondly the magnetic form factor falls off strongly with increasing wave vector transfer (see figure 2.4) and hence high-τ reflections are greatly reduced in intensity. Additionally it can be seen that the nuclear and magnetic Bragg peaks appear at the same position

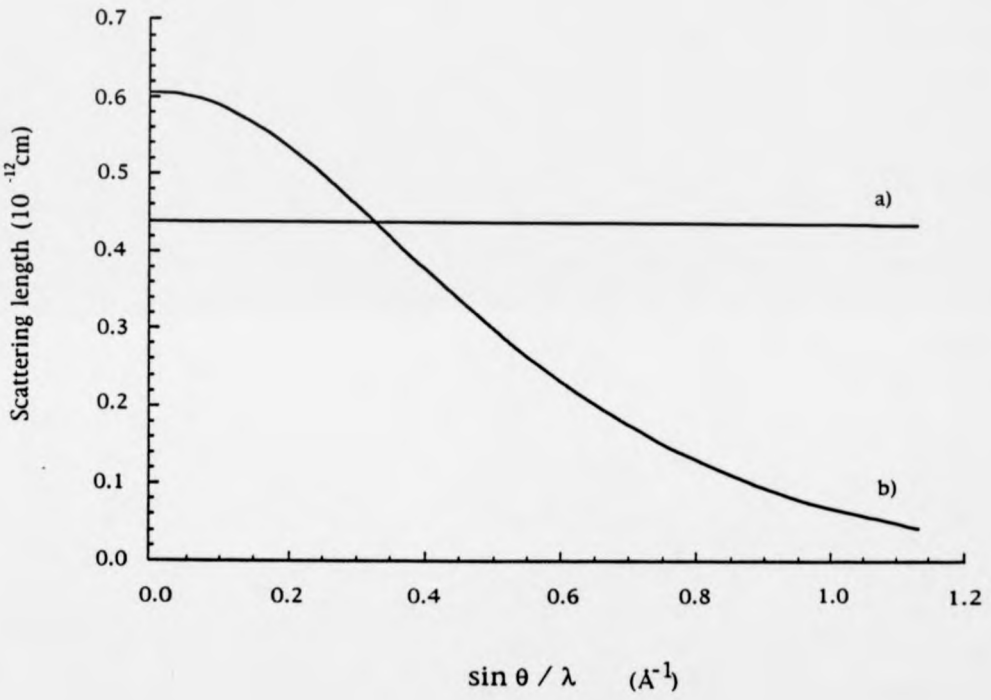

Figure 2.4: The scattering lengths for praesodynium. a) The nuclear scattering length. b) The magnetic scattering length for a Pr^{3+} ion multiplied by the magnetic form factor, (Lebech et al 1979).

in reciprocal space due to the equivalence of the nuclear and magnetic unit cells. The separation of the magnetic and nuclear components from the full scattered intensity can be best achieved using polarised neutrons and will be discussed shortly.

For an antiferromagnetic crystal the same general arguments apply to the magnetic cross section as in the ferromagnetic case. In an antiferromagnet the average spin, $\langle s_\eta \rangle$, over a domain will be zero, forcing the magnetic cross section also to be zero. If we restrict our discussion to a simple antiferromagnet with spins lying parallel or anti-parallel to one crystallographic direction we can avoid the implications of $\langle s_\eta \rangle = 0$ by defining a sublattice of parallel spins and $\langle s_\eta \rangle$ as the average spin within that sublattice. The magnetic unit cell of the crystal is defined as the unit cell of this sublattice and therefore the magnetic and nuclear unit cells are often not the same and hence the magnetic peaks occur at different positions in reciprocal space.

2.6 Scattering of polarised neutrons.

So far we have only dealt with the momentum state of the neutron neglecting its spin state by assuming a random orientation of spins. If the initial and final spin states are known additional information on the scattering process may be found. The use of polarised neutrons, neutrons of known initial spin state, is highly important in the study of magnetic scattering, especially in the area of magnetisation-density studies.

The spin state of a neutron can be defined, relative to a direction known as the polarisation direction, as (+) for the 'spin up' state and (-) for the 'spin down' state. The polarisation of a neutron beam can be defined as twice the average value of the neutron spin, $\mathbf{P} = 2\langle \mathbf{s} \rangle$. Within the scattering process the spin state may change and hence four cross sections may be measured corresponding to the transitions,

$$(+) \rightarrow (+), \qquad (+) \rightarrow (-), \qquad (-) \rightarrow (+), \qquad (-) \rightarrow (-). \tag{2.24}$$

The transitions involving no change of spin state, ie (+) → (+) and (-) → (-), are commonly known as non-spin-flip transitions and those involving a change in spin state, ie (+) → (-) and (-) → (+), as spin-flip transitions. The four spin-dependent cross sections are related to the cross section for an unpolarised beam by,

$$\left(\frac{d^2\sigma}{d\Omega\, dE}\right)_{\text{unpolarised}} = \frac{1}{2}\left[\left(\frac{d^2\sigma}{d\Omega\, dE}\right)_{+\rightarrow+} + \left(\frac{d^2\sigma}{d\Omega\, dE}\right)_{+\rightarrow-} + \left(\frac{d^2\sigma}{d\Omega\, dE}\right)_{-\rightarrow+} + \left(\frac{d^2\sigma}{d\Omega\, dE}\right)_{-\rightarrow-}\right] \tag{2.25}$$

The factor of 1/2 arises from the fact that the initial neutron spins occur with equal probability in the (+) and (-) spin states.

To take into account the spin state of the neutron the partial differential cross section must be written as,

$$\frac{d^2\sigma}{d\Omega\, dE} = \left| \sum_j \left\langle \mathbf{k}'\sigma' \middle| \hat{V} \middle| \mathbf{k}\sigma \right\rangle \right|^2 d\,(E_k - E_{k'} + \hbar\omega) \tag{2.26}$$

where σ and σ' are the initial and final spin states of the neutron respectively. A generalised form of the interaction potential, $\hat{V}$, can be defined as,

$$\hat{V} = \hat{\beta} + \hat{\alpha} \cdot \hat{\sigma} \tag{2.27}$$

$\hat{\beta}$ and $\hat{\alpha}$ are variables referring to the scattering system and $\hat{\sigma}$ is the Pauli spin operator. The generalised scattering amplitudes can therefore be written as (Williams. 1988),

$$U_{++} = \hat{\beta} + \hat{\alpha}_z \tag{2.28a}$$

$$U_{--} = \hat{\beta} - \hat{\alpha}_z \tag{2.28b}$$

$$U_{+-} = \hat{\alpha}_x + i\,\hat{\alpha}_y \tag{2.28c}$$

$$U_{+-} = \hat{\alpha}_x - i\,\hat{\alpha}_y \tag{2.28d}$$

where $\hat{\alpha}_z$ is the component of $\hat{\alpha}$ in the polarisation direction, defined as the z direction.

In the case of nuclear coherent scattering the interaction potential is,

$$\hat{V}_N = b \exp(i\mathbf{K} \cdot \mathbf{R}_j) \tag{2.29a}$$

and

$$b = A_j + B_j(\mathbf{I} \cdot \hat{\sigma}) \tag{2.29b}$$

where $\mathbf{I}$ is the operator describing the spin angular momentum of the nucleus. If we assume the nuclear spins are randomly orientated U_{+-} and U_{-+} both become zero and hence the coherent nuclear scattering is non-spin-flip scattering.

Incoherent nuclear scattering due to isotopic disorder is also non-spin-flip scattering. In contrast, incoherent spin disorder scattering contains both spin-flip and non-spin-flip scattering terms in the cross section, due to the the components of the nuclear spin parallel and perpendicular to the polarisation direction respectively.

The interaction potential for purely magnetic scattering has the form,

$$\hat{V}_M = \hat{\sigma} \cdot \hat{\mathbf{Q}}_\perp \tag{2.30}$$

For the components of spin parallel to the polarisation direction the scattering is non-spin-flip. However for the other components perpendicular to this direction the spin states will change and hence will be spin-flip scattering. This is true for all forms of magnetic scattering, coherent, incoherent, elastic and inelastic. The use of polarised neutrons thus provides a way of separating the paramagnetic scattering from other diffuse scattering.

2.7 Polarised-neutron scattering from magnetically ordered crystals.

In the treatment of magnetically ordered crystals both the nuclear and magnetic scattering need to be considered jointly due to the appearance of a nuclear - magnetic interference term in the final cross section.

The total interaction potential for an ordered array of nuclei, the sum of the nuclear potential, $\hat{V}_N$ (equation 2.29) and the magnetic potential, $\hat{V}_M$ (equation 2.30), may be written as,

$$\hat{V}_{total} = \sum_j \hat{b}_j \exp(i\kappa \cdot R_j) - r_0 \hat{\sigma} \cdot \hat{Q}_\perp$$

$$= \sum_j \exp(i\kappa \cdot R_j)\left(A_j + \hat{\sigma} \cdot (B_j I - C)\right) \qquad (2.31)$$

where

$$C = \frac{g}{2} r_0 f_M(\kappa)\left[\kappa \times (\hat{s}_j \times \kappa)\right] \qquad (2.32)$$

Using the generalised approach to the scattering potential (equation 2.27), assuming, as previously that the nuclear spins are randomly orientated, the scattering amplitudes may be represented by,

$$U_{++} = \bar{b} - C_z \qquad (2.33a)$$

$$U_{--} = \bar{b} + C_z \qquad (2.33b)$$

$$U_{-+} = -(C_x + iC_y) \qquad (2.33c)$$

$$U_{+-} = -(C_x - iC_y) \qquad (2.33d)$$

where $b = \langle A \rangle$.

In the particular case of magnetisation-density measurements, of interest in this work, the moments within the crystal are aligned by a magnetic field. The direction of alignment η is along the polarisation direction and perpendicular to the scattering vector κ. Within the coordinate system used the polarisation direction is the z direction and therefore the spin components are

$$\langle s_z \rangle = \langle s \rangle \quad \text{and} \quad \langle s_x \rangle = \langle s_y \rangle = 0$$

hence the spin-flip scattering lengths U_{-+} and U_{+-} are zero and the scattering is due to entirely non-spin-flip scattering processes. The spin-dependent cross sections can be written as,

$$\left(\frac{d\sigma}{d\Omega}\right)_{++} = N\frac{(2\pi)^3}{v_o}\sum_{\tau}\delta(\kappa - \tau)\left(\bar{b}^2 + \bar{b}\, r_0 g f_M(\kappa)\hat{s}) + (r_0\frac{g}{2}f_M(\kappa)\hat{s}))^2\right) \quad (2.34)$$

$$\left(\frac{d\sigma}{d\Omega}\right)_{--} = N\frac{(2\pi)^3}{v_o}\sum_{\tau}\delta(\kappa - \tau)\left(\bar{b}^2 - \bar{b}\, r_0 g f_M(\kappa)\hat{s}) + (r_0\frac{g}{2}f_M(\kappa)\hat{s}))^2\right) \quad (2.35)$$

The terms in each cross section are the nuclear, the nuclear - magnetic interference and magnetic terms respectively. In a polarised experiment, in which the incident beam is fully polarised for each preferred spin state, the two cross sections may be measured independently and the ratio of the two, the flipping ratio R, is given by,

$$R = \frac{\left(\bar{b} + r_0\frac{g}{2}f_M(\kappa)\hat{s})\right)^2}{\left(\bar{b} - r_0\frac{g}{2}f_M(\kappa)\hat{s})\right)^2} \quad (2.36)$$

The flipping ratio may also be expressed in terms of the ratio of the magnetic and nuclear structure factors, $r = F_M(\kappa)/F_N(\kappa)$.

$$R = \frac{(1 - r)^2}{(1 + r)^2} \approx 1 - 4r \quad (2.37)$$

The magnetic scattering is generally small in comparison to the nuclear scattering. For an unpolarised beam the peak intensity is proportional to $\bar{b}^2(1 + r^2)$ and for a typically weak magnetic scattering amplitude of $0.01\bar{b}$ the magnetic contribution to the scattered intensity would be 10^{-4} that of the nuclear contribution. In the polarised beam case the additional presence of the nuclear - magnetic interference term enables these small magnetic amplitudes to be measured accurately. The same weak scattering amplitude

will give a flipping ratio of 1.04. An additional benefit of polarised neutrons is that the sign of the magnetic structure factor may be determined.

By using this technique if the nuclear structure factor, $F_N(\kappa)$, is known then the magnetic structure factor, $F_M(\kappa)$, can be found. An important application of polarised-neutron diffraction is the determination of the magnetic form factors, $f_M(\kappa)$, from which the magnetisation density may be deduced. The magnetisation density is related to the magnetic structure factor by equation 2.18 and more directly by the relationship

$$\mathbf{M}(\mathbf{r}) = \frac{1}{v_o} \sum_{\tau} f_M(\tau) \exp\left(-i\boldsymbol{\tau} \cdot \mathbf{r}\right) \tag{2.38}$$

2.8 Polarised-neutron reflectivity.

Due to the wave nature of neutrons they uphold the general principles of optics. By considering a neutron passing from one medium to another its wave vector changes from $\mathbf{k}_1$ to $\mathbf{k}_2$ and we can define the neutron refractive index at the interface as,

$$n_{1 \rightarrow 2} = \frac{k_2}{k_1} \tag{2.39}$$

If the initial energy is $E_1 = h^2 k_1^{\,2}/2m$ and the average potential difference between the two media is $\langle \delta V \rangle$ the refractive index becomes,

$$n_{1 \rightarrow 2} = \left[\frac{E_1 - \langle \delta V \rangle}{E_1}\right]^{\frac{1}{2}} \approx 1 - \frac{\langle \delta V \rangle}{2E_1} \tag{2.40}$$

For a neutron entering a magnetic material the average interaction potential is the sum of the average nuclear and magnetic potentials. The nuclear potential is described by the Fermi pseudopotential (equation 2.6). The magnetic potential, due to the interaction between the neutron and the magnetic field produced by the unpaired electrons, is described by the dipole - dipole potential (equation 2.15). Hence the refractive index becomes,

$$n = 1 - \lambda^2\left(\frac{N\bar{b}}{2\pi} + \frac{m}{h^2}(\mu_n \cdot B)\right) \tag{2.41}$$

For most materials $n < 1$ and the material appears optically less dense than a vacuum. An important consequence of this is that the neutrons can be totally reflected from the interface if the incident angle is less than the critical angle θ_c.

$$n = \cos\theta_c \approx 1 - \frac{\theta_c^2}{2} \tag{2.42}$$

Even at angles slightly less than θ_c the reflectivity is sizeable. The common use of this phenomenon is in the development of neutron guide tubes but it has also been applied to the study of surface magnetism, a technique pioneered by Felcher (Felcher. 1981).

For a thin-film superconductor magnetised in an applied field the magnetic induction B will vary as a function of the distance z from the surface. If we consider the reflection of polarised neutrons, where the neutrons are polarised parallel (+) or anti-parallel (-) to the direction of the applied field H, from equation 2.41 the depth-dependent refractive index is,

$$n^{\pm}(z) = 1 - \frac{\lambda^2}{2\pi}\left(\frac{\bar{b}}{v} \pm c\left(B(z) - \mu_0 H\right)\right) \tag{2.43}$$

where λ is the neutron wavelength, $\bar{b}/v$ is the average scattering amplitude per unit volume and $c = 2\pi\mu_n m/h^2$. The measurement of the reflectivity in the region of the total reflectivity as a function of the incident angle, or equivalently the neutron wavelength, n(z), is directly proportional to the depth profile of the magnetic induction can be determined. As B(z) is averaged over each plane at a depth z the reflectivity only contains information on the average depth profile and not on the lateral magnetic perturbations expected near the surface.

CHAPTER THREE

INSTRUMENT AND EXPERIMENTAL TECHNIQUES.

3.1 Magnetic ordering in $PrBa_2Cu_3O_{7-\delta}$.

The magnetic ordering of praseodymium and copper in $PrBa_2Cu_3O_{7-\delta}$ was investigated by neutron diffraction on the triple-axis spectrometers TAS1 and TAS3 at the Risø National Laboratory, Denmark. Two separate crystals of $PrBa_2Cu_3O_{7-\delta}$ were studied, a ~100mg crystal grown by the CuO flux method at the National Crystal Growth Facility, University of Oxford and a smaller ~60mg crystal grown by the same method at the Risø National Laboratory. Three separate studies, (~28 days), were carried out on the former crystal and between each experiment the oxygen concentration of the crystal was further increased by heating the crystal at length in an oxygen furnace. This enabled the magnetic order to be studied as a function of oxygen concentration.

3.1.1 The TAS1 and TAS3 triple-axis spectrometers.

The TAS1 and TAS3 spectrometers are situated at the DR3 reactor (10MW) at Risø National Laboratory. TAS1 is a triple-axis spectrometer and TAS3 is a multi-purpose instrument that can be operated with a number of possible detector arms. In this study TAS3 was used with an analyser arm in a triple-axis spectrometer mode.

The TAS1 instrument lies on a beam tube from the cold source (H_2 gas at 38K). The spectrum of neutron wavelengths is enhanced in the long wavelength range of $2 < \lambda < 5$Å producing a maximum neutron flux of 8.7×10^6 $n\,c\,m^{-2}s^{-1}$ at the sample at $\lambda = 2.44$Å. A schematic representation of the instrument is shown in figure 3.1. The beam is monochromated using the (002) reflection from a pyrolytic graphite monochromator. Four fixed

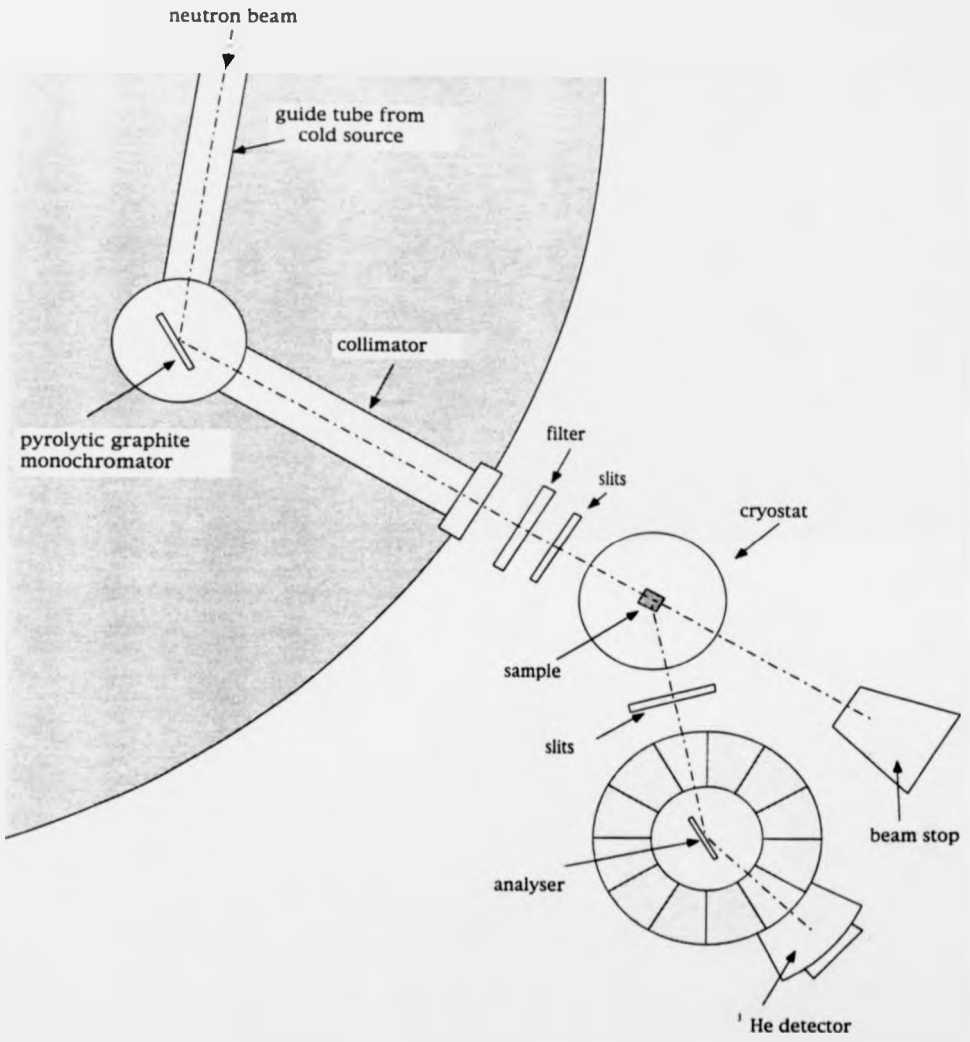

Figure 3.1 : A schematic plan of the triple-axis spectrometer TAS1.

incident-angle orientations allow the selection of one of four different wavelengths, in the range of 2.44Å to 4.77Å. The monochromated beam then passes through a Soller collimator, with exchangeable collimator plates, to the sample position. $\lambda/2$ contamination from the monochromator is effectively removed by beryllium or pyrolytic graphite filters placed in front of the sample. A variety of cryostats and furnaces may be mounted on the instrument permitting a large range of accessible environment conditions. An analyser, a further pyrolytic graphite crystal, is situated between the sample and the ^{3}He gas detector. The detection process, within the ^{3}H e detector, involves the absorption of a neutron by a ^{3}He nuclei,

$$^3\text{He} + \text{n} \rightarrow {}^3\text{H} + \text{p} + 0.770\ \text{MeV}$$

and the detection of the strong ionisation caused by the high-energy ions produced. The pre-sample slit size is determined by the sample size and are generally chosen so that for any measured reflection the sample is completely bathed in the incident beam but not too large to increase the background unnecessarily. The instrument sits on a set of air cushions and angles may be set with a precision of better than a hundredth of a degree. The control of the detector position, sample orientation and temperature is fully automated and operated from a PDP11 computer.

TAS3 is situated on a beam tube from the thermal source. The neutron flux is in equilibrium with the D_2O moderator and the distribution is peaked at 1.1Å. The maximum flux at the sample position is 7.7×10^6 $ncm^{-2}s^{-1}$. Just as for TAS1 the beam is monochromated by a pyrolytic graphite monochromator. The wavelength may be changed by varying the take-off angle from the graphite crystal, which can be varied continuously from 0° to 90° using a system of pneumatically operated shielding wedges. A Soller collimator directs the beam to the sample position. The instrument geometry, the analyser and the detector are equivalent to those of TAS1, when TAS3 is

operated with an analyser arm in the triple-axis configuration (as shown in figure 3.1 for TAS1).

3.1.2 Experimental procedure.

In each study the $PrBa_2Cu_3O_{7-\delta}$ crystals were wrapped in aluminium foil and secured to an aluminium pin using a small screw. The crystals were oriented with the (110) direction roughly perpendicular. The sample was then sealed inside an aluminium can under a vacuum. The can was mounted in a cryorefrigerator or cryostat depending on the desired sample environment. The cryorefrigerator provided stable temperatures within the range of 10K to 300K. For investigations at lower temperatures, to a base of 1.5K, a bottom-loading cryostat was used. Neutrons of wavelength 2.44Å and 1.9Å were used for investigations on TAS1 and TAS3 respectively.

The orientation of the crystal and therefore of the reciprocal lattice with respect to the instrument was determined first. Several strong nuclear Bragg reflections were located and these reciprocal lattice positions were used to define the matrix which relates the reciprocal lattice to the laboratory reference frame. This matrix was refined, by the instrument computer, by locating further nuclear peaks. The integrated intensities of the nuclear and magnetic Bragg peaks were measured by performing either $\omega : 2\theta$ scans or scans along a specific reciprocal lattice direction through each Bragg peak position. The range of the scans within reciprocal space was chosen to enable the background to be determined accurately.

3.1.3 Corrections to the measured intensities.

The measured intensities for both the nuclear and magnetic reflections are not directly comparable to each other or to theoretically calculated intensities without several corrections being made, due to geometrical factors and crystal effects. The corrected intensity I'_{hkl}, for a Bragg reflection, equal to

the observed squared structure amplitude to within a scale factor that is constant for all reflections, may be represented by the measured intensity, I_{hkl}, multiplied by various correction factors.

$$I'_{hkl} = I_{hkl}\ L^{-1}\ A^{-1}\ y^{-1} \qquad (3.1)$$

where L is the Lorentz factor, A is the absorption factor, y is the correction factor due to extinction.

The Lorentz factor is a geometrical term which corrects for the different rates at which the individual reciprocal lattice points pass through the Ewald sphere. The Lorentz factor for an angular scan about an axis perpendicular to the plane of diffraction is $L = 1/\sin 2\theta$.

The absorption correction for each reflection is dependent on the path length of the neutrons within the crystal. The thin nature and the orientation of the crystal, along with the relatively small absorption cross sections for the elements in $PrBa_2Cu_3O_{7-\delta}$, mean the absorption effects are small and may be neglected.

Diffraction from real crystals is not accurately described by kinematic theory. Our theoretical approach in Chapter 2 assumes that there is no reduction in the intensity of the beam by scattering and that no further scattering of the diffracted beam occurs. The departure from kinematic theory by which intensity is lost from the diffracted beam as the degree of perfection within the crystal increases is termed extinction and was first treated quantitatively by Darwin 1922. It is necessary to modify the measured intensity with an extinction correction factor. (The phenomenon of extinction is dealt with in more detail shortly.)

An additional consideration is the effect of the thermal vibration of the atoms which leads to thermal diffuse scattering which reduces the intensity of a Bragg peak due to inelastic scattering processes. This scattering is not isotropic across reciprocal space but occurs as broad peaks centred at the

same positions as the Bragg reflections. Within this study the effect of thermal diffuse scattering is assumed to be small and can be neglected due to the fact that the measurements were taken near T = 0K.

3.1.4 Extinction.

A major concern in single-crystal diffraction is the problem of extinction. (Note: For a more detailed examination of extinction phenomena see James 1982). The scattering from a real crystal is less than predicted by our theoretical approach which assumes an ideally imperfect crystal. A real crystal may be considered as a series of domains oriented at slighly different angles to each other, commonly known as the Darwin mosaic domain model (Darwin 1922). The departure from theory may be accounted for by considering the relative effects on the scattered beam of the two extreme limits of this model, which are described by processes known as primary and secondary extinction.

Primary extinction concerns near-perfect crystals or crystals with large perfect blocks. Neutrons incident on a crystal, at the appropriate Bragg angle, are strongly reflected. This strong reflectivity near the surface curtails the penetration of neutrons deep within each perfect crystal block and hence the atomic planes further from the surface, which otherwise would have reflected, contribute little to the overall reflected intensity (see figure 3.2a). These planes are effectively screened from the neutrons by the atomic planes nearer the surface of each block.

Secondary extinction occurs within crystals which can be described as a composition of small mosaic blocks. Due to their thin nature the reduction of beam intensity through each mosaic block is relatively small and primary extinction is negligible. Components of the neutron beam will be diffracted during passage through the crystal when incident on correctly oriented blocks. If the crystal is of great enough thickness or the blocks are only

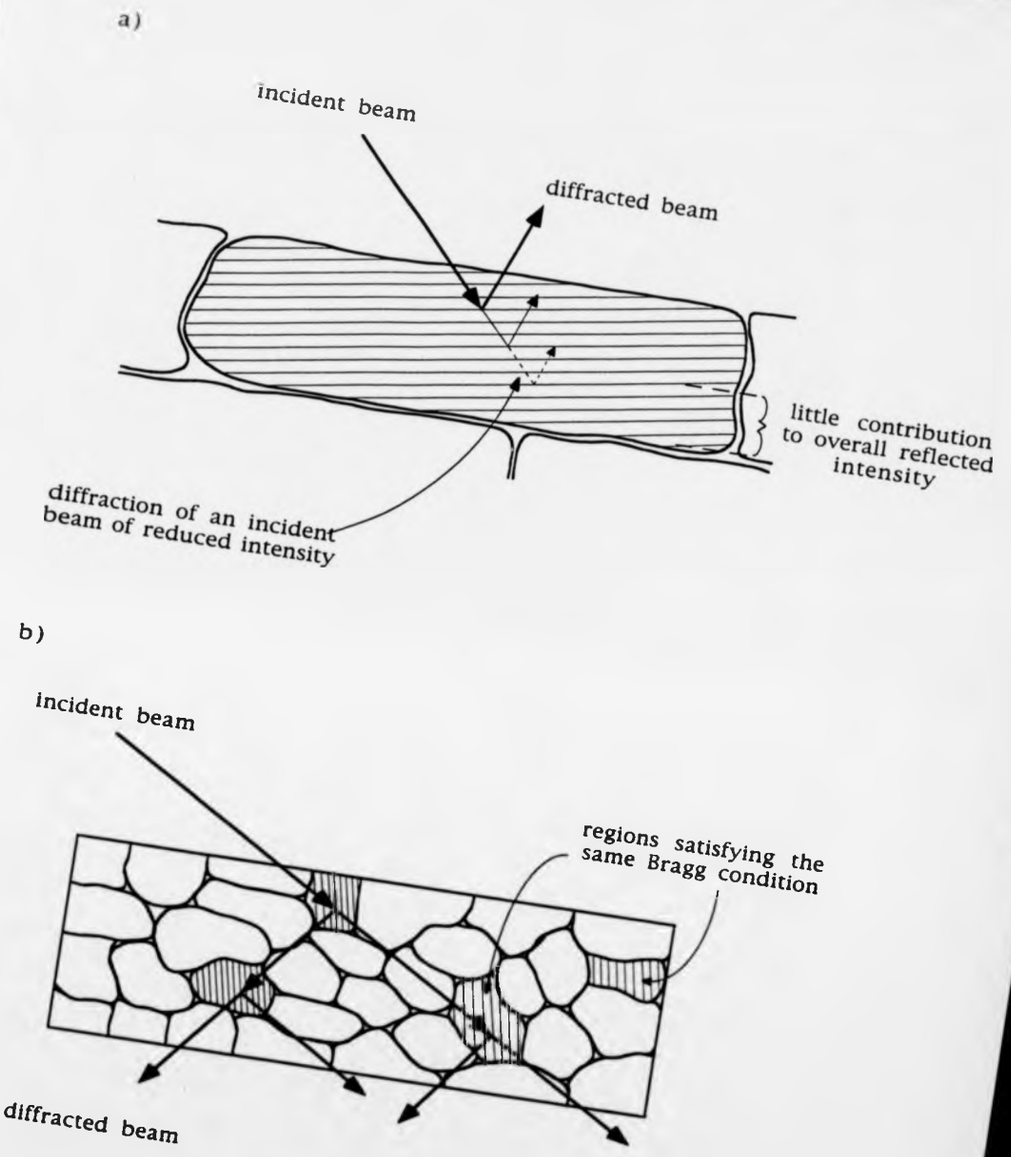

Figure 3.2 : The phenomenon of extinction. a) primary extinction b) secondary extinction.

slightly misoriented the same diffraction conditions, as previously encountered, will be met further within the crystal and diffraction occurs of a reduced intensity beam (see figure 3.2b).

Both primary and secondary extinction can also act on the diffracted beam by rediffraction from atomic planes within the same block or by other correctly oriented blocks. The essential difference between primary and secondary extinction is that within secondary extinction the individual mosaic blocks are optically independent and the diffracted neutrons from different blocks have no phase coherence, in contrast to the primary extinction case.

Various theoretical studies have been made of the extinction phenomenon and two commonly used approaches are Zachariasen 1967, and Becker and Coppens 1974. To account for extinction a correction must allow comparison of the experimental intensities to the theoretically predicted intensities.

$$I_{experimental} = I_{theoretical}\ y \tag{3.2}$$

We assume that the extinction correction factor, y, can be written as the product of the primary and secondary extinction factors,

$$y = y_{primary}\ y_{secondary} \tag{3.3}$$

where both factors may be written in a general form given by

$$y = (1 + 2x + \text{higher order terms in } x)^{-1/2} \tag{3.4}$$

with

$$2x = 2\,(t\lambda^3 / V^2 \sin^2\theta)\, g\, F_N \tag{3.5}$$

where t is mean path length for the reflection, V is the crystal volume, g is an extinction parameter and F_N is the nuclear structure factor (Becker and Coppens 1974).

3.2 Polarised-neutron diffraction.

Polarised-neutron diffraction is a valuable tool in the investigation of the magnetic properties of materials, allowing the separation of the magnetic scattering contribution from other scattering contributions Unfortunately the production of a polarised beam greatly reduces the flux incident on the sample, approximately by an order of magnitude. Only with the advent of high-flux reactor sources did polarised-neutron diffraction become a viable technique.

3.2.1 Production of a polarised beam.

Various methods exist for producing a polarised beam and the choice is dependent on the type of instrument and the intended application.

A common method for the production of a monochromated polarised beam is the use of a polarising crystal monochromator. The usual configuration, shown in figure 3.3, involves a ferromagnetic crystal within an applied field, and oriented to give a Bragg reflection. The applied field, **B**, lies perpendicular to the scattering vector, **K**, and aligns all the moments within this direction. The incident unpolarised beam may be regarded as the sum of 2 beams, one polarised parallel (+) with respect to **B** and one anti-parallel (-). The spin-dependent cross sections (equations 2.34 and 2.35) for the Bragg reflection may be written as,

$$\left(\frac{d\sigma}{d\Omega}\right)_{\pm} = \left(F_N(\tau) \pm F_M(\tau) \right)^2 \qquad (3.6)$$

A crystal for which $F_N(\tau) = F_M(\tau)$ will thus give a scattering cross section of zero for anti-parallel spins and therefore the reflected beam will only consist of neutrons of parallel spin, i.e. producing a polarised beam. In real crystals the polarisation will not be complete as a degree of depolarisation will occur

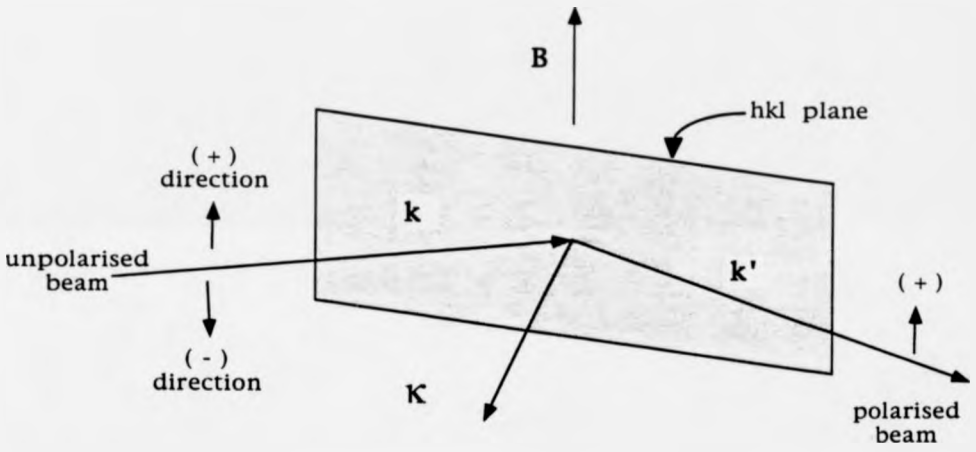

Figure 3.3 : The geometry and principle used for producing polarised beams by Bragg reflection.

within the crystal, due to magnetic inhomogeneities. The polarising efficiency of a crystal is defined as,

$$P = \frac{(N^+ - N^-)}{(N^+ + N^-)} \qquad (3.7)$$

where N^+ is the number of neutrons in the parallel spin state in the polarised beam.

Several crystals satisfy the condition $|F_N(\tau)| = |F_M(\tau)|$, in particular the (200) reflection from $Co_{0.92}Fe_{0.08}$ and the (111) reflection from Cu_2MnAl (Heusler alloy). The choice of monochromator is a compromise amongst intensity, polarising efficiency, resolution and instrumental considerations. $Co_{0.92}Fe_{0.08}$ is a well established and commonly used monochromator but its major disadvantage is the high absorption cross section of Co and therefore thin crystals are usually used as the reflectivity cannot be improved with the use of thicker crystals. The effect of absorption is reflected in the relative flux where the resulting polarised beam is more than a factor of five lower in flux than the incident unpolarised beam. A modern development is the Heusler alloy which does not suffer the same absorption problems although the low take-off angle (~16.7°) and lower resolution are disadvantageous.

Mirror reflection from a ferromagnetic crystal can be used to polarise a polychromatic beam due to the dependence of the refractive index on the neutron spin state (see equation 2.43). Each spin state will have a slightly different critical angle of reflection and hence in the region of the critical angle an angular range exists where neutrons of one spin state are totally reflected and those of the other spin state are only weakly reflected. The angular range is maximised using a material with a magnetic scattering amplitude comparable to or larger than its nuclear scattering amplitude. Additionally the unreflected neutrons must be removed from the beam which can be achieved by using absorption or incoherent scattering processes

within a substrate layer. An important limitation of polarising mirrors is the small ratio of critical-angle to wavelength which can result in loss of solid angle. A further development of the polarising mirror uses a multi-layer arrangement of alternating magnetic and non-magnetic layers. The thickness of the layers are controlled providing, through interference effects, high reflectivities up to three times the critical (θ/λ) values of normal mirrors. The first polarising mirror of this type, developed by Mezei and Dalgleish (1977) and known as a supermirror, was made from alternating iron and silver layers on a glass substrate.

3.2.2 Control of the polarisation direction.

The neutron's spin polarisation may be maintained before and after the sample with magnetic guide tubes which produce a small uniform field in the direction of the polarisation. The direction of the polarisation may be changed using spin-flipping devices, known as spin flippers which fall into two categories, adiabatic and non-adiabatic spin flippers. The flipping efficiency, f, is defined as the fraction of both (+) and (-) spins which undergo spin reversal. The polarisation of the spin-flipped beam, P', is then,

$$P' = P(1 - 2f) \tag{3.8}$$

In a magnetic field the polarisation will precess around the field direction at its Larmor frequency, $\omega_L = \gamma |\mathbf{B}|$. If the field experienced by the neutron varies along its trajectory then changes in the direction of P are possible. If the rate of change of field is much lower than the Larmor frequency the polarisation will follow the field and the component along the field direction remains unchanged. This effect is utilised in adiabatic spin flippers where radio frequency fields are used to change the polarisation direction by 180° by dictating the precise number of precessions, 1/2(2n + 1), the neutron spins undergo. The required radio frequency for the flipper will be

dependent on the velocity of the neutron and hence is a suitable spin flipper for only a monochromatic beam.

In a non-adiabatic spin flipper the applied field changes sign very rapidly with respect to the Larmor frequency so that the polarisation vector remains unchanged in the laboratory frame; the spins are in effect flipped with respect to the field. The primary benefits of this form of flipper are that they can be used to flip white beams because the flipping process is independent of the neutron's velocity and they are also efficient flippers for large area beams.

3.2.3 Analysis and instrumental corrections.

Experimentally the polarisers and spin flippers are imperfect and have efficiencies less than 100% and therefore the experimental data must be corrected for this. It can be shown that the flipping ratio, see equation 2.37, becomes,

$$R = \frac{1 + 2Pr + r^2}{1 + 2P(1 - 2f)r + r^2} \qquad (3.9)$$

when the polarisation and spin-flipping efficiencies are considered. The actual polarisation and flipping efficiencies and the degree of instrumental depolarisation of the beam, caused by imperfect guide tubes, can be determined by performing a calibration experiment with a standard sample such as $Co_{0.92}Fe_{0.08}$ for which $F_M = F_N$.

An additional instrumental consideration required, with the use of polarising crystal monochromators, is $\lambda/2$ contamination. This may be removed using resonance filters which capture the neutron through resonance absorption processes or it can be accounted for with a further correction to the flipping ratio.

The effect of primary extinction on the flipping ratio is generally small compared to the other considerations and may be neglected. In contrast, the

effect of secondary extinction often is important in polarised-neutron experiments and hence the necessary corrections were made to measured flipping ratios (Delapalme 1979).

3.3 Magnetisation density measurements.

Investigations of the magnetisation density distribution in $PrBa_2Cu_3O_{7-\delta}$ single crystals were performed using polarised-neutron diffraction. An initial study was carried out on a 1.6mg crystal on D3B at the Institut Laue-Langevin (7 days, December 1990) and a further experiment was performed on a larger 100mg crystal on Poldif at the Laboratoire Léon Brillouin (14 days, September 1992). Both crystals were grown by the CuO flux method at the National Crystal Growth Facility, University of Oxford. (Note: The 100mg crystal was the same crystal used in the study of the magnetic ordering of praseodymium and copper.) The crystals were thin rectangular plates with the **a** and **b** unit cell directions approximately along the plate edges.

3.3.1 The D3B Spectrometer.

D3B is a polarised-neutron diffractometer (figure 3.4) on the H4 beam tube from the horizontal hot source of the high flux reactor (58MW) at the Institut Laue-Langevin (I.L.L), Grenoble. The Maxwellian distribution of the neutrons is modified by the hot source to produce an enhancement of the intensity in the wavelength range $0.4 < \lambda < 0.8$Å. The short wavelengths allow magnetic structure factors up to $\sin\theta/\lambda = 2$Å^{-1} to be measured.

The initial polarisation of the beam is achieved using easily exchangeable $Co_{0.92}Fe_{0.08}$ and Cu_2MnAl (Heusler alloy) crystal monochromators. The Heusler alloy provides a higher flux but with a lower resolution and polarising efficiency than the $Co_{0.92}Fe_{0.08}$ monochromator. Various resonance filters, mounted on an automated carousel, may be placed in the beam to remove $\lambda/2$ contamination.

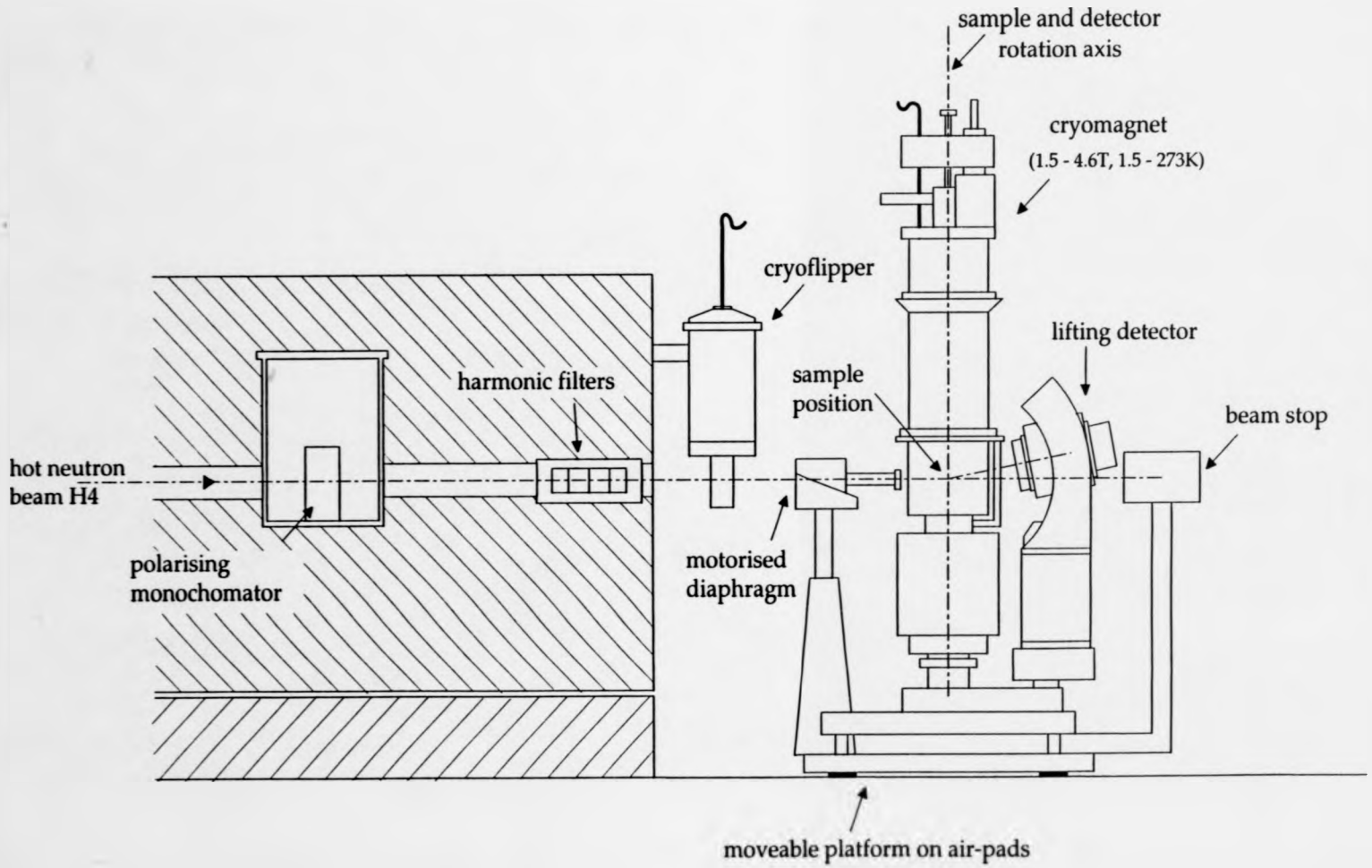

Figure 3.4: The D3B polarised-neutron diffractometer.

The polarisation is controlled by a cryoflipper (Tasset 1991a, 1991b) which utilises the Meissner effect of a superconductor within a non-adiabatic spin flipper. The cryoflipper consists of two magnetic field guides positioned closely either side of a thin sheet of superconducting niobium foil which lies transverse to the beam. In the flipper 'on' state the fields lie anti-parallel to each other and the neutrons will experience a rapid reversal of field across the narrow width of the superconducting foil. These non-adiabatic conditions cause a change in neutron spin state relative to the field. In the flipper 'off' state the fields lie parallel and no reversal of field occurs across the superconducting foil. This spin-flipping technique is insensitive to stray magnetic fields and is independent of wavelength, hence no modification is required with changes in wavelength.

The diffraction geometry of the instrument is illustrated in figure 3.5, where the angular limits are $-135^\circ < \gamma < 0^\circ$, $-190^\circ < \omega < 190^\circ$ and $-5^\circ < \nu < 23^\circ$. The flux at the sample, at a wavelength of 0.843Å, is ~ 2 x 10^6 $ncm^{-2}s^{-1}$ and ~ 1 x 10^7 $ncm^{-2}s^{-1}$ for the $Co_{0.92}Fe_{0.08}$ and Heusler alloy crystal monochromators respectively. The scattered neutrons are detected using a single ^3He detector. To provide the low-temperature and high-field conditions a 4.6T Oxford Instrument cryomagnet is used, providing stable sample conditions from 1.5 to 273K and from 1.5 to 4.6T. The instrument is extensively automated with the temperature, applied field, instrument position and data recording controlled by a PDP11/73 computer.

3.3.2 The Poldif spectrometer.

Poldif is a single-crystal diffractometer for polarised neutrons at the Orphée Reactor (14MW), Laboratoire Léon Brillouin (L.L.B), Saclay. The instrument is positioned on the 5C1 beam tube from the hot source.

The neutron flux is modified by the hot source and enhanced in the wavelength range $0.5 < \lambda < 1.2$Å. Poldif is of a similar instrument design to D3B

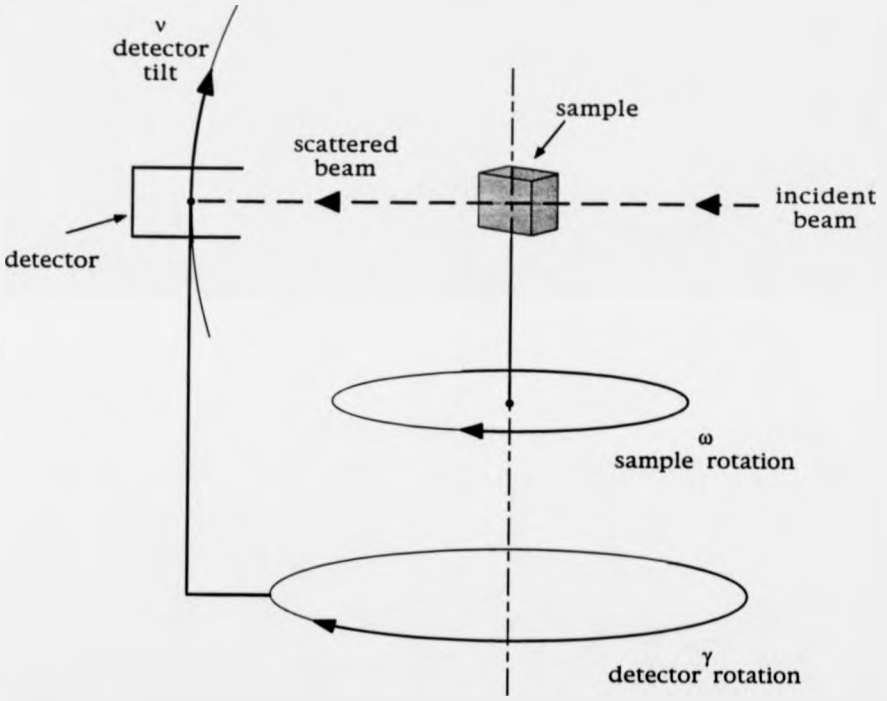

Figure 3.5 : Diffraction angles for D3B.

at the I.L.L, as described above, but with an estimated incident neutron flux on the sample a factor of 5 - 10 lower. A schematic representation of the instrument is shown in figure 3.6. The incident neutron beam is initially polarised by either a $Co_{0.92}Fe_{0.08}$ or a Heusler-alloy crystal monochromator and the spin orientation is controlled by a cryoflipper. The sample environment is provided by a cryomagnet providing stable temperature and magnetic fields in the ranges 1.5 to 273K and 1.3 to 6T respectively. The scattered neutrons are detected with a ^3He detector. The cryostat and sample rotations are fully automated.

3.3.3 Experimental Procedure.

For the initial study on D3B the $PrBa_2Cu_3O_{7-\delta}$ crystal was fixed on a Cd tipped Al pin with "Kwikfill", an epoxy body-filler, and mounted on the cold tip of the cryomagnet. The crystal was protected by an Al can. The crystal was mounted in a suitable orientation to allow access to the hhl reflections. The experiment was performed at a temperature of 20K, above the expected ordering temperature for the Pr^{3+} ions, under a 4.5T applied field. The collimation after the $Co_{0.92}Fe_{0.08}$ monochromator was relaxed to obtain the higher intensity beam of wavelength 0.843Å.

For the experiment involving the larger crystal, on Poldif, the crystal was mounted and oriented in a similar manner as in the D3B experiment. Although in this case the crystal was fixed on the Cd tipped Al pin with "Araldite Rapide". The experiment was performed at a temperature of 15K, above the lower ordering temperature observed for this crystal during the investigation of its magnetic properties on TAS1. A 5T magnetic field was also applied to the sample. A monochromatic polarised-neutron beam, of wavelength 0.829Å, was used, obtained from the Heusler-alloy monochromator.

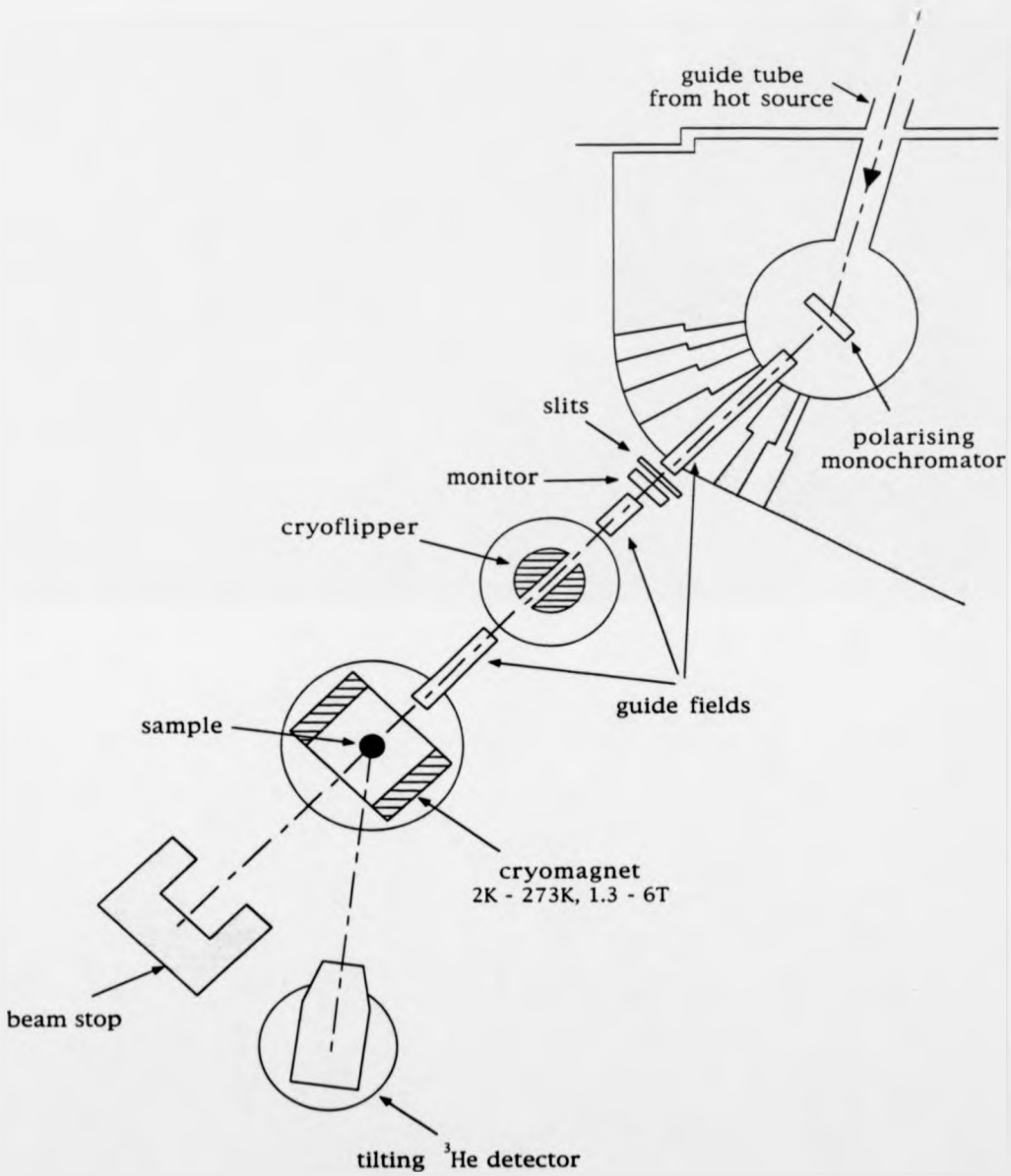

Figure 3.6 : A schematic plan of the polarised-neutron diffractometer Poldif.

The orientation of the crystal and its reciprocal lattice with respect to the instrument was performed in a similar manner as described for the magnetic ordering experiments on TAS1 and TAS3. An applied magnetic field oriented the magnetic moments within the crystal ferromagnetically along the direction of the field. The flipping ratios, the ratio of the scattered intensity for neutrons of each spin state, were measured for a large number of Bragg peaks. The location of the centre of the Bragg peak and the measurement of the flipping ratio and background were performed under computer control.

3.3.4 The effect of crystal twinning.

The range of measurable reflections was severely restricted due to the twinning of the crystal, a consequence of the crystal growth, (McIntyre and Renault 1989). Initially during growth the $PrBa_2Cu_3O_{7-\delta}$ crystals are oxygen deficient and tetragonal in structure. During oxidation the crystals undergo a transition to an orthorhombic structure. In this transition neither of the tetragonal basal-plane axes is an advantageous direction for the shorter orthorhombic axis to lie along and hence this axis can lie along either, with equal probability. This will manifest itself in two ways within the crystal. On a macroscopic scale the orthorhombic **a** and **b** axes may interchange forming domains at 90^{o} to each other and on a microscopic scale the very similar a and b unit cell dimensions mean that local twinning will occur about the (110) planes. The result of this twinning is a quadrupling of the orthorhombic reciprocal lattice, (see figure 3.7).

Due to the small differences in the basal-plane unit-cell dimensions the four related hkl and khl reflections are tightly grouped around the hkl reflection position for the tetragonal structural approximation to the twinned crystal. The broad resolution of the polarised-neutron diffactometers used did not permit the individual reflections to be separated and therefore the peak profile always contained contributions from several of the related

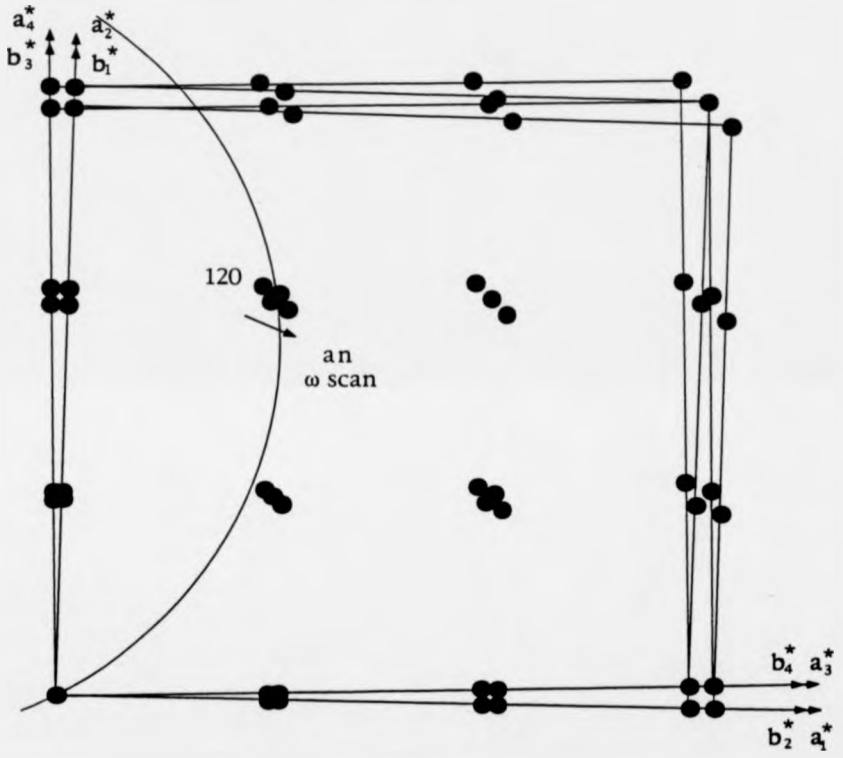

Figure 3.7 : The effect of twinning on the hk0 reciprocal lattice plane of $PrBa_2Cu_3O_{7-\delta}$.

reflections. (Note: Using a two-dimensional position-sensitive detector on a high resolution 4-circle diffractometer the individual untwinned reflections of $YBa_2Cu_3O_{7-\delta}$ have been observed (McIntyre et al 1988). The splitting expected in $PrBa_2Cu_3O_{7-\delta}$ is a factor of ~2 smaller since the degree of orthorhomicity is smaller, and thus would be more difficult to observe.) If we consider a reflection group where $h \neq k$, e.g. the 120 reflection group, then the peak will contain contributions from the nuclear and magnetic scattering components from the hkl and khl Bragg reflections. As these orthorhombic reflections are not equivalent then the resulting measured flipping ratio will be related to both of the non-identical magnetic structure factors. It is impossible to separate these terms from the flipping ratio as their relative contribution to the peak profile are indeterminable. Only for twinned reflections with $h = k$, e.g. the 110 reflection, will be peak profile contain only equivalent reflections and hence the flipping ratio will be dependent on only one magnetic structure factor. The measurable flipping ratios, from which the magnetic structure factors may be determined, are thus restricted to the subset of hhl reflections.

3.4 Polarised-neutron reflectivity.

The magnetic field depth profile within a lead superconductor, in the bulk and surface superconducting states, were investigated using polarised-neutron reflectivity. Experiments were performed on thin lead films at ISIS at the Rutherford Appleton Laboratory, (~14 days). The films were prepared by vapour deposition of lead on the highly polished (111) faces of silicon wafers. Films of area 30 x 30 mm^2 and of thickness a few microns were deposited.

3.4.1 The CRISP spectrometer.

CRISP is a neutron reflectometer at the pulsed spallation neutron source ISIS at the Rutherford Appleton Laboratory, UK and can be used in either a

polarised or unpolarised mode. A high intensity pulse of protons from a 800MeV proton synchrotron hits a uranium target producing a pulse of neutrons. The repetition frequency is 50Hz resulting in a maximum neutron yield of ~4 x 10^{16}n/s. As all the neutrons are emitted from the target at the same time the velocity and hence the wavelength of a neutron can be determined by measuring its time of flight across a known distance. Within an elastic scattering process a neutron undergoes no change in wavelength and therefore the wavelength of the scattered neutron will be directly related to the time of arrival at the detector.

CRISP, see figure 3.8, lies on a beam tube from the cold moderator (H2 at 25K) which provides neutrons in the wavelength range $0.5 < \lambda < 6.5$Å. Initially a series of thin-film nickel mirrors, set at 3°, reflect long wavelength neutrons (> 26Å) out of the beam. The beam is then polarised using a cobalt-titanium supermirror (Schärpf 1982) which has a (θ/λ) range of polarising reflection extending from ~0 to ~3.3 mradÅ^{-1}. The orientation of the neutron spins is controlled by a two-coil non-adiabatic spin flipper (Hughes and Burgy. 1951). In this spin flipper two coils lie coaxially about the neutron trajectory producing magnetic fields of opposite polarity, (see figure 3.9). Midway between the two coils the neutron experiences a rapidly reversing magnetic field and its spin undergoes a non-adiabatic transition of state with respect to the field. Stray magnetic fields which can reduce the flipping efficiency are minimised by surrounding the coils with magnetic shielding. An orange cryostat with quartz windows provides a sample environment with temperatures in the range of 1.5 to 273K and a magnetic field parallel to the surface of the films is provided by an electromagnet external to the cryostat. The quartz windows of the cryostat allow the alignment of the films with a laser. The temperature of the cryostat is controlled by a computer. After reflection from a sample the neutrons are detected by a single ^{3}He gas detector.

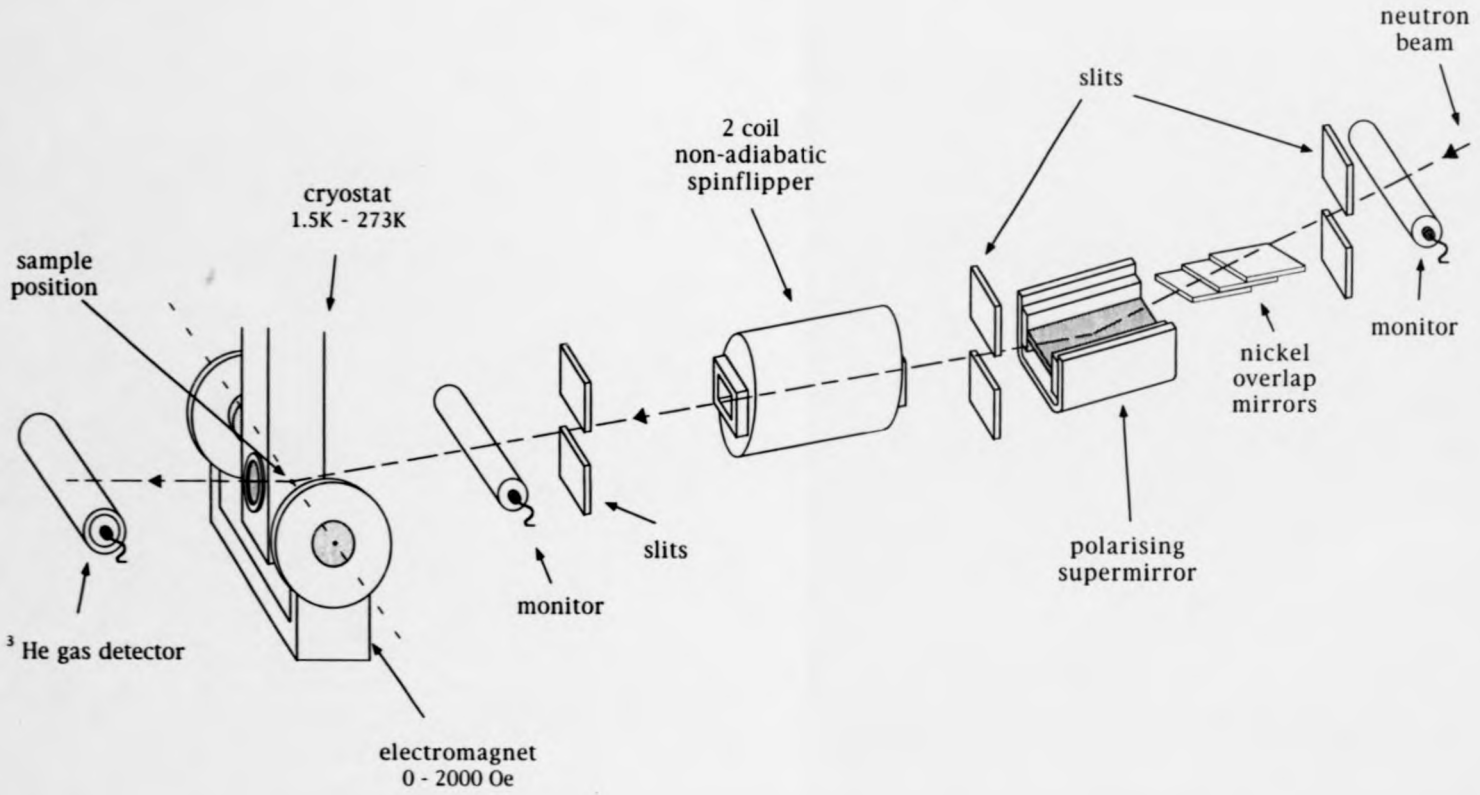

Figure 3.8 : The CRISP polarised-neutron reflectometer.

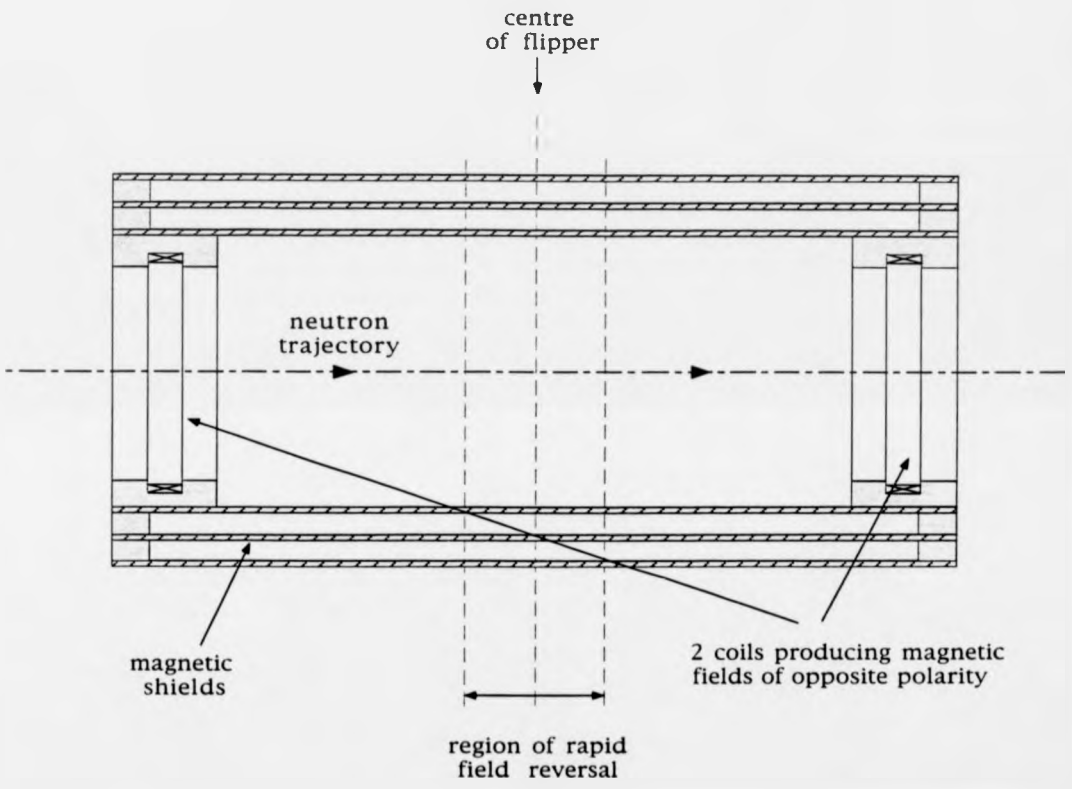

Figure 3.9 : A 2-coil non-adiabatic spin flipper.

3.4.2 Experimental procedure.

The films were attached to support plates using a small amount of vacuum grease and mounted on a specially designed sample stick, and placed within the cryostat, (see figure 3.10). The mounting assembly enables four films to be separately investigated and the best film to be selected for a detailed study without warming the cryostat and exchanging the samples. This avoids the problem of the lead films being badly oxidised by water condensing on the surface during warming and extraction. The tilt of the support plates is finely controllable and the films could be accurately aligned at 0.3° to the beam. The experiment was performed at 1.5K, below the superconducting transition of lead and in a region where surface superconductivity is theoretically predicted, within applied fields in the range of $0 < B < 1000$ Oe. Measurements are taken for each spin state in rapid alternation by energising the spin flipper.

3.4.3 Instrumental and sample corrections.

The time-of-flight analysis of the detected beam and the instrumental corrections for the polarisation and spin-flipping efficiencies are carried out by the instrument computer. Additional sample considerations due to the imperfect nature of the lead films have to be made. The surfaces of the films are not smooth and exhibit a degree of surface roughness. This is taken into account by modifying the measured reflectivities by a Debye-Waller type function. In the analysis of the data a surface oxide layer must be considered due to a small degree of surface oxidation which occurs while the samples are exposed to air during the mounting and loading procedures.

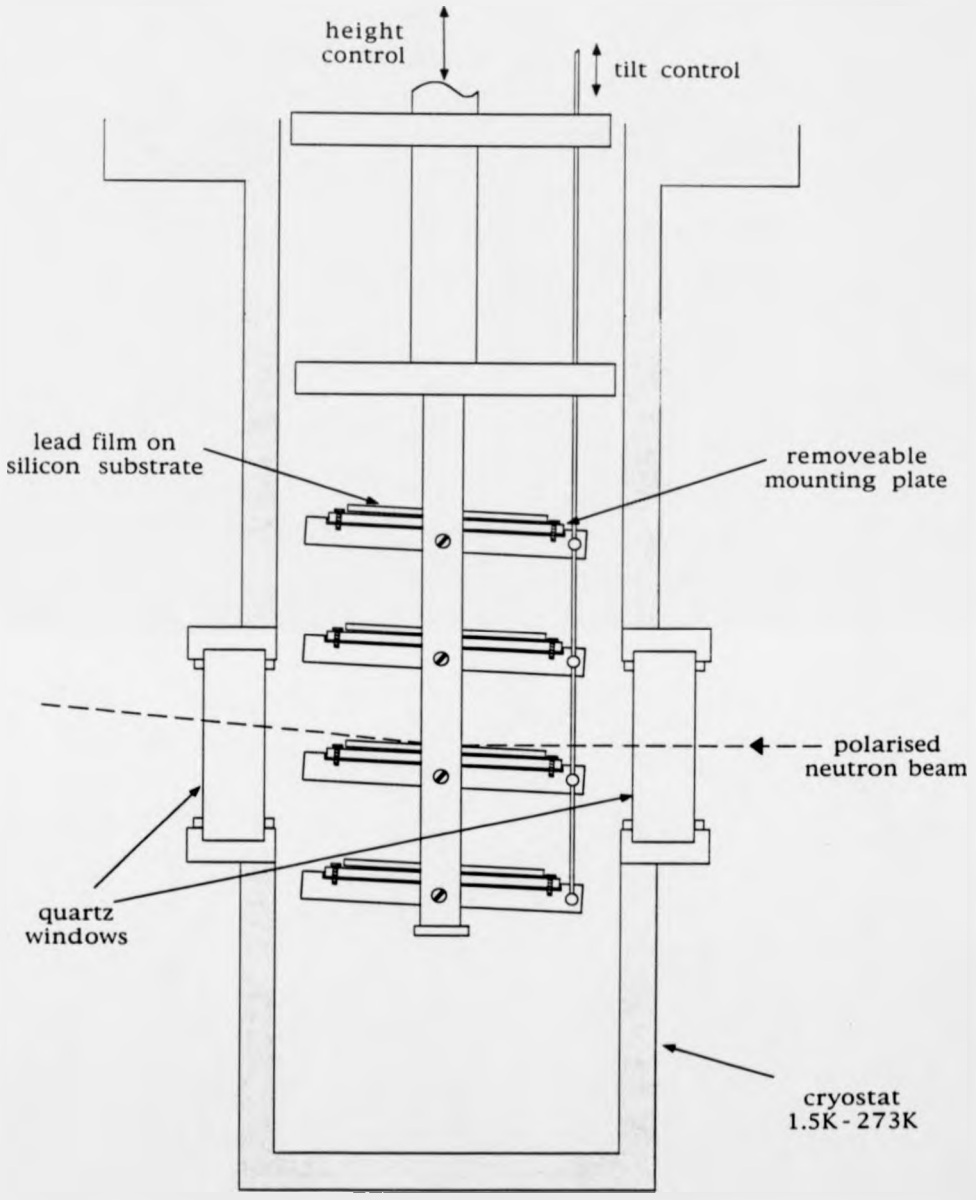

Figure 3.10 : A schematic representation of the sample stick and cryostat used for the study of superconducting lead films.

CHAPTER FOUR

MAGNETIC ORDERING IN $PrBa_2Cu_3O_{7-\delta}$.

4.1 Introduction.

We have performed three separate studies to determine the magnetic ordering within $PrBa_2Cu_3O_{7-\delta}$. All the measurements have been performed upon the same single crystal although between each experiment the crystal has undergone further oxygenation. This has enabled us to study the magnetic ordering as a function of increasing oxygen concentration.

After growth, see section 2.2, the crystal was initially annealed in 340 - 370 bar of O_2, at 425°C for ~200 hours. We shall refer to this oxygenated state as $\delta = \delta_1$. After the first experiment the crystal was annealed for a second time in 1 bar of O_2, at 450°C for ~1500 hours, ($\delta = \delta_2$). At this oxygen concentration the crystal was also examined on a 4-circle diffractometer in order to determine the crystallographic structure, see section 5.2. From these measurements δ_2 was calculated to be 0.27 ± 0.02. Before the final study of the magnetic order, the crystal underwent a third oxygenation in 1 bar of O_2, at 450°C for ~3000 hours, ($\delta = \delta_3$). We know from the history of the sample that $\delta_3 < \delta_2 < \delta_1$, but only δ_2 is known. In this chapter the final study, where $\delta = \delta_3$, forms the major basis of our results. The results of the two earlier investigations will be discussed in relation to this study.

At room temperature antiferromagnetic order is already present, apparent from the observation of magnetic Bragg peaks. This ordering can be attributed to the Cu moments within the CuO_2 planes. The Néel temperature, T_{N1}, for this ordering may be extrapolated from the temperature dependence of the magnetic Bragg peaks and found to be ~ 400 K. At much lower temperatures, T < 50K, the Cu moments along the chains also order at $T = T_{N2}$, changing the overall magnetic structure. Additionally, in this low

temperature range, diffuse scattering is observable from two-dimensional correlations of the Pr spins.

4.2 The high-temperature copper ordered phase, $T_{N2} < T < T_{N1}$.

Preliminary investigations at 40K revealed the presence of a number of magnetic Bragg peaks of the type ($h=(2n_1+1)/2$, $k=(2n_2+1)/2$, $l=n_3$), where n_1, n_2 and n_3 are integers and where $n_1 = n_2$. (Note: these reflections which were the only accessible magnetic reflections within our scattering plane will be refered to as (h/2, k/2, *l*) reflections.) No magnetic Bragg peaks of the form ($h=(2n_1+1)/2$, $k=(2n_2+1)/2$, $l=(2n_3+1)/2$), to be refered to as (h/2, k/2, *l*/2) reflections, were found to be present at this temperature. If we assume the origin of this magnetic scattering to be ordering of the Cu spins, as shown to be the case in earlier studies of $PrBa_2Cu_3O_{7-\delta}$, (Rosov et al. 1992)), and in the studies of other $ReBa_2Cu_3O_{7-\delta}$ compounds, (Li et al. 1990), then the observation of peaks with $h=(2n_1+1)/2$ and $k=(2n_2+1)/2$ implies that neighbouring Cu spins are coupled antiferromagnetically along the **a** and **b** unit cell directions. This antiferromagnetic arrangement results in a magnetic unit cell quadrupled in area, to the chemical unit cell, in the **a** - **b** plane. In contrast, as the reflections also have $l=n_3$ then this requires the chemical and magnetic unit cells to be the same in the **c** direction. An explanation consistent with this requirement is one where the spins of the Cu ions in the CuO_2 planes order, of which there are two per chemical unit cell, and the Cu spins along the chains remain disordered. This may possibly be due to the weaker coupling between the chain Cu spins caused by the reduced oxygen concentration within these layers. In addition, the absence of a (0.5, 0.5, 0) magnetic Bragg reflection means that neighbouring Cu spins on adjacent CuO_2 planes along the **c** direction, must also be coupled antiferromagnetically.

In order to determine the Cu moment's direction and size the intensities of the measured magnetic peaks, corrected for the Lorentz factor, (see Section

3.1.3), have to be compared to theoretically modelled intensities. Accurate profiles of a set of magnetic reflections, of the type (h/2, k/2, *l*) where h = k, were obtained using ω scans, where the crystal was rotated through the Bragg position with the detector fixed, and are shown in figure 4.1. Each peak is fitted by the method of least squares to a Gaussian, where the average half-width at half-height, hwhh, for this set of reflections is $0.276^{o} \pm 0.009^{o}$. The small shoulder on the right-hand side of each peak is attributed to small misaligned crystallites on the surface of the crystal.

The intensity of a magnetic Bragg peak, arising from one magnetic species, is theoretically expressed as

$$I_{hkl} = C <\mu>^2 f^2(\kappa) <1 - (\hat{\kappa} \cdot \hat{\mathbf{M}})^2> \left| \sum_{j=1}^{N} e^{-W_j} e^{i\kappa \cdot r_j} \right|^2 \qquad (4.1)$$

where C is a constant, $<\mu>$ is the thermal average of the aligned magnetic moments, $\hat{\kappa}$ and $\hat{\mathbf{M}}$ are unit vectors in the direction of the reciprocal lattice vector and spin direction respectively, $f(\kappa)$ is the magnetic form factor, N is the number of magnetic ions in the magnetic unit cell, r_j is the position of the jth atom and W_j is the Debye-Waller factor for the jth atom, (e.g. see Bacon. 1976). The orientation factor $<1 - (\hat{\kappa} \cdot \hat{\mathbf{M}})^2>$ must be calculated for all the possible magnetic domains. A fitting of the modelled intensities to the experimental intensities, was performed, based upon a least squares approach, using programs from the Cambridge Crystallography Subroutine Library (Brown and Matthewman 1993). In our analysis we used a spherically symmetric form factor for Cu^{2+} (Brown 1990) and assumed the moments on the two Cu sites to be identical. The moment size was obtained by fitting the magnetic peaks in conjunction with a number of nuclear Bragg peaks. The initial atomic positions and site occupancies were taken from the 4-circle diffraction study performed upon the crystal in its earlier oxygenation state, see table 5.1.

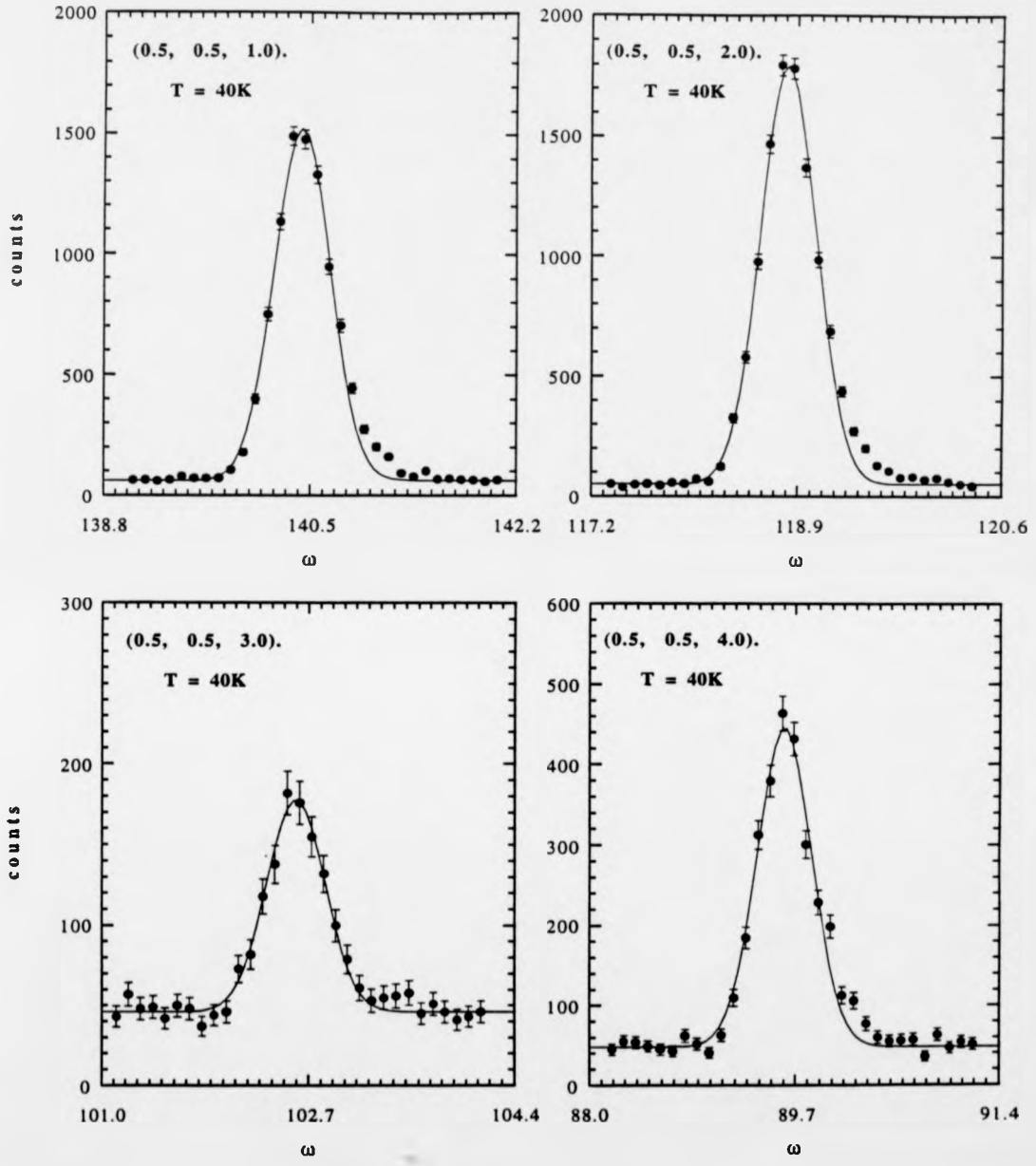

Figure 4.1: Several antiferromagnetic, (h/2, k/2, *l*) type magnetic Bragg peaks, where h = k, obtained for the $\delta = \delta_3$ crystal at 40K.

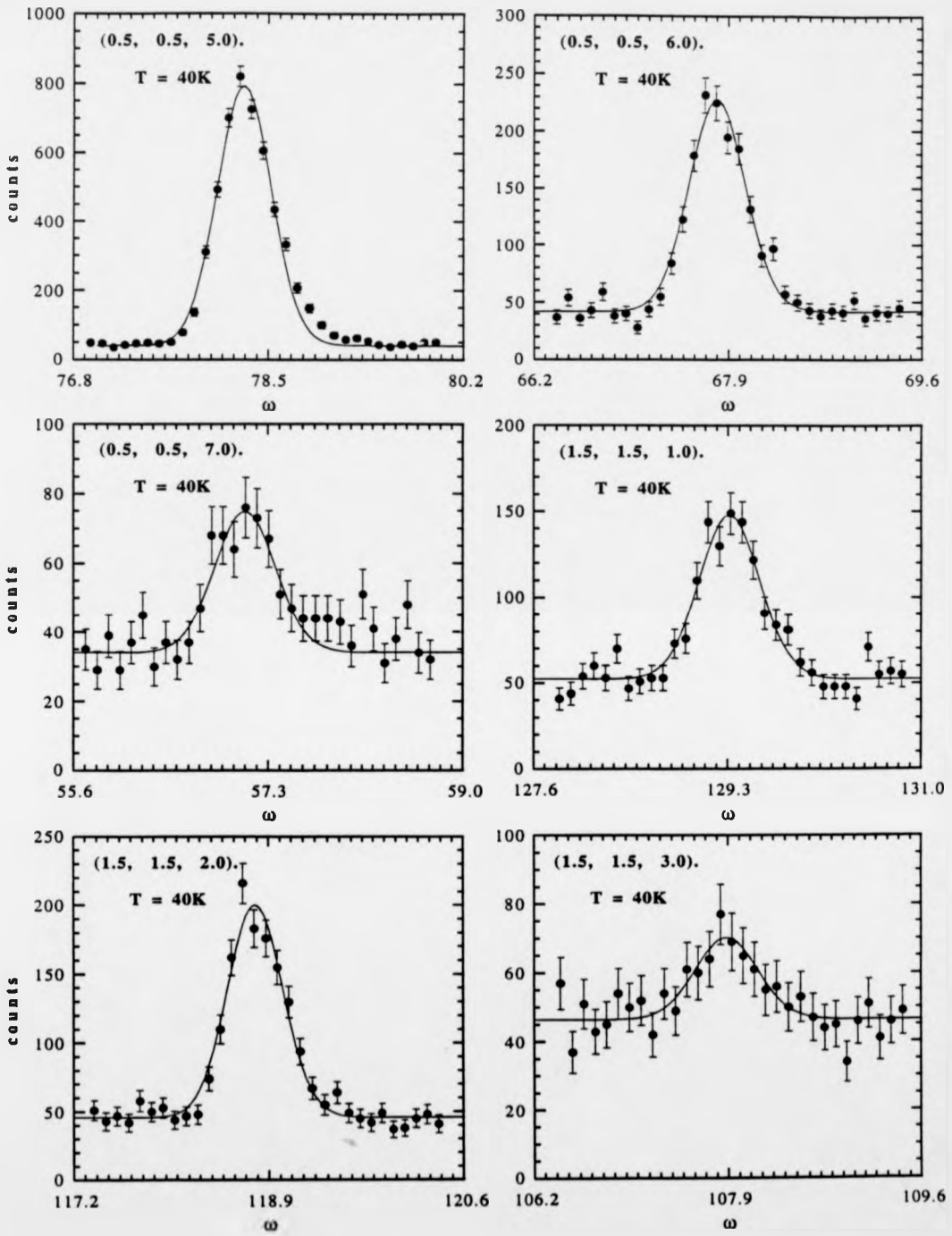

Figure 4.1 (continued): Several antiferromagnetic, (h/2, k/2, *l*) type, magnetic Bragg peaks, where h = k, obtained for the $\delta = \delta_3$ crystal at 40K.

The magnetic structure which agreed most closely with the experimental results at 40K involved Cu moments, of (0.55 ± 0.04)μ_B, lying within the **a-b** plane, as shown in figure 4.2. It is impossible to establish whether there is a preferred orientation within the **a-b** plane as information on the moment direction is lost when the domain average is taken. The close agreement between the measured and calculated intensities is shown in Table 4.1.

For this high-temperature Cu-ordered state the model also agrees well with the magnetic peak intensities for the two earlier studies, $\delta = \delta_1$ and $\delta = \delta_2 = 0.27$. Figure 4.3a shows the temperature dependence of the strongest peak, (0.5, 0.5, 2.0), for the $\delta = \delta_1$ crystal. The peak intensity appears to saturate with decreasing temperature and indicates that the ordered moment has reached its maximum value. From this temperature dependence we estimate T_{N1} to be (400 ± 30) K. An accurate determination of T_{N1} was not possible due to the limited temperature range of the Displex cryorefrigerator. The behaviour of the same reflection for the $\delta = 0.27$ crystal, at high temperatures, was very similar. Although no temperature dependence of this peak was performed for the $\delta = \delta_3$ crystal, checks at room temperature showed the presence of (h/2, k/2, *l*) type magnetic Bragg peaks. An earlier study of the Cu order in $PrBa_2Cu_3O_{7-\delta}$ using single crystals of estimated low oxygen concentrations, $\delta > 0.4$ (Rosov et al. 1992), showed $T_{N1} = 370$ K. This agrees closely with the results for our crystal, in its higher relative oxygenation states. We may therefore conclude that T_{N1} appears to be insensitive to the overall oxygen concentration. This is in contrast to the behaviour of T_{N1} for the other $ReBa_2Cu_3O_{7-\delta}$ compounds, (Li et al. 1990) where T_{N1} decreases from ~430 K at δ = 1.0 to 0 K at $\delta = 0.5$.

4.3 The low-temperature copper ordered phase, $T < T_{N2}$.

At (10 ± 1) K the intensity of the (h/2, k/2, *l*) type reflections, for the $\delta = \delta_3$ crystal, begins to decrease with decreasing temperature, as illustrated by the

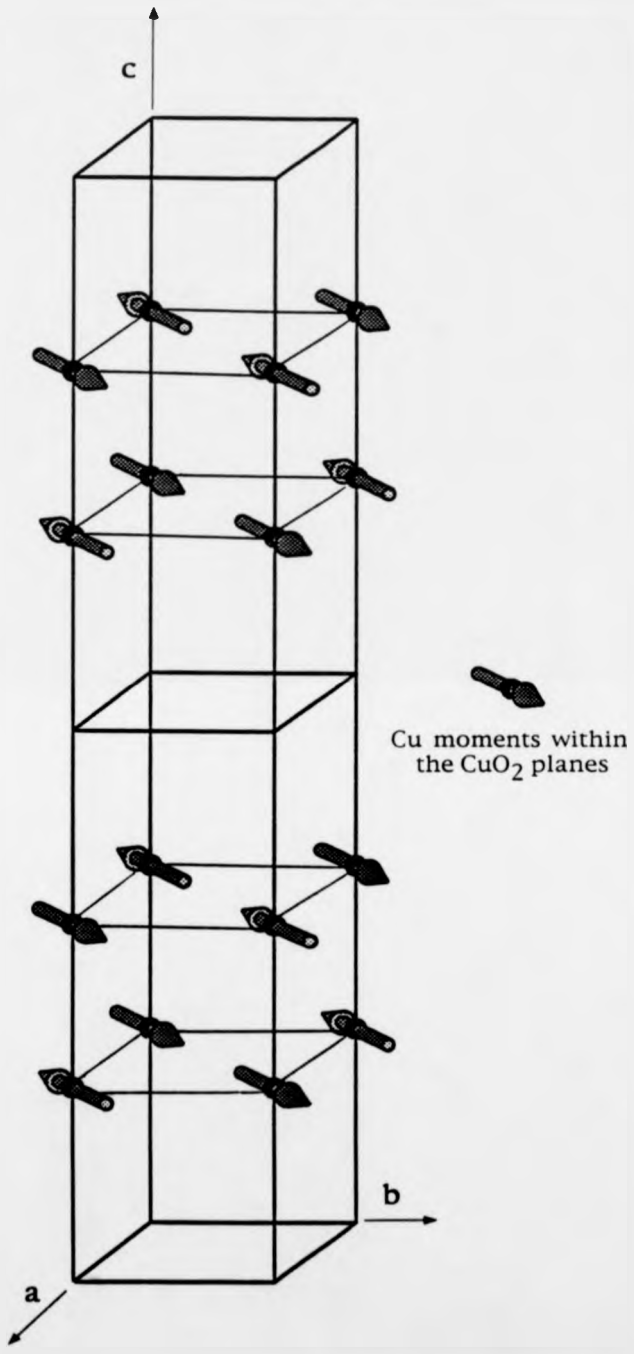

Figure 4.2: The magnetic spin configuration for the Cu moments, within the CuO_2 planes, in the high-temperature ordered phase. In this phase the Cu spins within the Cu chains remain disordered. (Note : The chosen direction of the moments within **a-b** plane is arbitrary, as no evidence is available which would indicate a preferred orientation.)

Reflection. (h, k, *l*)	I_{obs}	I_{calc}
0.5, 0.5, 0	0.00 ± 0.02	0.00
0.5, 0.5, 1	0.67 ± 0.03	0.65
0.5, 0.5, 2	1.00 ± 0.03	1.00
0.5, 0.5, 3	0.09 ± 0.02	0.10
0.5, 0.5, 4	0.30 ± 0.03	0.30
0.5, 0.5, 5	0.68 ± 0.04	0.65
0.5, 0.5, 6	0.19 ± 0.03	0.15
0.5, 0.5, 7	0.04 ± 0.02	0.03
1.5, 1.5, 0	0.00 ± 0.02	0.00
1.5, 1.5, 1	0.10 ± 0.04	0.16
1.5, 1.5, 2	0.15 ± 0.03	0.20
1.5, 1.5, 3	0.03 ± 0.02	0.02
		$\chi^2 = 0.189$

Table 4.1 : The observed and calculated intensities for our single crystal of $PrBa_2Cu_3O_{7-\delta}$ at 40 K, where $\delta = \delta_3$. In the calculation the moments on the planar Cu sites are $(0.55 \pm 0.04)\mu_B$ whilst the Cu spins within the Cu chains remain disordered. The (0.5, 0.5 2) peak has been defined to have an intensity of unity for convenience and to allow a direct comparision to previously published results to be made, (e.g. Li et al. 1990).
(Note: $\chi^2 = \frac{1}{n_{obs} - n_{par\ obs}} \sum \frac{(I_{obs} - I_{calc})^2}{(\sigma_{obs})^2}$ where n_{obs} and n_{par} are the number of observations and parameters respectively.)

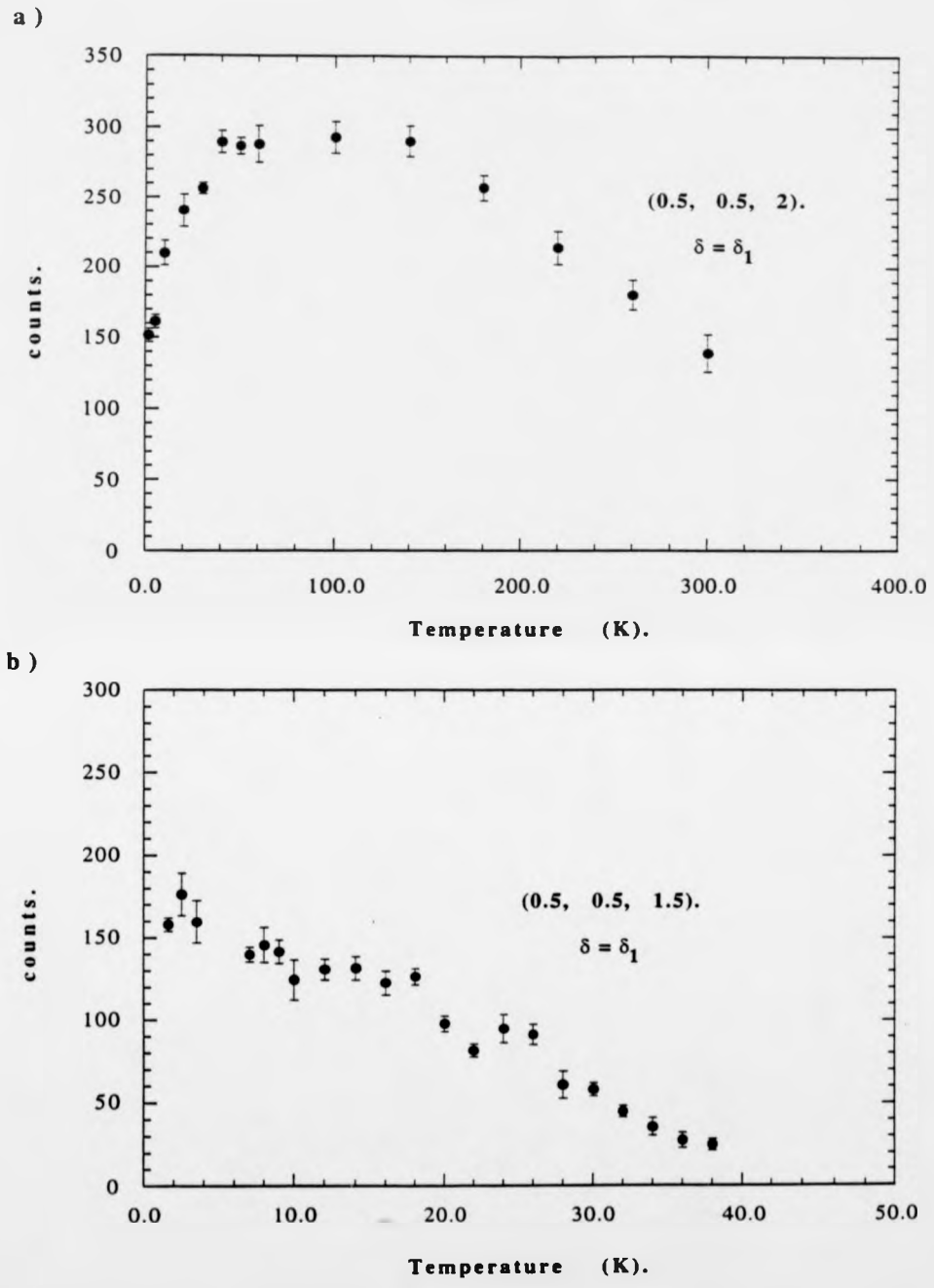

Figure 4.3: The temperature dependence of a) the (0.5, 0.5, 2) reflection and, b) the (0.5, 0.5, 1.5) reflection, for the $\delta = \delta_1$ crystal. T_{N1} may be extrapolated from the temperature dependence of the (0.5, 0.5, 2) peak to be (375 ± 25) K. The onset of the ordering of the chain Cu spins, T_{N2}, occurs at (40 ± 3) K.

temperature dependence of the (0.5, 0.5, 2) reflection, shown in figure 4.4a. Associated with this decrease is the appearance of, and subsequent increase in, the intensities of (h/2, k/2, *l*/2) type magnetic Bragg reflections. This indicates that a change in the spin configuration has occurred. As the new Bragg reflections occur at $l=(2n_3+1)/2$ this implies that the magnetic unit cell is now doubled along the c direction. This change in the magnetic structure may be attributed to antiferromagnetic ordering of the chain-Cu spins. The introduction of ordered magnetic moments along the Cu chains complicates the spin configuration.

If we consider the exchange coupling interaction between Cu spins along the c direction then above T_{N2} the exchange coupling between Cu spins in adjacent CuO_2 planes, J_{pp}, is strongly antiferromagnetic, (Kadowaki et al. 1988). There is also an antiferromagnetic interaction, J_{ip}, between two planar Cu spins, separated by the Cu chains. J_{ip} is mediated by ions within these Cu chains and can be regarded as a next-nearest-neighbour interaction and therefore weaker than J_{pp}. Below T_{N2} there is now an additional antiferromagnetic coupling, J_{cp}, between the Cu spins in adjacent Cu chains and CuO_2 planes. The competition between the interactions J_{ip} and J_{cp} gives rise to the frustration within the spin configuration. The result of these competing interactions is a non-collinear spin structure with spin components of a periodicity of either c or 2c along the c direction which results in the presence of both (h/2, k/2, *l*/2) and (h/2, k/2, *l*) type magnetic Bragg reflections.

To model this non-collinear spin structure we are able to use a similar approach to the one used to model the high-temperature phase. Since the (h/2, k/2, *l*/2) type reflections and the (h/2, k/2, *l*) type reflections come from separate series of Fourier components we were able to model the two responsible spin configurations independently and form an overall spin configuration by superimposing the two models.

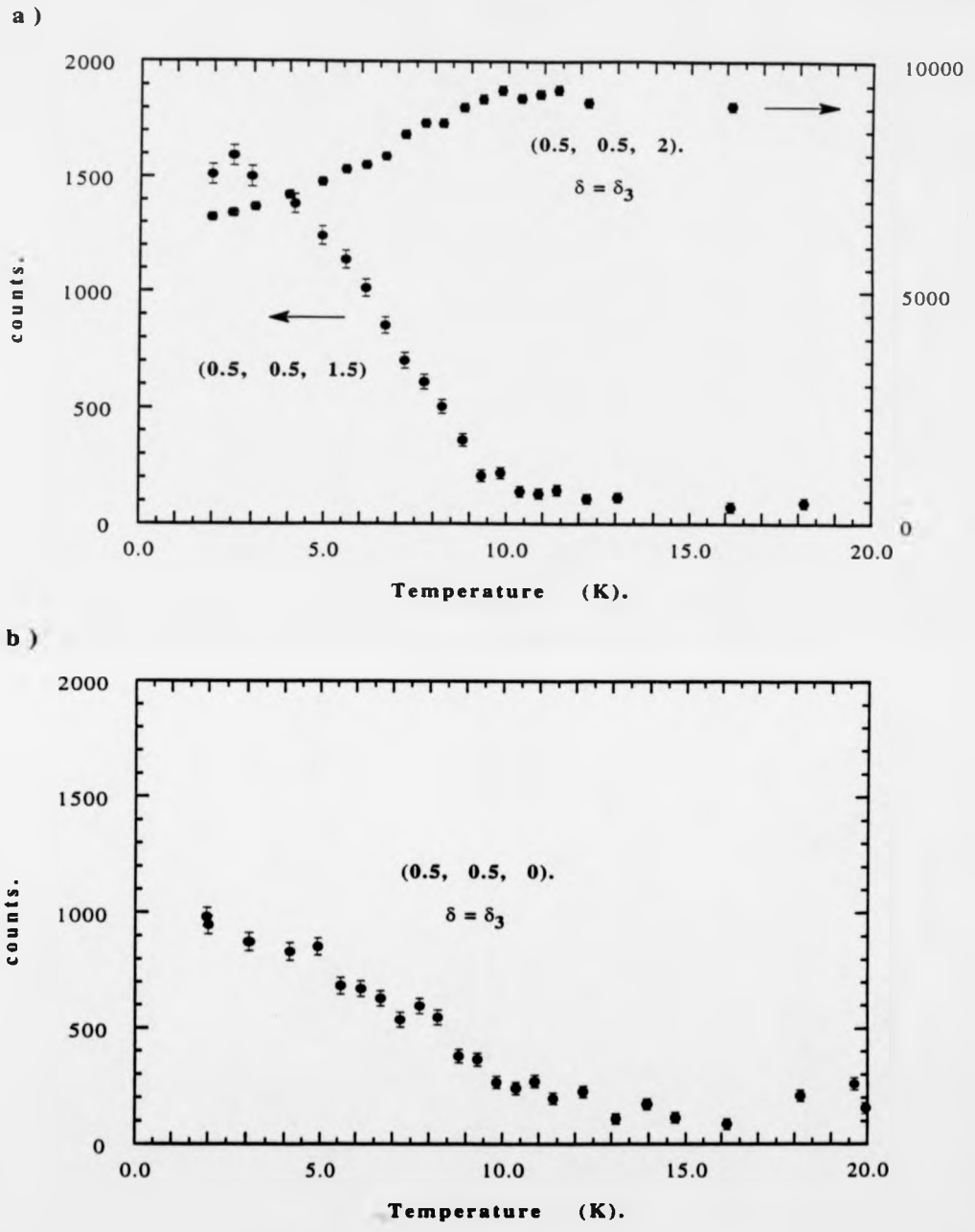

Figure 4.4: The temperature dependence of a) the (0.5, 0.5, 2) and the (0.5, 0.5, 1.5) peaks, and b) the diffuse scattering centred on the (0.5, 0.5, 0) Bragg position, for the $\delta = \delta_3$ crystal. From a) T_{N2} is found to be (10 ± 1) K (*Note : different scales in a) for the two reflections).

Accurate determination of the magnetic peak intensities from the measured peak profiles, in this low-temperature region, was complicated by the presence of diffuse scattering from short-ranged correlations of the Pr spins, (this diffuse scattering will be discussed in more detail in section 4.4). Two-dimensional correlations of the Pr spins, in the **a**-**b** plane, resulted in a narrow rod of diffuse scattering through the (0.5, 0.5, 0) scattering position and along the l direction of reciprocal space. Small three-dimensional correlations produced very broad peaks of scattering centred upon the (h/2, k/2, l) Bragg positions, which decreased in intensity with increasing l. In the estimation of the observed magnetic peak intensities this diffuse scattering had to be taken into account.

For the $l=n_3$ peaks a comparison between peak profiles measured above and below T_{N2}, at 40K and 2K respectively, clearly illustrates the presence of the diffuse scattering beneath the magnetic Bragg peak, see figure 4.5. For each 2K profile, for $n_3 < 6$, the data points corresponding to the background of the 40K profiles, 5 - 8 points on the extreme left-hand and right-hand sides of each profile, were fitted with broad Lorentzians in order to account for this diffuse scattering. The effect of the diffuse scattering rod was neglected due to its small size relative to the diffuse scattering centred on the magnetic Bragg positions. An accurate profile of the diffuse scattering, due to the three-dimensional correlations, at the (0.5, 0.5, 0) position, where no magnetic Bragg scattering occurs, allowed us to characterise this scattering at one $l=n_3$ position and thus enabled us to model the diffuse scattering with a reasonable accuracy at other $l=n_3$ positions. Once the diffuse scattering was subtracted from the peak, the remaining peak was fitted with a Gaussian by least squares. This approach to obtaining the peak intensities can be justified in several ways. Firstly, by the overall excellent fits to the data obtained using a Lorentzian plus a Gaussian, see figures 4.5b and 4.6, and secondly by the reasonable agreement found between the Gaussian hwhh's for the magnetic

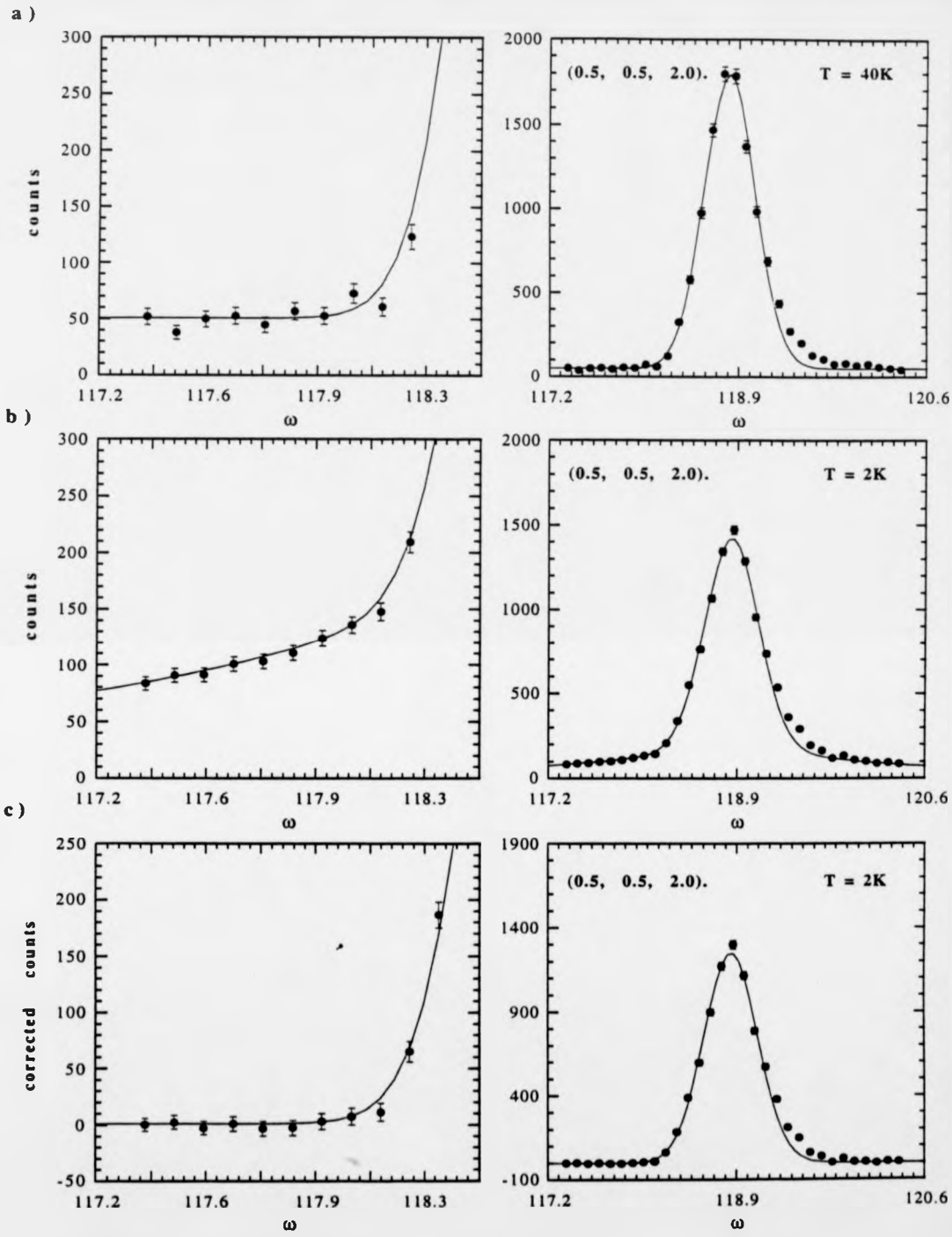

Figure 4.5: a) The (0.5, 0.5, 2.0) peak profile, measured at 40K, fitted with a Gaussian. b) The complete 2K profile, fitted with a Gaussian, for the magnetic Bragg peak, plus a Lorentzian, for the diffuse scattering. c) The (0.5, 0.5, 2.0) peak profile, measured at 2K, with the calculated diffuse scattering subtracted from the raw data. The fit is again Gaussian. (Note: the left hand plots correspond to an expanded view of the lefthand side of each peak profile.)

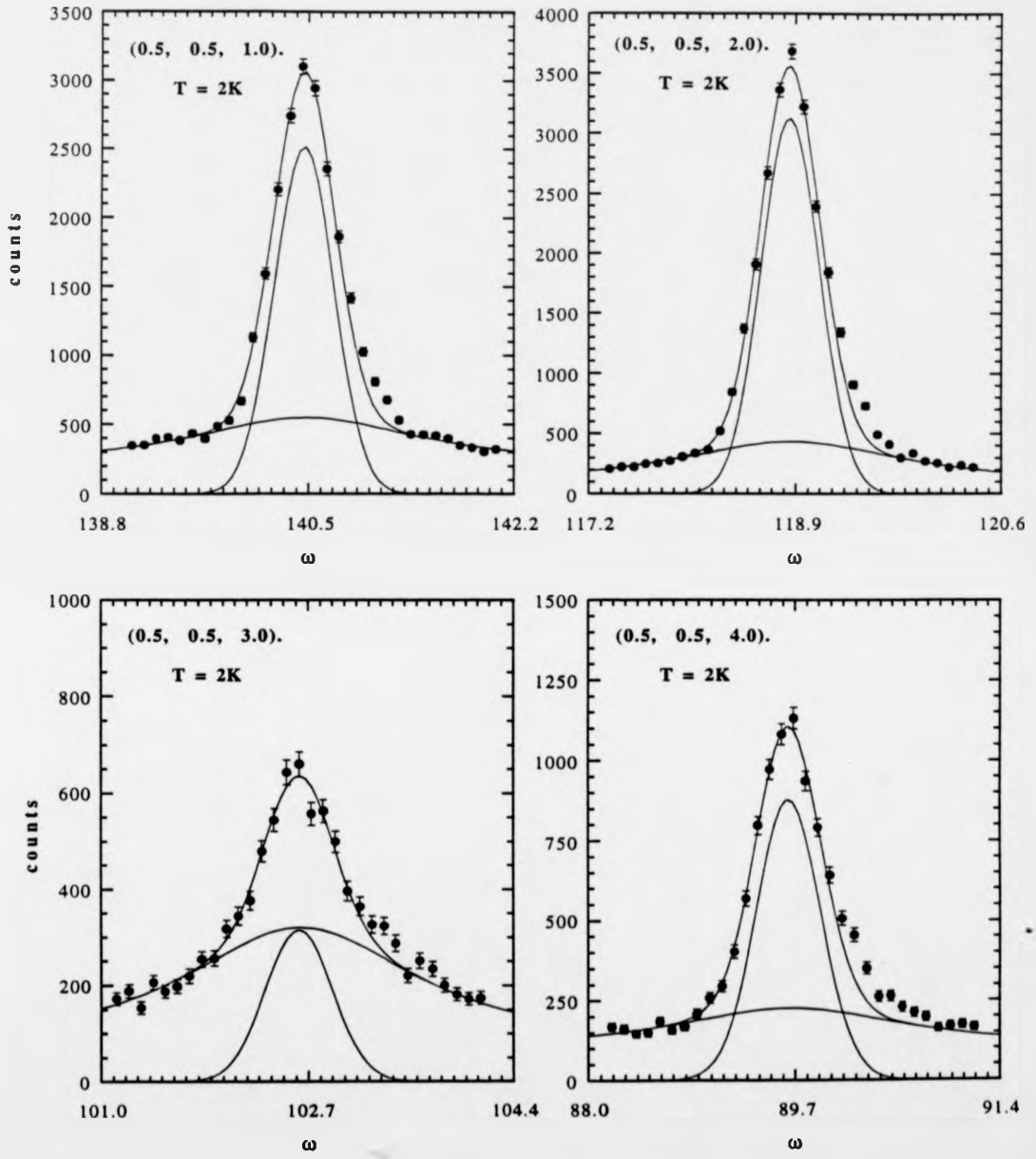

Figure 4.6: Several antiferromagnetic, (h/2, k/2, *l*) type, magnetic Bragg peaks obtained for the $\delta = \delta_3$ crystal at 2K. The solid lines show the diffuse and magnetic Bragg scattering components to the profile in addition to their sum. (*Note : Different measurement time than used in figure 4.1).

Bragg peak profiles measured at 40K and 2K, $0.276^{o} \pm 0.009^{o}$ and $0.30^{o} \pm 0.01^{o}$ respectively. For the higher order (h/2, k/2, *l*) peaks, where $n_{\lambda} > 5$, the effect of the diffuse scattering was found to be negligible and pure Gaussians were fitted to the data.

In order to obtain the peak intensities for the (h/2, k/2, *l*/2) type of reflections a slightly different problem was encountered. These magnetic Bragg peaks were not situated upon diffuse scattering from three-dimensional correlations but just on the diffuse scattering rod. Due to the ω scans used the instrumental resolution ellipsoid swept through the diffuse rod at different angles, depending on the position in reciprocal space and hence the contribution of the rod to the profile varied for different magnetic reflections. As a result each profile was fitted with a narrow Gaussian, with a hwhh of a similar size to the other measured magnetic Bragg peaks, in addition to a broader Gaussian which accounts for the diffuse scattering rod. The quality of the fits to the experimental profiles for the (h/2, k/2, *l*/2) refections is illustrated in figure 4.7. The (0.5, 0.5, 4.5) and (0.5, 0.5, 5.5) reflections were measured but later rejected due to contamination problems from Al powder diffraction lines arising from the Al sample can protecting our crystal.

We have attempted to model the spin configuration using several different models. In the model which provided the best agreement with the observed intensities, the Cu moments within the chains and the planes both lay within the **a**-**b** plane. Within each layer all the Cu spins are ordered antiferromagnetically with respect to their nearest neighbours. Along the **c** direction the Cu spins, within the CuO_2 planes, are ordered antiferromagnetically with respect to their neighbour in the adjacent CuO_2 plane and lie at an angle α to the Cu spins within the chains. Additionally, the spins of the Cu ions within one CuO_2 plane are rotated in the opposite sense, with respect to the chain moments, to those within the CuO_2 plane on the

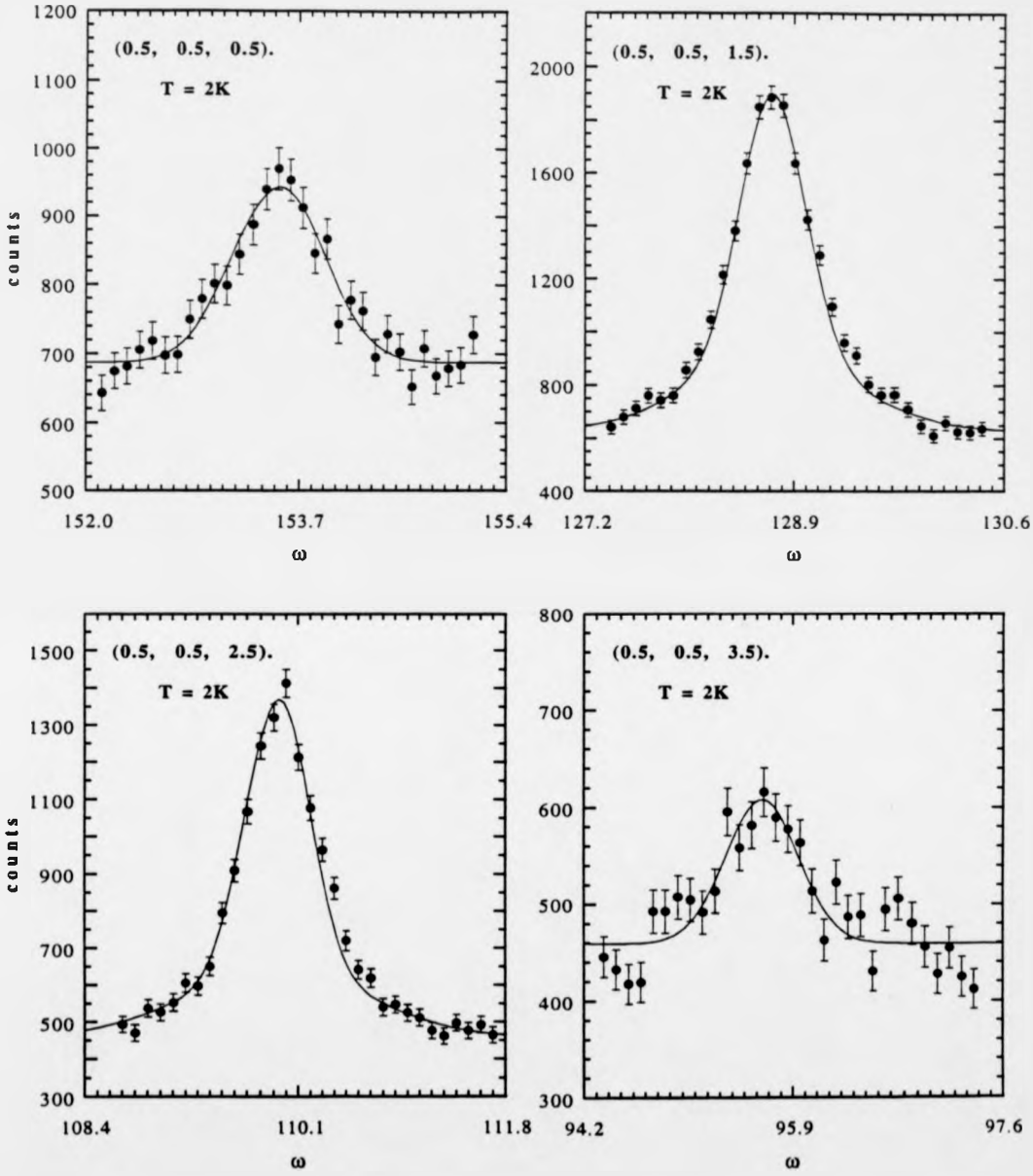

Figure 4.7: Several antiferromagnetic, (h/2, k/2, *l*/2) type, magnetic Bragg peaks obtained for the $\delta = \delta_3$ crystal at 2K. The calculated fits include the diffuse and magnetic Bragg scattering components to the profile.

opposite side of the Cu chain, see figure 4.8. A comparison between the observed intensities and the calculated intensities, obtained using this model, is presented in to Table 4.2. Employing this model we obtained a chain Cu moment of $(0.25 \pm 0.03)\mu_B$ and a planar Cu moment of $(0.54 \pm 0.06)\mu_B$ orientated at a relative angle of $23^o \pm 2^o$.

An overall representation of the development of the spin configuration with decreasing temperature, within this low-temperature phase, may be simply described by the chain Cu spins ordering at right angles to the planar spins at T_{N2} and as the temperature decreases the magnitude of the chain moments increases and the planar spins rotate towards them.

This model of the spin configuration does not match the model to describe the magnetic structure of the Cu spins in $PrBa_2Cu_3O_{7-\delta}$ proposed by Rosov et al, 1992. Their proposed model contains an ordered component of the chain Cu spins along the **c** direction. All attempts to model our data with a similar component in the **c** direction worsened the agreement between our observed intensities and the calculated intensities considerably.

In contrast, our model is very similar to the model found to describe the Cu spin configuration of $NdBa_2Cu_3O_{7-\delta}$ a typical $ReBa_2Cu_3O_{7-\delta}$ compound, at temperatures just below T_{N2}, (Li et al. 1990) In $NdBa_2Cu_3O_{7-\delta}$, the (h/2, k/2, *l*) peaks appear to fall to zero as the temperature approaches T = 0 K, leaving only (h/2, k/2, *l*/2) peaks, indicating that the Cu planar spins have rotated fully through 90^o to lie parallel and anti-parallel to the chain Cu spins forming a linear antiferromagnetic spin configuration. This behaviour occurs in $NdBa_2Cu_3O_{0.63}$ where the chain Cu spins order at 10K, the same T_{N2} as for our $\delta = \delta_3$ crystal, and the (0.5, 0.5, 1.5) peak appears and quickly increases in intensity while the (0.5, 0.5, 2) peak falls away to zero intensity at 0 K, see figure 1.7. In contrast, though, for our $\delta = \delta_3$ crystal the (0.5, 0.5, 2) peak shows no sign of dropping to zero intensity, see figure 4.4, and remains a

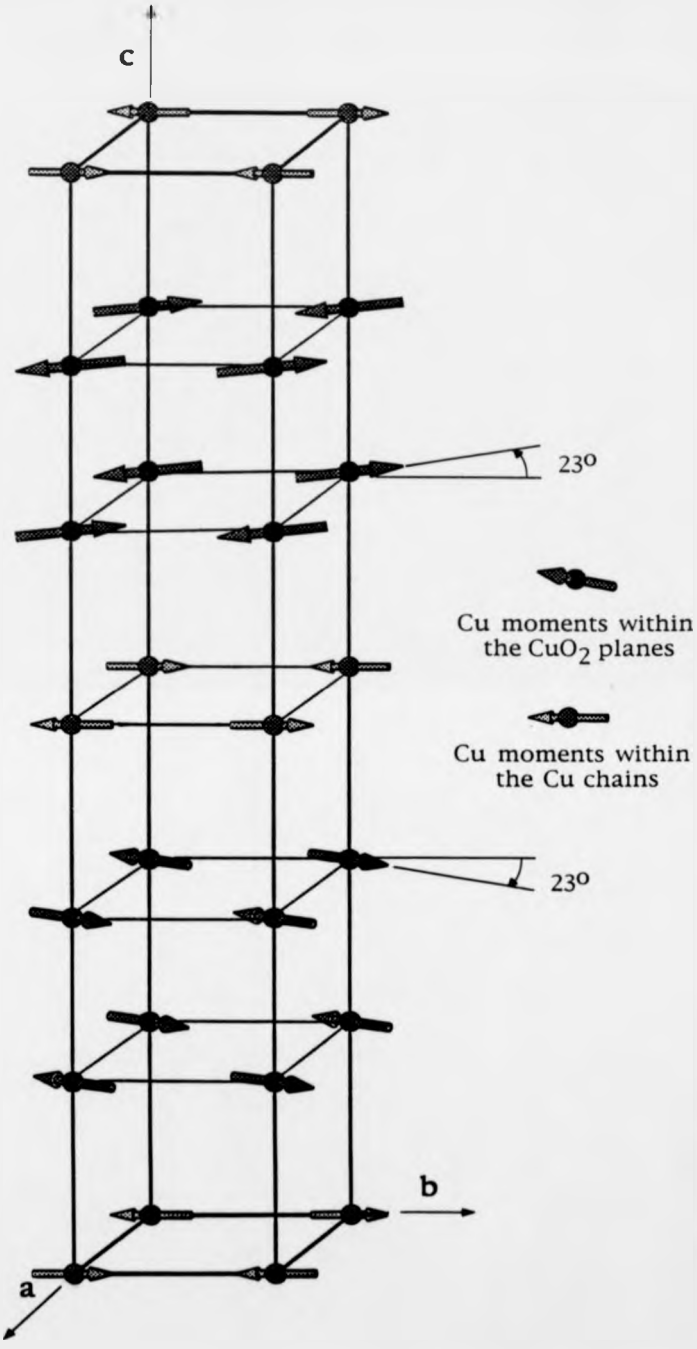

Figure 4.8: The magnetic spin configuration for the Cu moments in the low-temperature ordered phase. (Note : The direction of the chain Cu moments in the **a** - **b** plane is arbitrary and has been chosen to be along the **b** direction to aid the eye in distinguishing the relative moment directions.)

Reflection. (h, k, *l*)	I_{obs}	I_{calc}
0.5, 0.5, 0.5	0.030 ± 0.004	0.033
0.5, 0.5, 1.5	0.106 ± 0.020	0.109
0.5, 0.5, 2.5	0.096 ± 0.018	0.072
0.5, 0.5, 3.5	0.046 ± 0.020	0.022
1.5, 1.5, 0.5	0.010 ± 0.008	0.011
1.5, 1.5, 1.5	0.029 ± 0.014	0.032
1.5, 1.5, 2.5	0.015 ± 0.010	0.019
0.5, 0.5, 1	0.65 ± 0.03	0.63
0.5, 0.5, 2	1.00 ± 0.03	1.00
0.5, 0.5, 3	0.14 ± 0.02	0.11
0.5, 0.5, 4	0.44 ± 0.03	0.32
0.5, 0.5, 5	0.76 ± 0.04	0.77
0.5, 0.5, 6	0.28 ± 0.03	0.21
0.5, 0.5, 7	0.11 ± 0.02	0.04
1.5, 1.5, 1	0.13 ± 0.04	0.21
1.5, 1.5, 2	0.18 ± 0.03	0.29
1.5, 1.5, 3	0.03 ± 0.02	0.03
		$\chi^2 = 0.548$

Table 4.2 : The observed and calculated intensities for our single crystal of $PrBa_2Cu_3O_{7-\delta}$ at 2.0 K, where $\delta = \delta_3$. In the calculation the moments on the chain and planar Cu sites are $(0.23 \pm 0.03)\mu_B$ and $(0.54 \pm 0.06)\mu_B$ respectively and are at a relative angle of $23^\circ \pm 2^\circ$. The (0.5, 0.5 2) peak has been defined to have an intensity of unity for convenience.

much stronger reflection than the strongest $l=(2n_3+1)/2$ reflection, the (0.5, 0.5, 1.5).

Another major difference between the behaviour of the Cu spins in $NdBa_2Cu_3O_{7-\delta}$ and in $PrBa_2Cu_3O_{7-\delta}$ is the relative moment size of the planar Cu ions above and below T_{N2}. In our study we found the magnitude of the Cu planar moment remained the same within experimental error above and below T_{N2}, (0.54 ± 0.06) μ_B and (0.55 ± 0.04) μ_B respectively, whilst in $NdBa_2Cu_3O_{7-\delta}$ the Cu planar moment was found to increase above its saturated high-temperature phase magnitude in the low-temperature region from 0.65 to 0.8μ_B.

The model found to describe well the low-temperature Cu spin phase within the $\delta = \delta_3$ crystal also provided a reasonable model for the behaviour of the crystal in its two previous oxygenation states. Studies with the $\delta = \delta_1$ crystal showed the chain Cu spins ordered at (40 ± 3) K as shown by the temperature dependence of the (0.5, 0.5, 2) and (0.5, 0.5, 1.5) peaks, see figure 4.3. The temperature dependence of the (0.5, 0.5, 2) peak at low temperatures, near 0 K, was consistent with the behaviour of the same peak for the $\delta = \delta_3$ crystal in that there is no evidence that the intensity would fall to zero at 0 K. For the δ = 0.27 crystal T_{N2} was found to be slightly higher than T_{N2} for the $\delta = \delta_3$ crystal at (11 ± 1) K, as illustrated by the temperature dependence of the (0.5, 0.5, 0.5) and (0.5, 0.5, 1.5) peaks shown in figure 4.9. We then conclude that T_{N2} is strongly dependent on the oxygen concentration of the crystal, in contrast to T_{N1}. Results from an uncompleted study of a smaller $PrBa_2Cu_3O_{7-\delta}$ crystal, see figure 4.10, would indicate that our $\delta = \delta_3$ crystal is still not fully oxygenated if we assume T_{N2} decreases with increasing oxygen concentration, as implied by our results, as no (h/2, k/2, *l*/2) type reflections are observed nor any associated drop in the intensity in the (h/2, k/2, *l*) type of reflections down to 8 K, characteristic of chain Cu ordering.

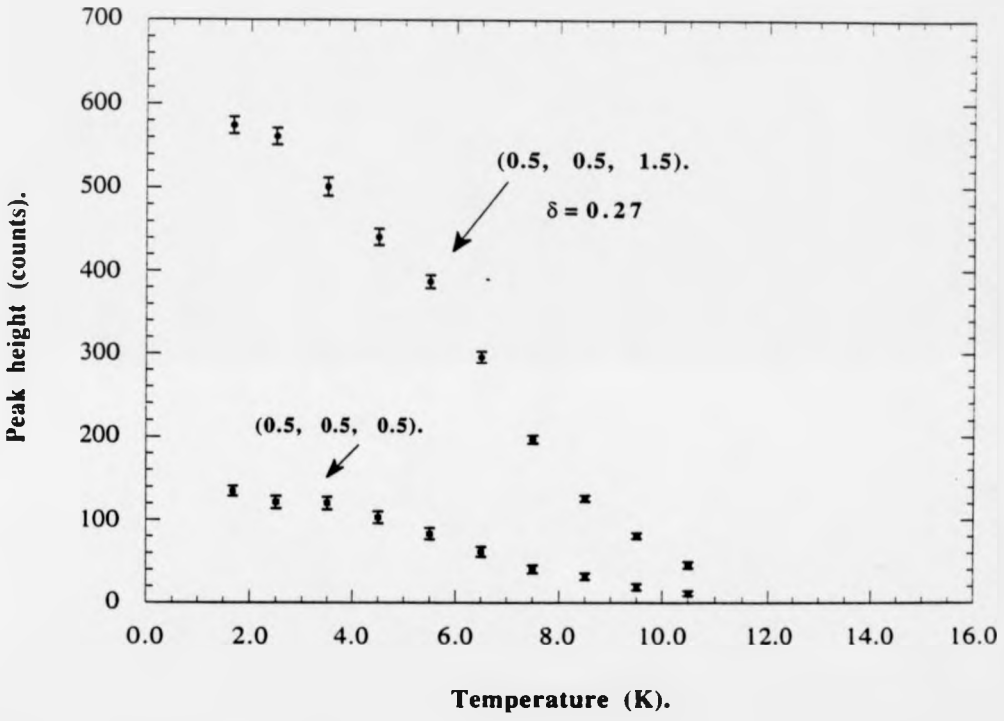

Figure 4.9: The temperature dependence of the (0.5, 0.5, 0.5) and the (0.5, 0.5, 1.5) peaks, for the $\delta = 0.27$ crystal. T_{N2} can be seen to be (11 ± 1) K.

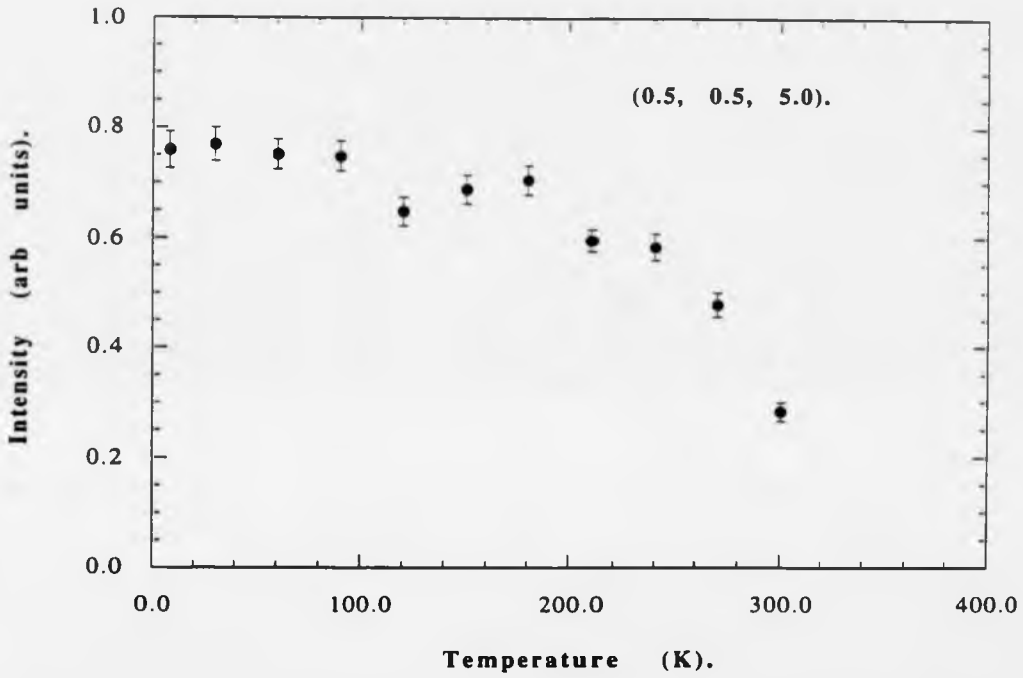

Figure 4.10: The temperature dependence of the (0.5, 0.5, 5) peak, for a second, smaller, $PrBa_2Cu_3O_{7-\delta}$ single crystal.

4.4 Short-range praseodymium spin correlations.

At low temperatures, T < 20 K, as well as the magnetic Bragg scattering, which can be attributed to the magnetic ordering of the Cu spins, additional magnetic scattering is observed. This scattering takes the form of ridges, or rods, lying along the *l* direction of reciprocal space which pass through, and are broadly peaked, at the (h/2, k/2, *l*) reciprocal lattice positions, as illustrated in figure 4.11.

The scattering centred upon the (h/2, k/2, *l*) reciprocal lattice positions can be distinguished from magnetic Bragg scattering by firstly, the shape and width of the peaks and secondly, by their temperature dependence. Experimentally, the profile of a magnetic Bragg reflection, for a single crystal, is Gaussian in shape and has an intrinsic width dependent upon the mosaicity of the crystal, the magnetic domain size and the instrumental resolution. Generally the instrumental resolution function is the dominant factor and for high quality crystals accounts for > 95% of a Bragg peak width. Therefore magnetic Bragg peaks, at similar positions in reciprocal space, arising from the ordering of different spins will be of a similar width. This is illustrated by the similarity of the different magnetic peak profiles measured within the high-temperature and low-temperature Cu spin ordered phases, see section 4.3. In contrast, this broad peaked scattering along the rod is Lorentzian in shape, characteristic of short-range order, with a hwhh equal to (0.056 ± 0.002) reciprocal lattice units (rlu), approximately five times the width of a normal Bragg peak on this instrument along the same reciprocal lattice direction. The temperature dependence of the intensity at the (0.5, 0.5, 0) reciprocal lattice position, see figure 4.4b, differs strongly from the typical Brillouin form of the temperature dependence of an antiferromagnetic magnetic peak, e.g. the (0.5, 0.5, 1.5) reflection, see figure 4.4a (Bacon. 1976), and is also representative of the temperature dependence of magnetic diffuse scattering. We may therefore attribute this additional scattering to short-

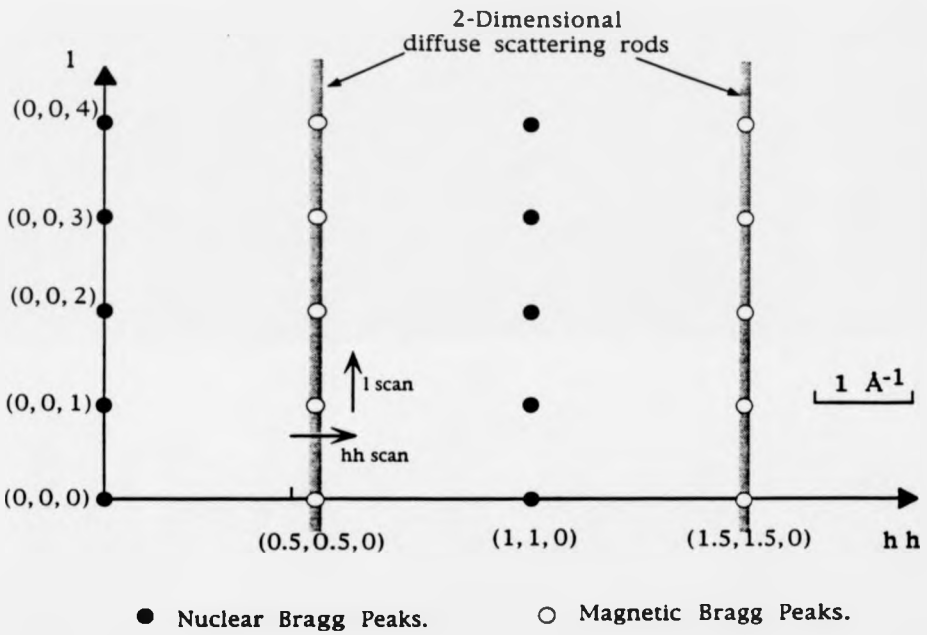

Figure 4.11: The section of the scattering plane in reciprocal space, where the majority of our measurements were taken.

range correlations of the Pr spins, as the Cu spins have already been accounted for, where the diffuse scattering rod and the scattering centred on (h/2, k/2, *l*) reciprocal lattice positions are due to two-dimensional and three-dimensional correlations respectively, (Birgeneau et al. 1970).

We have performed a number of measurements at 2K, hh0 and *l*00 scans, scans parallel to the (110) and (001) directions in reciprocal space as shown in figure 4.11, in order to characterise the diffuse scattering. The underlying feature is the diffuse scattering rod which has a narrow Lorentzian shaped cross section with a hwhh of (0.014 ± 0.001) rlu (or 0.032 ± 0.002 $Å^{-1}$) , as shown in figure 4.12. The broad peak at the (1/2, 1/2, 0) reciprocal lattice position, and typical of all the $l=n_3$ positions, is illustrated well by figures 4.13 and 4.14. This broad peak has a hwhh of (0.056 ± 0.001) rlu, (or 0.030 ± 0.0005 $Å^{-1}$), along the direction of the rod. No sign of an additional broad diffuse peak at the (0.5, 05, 0.5) reciprocal lattice position was found from scans along the rods direction and the overall magnetic scattering at this position could be simply and accurately explained by a small magnetic Bragg peak sitting upon the flat diffuse rod. As the diffuse scattering is peaked only at the (h/2, k/2, *l*) reciprocal lattice positions, as seen in section 4.3, we may conclude that the diffuse scattering arises from antiferromagnetic correlations of the Pr spins along the **a** and **b** directions and ferromagnetic correlations along the **c** direction. Calculated peak intensities, obtained from a model of this proposed spin configuration, agreed reasonably well with the observed intensities of the diffuse scattering arising from the three-dimensional short-range correlations. A schematic representation of a section of the diffuse scattering rod in reciprocal space is shown in figure 4.14 and illustrates the broad nature of the scattering centred upon the (h/2, k/2, *l*) reciprocal lattice positions.

Within the framework of the mean field theory we were able to estimate the correlation lengths of the Pr spins within the **a** - **b** plane and along the **c**

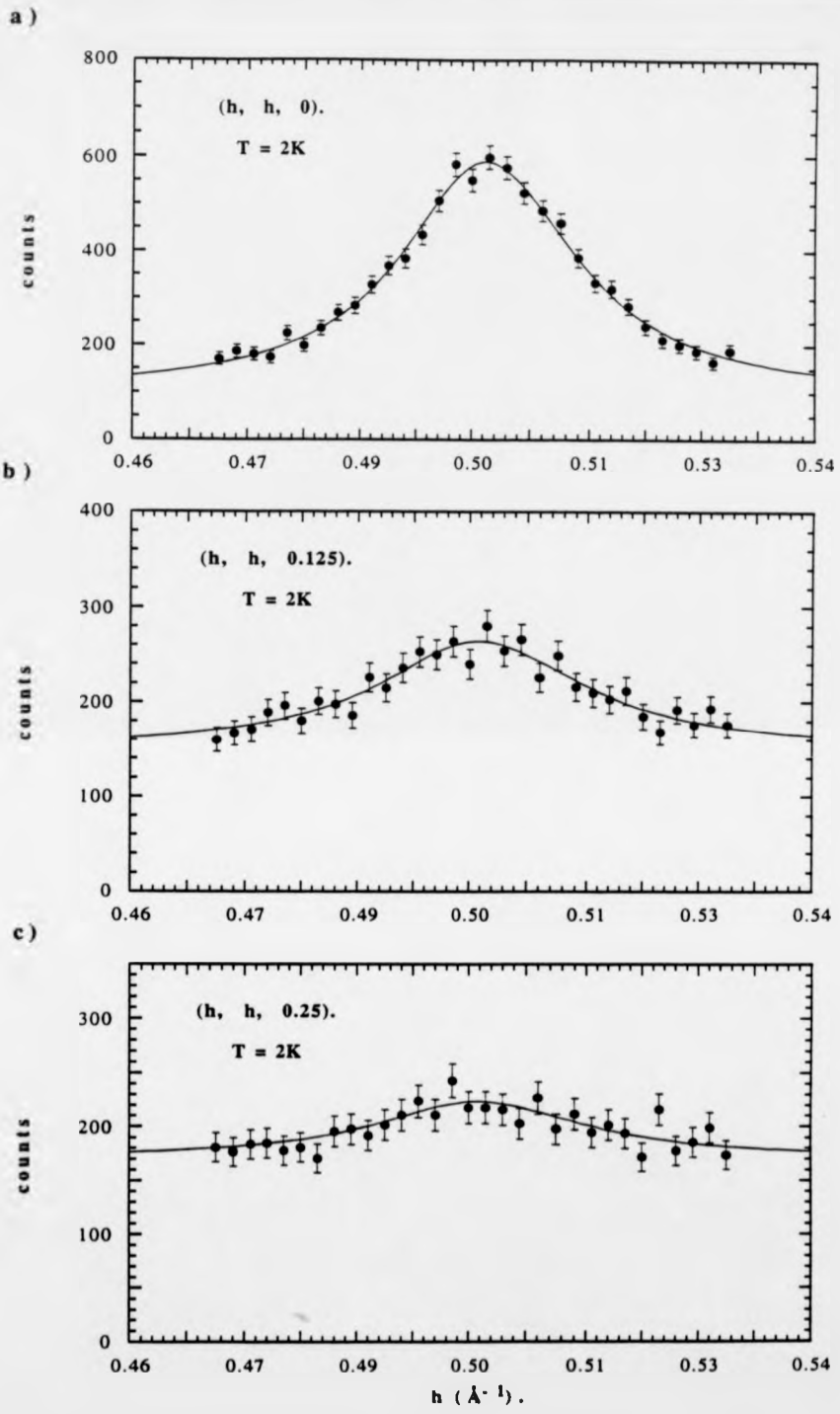

Figure 4.12: Three scans across the diffuse scattering rod, for the $\delta = \delta_3$ crystal at 2K, at different positions in reciprocal space, indicating the diffuse scattering arising from two-dimensional and three-dimensional correlations of the Pr spins.

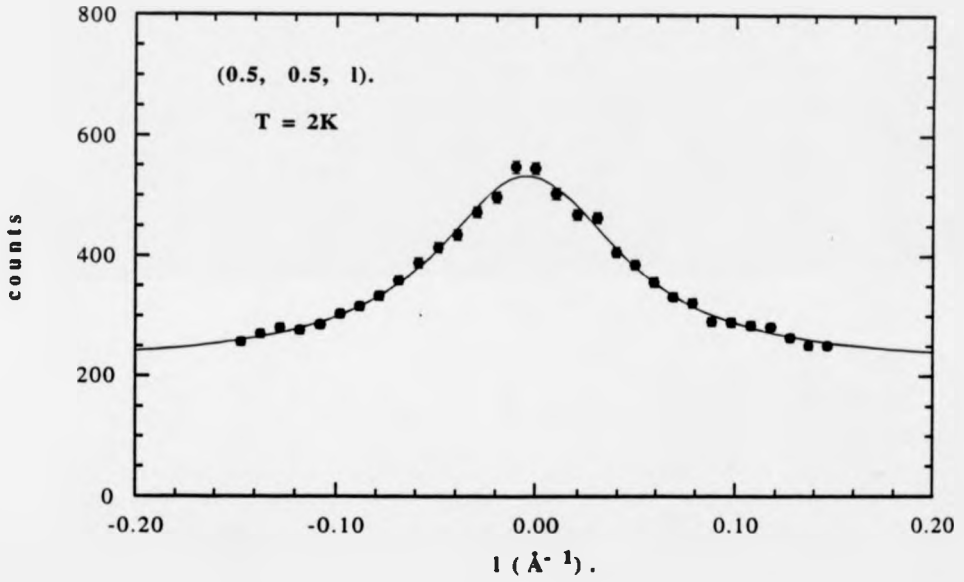

Figure 4.13: A scan along the diffuse scattering rod, for the $\delta = \delta_3$ crystal at 2K, centred upon the (0.5, 0.5, 0) position in reciprocal space, illustrating the broad peaking of diffuse scattering at the (h/2, k/2, *l*) reciprocal lattice positions.

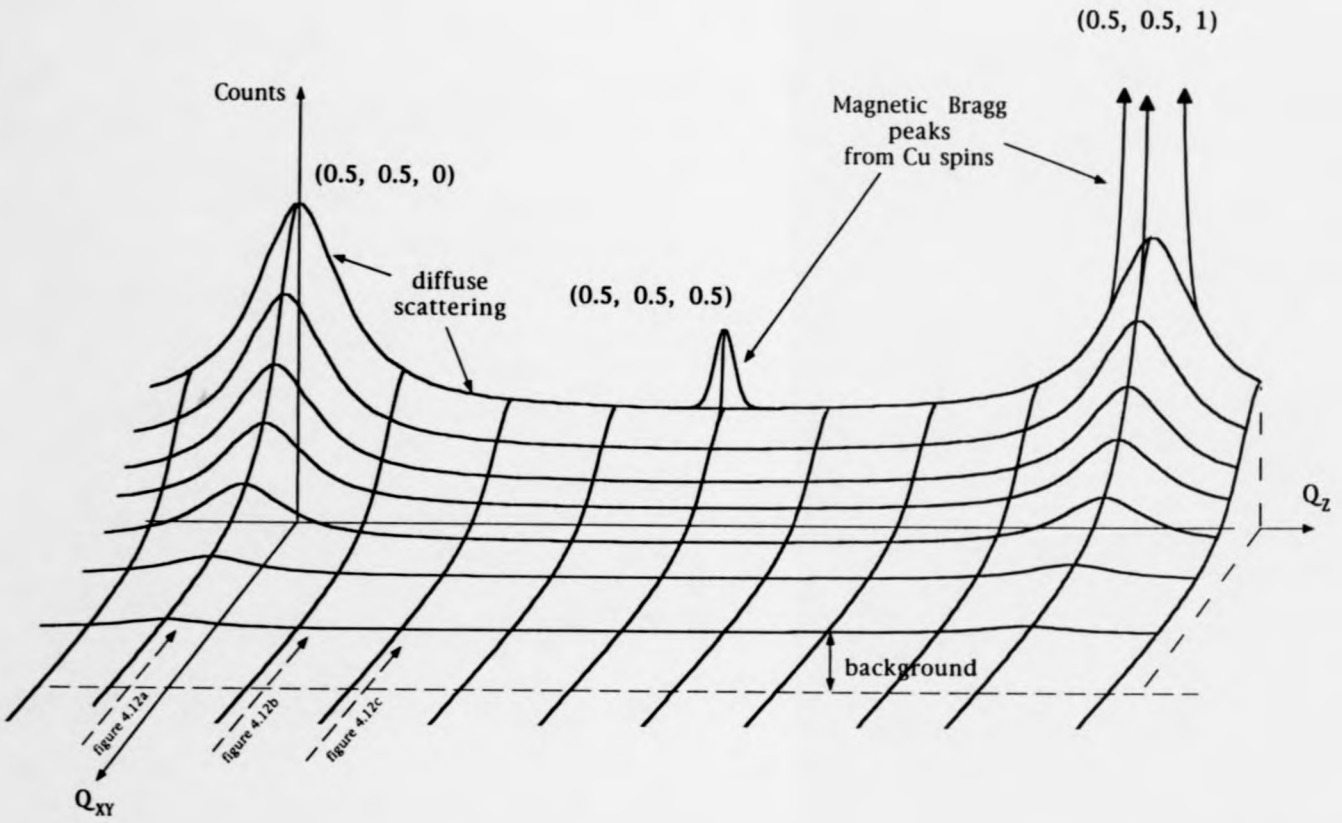

Figure 4.14: A schematic representation of the diffuse scattering, within a section of reciprocal space, within the $PrBa_2Cu_3O_{7-\delta}$ single crystal in the $\delta = \delta_3$ oxidation state.

axis, (Hirakawa. 1982 and Als-Neilsen et al. 1993). From the mean field formulation of the wavevector-dependent susceptibility the magnetic scattering S(q), as a function of the wavevector q, may be approximately expressed as a Lorentzian type function of the form

$$S(q) = \frac{c}{\kappa^2 + q_{ab}^2 + \left(\frac{J'}{J}\right) q_c^2} \tag{4.2}$$

where c is a constant, q_{ab} and q_c represent the wavevector displacements from a reciprocal lattice point in the **a** - **b** plane and along the **c** axis respectively, J and J' are the two-dimensional and three-dimensional exchange couplings respectively and κ is the Lorentzian hwhh. Within the Ornstein-Zernike mean-field model κ is equal to the inverse of the correlation length, ξ, where the thermal average of the correlation between two spins separated by a distance r may be expressed as

$$\langle S_0 S_r \rangle = C \exp\left(-\frac{1}{\xi} r\right) \tag{4.3}$$

where C is a constant, (e.g. Stanely. 1987 and Marshall and Lowde. 1968).

Experimentally the observed magnetic scattering is a convolution of S(q) with the instrumental resolution function. Due to the narrow width of the diffuse scattering rod we would expect this resolution function to contribute significantly to the overall width and hence must be taken into consideration. Ideally, in order to account for the resolution function we should perform a three-dimensional convolution of S(q) with the instrumental resolution function and fit our measured profiles with the result. This approach is extremely complicated and an accurate representation of the instrumental resolution function in three dimensions is required for that position in reciprocal space, a requirement beyond the bounds of our experiment. One alternative solution is simply to estimate the width due to the resolution function and subtract its contribution from the overall measured width. This

approach will only allow an approximation to within a factor two to be made. We were able to estimate the width of the resolution function by measuring the width of a nearby Bragg reflection, the (0.5, 0.5, 1) reflection for which the resolution function may be assumed to contribute most to the peak`s width. (Note : A more suitable reflection would have been the one arising from $\lambda/2$ contamination from the (1, 1, 0) nuclear Bragg reflection, measured above the onset of the diffuse scattering, which would have occurred at the same (0.5, 0.5 0) position in reciprocal space.) By removing the contribution of this width from one measured from the hh0 scan across the rod at the (0.5, 0.5 0) reciprocal lattice position we were able to estimate the correlation length of the Pr spins within the **a - b** plane to be ~ 200 reciprocal lattice spacings at 2K. Additionally, it may be simply shown, using equation 4.2, that the ratio of the hwhh of the measured profiles parallel and perpendicular to the rod, κ_l and κ_h respectively, may be written as

$$\frac{\kappa_l}{\kappa_h} = \left(\frac{J'}{J}\right)^{\frac{1}{2}} \qquad (4.4)$$

Using equation 4.4 we are able to estimate the weak three-dimensional coupling J' to be < 100 J.

In the earlier studies, where $\delta = \delta_l$ and $\delta = 0.27$, similar diffuse scattering was also observed below 20K and hence it appears that the onset of the short-range correlations between the Pr spins is largely independent of the oxygen concentration of our crystal. The onset of the diffuse scattering coincides with the Neel temperature, ~17K, proposed for the long range ordering of the Pr spins from earlier specific heat and powder diffraction studies of $PrBa_2Cu_3O_{7-\delta}$, (Li et al. 1989). If we were able to determine accurately the instrumental resolution function for the (0.5, 0.5, 0) position in reciprocal space we would be able to refine the temperature dependence of the diffuse scattering. This would enable us to gain further insight into the behaviour of

the spins below 2K and allow us to predict whether a transition to long range three-dimensional order would occur just below 2K or whether the spins would remain ordered over only short distances, possibly due to frustration within the system. Unfortunately we were unable to do this within the limits of our experimental measurements. (Note: A further experiment tailored to the investigation of quasi-elastic scattering would provide a more suitable probe of the Pr short-range correlations.)

Within typical quasi-two-dimensional magnets diffuse scattering, arising from short-range correlations of the spins, is often observed at temperatures up to twice their Neel temperature. This is well illustrated by K_2NiF_4 where T_N is 97.1K and diffuse scattering is observed at temperatures up to 200K, (Birgeneau et al. 1970). The Re ions, in $ReBa_2Cu_3O_{7-\delta}$, may also be similarly treated as quasi two-dimensional magnets because their separation along the **c** axis is approximately three times that in the **a-b** plane. In $ErBa_2Cu_3O_{7-\delta}$ two-dimensional correlations are observed, again in the form of diffuse scattering, up to ~1K, where the three-dimensional Néel temperature is 0.62K, (Lynn et al. 1987, and Lynn et al. 1989). In sharp contrast, in $PrBa_2Cu_3O_{7-\delta}$ we have observed diffuse scattering up to 20K while no long-range magnetic order has been observed at temperatures down to 2K. This would seem to indicate that disorder is present within our crystal and restricts the development of full long-range Pr spin order.

The behaviour of the Pr spins, in our $PrBa_2Cu_3O_{7-\delta}$ crystal, differs markedly from that found in previous studies of $PrBa_2Cu_3O_{7-\delta}$ and also, as expected, from the behaviour of the Re spins in the other $ReBa_2Cu_3O_{7-\delta}$ compounds. The Re spins all order antiferromagnetically at low temperatures, less than 2.3K, and can be separated into three categories with respect to their spin configurations. First there are those where the Re spins order along the **c** direction and no diffuse scattering is observed above T_N, such as $NdBa_2Cu_3O_{7-\delta}$ (Yang et al. 1989) and $GdBa_2Cu_3O_{7-\delta}$ (Paul et al. 1988). Secondly there are those

where the Re spins also order along the c direction but where three-dimensional correlations are observed above T_N, such as $DyBa_2Cu_3O_{7-\delta}$ (Goldman et al. 1987), and thirdly where the Re spins order within the a-b plane and only two-dimensional correlations are observed above T_N, such as $ErBa_2Cu_3O_{7-\delta}$ (Lynn et al. 1989).

The only previous neutron study of the Pr order in $PrBa_2Cu_3O_{7-\delta}$ involved powder diffraction where the proposed spin configuration, based upon only two measured magnetic Bragg peaks which occurred in different positions than we observed, consisted of Pr spins coupled antiferromagnetically along all three unit cell directions, (Li et al. 1990). This disagrees with the spin configuration, proposed for the regions of short-range order, within our crystal where the spins are aligned ferromagnetically along the c direction. A similar Pr spin structure, to our spin configuration, was found in the $PrBa_2Cu_{2.7}Zn_{0.3}O_{7-\delta}$ compound in which 15 atomic % of the Cu ions in the CuO_2 plane have been replaced by Zn, (Li et al. 1993). If we now consider the possible effect of impurities, or substitutions, within our crystal we may formulate a possible explanation for the observed behaviour of the Pr spins. From our spin-density measurements, see chapter 5, we have established that a small amount of Pr is located upon the Ba sites. Additionally we believe there is a small amount of Al upon the Cu chain sites, a product of the crystal growth in which Al crucibles were used. The combined effect of these impurities may be to introduce the disorder in our crystal which restricts the long-range ordering of the Pr spins.

4.5 Discussion.

From our measurements on single crystals of $PrBa_2Cu_3O_{7-\delta}$ in various oxygenation states, we have found that the ordering of the Cu spins in the high-temperature and low-temperature phases can be modelled accurately with all the Cu moments lying in the a-b plane. In the high-temperature

phase the Cu spins in the CuO_2 planes order antiferromagnetically with respect to their nearest neighbours in all three unit cell directions while the Cu spins within the chains remained disordered, as shown in figure 4.2. The Néel temperature, T_{N1}, for this phase appears to be independent of the oxygen concentration of the crystal as illustrated in Table 4.3, in which a summary of the ordering temperatures is given. At T_{N2} the Cu spins within the chains also order and an antiferromagnetic non-collinear spin configuration results, see figure 4.8. In contrast to T_{N1}, T_{N2} is found to be dependent on δ, decreasing as the oxygen concentration increases. The failure of the Cu spins to form a linear spin configuration at low temperatures, T=0 K, may be due to the impurities within the crystal which are also believed to hinder the three-dimensional ordering of the Pr spins.

The onset of the diffuse scattering, due to short range correlations of the Pr spins, occurs below 20K. If the temperature dependence of the diffuse scattering behaved in a similar manner to other quasi two-dimensional magnets we would expect full three-dimensional order to set in at approximately 10 K. The previously published value of 17K for the Néel temperature, T_N, of the Pr spins was obtained for a fully oxygenated powder sample (Li et al. 1989), and susceptibility studies on lower oxygenated samples have shown that T_N decreases below 10K as oxygen is removed, (Felner et al. 1989, Kebede et al. 1991). A Néel temperature of ~10K for our crystal would be fully consistent with this dependence of T_N upon oxygen concentration as the estimated value of δ_3 for our crystal is greater than 0.0, as indicated by the very similar T_{N2} for the crystal in the δ = 0.27 and δ_3 oxygenation states, see table 4.3. A T_N of the order of 10K would be an order of magnitude higher than would be expected if one scaled T_N for the other rare earths assuming a purely dipolar or RKKY exchange interaction, see section 1.6.2. We may therefore conclude that a likely explanation for the Pr spins failing to order is the disorder within the crystal caused by the Al and Pr impurities and that if the

Oxygenation state	Copper Spins		Praseodymium spins : onset of diffuse scattering (K).
	T_{N1} (K).	T_{N2} (K).	
δ_1	400 ± 30	40 ± 3	16 ± 2
$\delta_2 = 0.27$	400 ± 25	11 ± 1	< 20
δ_3	> 300	10 ± 1	< 20

Table 4.3 : A summary of the ordering temperatures for our single crystal of $PrBa_2Cu_3O_{7-\delta}$ in its three oxygenation states. i.e. the Néel temperatures for the high-temperature and low-temperature copper spin ordered phases, T_{N1} and T_{N2} respectively, and the temperature onset of the diffuse scattering, associated with the short range Pr spin correlations.

the crystal was of a higher quality, with fewer site substitutions and impurities, we would expect, from previous evidence, the Pr spins to order at a higher temperature, with respect to the other Re ions.

CHAPTER FIVE

MAGNETISATION DENSITY IN $PrBa_2Cu_3O_{7-\delta}$.

5.1 Introduction.

Polarised-neutron diffraction has been used to examine the spatial distribution of the induced magnetisation within single crystals of $PrBa_2Cu_3O_{7-\delta}$. This has enabled us to investigate the possible hybridisation of the Pr 4*f* electrons with the CuO_2 plane conduction electrons. If these covalency effects were present, possibly localising the superconducting charge-carrying holes within the planes and destroying superconductivity, we would expect to observe a departure from the normal behaviour of the induced magnetisation density for free Pr ions.

Preliminary polarised-neutron investigations were performed upon a small single crystal, of mass ~1.6mg, on D3B at the I.L.L. Later, a more extensive study was carried out upon a much larger single crystal, of mass ~100mg, on Poldif at Saclay. In addition, a full structural study of the larger crystal, providing structural information required in the analysis of the polarised neutron data, was performed on a four-circle diffractometer at Risø. Due to the small size of the first crystal, which greatly restricted the number and accuracy of the measurable flipping ratios, and the absence of a full structural study for this crystal, only limited conclusions could be drawn from the preliminary study. Therefore the majority of this chapter will be concerned with the more extensive later study upon the larger crystal and the conclusions from the preliminary study will be included where appropriate.

5.2 Structural Refinement.

In order to calculate the magnetic structure factors from the flipping ratios, measured in the polarised neutron study, an accurate knowledge of the

crystal structure and knowledge of the degree of extinction in the crystal are required. Integrated nuclear intensities were measured, at room temperature, on the TAS2 four-circle diffractometer at Risø with neutrons of wavelength 1.013Å. The structural, thermal and extinction parameters for the crystal were refined using a weighted least-squares refinement approach. [Note : For convenience, this structural study was performed and the data analysed by Dr H. Casalta, Risø.] The cell parameters and initial atomic positions were taken from a previous study of $PrBa_2Cu_3O_{7-\delta}$ by Jorstarndt et al. (1992) and the structure refined assuming an orthorhombic cell structure with space group Pmmm. In the analysis the anisotropic temperature parameters B_{11} and B_{22} were constrained to be equal for all the atomic sites except the O(4) and O(5) oxygen sites. The final refined atomic coordinates, site occupancies and anisotropic thermal parameters are given in table 5.1. As a result of the refinement the overall oxygen content of the crystal was determined to be 6.73 ± 0.02 oxygen atoms per unit cell, corresponding to $\delta = 0.27 \pm 0.02$. The relatively low site occupancy of 0.750 for the Cu(1) site may possibly explained by the presence of Al on this site, a product of the crystal growth in which Al_2O_3 crucibles were used.

The extinction within the crystal was modelled using the Becker-Coppens extinction formalism assuming a Lorenztian mosaic distribution, (Becker and Coppens. 1974), (for a more detailed explanation of extinction see section 3.1.4). The degree of extinction was found to be relatively small, characterised by a mosaic spread of $(0.076 \pm 0.004) \times 10^{-4}$ rad, where the intensity reduction due to extinction in the strongest reflection, the (220) reflection, was estimated to be only ~8%.

Unfortunately, during the measurement of the integrated intensities, no specific scans where performed to search for evidence of twinning within the crystal, which is a consequence of the assumed orthorhombic nature of the unit cell, (see section 3.3.4). Direct evidence would however have been

$PrBa_2Cu_3O_{7-\delta}$.

Space Group	:		Pmmm	
Lattice Parameters (Å)	:	a = 3.873	b = 3.928	c = 11.710
wR(F) (%)	:		6.2	
δ	:		0.27(2)	

Atomic Coordinates.

	x/a	y/b	z/c	occupancy
Pr	0.5	0.5	0.5	0.998(8)
Ba	0.5	0.5	0.1847(2)	0.993(5)
Cu(1)	0.0	0.0	0.0	0.750(5)
Cu(2)	0.0	0.0	0.3509(1)	1.000
O(1)	0.0	0.0	0.1537(2)	0.909(5)
O(2)	0.5	0.0	0.3702(1)	1.000
O(3)	0.0	0.5	0.3689(1)	1.000
O(4)	0.0	0.5	0.0	0.666(7)
O(5)	0.5	0.0	0.0	0.247(5)

Anisotropic thermal parameters. ($Å^2$)

	B_{11}	B_{22}	B_{33}
Pr	0.69(6)	0.69(6)	0.69(8)
Ba	0.99(4)	0.99(4)	0.85(6)
Cu(1)	2.21(8)	2.21(8)	0.63(8)
Cu(2)	0.54(2)	0.54(2)	0.88(3)
O(1)	3.32(8)	3.32(8)	1.90(8)
O(2)	0.63(2)	0.63(2)	1.13(5)
O(3)	0.63(2)	0.63(2)	1.13(5)
O(4)	2.84(16)	1.50(16)	1.26(16)
O(5)	1.50(16)	2.84(16)	1.26(16)

Table 5.1: The lattice parameters and refined atomic coordinates, occupation factors and thermal parameters for orthorhombic $PrBa_2Cu_3O_{6.73}$ at 330K. The numbers in the parentheses are the uncertainties in the last digits.

difficult to obtain due to the orthorhombicity of the compound being small and the limited resolution of the diffractometer. This assumption is consistent with the structure of similarly oxygenated $PrBa_2Cu_3O_{7-\delta}$ and other $ReBa_2Cu_3O_{7-\delta}$ crystals, (e.g. Jorstarndt et al 1990 and McIntyre et al. 1988). In the analysis of our polarised neutron data, if this assumption was incorrect and the lattice was tetragonal, there would be no effect upon our analysis although we would unnecessarily have restricted ourselves to the (hh*l*) subset of reflections.

5.3 Calculation of the magnetic structure factors.

In our polarised-neutron study we measured a total of 290 flipping ratios, for reflections of the type (hh*l*) of $\sin\theta/\lambda < 0.8$Å, at 15K. When averaged over the equivalent reflections these produced flipping ratios for 39 unique reflections, see table 5.2.

Unfortunately, because of instrumental limitations at the time, the structural study could only be performed at room temperature and therefore in order to calculate the magnetic structure factors, from the flipping ratios measured at 15K, we had to account for the change in the structural and thermal parameters with temperature. The effect of temperature on the atomic positions and site occupancies was assumed to be negligible and only the anisotropic temperature parameters were considered to change significantly between 300K and 15K. By examining the temperature dependence of the anisotropic temperature parameters for the structurally similar $YBa_2Cu_3O_{7-\delta}$ compound, obtained from single-crystal and powder-neutron diffraction measurements (McIntyre et al. 1988, Hewat et al. 1987 and Sharma et al. 1991), a general scaling factor for the individual temperature parameters was calculated and applied to our values measured at 300K. Although a structural study at the same temperature as the polarised-neutron study would have been more suitable, a degree of confidence can be placed in

Reflection.			Flipping Ratio.	F_M(obs)	Spherical atom Model.		Aspherical atom Model.	
h	k	l			F_M(calc)	ΔF_M	F_M(calc)	ΔF_M
0	0	3	0.849(1)	-0.326(3)	-0.337	0.013	-0.327	0.002
0	0	4	0.901(2)	0.310(7)	0.314	-0.005	0.305	0.006
0	0	5	0.929(1)	-0.234(4)	-0.229	-0.005	-0.235	0.001
0	0	6	1.060(1)	0.314(3)	0.322	-0.009	0.317	-0.003
0	0	7	1.135(5)	-0.277(9)	-0.248	-0.028	-0.261	-0.015
0	0	8	1.059(2)	0.203(8)	0.206	-0.003	0.229	-0.026
0	0	11	0.961(2)	-0.173(8)	-0.125	-0.047	-0.133	-0.040
0	0	14	1.046(2)	0.153(12)	0.105	0.048	0.128	0.025
0	0	15	1.041(4)	-0.066(7)	-0.091	0.025	-0.068	0.002
0	0	16	1.034(15)	0.076(31)	0.100	-0.024	0.038	0.038
0	0	17	1.005(7)	0.010(10)	-0.061	0.071	-0.030	0.040
1	1	0	1.228(4)	0.364(5)	0.378	-0.015	0.368	-0.004
1	1	1	0.806(2)	-0.272(3)	-0.268	-0.003	-0.267	-0.005
1	1	2	0.731(7)	0.264(7)	0.279	-0.016	0.253	0.011
1	1	3	1.127(3)	-0.335(6)	-0.300	-0.036	-0.325	-0.010
1	1	4	1.522(26)	0.294(11)	0.278	0.016	0.288	0.005
1	1	5	1.321(6)	-0.190(3)	-0.205	-0.014	-0.201	0.011
1	1	6	1.101(3)	0.291(8)	0.286	0.004	0.302	-0.011
1	1	8	0.908(3)	0.193(6)	0.184	0.009	0.180	0.012
1	1	12	1.043(3)	0.153(9)	0.142	0.011	0.133	0.020
1	1	13	1.061(5)	-0.137(10)	-0.127	-0.010	-0.106	-0.031
2	2	0	1.036(1)	0.306(8)	0.264	0.042	0.294	0.012
2	2	1	1.191(7)	-0.174(6)	-0.191	0.017	-0.190	0.016
2	2	3	0.890(3)	-0.235(7)	-0.216	-0.019	-0.246	0.010
2	2	4	0.921(4)	0.238(11)	0.198	0.040	0.276	-0.038
2	2	5	0.945(3)	-0.171(8)	-0.150	-0.022	-0.152	-0.019
2	2	6	1.048(2)	0.235(9)	0.207	0.029	0.234	0.001
2	2	7	1.079(4)	-0.173(7)	-0.164	-0.009	-0.148	-0.025
2	2	8	1.049(4)	0.164(11)	0.136	0.028	0.143	0.021
2	2	11	0.966(3)	-0.146(11)	-0.089	-0.057	-0.067	-0.079
2	2	14	1.033(6)	0.107(17)	0.075	0.031	0.052	0.054
3	3	0	1.154(9)	0.205(11)	0.160	0.045	0.193	0.012
3	3	3	1.085(6)	-0.191(12)	-0.135	-0.056	-0.172	-0.019
3	3	6	1.058(5)	0.144(11)	0.130	0.014	0.156	-0.012
3	3	8	0.948(7)	0.104(14)	0.087	0.016	0.127	-0.023
4	4	0	1.012(2)	0.084(12)	0.089	-0.005	0.098	-0.015
					$\chi^2 = 11.0$		$\chi^2 = 6.73$	

Table 5.2 : The experimental flipping ratios and magnetic structure factors, F_M(obs), in Bohr magnetons (μ_B) for the 36 unique reflections measured at 15K in a 4.6T applied field. F_M(calc) and ΔF_M are the calculated magnetic structure factors and (F_M(calc) - F_M(obs)) respectively for the most accurate models of the magnetisation density distribution assuming both spherical and aspherical atomic magnetisation density distributions. The numbers in the parentheses are the uncertainties in the last digits.

this approach due to the little effect different temperature parameter scaling factors had on the final modelled, magnetisation density distributions.

Magnetic structure factors were calculated from the averaged flipping ratios, see section 2.7, using the scaled parameters of the structural study and by considering corrections for extinction, $\lambda/2$ contamination, flipping ratio efficiency and the incomplete polarisation of the beam. Two reflections, the (001) and the (002), were omitted due to the high sensitivity of their magnetic structure factors on small structural changes. A further magnetic structure factor, corresponding to the (1 1 14) reflection, obtained from a small nuclear peak, was also neglected due to an inability to reasonably model this magnetic structure factor, in comparison to the rest of the calculated structure factors, with any model magnetisation density. The 36 calculated magnetic structure factors modelled within our analysis are given in table 5.2.

5.4 Determination of the magnetisation density distribution.

The magnetic structure factors are the Fourier components of the magnetisation within the unit cell, as described in section 2.7. However, simply taking the Fourier transform of the experimentally obtained magnetic structure factors is not a suitable mechanism for determining the magnetisation density distribution due to the limited data set available. Within such a Fourier transform unmeasured magnetic structure factors, which contain valuable information, are assumed to be zero which results in unnatural artifacts in the observed magnetisation density distribution. This problem is especially severe within our study as we were only able to measure accurately 36 magnetic structure factors. An additional complication, due to the effect of twinning, is the restriction of the magnetic structure factors to the (hh*l*) subset of reflections. As a result we were only able to model the projection of the magnetisation density distribution onto the [110]/[001] plane, see figure 5.1. Additional care had to be taken in interpreting the

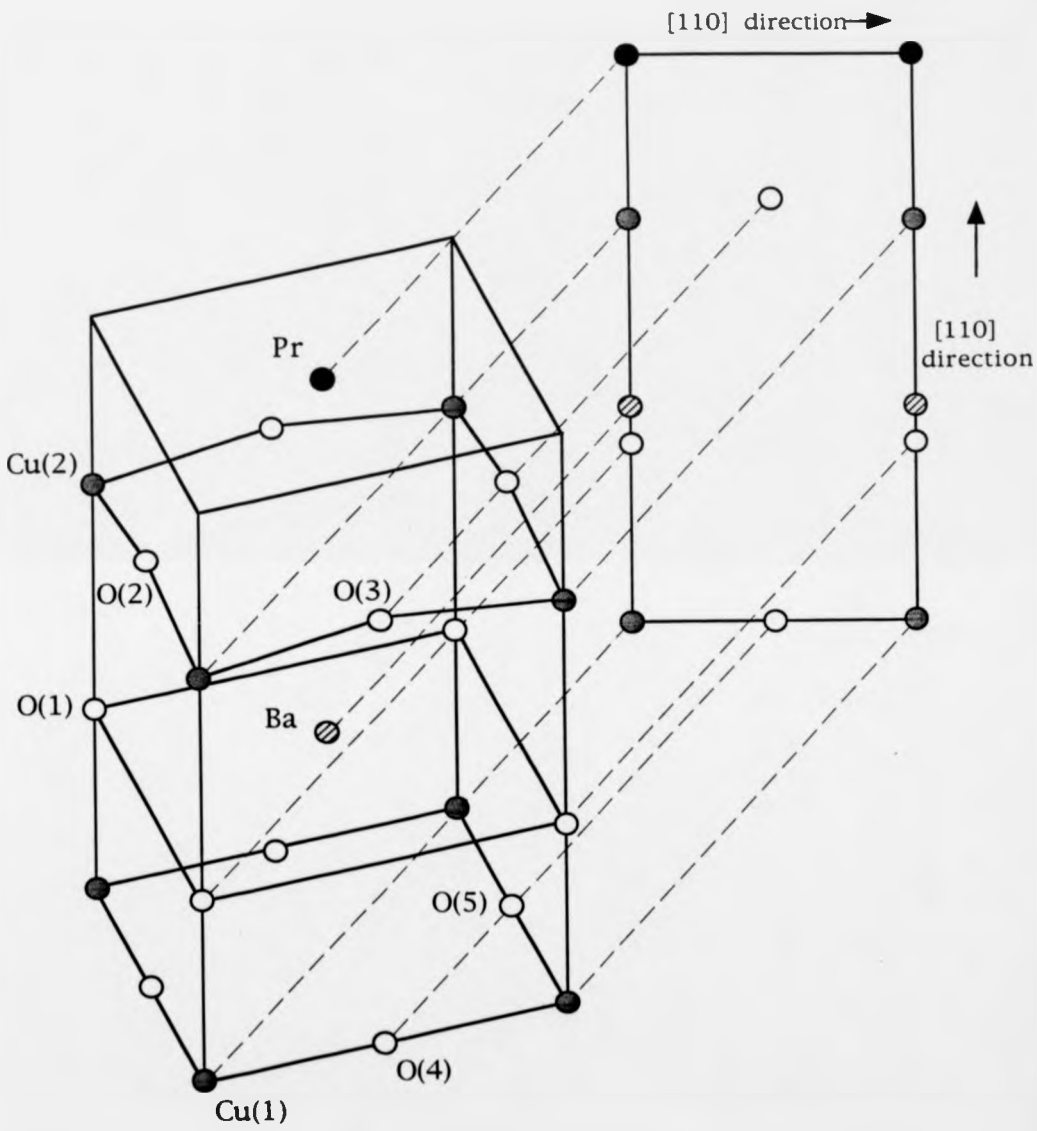

Figure 5.1: The projection of quarter of the unit cell of $PrBa_2Cu_3O_{7-\delta}$ onto the [110]/[001] plane.

modelled magnetisation densities due the position of neighbouring atoms within this projection.

In our analysis we chose to calculate magnetic structure factors from a modelled magnetisation density distribution and refine the model by comparing the calculated and observed magnetic structure factors, $F_M(calc)$ and $F_M(obs)$ respectively. This refinement process was performed using SFLSQ, a weighted least-squares refinement program of the Cambridge Crystallographic Subroutine Library, (Brown and Matthewman. 1993). Deficiencies in our model could be detected by examination of difference density plots, calculated by Fourier transforming the difference between the observed and calculated magnetic structure factors, $F_M(obs) - F_M(calc)$. This had to be performed with care and the observations not over interpreted as structure in the difference density plots may also have been caused by errors in the observed magnetic structure factors.

5.4.1 Modelling with spherical form-factors.

Initially, in our modelling of the magnetisation density distribution we restricted the magnetic form factors to be spherical and assumed that the induced magnetic moments in the sample were restricted to the Pr sites. The form factor for a Pr^{3+} ion was taken from a previous polarised-neutron study, where the observed form factor was found to agree with the form factor calculated from relativistic Dirac-Fock radicals, (Lebech et al. 1979). Using this simple approach we were only able to model the observed magnetic structure factors relatively poorly as reflected by a χ^2 of 47.7, after the least-squares refinement,

$$\chi^2 = \frac{1}{n_{obs} - n_{par}} \sum_{obs} \frac{[F_M(obs) - F_M(calc)]^2}{(\sigma_{obs})^2} \qquad (5.1)$$

where n_{obs} and n_{par} are the number of observations and parameters respectively and σ_{obs} is the error in F_M(obs). The failure of this simple model to reasonably explain the magnetisation density distribution can be seen more clearly by comparing the observed magnetic structure factors with the product of the Pr^{3+} magnetic moment and form factor, shown in figure 5.2 (Note : A direct comparision between these two can only be simply made when there is only one type of magnetic species per unit cell). The large discrepancies between the observed magnetic structure factors and the form factor can be possibly explained by the presence of further magnetic ions within the unit cell, a non-spherical form factor or more probably a combination of these two. Examination of the difference density plot, after refinement of this simple model, indicated that magnetisation density was also possibly concentrated on the Ba site.

A possible explanation of the presence of spin density on the Ba site is the substitution of a small percent of the Pr onto this site. It has been shown chemically by Soderholm and Goodman, (1989) that the Re^{3+} ion, in $ReBa_2Cu_3O_{7-\delta}$, can be deliberately substituted onto this site, and due to the similar ionic radii of Pr and Ba ions, it would seem more likely if any Re was to be unintentionally present on this site it would be Pr. Incorporation of a magnetic moment on the Ba site, corresponding to small percent of Pr on this site, within our model, significantly improved the fit between the calculated and observed magnetic structure factors. In this refinement χ^2 was minimised to 18.8, with a moment 8.7% the size of the moment on the Pr site. If we assume the same moment per Pr ion may be induced upon both atomic sites we may equate this Ba site moment with an 8.7% Pr substitution, (Note: In future references to the substitution of Pr on to the Ba site this assumption will be made). Results from the earlier polarised-neutron study, on the smaller crystal, where a similar substitution 8% of Pr on the Ba site provided the most

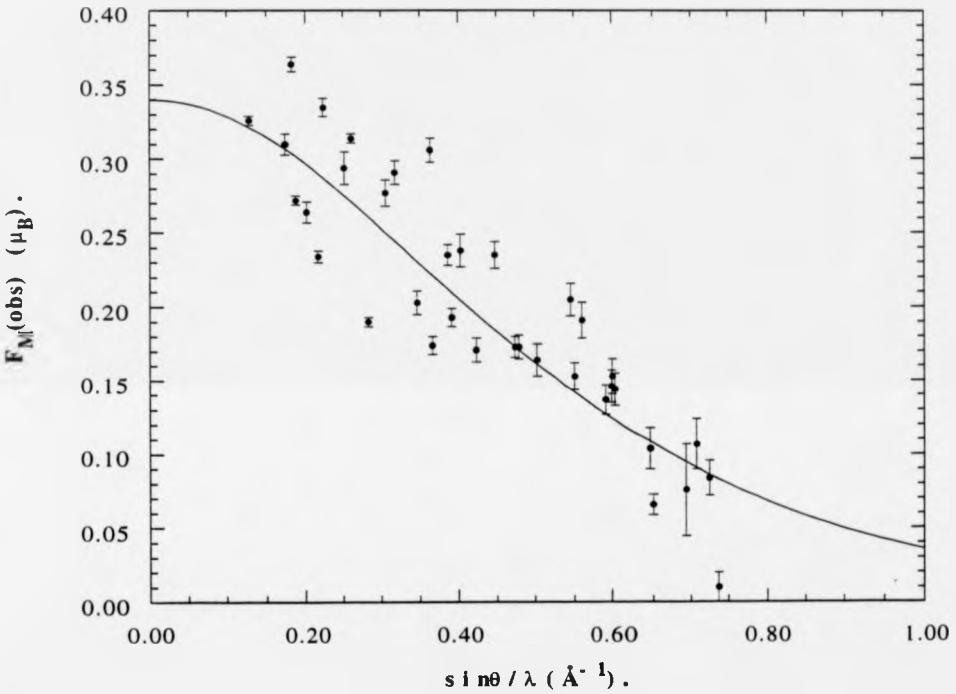

Figure 5.2: The 36 measured magnetic structure factors for $PrBa_2Cu_3O_{7-\delta}$, at 15K in a 4.6T applied field.. The solid line is the spherical magnetic form factor for a Pr^{3+} ion multiplied by the induced Pr magnetic moment, (Lebech et al. 1979).

accurate model of the observed magnetisation density also support this substitution hypothesis.

Re-analysis of the integrated intensities of the structural study, allowing Pr to substitute on to the Ba site, resulted in a ~7% substitution and produced a similar quality fit. Unfortunately due to the similar neutron scattering amplitudes for Pr and Ba, 0.458 and 0.508 respectively, the actual presence of Pr on the Ba site could not be clearly resolved, (Casalta. 1993).

Further improvement in our modelled magnetisation density was achieved by allowing some magnetic moments to be present upon the Cu sites. The form factors for the Cu^{2+} ions, as with the form factor for the Pr^{3+} ion, were assumed to be spherical (Brown. 1992). The refinement of this model, incorporating Cu moments on the two different Cu sites, resulted in an improved fit between the observed and calculated magnetic structure factors to give a χ^2 of 11.0. The magnetic moments found to describe most accurately the magnetisation density distribution were (0.34 ± 0.01) μ_B for the Pr^{3+} ion and (0.024 ± 0.003) μ_B and (0.006 ± 0.004) μ_B for the Cu ions on the Cu(1) and Cu(2) sites respectively. Additionally, (7.8 ± 0.4) % of the Pr moment was found to have substituted on to the Ba site, as similarly found in the previous models. From previously reported susceptibility measurements of a $PrBa_2Cu_3O_7$ powder the induced Pr moment in a 4.6T magnetic field may be calculated as 0.29 μ_B, (Kebede et al. 1989). This value agrees closely with our observed value considering the experimental error of the measured susceptibility. The induced moments upon the Cu(1) and Cu(2) sites are similar in size to those reported by Boucherle et al. 1993, (0.027 ± 0.003) μ_B and (0.010 ± 0.002) μ_B respectively, induced in the superconducting $YBa_2Cu_3O_7$ compound in the same applied field. The quality of the modelled magnetisation density distribution at this stage is reflected by the reasonable agreement between the observed and calculated magnetic structure factors, as shown in table 5.2 (spherical atom model). The improvement in our model with the systematic

inclusion of magnetic moments on different atomic sites, can be clearly seen by examining table 5.3, which summarizes the individual models and their refined parameters. A visual representation of the most accurate magnetisation-density model was obtained by Fourier transforming a complete set of magnetic structure factors, corresponding to all possible reflections up to $\sin\theta/\lambda = 1.25$Å, hence minimising the Fourier series termination effects, figure 5.3.

The possibility that the assumed spherical form factor for the Pr^{3+} ions has a different radial dependence to that used so far within our analysis has been examined by modelling the magnetisation density using different forms of the form factor. To a first approximation the orbital and spin contributions to the overall magnetisation density of an Re ion can both be assumed to be spherically symmetric, (Boucherle et al. 1982). Using this dipole approximation the form factor, $f_M(k)$ may be expressed as

$$f_M(k) = \langle j_0(k) \rangle + c_2 \langle j_2(k) \rangle \qquad (5.2)$$

where $\langle j_0(k) \rangle$ and $\langle j_2(k) \rangle$ are the spin and orbital form factors respectively, k is equal to $\sin\theta/\lambda$ and c_2 is a Re-ion-dependent constant. $\langle j_0(k) \rangle$ and $\langle j_2(k) \rangle$ may be expressed by spherical Bessel functions and may be calculated from tabulated parameters, (Brown 1992). In the case of a Pr^{3+} ion c_2 is equal to 1.644, (Boucherle et al. 1982). Using this representation of the form factor for Pr^{3+} ion, and allowing c_2 to vary we failed to improve the agreement between the observed and calculated magnetic structure factors. (Note : the form factor calculated from equation 5.2, where $c_2 = 1.4$, is almost identical to the one obtained from Lebech et al 1979 and, as would be expected, resulted in the same modelled magnetisation density distribution.)

The χ^2 of 11.0, from our most successful model of the magnetisation density, suggests that the model is less than perfect and the data contains further significant information. Examination of the difference plot, corresponding to

Model	Parameters		
Pr^{3+} on the Pr site	Pr moment (μ_B)	=	0.34(1)
	χ^2	=	47.7
Pr^{3+} on the Pr and Ba sites	Pr moment (μ_B)	=	0.34(1)
	% of Pr on Ba site	=	8.7(4)
	χ^2	=	18.8
Pr^{3+} on the Pr and Ba sites, Cu^{2+} on the Cu(1) site	Pr moment (μ_B)	=	0.35(1)
	% of Pr on Ba site	=	7.4(4)
	Cu(1) moment (μ_B)	=	0.028(3)
	χ^2	=	11.3
Pr^{3+} on the Pr and Ba sites, Cu^{2+} on the Cu(1) and Cu(2) sites	Pr moment (μ_B)	=	0.34(1)
	% of Pr on Ba site	=	7.8(4)
	Cu(1) moment (μ_B)	=	0.028(3)
	Cu(2) moment (μ_B)	=	0.006(4)
	χ^2	=	11.0

Table 5.3: A summary of the fitting parameters and for χ^2 the various models assuming a spherical atomic magnetisation density distribution, (Note: The % of Pr on the Ba site assumes that the induced moment upon both the Ba and Pr sites are the same). The numbers in the parentheses are the uncertainties in the last digits.

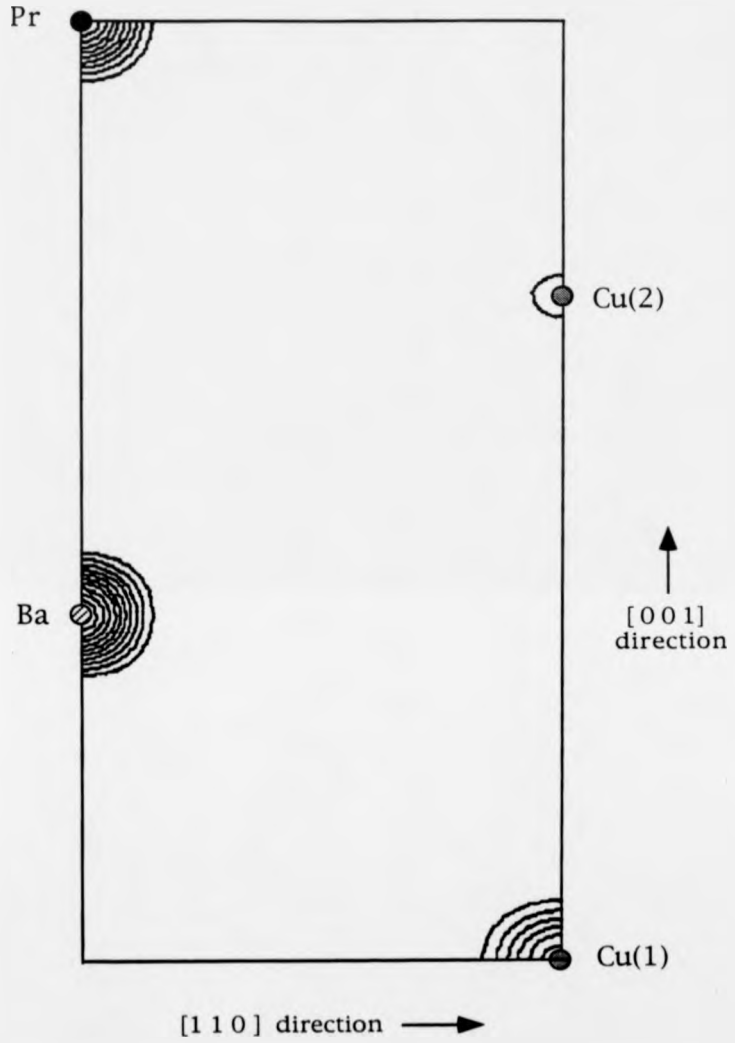

Figure 5.3: The modelled magnetisation density distribution for $PrBa_2Cu_3O_{7-\delta}$, assuming a spherical atomic magnetisation density distribution. The distribution is calculated by Fourier transforming a complete set of calculated magnetic structure factors, (all possible reflections up to $\sin\theta/\lambda = 1.25\text{Å}^{-1}$). The contours surrounding the Cu(1), Cu(2) and Ba sites are at 0.02 $\mu_B\text{Å}^{-3}$ intervals and the contours surrounding the Pr site are 15 times larger, at 0.3 $\mu_B\text{Å}^{-3}$ intervals.

this model, suggests that the magnetisation density is not entirely satisfactorily modelled on the Pr and the Ba sites, see figure 5.4b. The effect of missing reflections may be clearly visualised by examining the Fourier transform of the calculated magnetic structure factors corresponding to the measured reflections, see figure 5.4a. The presence of magnetisation density at positions in the projection which has not been directly modelled is a direct consequence of the Fourier transform assuming that missing magnetic structure factors are zero.

5.4.2 Modelling with aspherical form factors.

In an attempt to model the magnetisation density distribution more accurately we considered a non-spherical model of the magnetisation distribution, in contrast to the purely spherical approximation so far employed. The aspherical magnetisation distribution of a magnetic ion, ρ, may be expressed using a multipolar expansion of the form,

$$\rho = \sum_{l} \sum_{m} a_{l,m} Y(l,m) < j_l > \qquad (5.2)$$

with

$$l = 0, 1, 2, \ldots \qquad \text{and} \qquad m = -l, -l+1, \ldots 0, \ldots l-1, l$$

where $Y(l,m)$ is the spherical harmonic, $< j_l >$ is the radial integral and $a_{l,m}$ is the constant characterised by the operators l and m (e.g Kennedy et al. 1993 or Warren et al. 1992). (Note: Y(0,0) is spherical and corresponds to the previous model.) The spherical harmonics which may be used to describe the angular dependence of the magnetisation density are dictated by the site symmetry. The parameters $a_{l,m}$ were determined using MPLSQ, a weighted least-squares refinement program of the Cambridge Crystallographic Subroutine Library (Brown and Matthewman. 1993), which refined the modelled magnetisation density by comparing the calculated and observed magnetic structure factors. Within our analysis we restrained l to be no

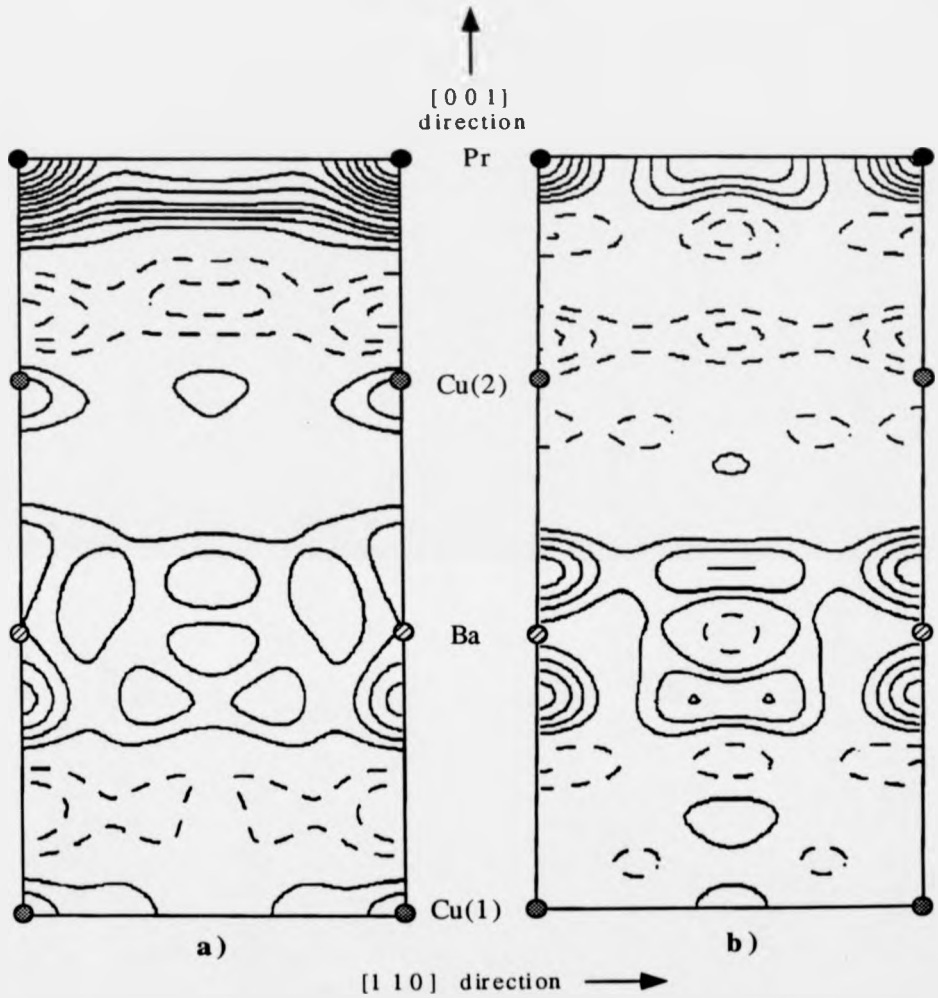

Figure 5.4: a) The Fourier transform of F_M(calc) for the limited set of the observed reflections. The contours are from -0.009 $\mu_B Å^{-3}$ to 0.012 $\mu_B Å^{-3}$ at intervals of 0.003 $\mu_B Å^{-3}$ and then at intervals of 0.006 $\mu_B Å^{-3}$. b) The difference plot, i.e. the Fourier transform of F_M(obs) - F_M(calc). The contours are from -0.0009 $\mu_B Å^{-3}$ to 0.0018 $\mu_B Å^{-3}$ at intervals of 0.0003 $\mu_B Å^{-3}$.

greater than 4, allowing us to model the magnetisation density distribution with spherical harmonics up to a quadrupole nature.

Initially only the magnetisation distribution surrounding the Pr site was considered to be asymmetric, with the magnetisation density upon the other magnetic sites restrained, as in our earlier analysis, to be spherical. Due to the Pr site symmetry of mmm the possible spherical harmonics, which may be used to describe the angular dependence of the magnetisation density, are $Y(l = 2i, m = +2j)$, where i and j are integers ≥ 0, as shown in figure 5.5, (Kara and Kurki-Suonio. 1981). Unfortunately, as previously discussed, we were experimentally restricted to the subset of (hh*l*) magnetic structure factors. One serious consequence of this restricted set of magnetic structure factors is that we are only able to model the projection of the magnetisation density distribution onto the [110]/[001] plane. If we project either the Y(2,+2) or Y(4,+2) spherical harmonic onto this plane the positive and negative lobes cancel completely, as is apparent by examining figure 5.5. Therefore as there is no component of either of these spherical harmonics within this plane we are unable to determine their respective constants, $a_{2,+2}$ and $a_{4,+2}$, and they were set to zero even though they might contribute significantly to the overall magnetisation density. As a result, we were restricted to modelling our magnetic structure factors with a magnetisation density distribution at the Pr site, ρ_{Pr}, expressed by

$$\rho_{Pr} = a_{0,0} < j_0 > + a_{2,0} < j_2 > Y(2,0) + < j_4 > (a_{4,0} Y(4,0) + a_{4,+4} Y(4,+4)) \qquad (5.2)$$

where $a_{0,0}$, $a_{2,0}$, $a_{4,0}$, and $a_{4,+4}$ are the parameters refined within MPLSQ. The radial integrals for Pr^{3+}, expressed as Bessel functions, were taken from the International Tables for Crystallography, (Brown. 1991), and are shown in figure 5.6.

An improvement in the quality of the fit between calculated and observed magnetic flipping ratios was obtained using this aspherical approach to the

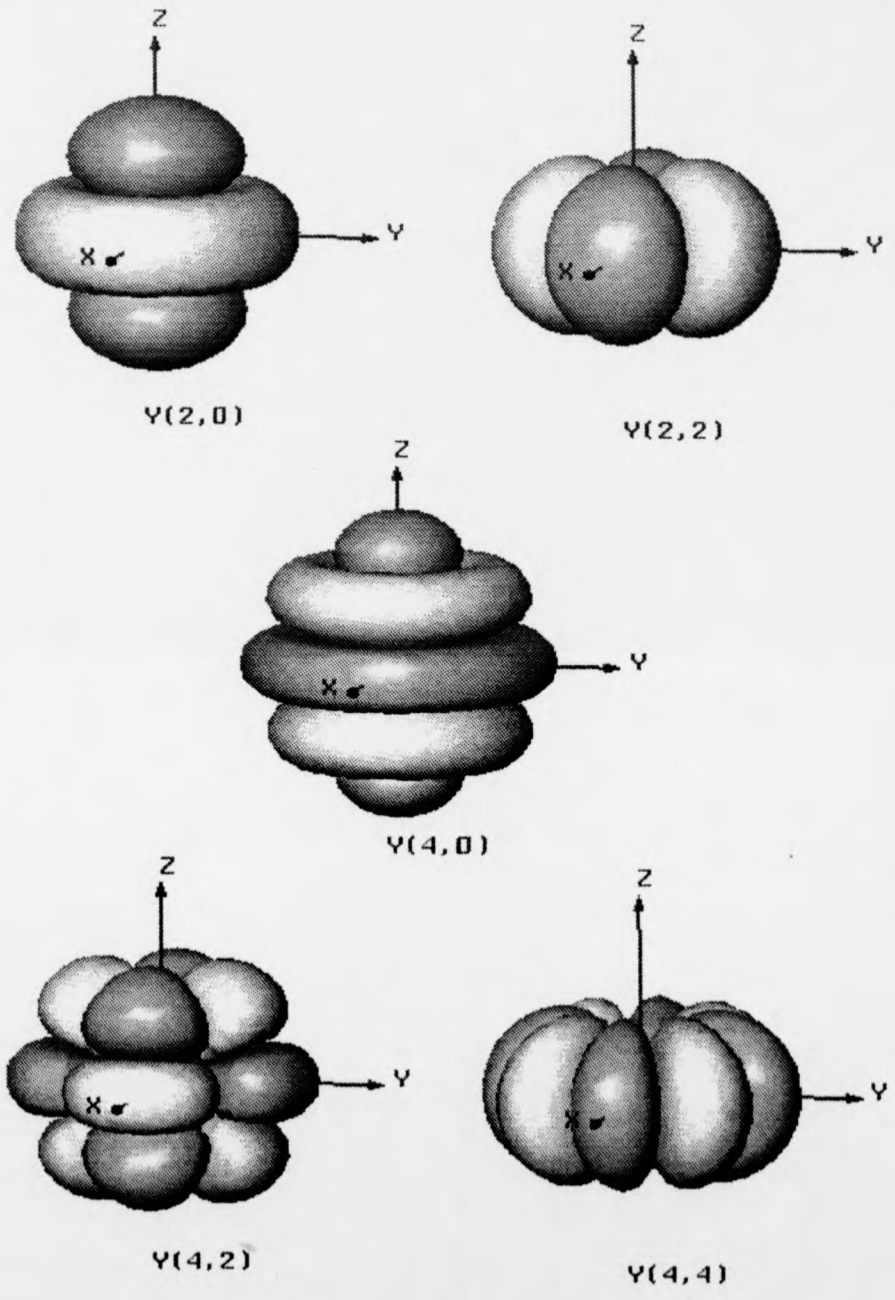

Figure 5.5: Spherical Harmonics.

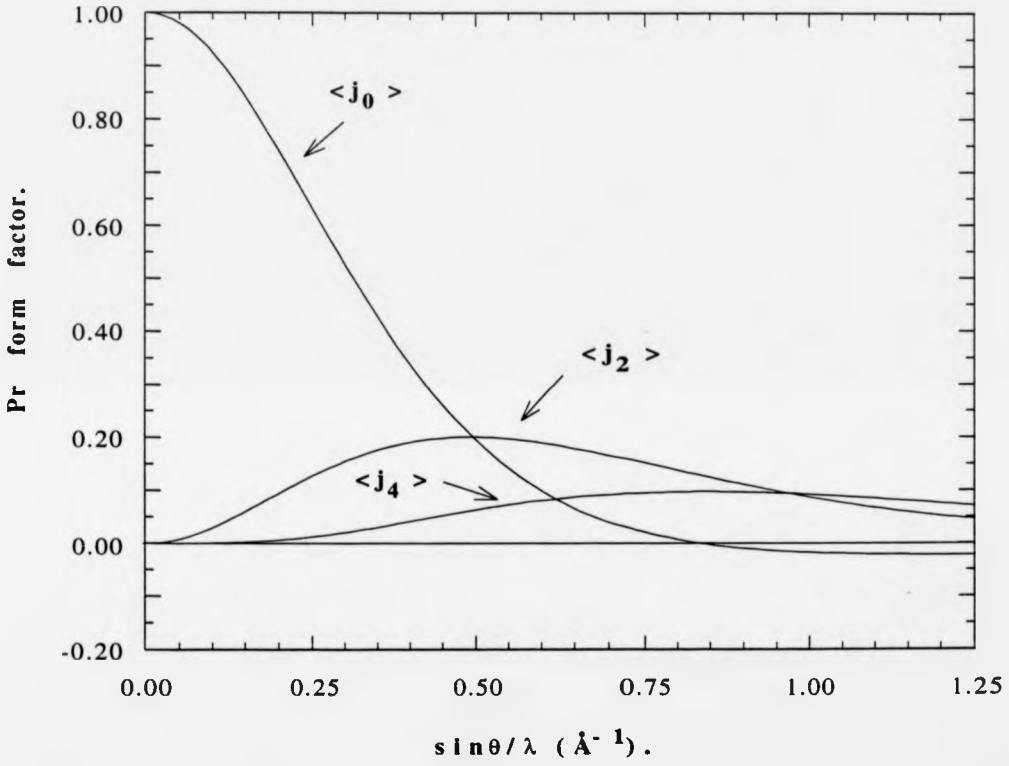

Figure 5.6: The radial integrals, $< j_l > l = 0, 2, 4$, for a Pr^{3+} ion.

Pr magnetisation density distribution and this is reflected by a decrease in χ^2 to 9.37 from 11.0, the χ^2 corresponding to our most accurate model using purely spherical form factors. The section of the total spherical and aspherical magnetisation density distribution, in the [110]/[001] plane, surrounding the Pr site is illustrated in figure 5.7, and was obtained by Fourier transforming a complete set, up to $\sin\theta/\lambda$ = 1.25Å, of modelled magnetic structure factors. The most striking deviation from a spherical distribution is the presence of magnetisation density extending towards the Cu(2) sites. The induced Pr moment of (0.36 ± 0.01) μ_B, agrees closely with the moments calculated upon the same site using the earlier spherical form factor approach to the modelling of the magnetisation density distributions, (see Table 5.3).

The modelled magnetisation density was further improved by allowing the magnetisation distributions surrounding the other atomic sites also to be asymmetric. The most significant further improvement within our model was achieved with an asymmetric modelling of the magnetisation distribution surrounding the Ba site. A small distortion of the magnetisation density is observed towards the Cu(2) sites, as is observed to a greater extent for the magnetisation density distribution on the Pr site, see figure 5.8. The induced moment upon this site of (0.36 ± 0.01) μ_B per Pr ion can be attributed to the presence of Pr ions on (8.0 ± 0.5) % of the Ba sites.

The most accurate model of our measured magnetic structure factors resulted in a χ^2 of 6.73 where the magnetisation density distribution surrounding the Pr, Ba, Cu(1) and Cu(2) sites were all asymmetrically modelled. Within this model the form of magnetisation density distribution on the Pr and Ba sites remained the same as found in previous models where just the magnetisation density distribution on these sites was assumed to be aspherical. The accuracy of this model is reflected in table 5.2, (aspherical model), where the calculated and observed magnetic structure factors are

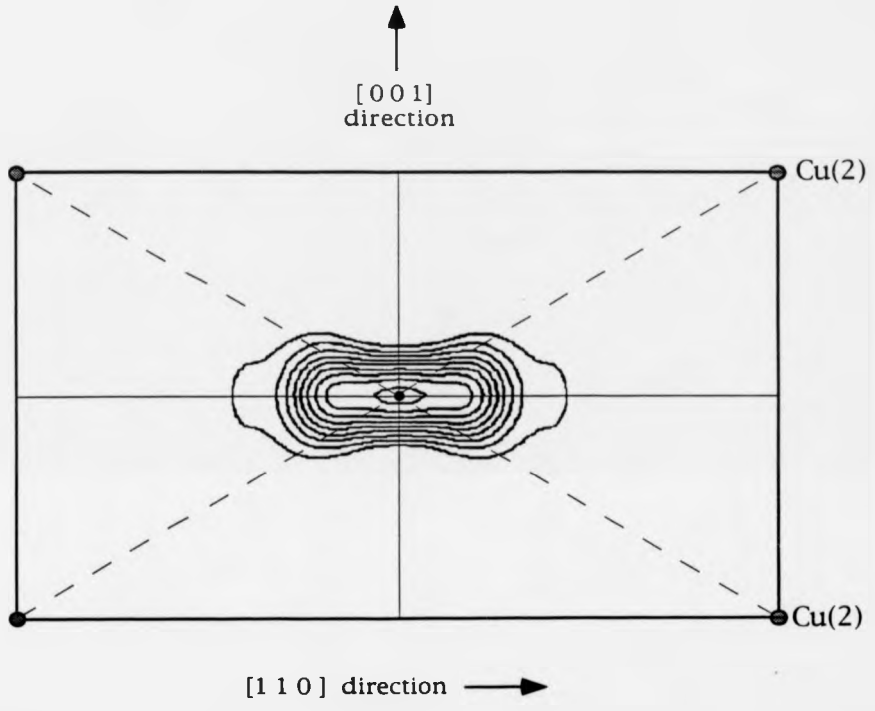

Figure 5.7: The section of the modelled aspherical magnetisation density distribution in the [110]/[001] plane surrounding the Pr site, for $PrBa_2Cu_3O_{7-\delta}$. The distribution is calculated by Fourier transforming a complete set of calculated magnetic structure factors, (all possible reflections up to $\sin\theta/\lambda$ = 1.25Å^{-1}). The contours are at 0.15 μ_BÅ^{-3} intervals.

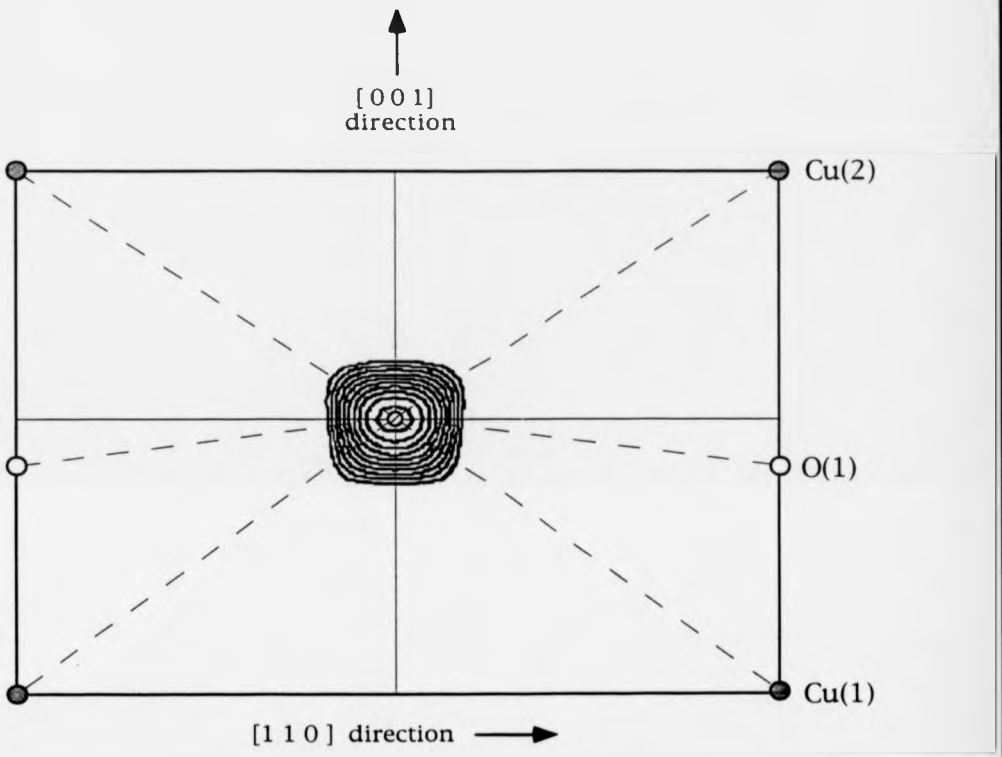

Figure 5.8: The section of the modelled aspherical magnetisation density distribution in the [110]/[001] plane surrounding the Ba site, for $PrBa_2Cu_3O_{7-\delta}$. The distribution is calculated by Fourier transforming a complete set of calculated magnetic structure factors, (all possible reflections up to $\sin\theta/\lambda$ = 1.25Å^{-1}). The contours are at 0.02 μ_BÅ^{-3} intervals.

tabulated. The Fourier difference map after the aspherical refinement, (figure 5.9), shows the improvement in our model compared to the spherical refinement. Although residual magnetisation density is still present there is noticeably less residual density surrounding the Ba and Pr sites than was found earlier when we assume the form factors were spherical, see figure 5.4b.

5.5 Discussion.

The modelled magnetisation density surrounding the Pr site, see figure 5.7, is strongly aspherical and is elongated in shape towards the Cu(2) sites, the Cu sites within the CuO_2 planes. Due to our limited data set and the restriction of our modelled aspherical magnetisation density distribution to the projection onto the [110]/[001] plane due to twinning, we are unable to determine whether the magnetisation density distribution is only extended towards the Cu(2) sites or also towards the O sites within the CuO_2 planes. From crystal field calculations the charge density of the Pr ion has maxima which point towards the oxygen sites, which when projected onto the [110]/[001] plane would lead to bulges similar to those observed in the magnetisation density distribution, (Boothroyd. 1993). This observed deviation from a purely spherical distribution may be interpreted as evidence for the possible hybridisation of the Pr 4f electrons with the conduction electrons of the CuO_2 planes.

The sizeable moment observed on the Ba site can be explained by the presence of Pr ions on this site. By assuming the same moment, per Pr ion, may be induced on both the Ba and Pr sites the observed moment corresponds to the presence of Pr ions on ~8% of the Ba sites. The modelled magnetisation density surrounding this site is extended, by a small degree, towards the Cu sites in the CuO_2 planes.

Ideally, in order to more accurately interpret our results, we would like to perform a comparison between our results and similar results for a

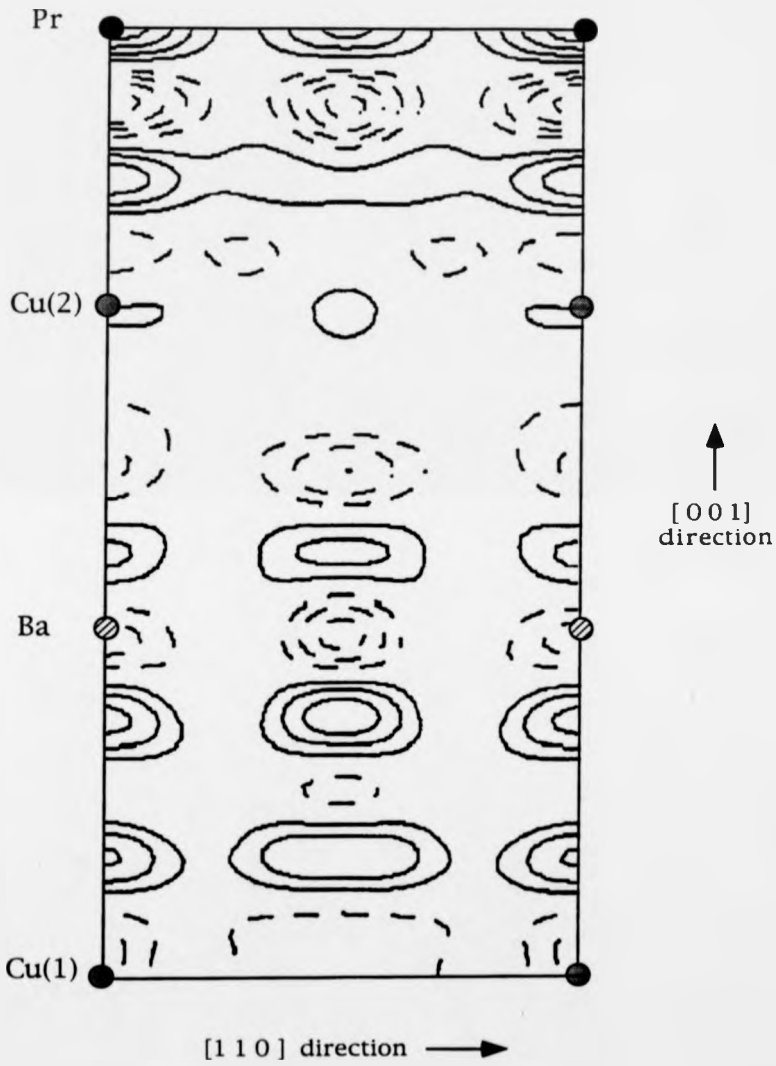

Figure 5.9: The difference plot, i.e. the Fourier transform of F_M(obs) - F_M(calc), for the aspherical atomic magnetisation density model. The contours are from -0.0009 $\mu_B Å^{-3}$ to 0.0012 $\mu_B Å^{-3}$ at intervals of 0.0003 $\mu_B Å^{-3}$.

superconducting member of the $ReBa_2Cu_3O_{7-\delta}$ family, e.g. $NdBa_2Cu_3O_7$ in which the magnitude of the spin and the structural parameters are very similar to $PrBa_2Cu_3O_7$. Deviations which occurred in the magnetisation density distribution with $PrBa_2Cu_3O_7$ and not with $NdBa_2Cu_3O_7$ could be less unambiguously ascribed to real magnetisation density distortions.

CHAPTER SIX

THE PENETRATION OF A MAGNETIC FIELD INTO SUPERCONDUCTING LEAD.

6.1 Introduction.

The superconducting properties of lead have been widely investigated in the past. This interest is partially due to its relatively high transition temperature of 7.22K, the second highest amongst the elemental superconductors, and the deviation of many of its superconducting properties from the behaviour predicted by BCS theory (Bardeen et al. 1957). Indications of the shortfall of BCS theory are reflected in the temperature dependence of the critical field (Finnemore et al. 1960) and in an energy gap which is much larger than predicted for a weakly-coupled superconductor, (Giaever et al. 1962).

A more accurate representation of the experimental results can be achieved by assuming a strong coupling between the electrons and phonons, (Nam. 1967a, 1967b). The consequences of this strong electron-phonon coupling on the electrodynamic properties of superconductors, in particular on the magnetic field profile within the material, have remained untested experimentally. This is mainly due to the indirect nature of the various methods of measuring the magnetic-field penetration depth, and the difficulties encountered in attempting to compare the results. These problems are reflected in the wide range of previously published values for the penetration depth, ranging from 390Å to 630Å. Because lead is a type I superconductor the evaluation of the penetration depth is further complicated by the possibility of non-local effects.

The presence of a surface superconducting layer at magnetic fields above the critical field, predicted by Saint-James and de Gennes (1964), has been

verified experimentally for lead. However the investigation of the field penetration within this region was severely restricted before the advent of the technique of polarised-neutron reflectometry, and little information on the validity of theories describing the magnetic field profile in a superconductor could be achieved using the available indirect experimental techniques.

The development of polarised-neutron reflectometry by Felcher (Felcher. 1981) has allowed a more direct investigation of the field profile in the regimes of both bulk and surface superconductivity. Early work on niobium yielded a bulk penetration depth comparable to results obtained by other techniques (Felcher. 1984). Experiments on a $Pb_{0.992}Bi_{0.008}$ alloy were successful in that they showed a clear signal from the surface superconducting region (Gray et al. 1990). The analysis of the data was restricted though, due to doubts concerning the homogeneity of the sample and the rather poor angular divergence of the neutron beam required to produce a measurable signal and it was not possible to fit accurate field profiles. Recent investigations have applied this technique to high-T_c superconductivity to measure the field penetration within $YBa_2Cu_3O_7$ (Mansour et al. 1989 and Felici et al 1987).

The use of lead samples in the present work was chosen to avoid the complications associated with a 'dirty' superconductor, such as $Pb_{0.992}Bi_{0.008}$, where the impurity atoms break up the coherence of the electron pair wavefunctions. It was thus hoped to be able to apply the basic theory without modification, to test the theoretical predictions for the field profile in the bulk and surface regimes in a pure type I superconductor. Additionally, the effects of strong coupling on the penetration depth within the bulk region, and deviations from local Ginsburg-Landau theory due to non-local effects in the surface superconducting region, can be examined.

6.2 Data analysis.

The neutron reflectivities from a surface are dependent on the orientation of the neutron spin and on the chemical and magnetic profiles within the material, as described in section 2.8. The depth profile of the magnetic part of the refractive index for a superconductor is directly proportional to the profile of the magnetic induction, and hence by measuring the polarised-neutron reflectivity in the region of total reflectivity the magnetic induction profile may be deduced.

The reflectivities cannot be given in a simple analytical form relative to the magnetic induction, due to the complexity of the transform, except in particular limiting cases, e.g. R>>1 (Felcher. 1986). A more general treatment of the problem is to imagine the Pb film to be a series of narrow layers each of constant magnetic induction, and hence refractive index. Because the thickness of the Pb film, ~5000 Å, is much larger than the penetration depth and coherence length for lead we could assume the film to be semi-infinite in thickness. This method is an adaptation of the general behaviour of an electromagnetic wave passing through a stratified media, and is described in more detail in Appendix A. Within our analysis we divided the film into ~300 layers each of the order of 10Å in thickness, extending to one thick layer far from the surface where the magnetic induction could be assumed to be zero. Additionally, it is not possible to derive an unique relationship between a single reflectivity curve and a magnetic field profile. In practice, analysis of the data takes the form of a comparison of the reflectivity and flipping ratio curves numerically calculated from model magnetic profiles with the experimental results.

In addition to the dependence of the reflectivity on the magnetic profile of the film, several sample and instrumental factors must be taken into account in the analysis of the raw data. The primary instrumental consideration is the divergence of the incident neutron beam which results in a distribution of

the incident angle of the neutrons, $\Delta\theta$, with respect to the sample surface. Within our calculations this distribution of angles was assumed to be Gaussian and the resultant reflectivities are an average over this angular spread, (Felcher et al. 1985). The effect of this is a blurring out of the features of the flipping ratio profiles.

A further sample consideration is the effect of the substrate. Each neutron will experience an abrupt change of refractive index at the film-substrate interface due to the dependence of the refractive index on the chemical profile. This can be modelled using a standard wave approach to reflection at an interface (Born. 1975). The reflectivity for the film and substrate system at a wavelength λ assuming a constant refractive index of the film, n, can be approximated by

$$R = \frac{r_f^2 + r_s^2 + 2r_f r_s \cos(4\pi z(n^2 - \cos^2\theta)^{1/2}/\lambda)}{1 + r_f^2 r_s^2 + 2r_f r_s \cos(4\pi z(n^2 - \cos^2\theta)^{1/2}/\lambda)} \qquad (6.1)$$

with $R_f = |r_f|^2$ and $R_s = |r_s|^2$,

where R_f and R_s are the reflectivities for the film and substrate respectively and z is the film thickness. The rapidly oscillatory nature of R is lost within the averaging of R over the spread of neutron incident angles. One reason for the choice of silicon as a substrate is its low reflectivity compared to lead (b/V = 2.02 x 10^{-6} Å^{-2} and 3.1 x 10^{-6} Å^{-2} for silicon and lead respectively). In practice the effect of the silicon substrate is small due to the relatively large thickness of the lead film, and the total measured reflectivity behaves in a very similar manner to that of a bulk material.

An unavoidable feature of our lead films is the local undulation of the films surface. A similar effect is often encountered in X-ray reflectivity experiments. The effect of this surface roughness is to scatter neutrons out of the incident and reflected beams resulting in a loss of reflected intensity. We have accounted for this surface roughness by modifying the calculated

reflected intensity, $I_0(\lambda)$, with a Debye-Waller-like factor (Névot and Croce, 1980).

$$I(\lambda) = I_0(\lambda) \exp\left(\frac{-16\pi^2}{\lambda^2} \sin\theta \ (n(0)^2 - \cos^2\theta)^{1/2} \langle z_D^2 \rangle\right) \tag{6.2}$$

where $\langle z_D^2 \rangle^{1/2}$ is the characteristic surface roughness parameter and n(0) is the refractive index at the surface of the lead film.

During the experiment the lead films were necessarily exposed to air for a short period of time while the samples were loaded into the cryostat. Lead oxidises very quickly and during the transfer a degree of surface oxidation will have resulted. Because of the change in chemical profile that this oxide layer creates, the reflectivities needed to be modified. Analysis of the films to determine the composition of the lead oxide layer was impossible due to the heavy oxidation of the films by water which condensed on the film surfaces during extraction from the cryostat. Although a number of lead oxides are possible, we assumed the surface oxide to be the orthorhombic PbO form. This assumption is supported by X-ray studies (Matthews et al. 1975, Light et al. 1974) on oxide layers on lead films, grown upon similarly-orientated silicon substrates. In our modelling we found the calculated profiles were only very weakly dependent on the oxide layer thickness, and we assumed the oxide layer to be 50Å thick, a typical thickness found in previous studies.

Initially the intention was to characterise the lead film outside the superconducting region by measuring the spin-independent reflectivity above T_c, in a zero applied field. In principle, by modelling the film in the simpler, normal metallic state, and taking into account the effect of the substrate and surface oxide layer, we would be able to obtain accurate values of the incident angle, θ, the angular spread, $\Delta\theta$, and the degree of surface roughness, $\langle z_D^2 \rangle^{1/2}$. These sample and instrumental factors could then be justifiably assumed to remain constant throughout the experiment enabling

us to directly compare individual flipping ratio profiles, at different applied magnetic fields, above and below the critical field of the bulk superconducting region, H_c. Unfortunately, experimental limitations proved this assumption to be wrong. Due to the large consumption of liquid helium required to maintain the cryostat at a constant temperature of T=1.5K, the cryostat needed refilling frequently. Later inspection of the data revealed small displacements of the reflectivity profiles with respect to wavelength which were caused by the most minimal contact with the cryostat during the helium refilling procedure.

The original intention to characterise the film only at the beginning of the experiment was driven by the desire to maintain a precise and constant temperature throughout the experiment. Rather than raising the temperature above T_c before each run, in a new applied magnetic field, we chose a simpler, but approximate, method to obtain the spin-independent reflectivity. We assumed the average of the two separate neutron-spin reflectivities would be similar to the spin-independent reflectivity in the normal state. This assumption stems from the form of the dependence of the refractive index on the neutron spin (see equation 2.43). Analysis of data, using this technique, taken in time periods without a helium refill support this assumption and give consistent results, within experimental error, for the incident angle. Further fine tuning of the estimation of the true incident angle was possible when the individual spin reflectivities and the resultant flipping ratio were considered during the full analysis of the data. This further refinement produced relatively small changes and the calculated spin independent profiles maintained a good fit to the averaged reflectivities. In contrast $\langle z_D^2 \rangle^{1/2}$ and $\Delta\theta$ remained unchanged and were not fitted for each individual profile. For all profiles we achieved a surface roughness, $\langle z_D^2 \rangle^{1/2}$, equal to (100 ± 8) Å, an angular divergence, $\Delta\theta$, equal to 0.01°, and a variation in incident angle of between 0.293° and 0.303°.

The dependence of the reflectivity profiles on these sample and instrumental factors is illustrated in figure 6.1. The data is an average of the two spin-dependent reflectivities for the film in a 5.6×10^4 Am^{-1} applied field, (700 Oe). In each of the calculated profiles the effects of the 50Å PbO surface layer and the silicon substrate are taken into account. The calculated profile is smeared out in the region of the critical wavelength (5.2Å) when an angular spread of the incident neutron beam is assumed. The effect of surface roughness is to reduce the intensity of the reflected beam at small wavelengths. For each profile a unique set of values for θ, $\Delta\theta$ and $\langle z_D^2 \rangle^{1/2}$ can be found. The fitted parameters for the profile of figure 6.1 were found to be $\theta = 0.293^\circ \pm 0.0005^\circ$, $\Delta\theta = 0.010^\circ \pm 0.0005^\circ$ and $\langle z_D^2 \rangle^{1/2} = (100 \pm 8)$ Å.

Due to the difference in the position of the critical edge for each polarisation state, (see section 2.8), the ratio of the spin independent reflectivities, i.e. the flipping ratio, deviates from unity. Within our analysis of the raw data the flipping ratios were mainly used in preference to the individual spin reflectivities in evaluating the field profiles because the variation of the flipping ratio with λ shows more structure. Care must be taken with this approach to consider the individual reflectivities as well as the flipping ratios because it is possible to find a magnetic profile which fits the flipping ratios well but which fails to describe accurately the reflectivity curves. The position of the flipping-ratio minimum reflects the accuracy of the determined incident angle and could be used to refine its value. Within the bulk superconducting region it was found that the position of the flipping ratio minimum was insensitive to the chosen field profile and dependent solely on the incident angle. This was found not to be the case in the surface superconducting region and will be discussed later.

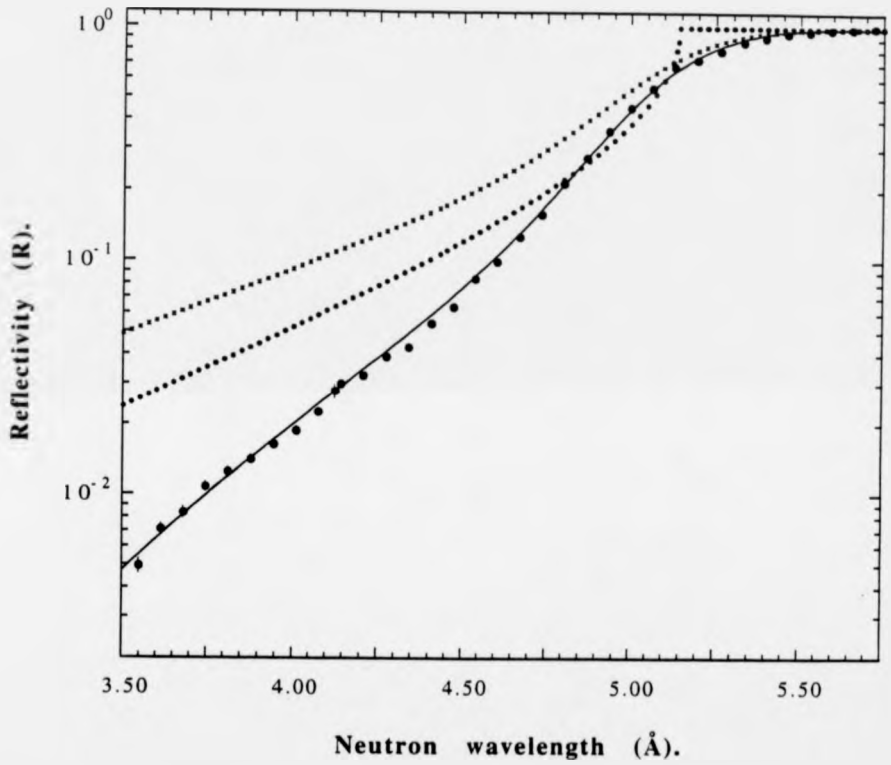

Figure 6.1: The calculated spin-averaged reflectivity of lead at 1.5K in a 5.6 x 10^4 Am^{-1}, (700 Oe), applied field (a 0.5μm Pb film with a 50Å PbO surface layer, on a Si substrate). The large points are the experimental observations. The dotted line (·····) represents the reflectivity for $\theta = 0.293^\circ \pm 0.0005^\circ$, the crossed line (·····) represents the same with the addition of a Gaussian spread of incident angles of $\Delta\theta = 0.010^\circ \pm 0.0005^\circ$. The continuous line includes the effect of surface roughness where $\langle z_D^2 \rangle^{1/2} = (100\text{Å} \pm 8)$ Å.

6.3 The bulk superconducting region, ($H < H_c$).

6.3.1 Results.

Statistically-more-accurate flipping-ratio profiles could be obtained at higher applied fields where the difference between the (+) and (-) reflectivity curves is greater. Figure 6.2 shows the measured flipping ratios for the film in a 6.0 x 10^4 Am^{-1} applied field, (750 Oe). Various types of magnetic induction profiles were modelled and their calculated flipping ratios compared to experiment. The most accurate fit to the data was a calculated flipping-ratio profile assuming an exponential decay of the magnetic induction, B(z), with respect to the depth from the surface of the film

$$B(z) = \mu_0 H_a \exp(-z / \lambda_p) \qquad (6.3)$$

where H_a is the applied field and λ_p is the characteristic penetration depth, (not to be confused with the neutron wavelength λ). This is the exact form applicable to a weakly-coupled, BCS superconductor in the local limit, (Bardeen et al. 1957). An excellent fit is achieved at most wavelengths assuming a penetration depth of (390 ± 10) Å. Interpretation of the effectiveness of the fit at lower wavelengths, $\lambda < 4.5$Å, is restricted due to the poorer quality of data. Due to the rapid fall-off of reflectivity with decreasing wavelength, see figure 6.3, the reflectivity at $\lambda = 4.5$Å was reduced to ~5% of the total reflectivity at higher wavelengths. Therefore it is difficult to say whether the tendency of the fit to give a flipping ratio greater than unity is a real effect, or a result of our assumption that the film behaves as a series of layers of a constant magnetic induction. Figure 6.3 depicts the two separate spin reflectivities together with the modelled profiles calculated from the expontential field decay, (equation 6.3). The agreement between the calculated and the experimental curves is seen to be good.

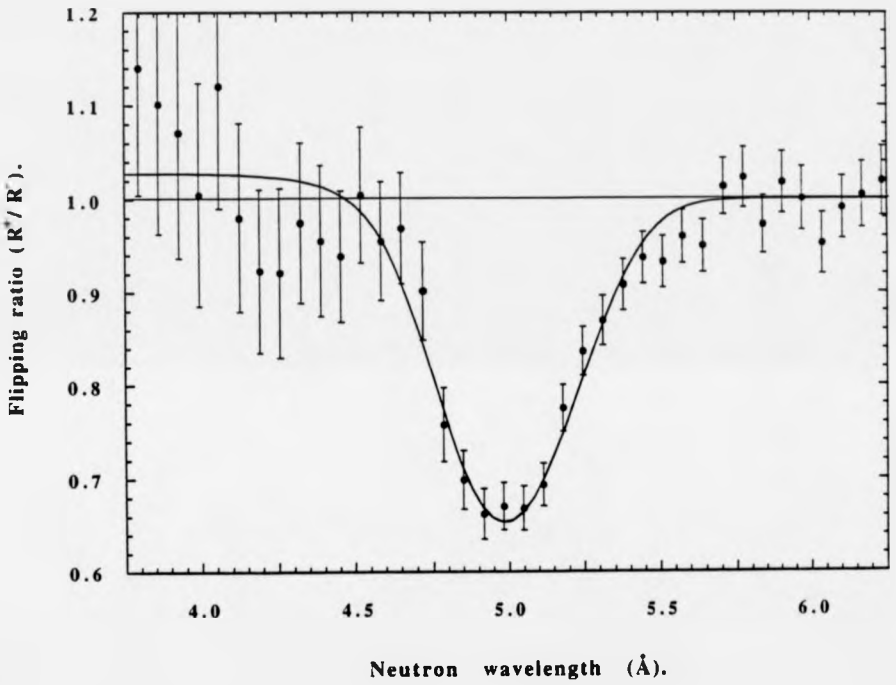

Figure 6.2: The observed flipping ratio for lead at 1.5K in a 6.0 x 10^4 Am^{-1}, (750 Oe), applied field. The continuous line represents a profile calculated from an exponentially decaying magnetic induction profile, with λ_p = (390 ± 10) Å.

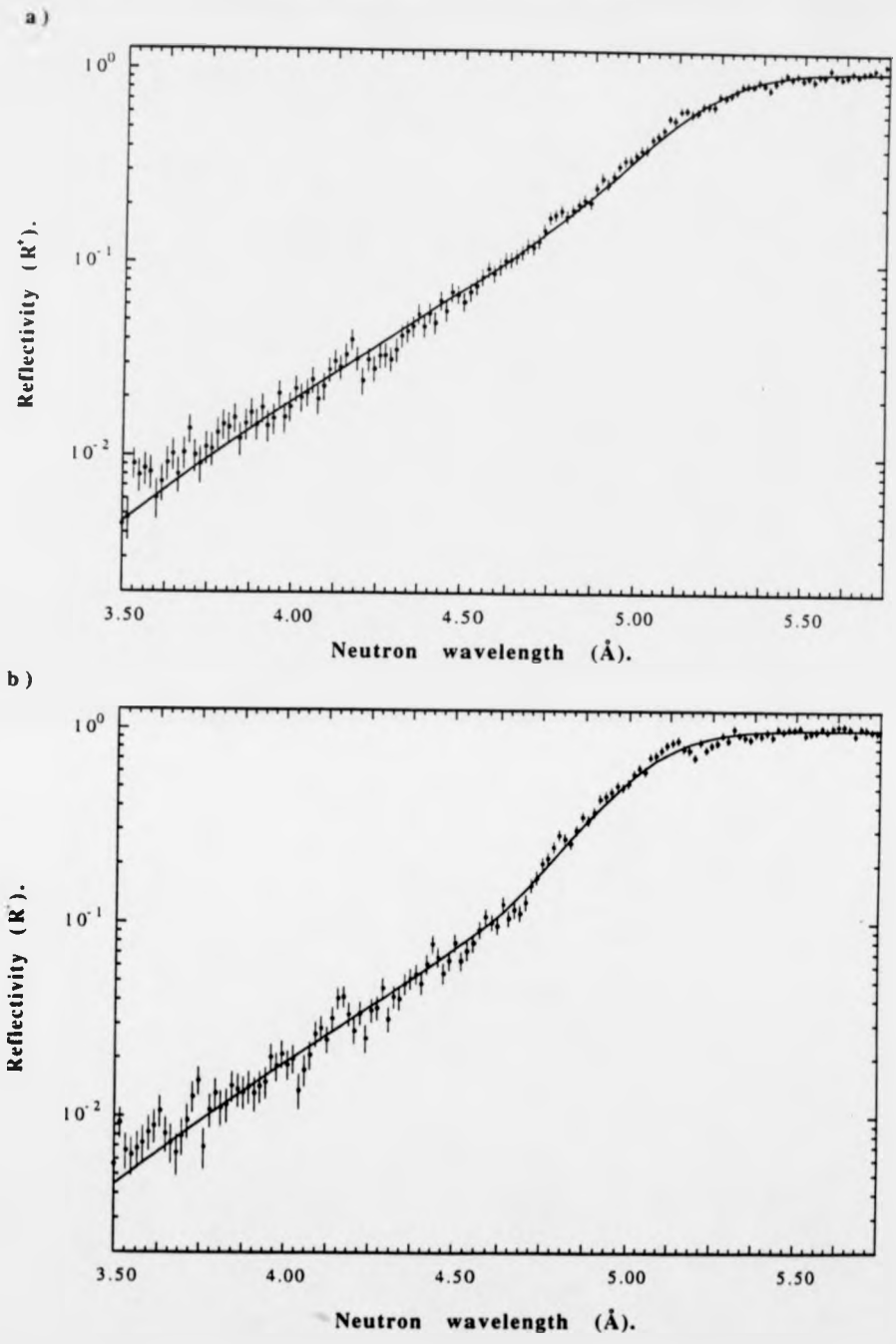

Figure 6.3: The reflectivities for lead at 1.5K in a 6.0 x 10^4 Am^{-1}, (750 Oe), applied field, a) spins down (-), b) spins up (+). The continuous lines represent a profile calculated from an exponentially decaying magnetic induction profile, with λ_p = (390 ± 10) Å.

The high sensitivity of the flipping ratio to the pentration depth is illustrated in figure 6.4 where the modelled profiles, for an applied field of 6.0 x 10^4 Am^{-1}, calculated for exponential decays of 370Å and 410Å are plotted along with the experimental results.

Figure 6.5 shows the flipping ratio for the film in a 4.8 x 10^4 Am^{-1} applied field, (600 Oe). The shift in the position minimum, by ~0.3Å, from its position for the 6.0 x 10^4 Am^{-1} applied field can be accounted for by the small change in incident angle from 0.293° to 0.303°. The calculated profile assumes an exponential decay of the magnetic induction, with a penetration depth of, in this case, 400Å. At this field the purely exponential decay models experiment even at lower wavelengths.

By comparing the modelled profiles, calculated for an exponential decay of 390 Å for all the profiles, to the measured flippings ratios we find a satisfactory fit for all the measured applied fields, see figure 6.6. (The field profiles for the two lower applied fields, 2.0 x 10^4 Am^{-1}, (250 Oe), and 4.0 x 10^4 Am^{-1}, (500 Oe), were not modelled independently due to the poorer quality of the data.) We may therefore may conclude that the field penetration in the bulk superconducting region of lead is accurately described, based on the fits of the individual profiles, by a pure exponential decay of (390 ± 10) Å.

During the modelling of the flipping ratios, assuming an exponential decay, for the applied fields of 5.6 x 10^4 Am^{-1} and 6.0 x 10^4 Am^{-1}, the calculated flipping ratios consistently fell below the data in the wavelength range of 4.6Å to 4.85Å. In order to investigate this shortfall in our model we attempted to model several variations of an exponential decay, namely smoothed exponential decays, to the experimental data. This approach would appear sensible as one effect of surface roughness may be to 'round off' the initial sharp decrease in the field profile at the films surface. A small improvement on the modelled profile in the range of 4.6Å to 4.85Å, for a 5.6 x 10^4 Am^{-1} applied field (see figure 6.7), was obtained by using an exponential decay, λ_p =

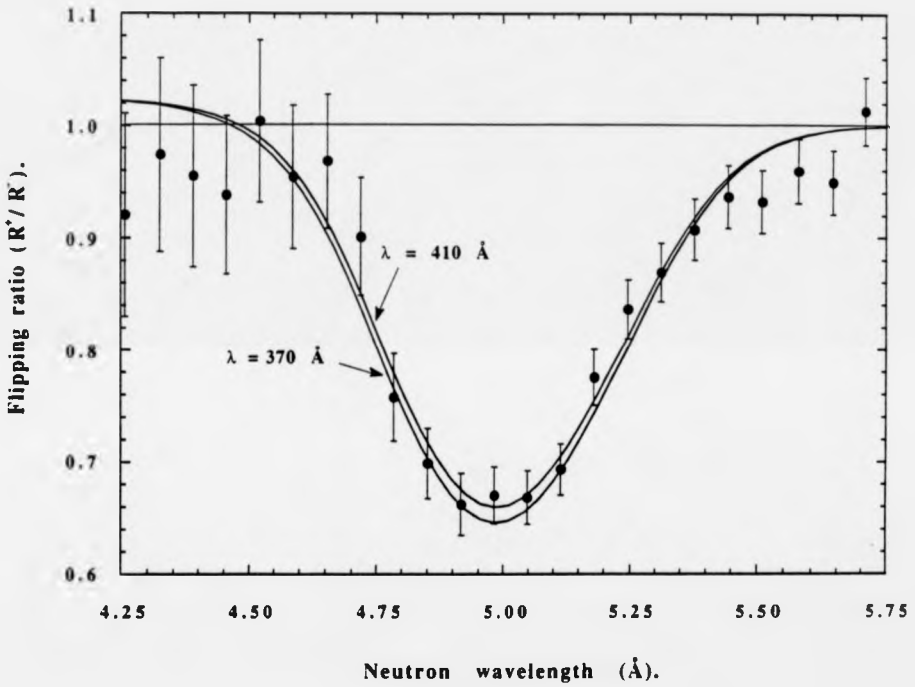

Figure 6.4: The observed flipping ratio for lead at 1.5K in a 6.0 x 10^4 Am^{-1}, (700 Oe), applied field. The sensitivity of the flipping ratio to variation in the penetration depth is illustrated by the two profiles calculated from exponentially decaying magnetic induction profiles, with λ_p= 370 Å and 410 Å.

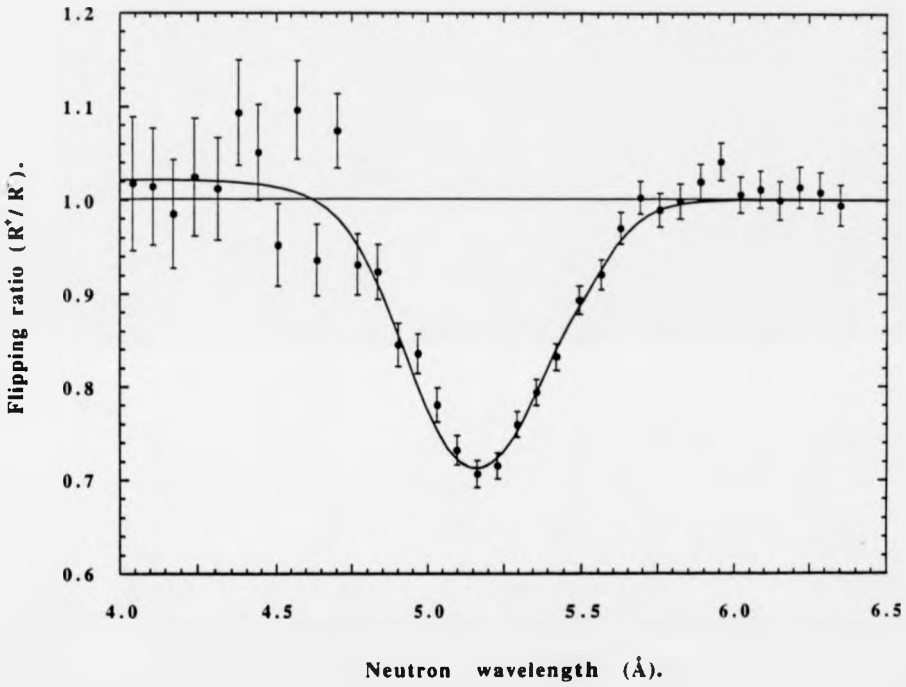

Figure 6.5: The observed flipping ratio for lead at 1.5K in a 4.8 x 10^4 Am^{-1}, (600 Oe), applied field. The continuous line represents a profile calculated from an exponentially decaying magnetic induction profile, with λ_p = (400 ± 10) Å.

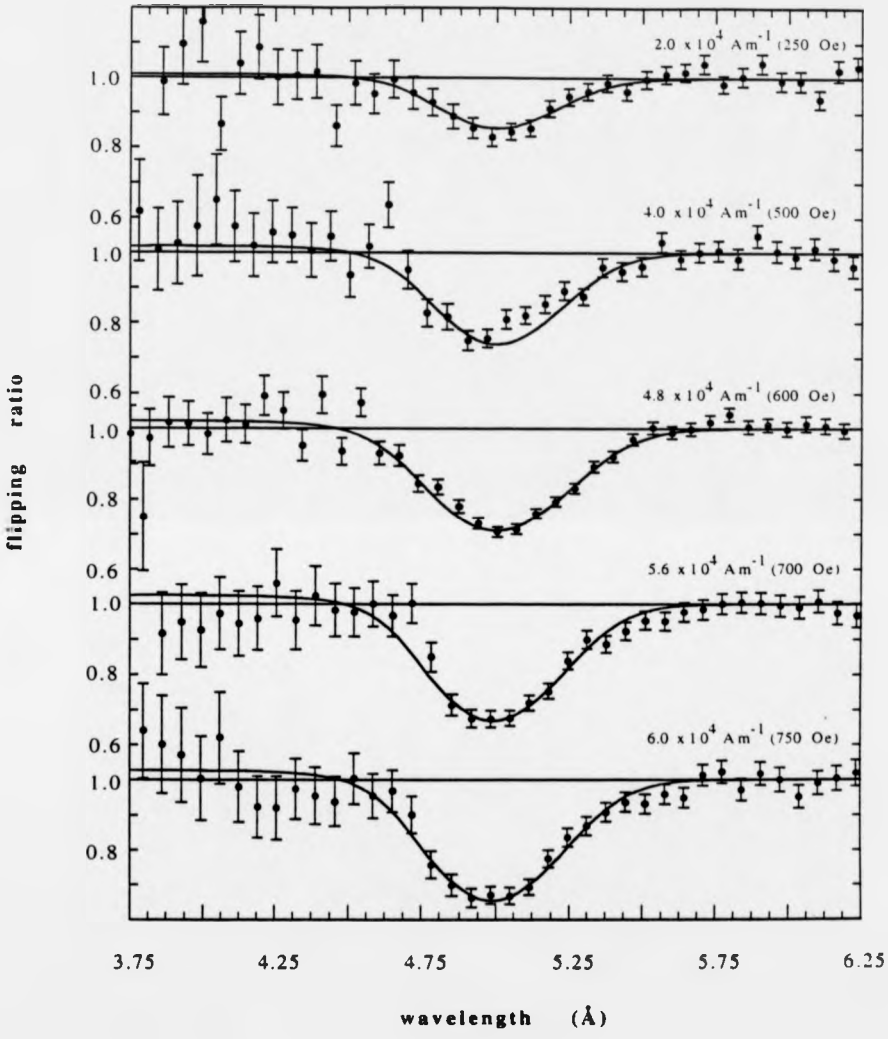

Figure 6.6: The evolution of the flipping ratio with increasing applied field, in the bulk superconducting region. For each applied field the continuous line represents a profile calculated from an exponentially decaying magnetic induction profile, with λ_p = (390 ± 10) Å.

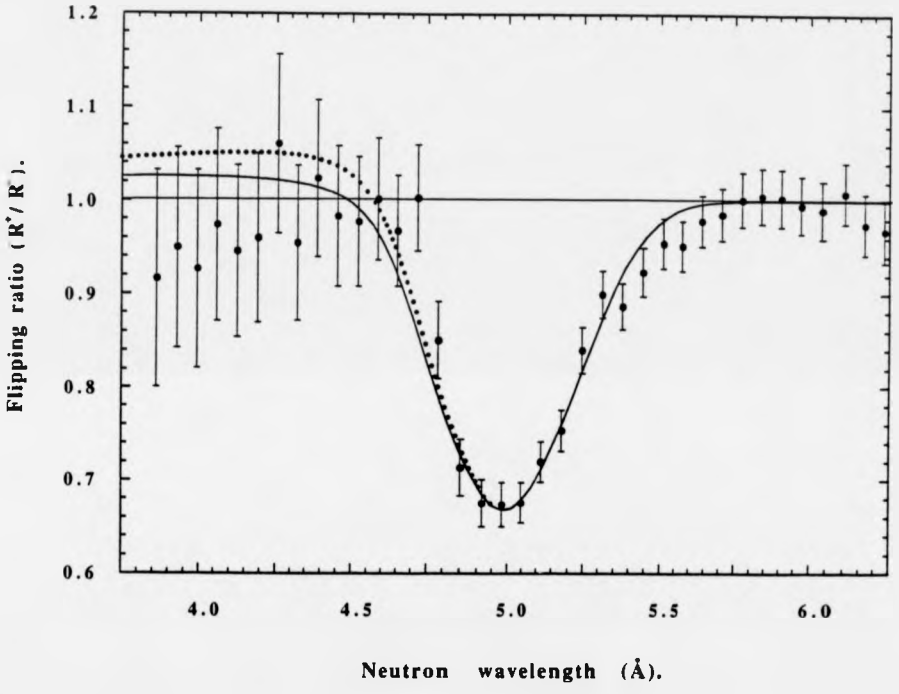

Figure 6.7: The observed flipping ratio for lead at 1.5K in a 5.6 x 10^4 Am^{-1}, (700 Oe), applied field. The continuous line represents a profile calculated from an exponentially decaying magnetic induction profile, with λ = (400 ± 10) Å., and the dotted line representss a profile calculated from a smoothed exponential decay, with λ_p = (330 ± 10) Å.

330Å, smoothed over a 40Å range and shifted so the critical edge of the decay remained at the interface. Figure 6.8 shows a comparison of this smoothed decay with two pure exponential decays, penetration depths of 330Å and 390Å. It can be seen that the behaviour of the smoothed decay more closely resembles that of the exponential decay with penetration depth of 390Å, although slightly displaced with depth. This is not surprising as the modelled flipping ratio profiles, heavily dependent on the slope of the magnetic induction decays, are very similar. Unfortunately flipping ratios calculated from the improved modelled profile deviate more seriously from the data at lower wavelengths than the flipping ratio profile modelled on an purely exponential decay. We can therefore conclude that to within the overall statistical accuracy of the data a smoothed exponential decay does not provide a better overall fit than a pure exponential decay.

6.3.2 Discussion.

For each of the applied fields below H_c a purely exponential decay, with a characteristic penetration depth of (390 ± 10) Å, described the magnetic induction profile well. As expected the penetration depth showed no field dependence, within experimental error.

6.3.2a Non-local effects.

At an initial inspection, the use of a purely exponential decay of field, characteristic of Londons' local theory (London and London. 1935), appears contradictory to the non-local approach first proposed by Pippard (Pippard. 1953) and implicit in BCS theory (Bardeen et. 1957).

Within Londons' approach a local relationship between the current density and field within a superconductor results in an exponential decay of the field, characterised by the London penetration depth λ_L. Within BCS theory the superconducting order parameter changes gradually over a

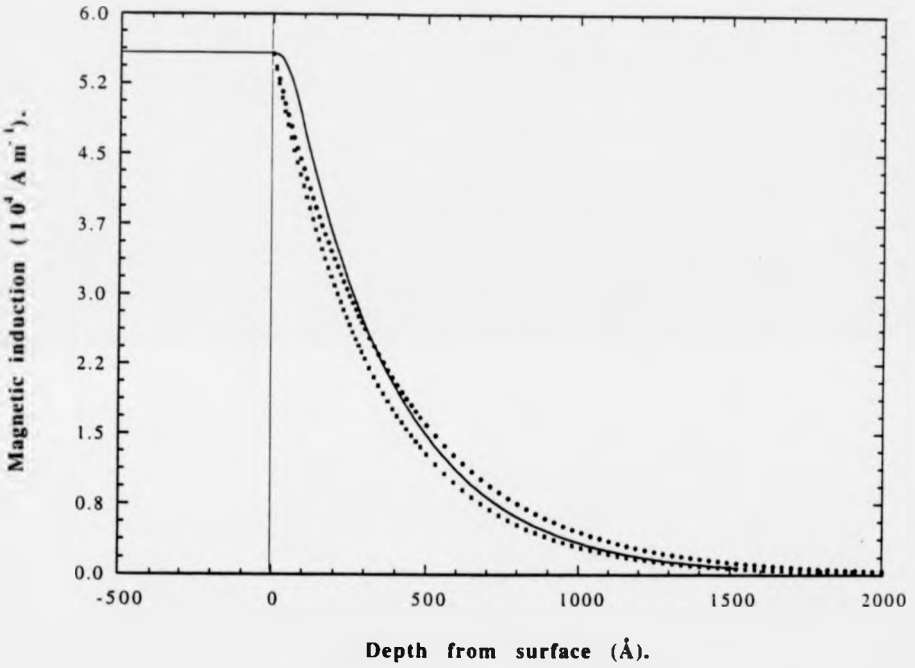

Figure 6.8: The modelled magnetic induction profiles for lead in a 5.6 x 10^4, (700 Oe), Am^{-1} applied field. The continuous line represents a smoothed exponential decay, with λ = 330Å (Note: the profile was smoothed over a 40 Å range, with the critical edge shifted so it remained at the interface.), the dotted line (·····) represents an exponential decay, with λ_p = 330Å and the crossed line (·····) represents an exponential decay, with λ_p = 390Å.

certain length ξ, the coherence length, which can be thought of as the size of the Cooper pairs, the superconducting charge carriers. If $\xi \geq \lambda_L$ then the local relation of Londons' approach is no longer valid and must be replaced by a non-local relationship. The assumption of this non-local relation between the current and field leads to a deviation from the exponential behaviour of the magnetic field, with a possible sign reversal of the field at a sizeable distance away from the surface, (Sommerhalder and Thomas. 1961a, 1961b). This sign reversal, and hence the demonstration of a non-local Meissner effect has been found experimentally in tin, (Drangeid and Sommerhalder. 1962). Further calculations by Halbritter (Halbritter. 1971) show the dependence of the non-local effects on κ, where $\kappa = \lambda_L/\xi$, and predict their occurrence even in type II superconductors with $\kappa \leq 1.6$. Within this framework, lead, with $\kappa \sim 0.5$ at 1.5K, should exhibit non-local effects and show a deviation from a exponential decay. Assuming $\kappa = 0.5$ the calculations by Halbritter predict a sign reversal of field at a depth $\sim 5.5\ \lambda_L$, reaching a maximum negative field of 0.1% of the applied field. These effects are very small and understandably not observed in the present experiment.

The consequences of non-locality is much greater at lower values of κ where, for example, a sign reversal of ~3% of the applied field is possible at depths $> 4.5\lambda_L$ for $\kappa < 0.01$. Due to the surface nature of this technique the field profile close to the surface dictates the shape of the flipping ratio profile. The effect of the field profile deeper in the material is illustrated in figure 6.9. The flipping ratio has been calculated for a superconductor in a 4.8×10^4 Am^{-1} applied field where the exponential decay, λ_p = 390Å, abruptly undergoes a sign reversal at a depth z. It can be seen that the effect at depths greater than $4\lambda_p$ (~1200Å) is negligible and therefore to observe a field reversal using polarised-neutron reflectivity a material with a very low κ and low λ_p would be needed.

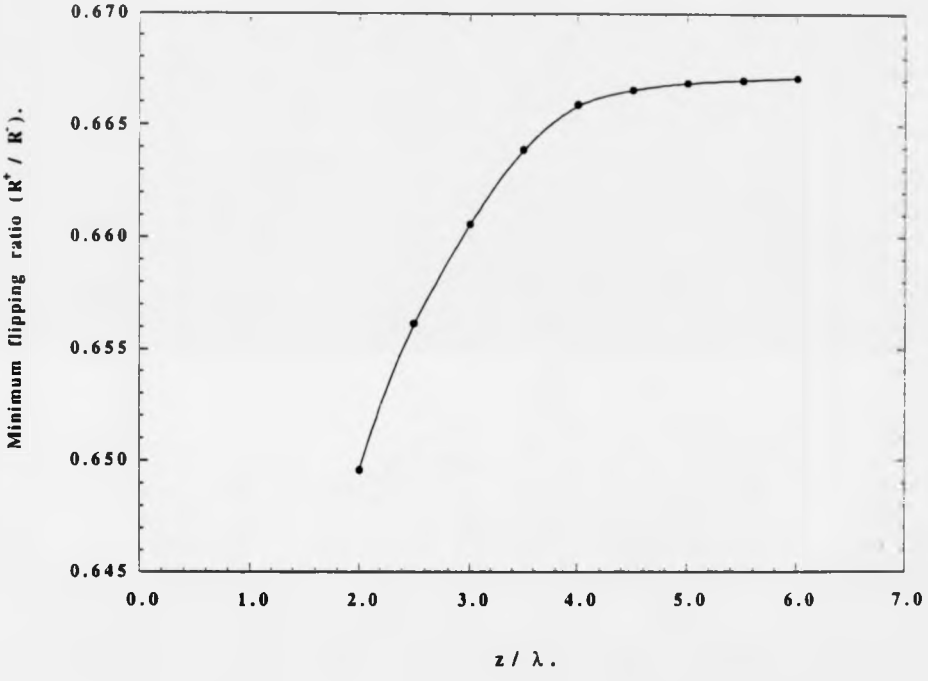

Figure 6.9: The minimum of the flipping ratio curve obtained from a modelled exponential decaying field profile (λ_p = 390Å) which undergoes a field reversal at a depth z. This figure shows the insensitivity of the polarised-neutron reflectivity to details at depths > ≈ $4\lambda_p$ below the surface.

6.3.2b Comparison of the observed penetration depth with theory and previous experimental results.

Previous indirect experimental techniques for measuring the penetration depth have failed to produce consistent results, and therefore it has been difficult to compare theory and experiment. An important consideration is that different techniques do not always measure the same penetration depth, and hence the results are often not directly comparable. Several techniques use measurements taken at temperatures close to T_c to determine the penetration depth. In this region of $T \approx T_c$, the London limit, $\xi << \lambda_p$ applies, and the measured penetration depth is equivalent to the London penetration depth, $\lambda_L(0)$. In contrast, other techniques, including polarised-neutron reflectivity, measure the penetration depth sufficiently away from T_c, where the London limit fails to hold, and hence they measure the bulk penetration depth. We may check the consistency of our results with theory and previous results by calculating the equivalent penetration depths, (Egloff et al. 1983). A summary of the various penetration depths is given Table 6.1.

Our measured bulk penetration depth, at T=1.5K, is approximately equal to $\lambda_p(0)$ if we assume a Gorter-Casimir temperature dependence of $\lambda_p(t)$, (Gaunt et al. 1948), where $\lambda_p(t) = \lambda_p(0)\ (1 - (t/t_c)^4)^{-1/2}$ or equivalently use the tabulated temperature dependence of $\lambda_p(t)$ calculated by Muhlschlegel using BCS theory, (Muhlschlegel. 1959).

In order to calculate the London penetration depth, $\lambda_L(0)$, we may use the results of BCS theory, produced graphically in their original paper where $\lambda_p(0)/\lambda_L(0)$ is shown as a function of $\xi_o/\lambda_L(0)$, see figure 6.10 (Bardeen et al. 1957). In order to use these BCS graphs we need to know ξ_o, the coherence length. The value for ξ_o has been quoted as lying between 830Å, calculated theoretically from BCS theory assuming weak coupling, (Bardeen and Schrieffer. 1961) and 1290Å, in the extreme limit applying strong coupling corrections, (Kerchner and Ginsburg. 1974). ξ_o may be calculated from the

		Measured (Å)		Calculated (Å)	
		$\lambda_p(0)$	$\lambda_L(0)$	$\lambda_p(0)$	$\lambda_L(0)$
Experiment	**Technique**				
Simon. 1950	surface impedance	540	-	-	-
Lock. 1951	magnetisation	390	-	-	-
Cody and Miller. 1968	magnetisation	440	-	-	-
Peabody and Meservey. 1972	Quantum Interference	557	-	-	-
Gasparovic and McLean. 1970	Passive resonator	-	305	-	-
Kerchner and Ginsburg. 1974	Magnetic field attenuation	-	315	453	-
Onuki et al. 1976	Microwave impendence	-	370	-	-
Mende et al. 1977	surface impedance	480	-	-	-
Egloff et al. 1983	Inductance	-	400	525	-
Present work.	polarised-neutron reflectrometry	390	-	-	280
Theory					
Swihart and Shaw 1972		-	-	405	269

Table 6.1 : A summary of previously measured and calculated penetration depths for superconducting lead.

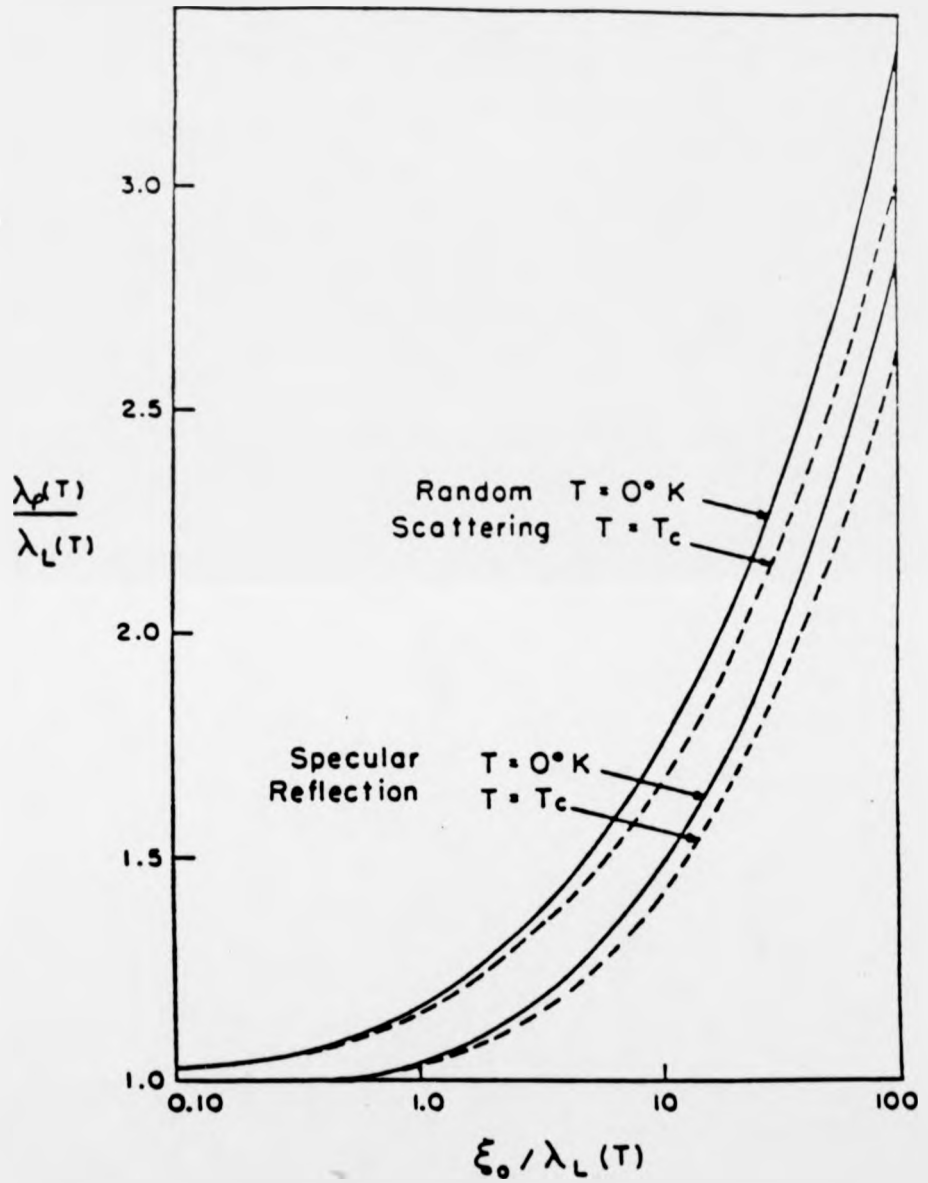

Figure 6.10: The ratio of $\lambda_p(T)/\lambda_L(T)$ vs. $\xi_0/\lambda_L(T)$ for the boundary conditions of random, or diffuse, scattering and specular reflection and for temperatures near T = 0 K and near T= T_c, (from Bardeen et al. 1957).

Fermi velocity, υ_f, and the energy gap, Δ_o, both averaged over the Fermi surface, using the relationship $\xi_o = h\upsilon_f/\pi\Delta_o$. A number of techniques allow a reliable estimation of $\upsilon_f = 0.61 \times 10^8$cm/s to be made for lead, (Gasparovic and McLean. 1970). A widely accepted value for $2\Delta_o$ for lead is $4.3kT_c$, which has been measured accurately in infrared and tunnelling experiments and reflects the strong coupling nature of lead, (in a weak-coupling superconductor, in the BCS limit, $2\Delta_o/kT_c = 3.53$). Assuming these values for Δ_o and υ_f we can calculate $\xi_o = 960$Å. If we assume the scattering in a bulk lead sample to be diffuse rather than specular, (Swihart and Shaw. 1972), we can extrapolate a value of $\lambda_L(0) = 280$Å from the BCS graph, corresponding to $\lambda_p(0) = 390$Å and $\xi_o = 960$Å. Corrections to the penetration depth due to the effect of impurities (Miller. 1959) may be neglected if we assume lead to be a pure superconductor where the mean free electron path is much greater than the coherence length.

One group of experimental techniques derive the actual bulk penetration depth at T=0, $\lambda_p(0)$. The earliest measurement of $\lambda_p(0)$ of (390 ± 30) Å was derived from the temperature dependence of the magnetic susceptibility of thick lead films, (Lock. 1951). Later, similar measurements found $\lambda_p(0) = 440$Å, (Cody and Miller. 1968). Still more recent measurements, using a quantum interference technique, obtained a much higher value of 557Å after sizeable corrections for non-local effects (Peabody and Merservey. 1972). In contrast, our result of $\lambda_p(0) = (390 \pm 10)$ Å agrees favourably with the early measurements.

As described earlier, a second group of techniques derive the penetration depth in the region where the London limit, $\xi_o << \lambda_p$ applies, and the measured penetration depth is equivalent to $\lambda_L(0)$. These results show little consistency other than being smaller than $\lambda_L(0)$, and fail to elucidate either the weak or strong coupling nature of lead. Measurements by Gasparovic and McLean. 1970, using radio-frequency fields, lead to a value of $\lambda_L(0) = 305$Å and a

temperature dependence of λ_L described well by weak-coupling BCS theory. Later measurements obtained from a microwave surface impedance technique support this weak-coupling approach and find $\lambda_L(0)$ = 370Å, (Onuki et al. 1976). In contrast to these results experiments measuring the attenuation of a dc magnetic field by cylindrical thin films have found lead to exhibit a strong-coupling behaviour and $\lambda_L(0)$ = 315Å, (Kerchner and Ginsburg. 1974). By calculating $\lambda_L(0)$ from our results, assuming strong coupling as discussed above, we find $\lambda_L(0)$ = 280Å, a lower value than previous experiments.

Theoretical calculations of the various penetration depths of lead have been made and compared for both a weak-coupling and a strong-coupling approach, (Swihart and Shaw. 1972, Swihart et al. 1965). In the case of the strong coupling this has involved the application of the theory proposed by Nam, (Nam. 1967a, 1967b). Our measured value of λ_p = (390 ± 10) Å is in good agreement with the theoretical value of 405Å assuming strong coupling within lead. Additionally our calculated value of $\lambda_L(0)$ = (280 ± 10) Å, using the simplified approach described above, also agrees well with strong-coupling theory, where $\lambda_L(0)$ = 269Å.

6.4 The surface superconducting region, ($H > H_c$).

6.4.1 Results.

The transition from the bulk superconducting state to a surface superconducting state in an applied field can be seen in the change of the shape of the flipping ratio profiles and, more dramatically, by the change in the integral of the polarisation, P, over momentum transfer, where $P = (R^+ - R^-)/(R^+ + R^-)$, with applied field (see figure 6.11).

Below an applied field of 6.0 x 10^4 Am^{-1} the integrated polarisation, P_i, mimics the form of the measured magnetisation curves for lead below the critical field, H_c (see Lock. 1951), i.e. P_i increases in proportion to H. This is

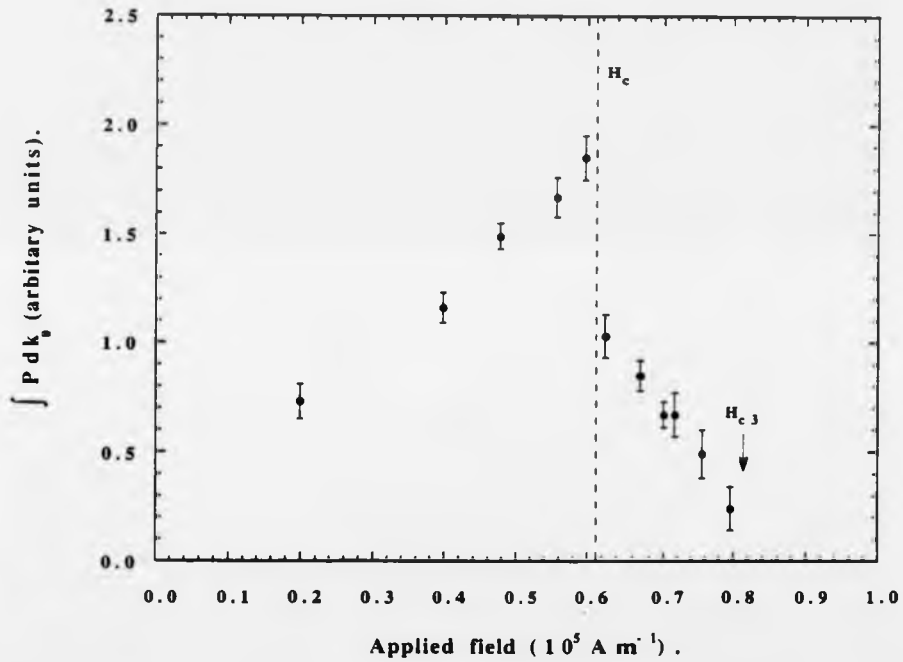

Figure 6.11: The integral of the polarisation, P, over momentum, k_0, plotted against the applied field. H_c is the critical field for the bulk superconducting state and H_{c3} is the critical field for the surface superconducting region.

not unexpected as the polarisation is directly proportional to the magnetisation if the magnetic induction profile is assumed to remain unchanged (Gray et al. 1990). Experimentally we have found that an exponential decay, with a constant penetration depth, accurately describes the bulk superconducting region and supports this assumption. Above 6.0 x 10^{3} Am^{-1} a sharp change in P_i occurs, and is interpreted as the transition to the surface superconducting state. Using this criteria we obtained a value of (6.13 ± 0.15) x 10^{4} Am^{-1} for H_c from figure 6.11.

Within Ginsburg-Landau theory, a local theory which allows us to calculate the field profile within a superconductor, the upper critical field of the surface superconducting region, H_{c3}, is related to H_c and κ for a type I superconductor by the expression $H_{c3} = 2.4\ \kappa\ H_c$ (Saint-James and de Gennes. 1964). By extrapolating the fall of P_i to zero, in figure 6.11, we were also able to estimate the value of H_{c3} as (8.12 ± 0.25) x 10^{4} Am^{-1} and hence we calculate κ to be 0.552 ± 0.005 at 1.5K.

Superficially, the dependence of P_i on applied field seems to resemble the bulk magnetisation curve for a conventional type II superconductor. This similarity is misleading. For a type II material P_i would be expected to behave in a similar way in the mixed state as in the bulk superconducting state due to similar field penetration at the surface. Additionally small oscillations in the individual reflectivity curves would be expected due to scattering from the flux lattice, which is also responsible for the persistence of magnetisation between the lower and upper critical fields in a type II material.

Above H_c the magnetic-field profile of the sample was modelled in a similar manner to that measured within the bulk superconducting region, described previously in section 6.2, taking into account the effects of the substrate and surface oxide layer. Two different approaches were used in the analysis of the individual flipping ratios within the surface superconducting region. First a curve which accurately described the experimental flipping ratios, but

which bore no direct relationship to theory, was obtained from an empirical relationship between the magnetic induction, B, and depth from the surface, z,

$$B(z) = \mu_0 H_a (1 - \alpha z \exp(-z^2/\beta^2)) \qquad (6.4)$$

where H_a is the applied field and α and β are variable parameters. Magnetic field profiles of this purely empirical form were found to describe the raw data reasonably accurately, see figure 6.12a, for the 6.25 x 10^4 Am^{-1} (785 Oe), 6.7 x 10^4 Am^{-1} (840 Oe) and 7.0 x 10^4 Am^{-1} (880 Oe) profiles.

A second approach used theoretical field profiles derived from Ginsburg-Landau theory, see section 1.3. For this purpose the non-linear Ginsburg-Landau equations, (Gray. 1983) were solved using an iterative process and a unique solution reached which minimised the Gibbs` free energy, (Felici and Gray. 1984). A direct comparison between theory and the experimental results proved difficult. To calculate the field profiles in the surface superconducting region by Ginsburg-Landau theory one needs to know two of the variables κ, λ_p and H_c, and then the third one is determined by the relationship

$$\kappa = 2\sqrt{2}\pi \frac{\mu_0 H_c \lambda_p^2}{\phi_0} \qquad (6.5)$$

where the magnetic flux quantum ϕ_0 = h/2e. The Ginsburg-Landau equations then give B(z) for a given H_a. Unfortunately our experimental values for H_c, κ and λ_p, given previously, are inconsistent with this relationship. If we are to proceed with the Ginsburg-Landau theory we must allow one of the three parameters to change. In order to generate sensible field profiles we needed to ensure that the theoretical value of H_c, was within our experimental range, (6.13 ± 0.15) x 10^4 Am^{-1} and also that H_c, κ and λ_p satisfied equation 6.5. Above H_c the most accurately determined flipping ratios were obtained in an applied magnetic field of 6.7 x 10^4 Am^{-1}, see figure 6.13, and initial attempts to model

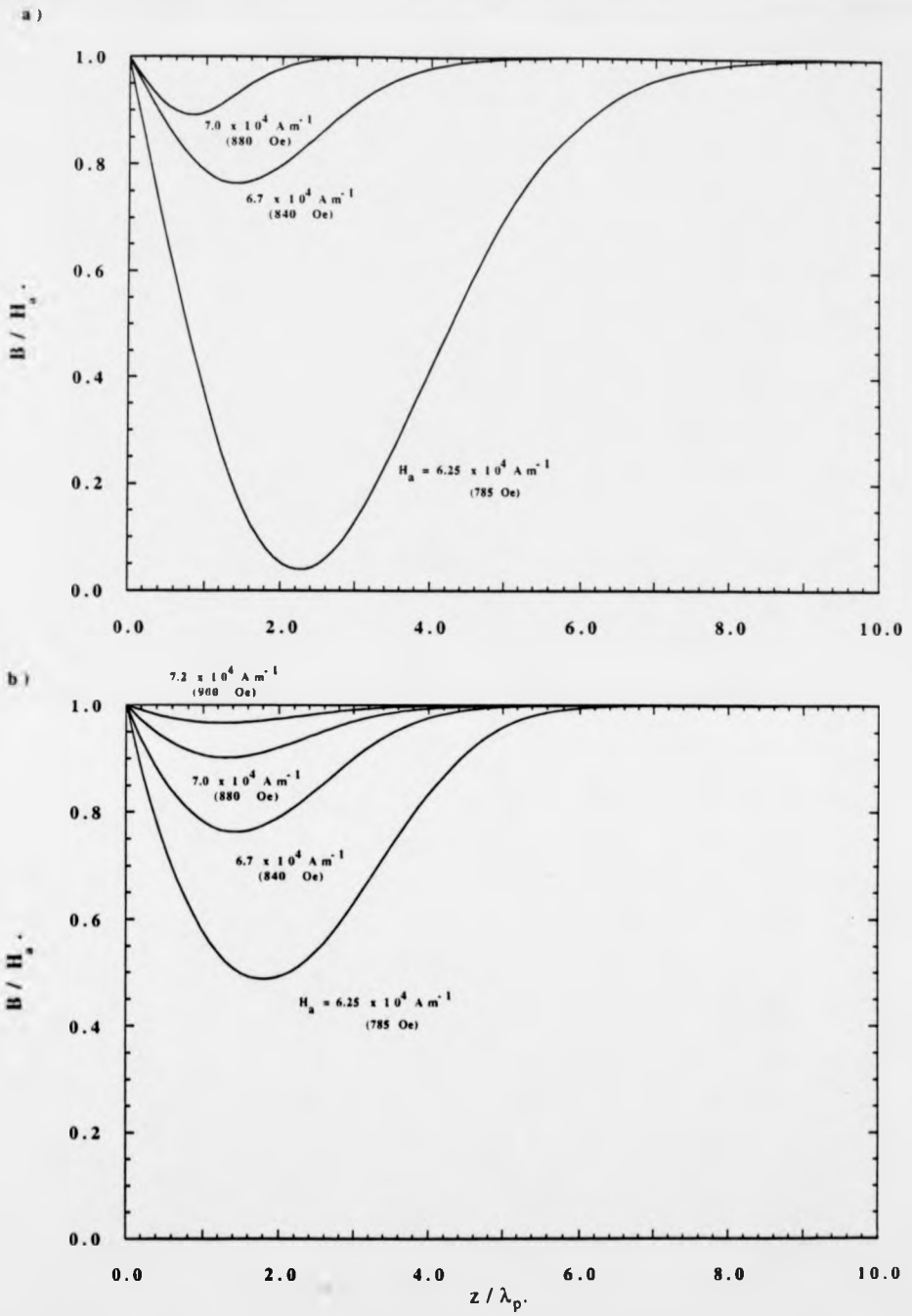

Figure 6.12: The modelled field profiles plotted as a function of distance z from the surface, with λ_p = 390 Å, for the surface superconducting region. a) using a general empirical form for the field profile and b) profiles theoretically calculated from Ginsburg-Landau theory.

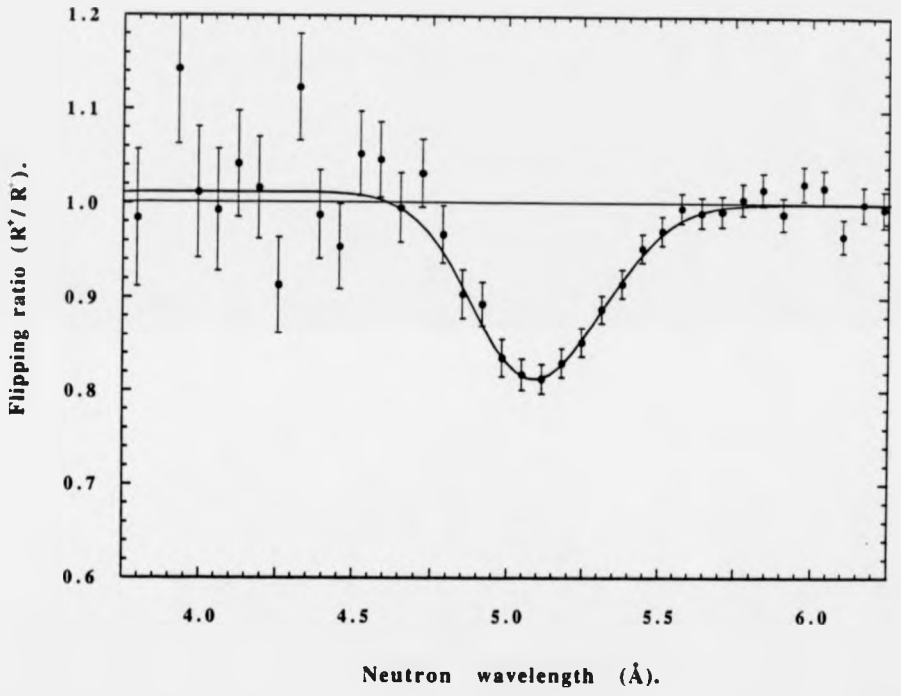

Figure 6.13: The observed flipping ratio for lead at 1.5K in a 6.7 x 10^4 Am^{-1}, (840 Oe), applied field. The continuous line represents the calculated flipping ratio from a field profile theoretically calculated from Ginsburg-Landau theory, (Note: the same field profile may be calculated for each κ using the correct H_c).

the experiment data, using Ginsburg-Landau theory, concentrated upon these measurements.

In our initial attempts to model theoretically the flipping ratios, κ was assumed to be 0.552, obtained from the critical fields, and λ_p set to 415Å in order to satisfy the requirement that $H_c \approx 6.13 \times 10^4$ Am^{-1}. Using this approach we were unsuccessful at modelling our measured flipping ratios.

A second theoretical approach which also satisfied the theoretical requirements involved fixing λ_p = 390Å, the value found in our earlier analysis of the bulk superconducting region, and setting κ to 0.503, to satisfy equation 6.5. Initial attempts to theoretically model the flipping ratio profile using this technique again resulted in a poor match to the data although there was a marked improvement over our initial attempts.

Further investigations revealed that the modelled flipping-ratio profile was highly sensitive to the value of κ. Small changes in κ produced sizeable deviations in the minimum value of the flipping ratio. We then were able to model accurately the data using a field profile generated with a κ = 0.497, a value within the experimental error of the observed value. Fixing λ_p and H_c to within their experimental uncertainties and allowing κ to vary seems to be the most sensible approach. First because λ_p was obtained using a pure exponential decay which was found to be virtually exact even when non-local and strong-coupling effects are present and secondly, H_c fixes the magnetic field scale so that all applied fields can be related to H_c, i.e. allowing H_c to be greater than 6.4×10^4 Am^{-1} would mean the 6.25×10^4 Am^{-1} profile corresponded to bulk superconductivity. Although a close fit to data was achieved for the 6.7×10^4 Am^{-1} profile (see figure 6.13) the calculated field profiles, assuming κ = 0.497, for the other applied fields failed to agree well with experiment. The major shortfall of this approach occurred at higher applied fields where the modelled flipping ratio profiles consistently fell well below measured flipping ratios. This is not surprising because theoretically a

κ of 0.497 corresponds to a H_{c3} of 7.40 x 10^4 Am^{-1}, see equation 1.12, which is much lower than the value for H_{c3} of (8.12 ± 0.25) x 10^4 Am^{-1} estimated from figure 6.11.

One solution to the problem of the inconsistency amongst the experimental values for H_c, H_{c3}, κ and λ_p was to assume that equation 6.5 was valid at H_c and then model the flipping-ratio profiles individually, allowing κ to vary. The value of κ which allowed us to most accurately model the strongest flipping ratio above H_c, the 6.7 x 10^4 Am^{-1}, (785 Oe), applied-field profile, was found to be heavily dependent upon the actual value of H_c. In order that κ behaved smoothly with an increasing applied field, H_c was fixed equal to 6.09 x $10^4 Am^{-1}$ (765 Oe), remaining within the experimental limits of the observed H_c, so that the κ calculated from equation 6.5 of 0.497 matched the κ which provided the most accurate model of the 6.7 x 10^4 Am^{-1} applied-field profile, see figure 6.14.

Due to the sensitivity of the calculated profiles upon κ, as illustrated in figure 6.15, we were able to model the observed flipping-ratio profiles more accurately than had been possible using a purely empirical form of the magnetic induction, e.g. the 7.0 x 10^4 Am^{-1}, (880 Oe) applied-field profile, as is shown in figure 6.16. In addition, using this approach we were also able to reasonably model the 7.2 x 10^4 Am^{-1}, (900 Oe), and 7.6 x 10^4 Am^{-1}, (950 Oe), applied field profiles. The evolution of the observed flipping-ratio profiles with an increasing applied field is shown in figure 6.17. The only observed profile which could not be modelled using this approach was one measured in a 8.0 x 10^4 Am^{-1}, (1000 Oe), applied field, where no flipping ratio is directly observable and the only indication of the continuing existence of the surface superconducting region is from the integral of the polarisation.

As would be expected, κ was found to increase as the applied field increased, forcing the superconducting layer to persist up to higher applied fields. Although, κ was only found to deviate strongly from its value at H_c at high applied fields, see figure 6.18.

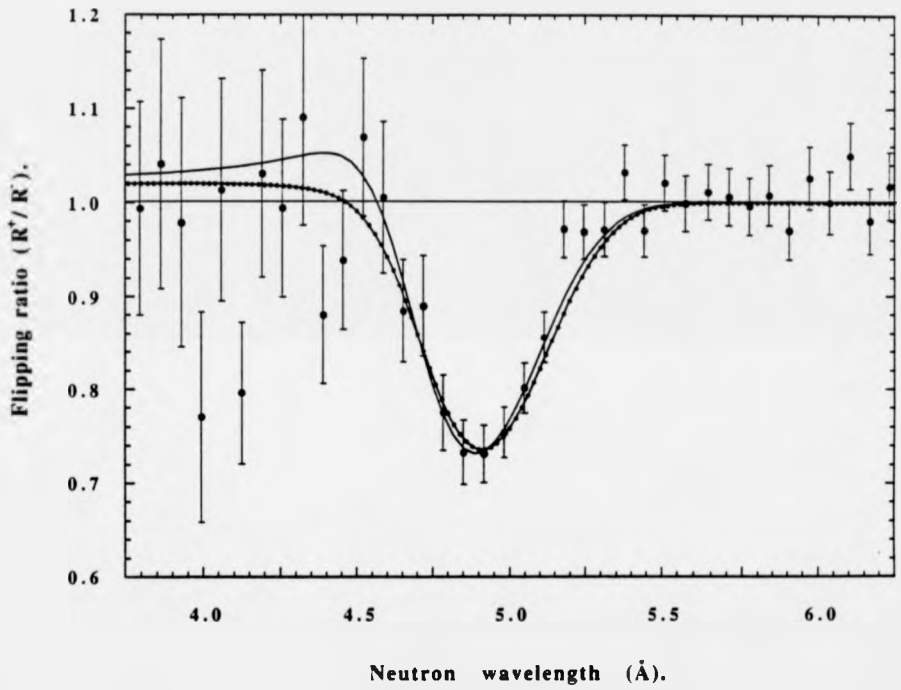

Figure 6.14: The observed flipping ratio for lead at 1.5K in a 6.25 x 10^4 Am^{-1}, (785 Oe), applied field. The continuous line represents the best fit to data using a general empirical form for the field profile. The dotted line represents the calculated flipping ratio from a field profile theoretically calculated from Ginsburg-Landau theory, for a superconductor with κ = 0.497, (H_c = 6.09 x 10^4 Am^{-1}).

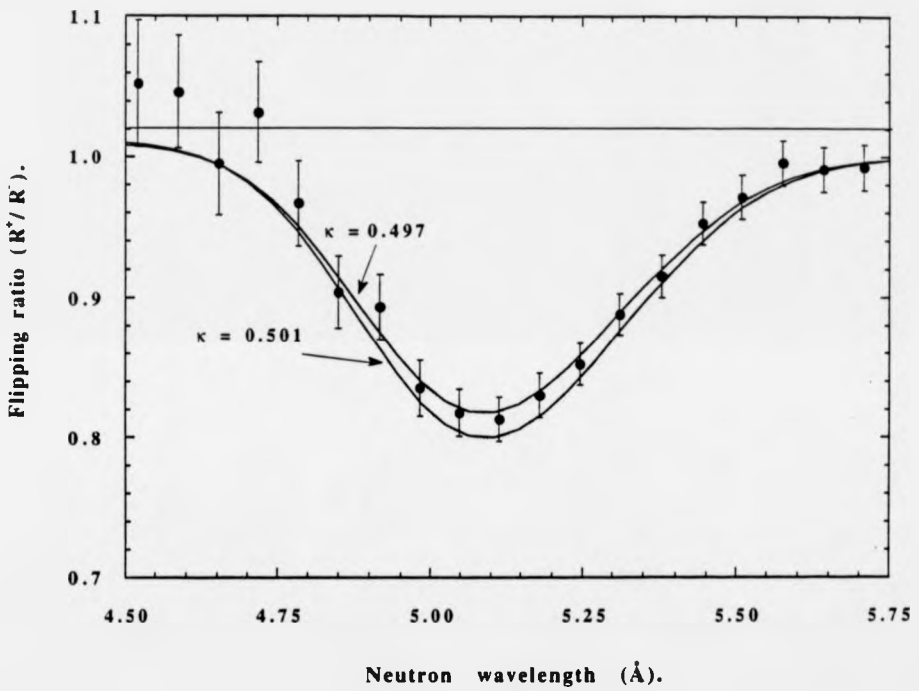

Figure 6.15: The observed flipping ratio for lead at 1.5K in a 6.7 x 10^4 Am^{-1}, (840 Oe), applied field. The sensitivity of the flipping ratio to small variations in the value of κ is illustrated by the two theoretical profiles, calculated from Ginsburg-Landau theory, for a superconductor with κ = 0.497 and κ = 0.501, (H_c = 6.09 x 10^4 Am^{-1}).

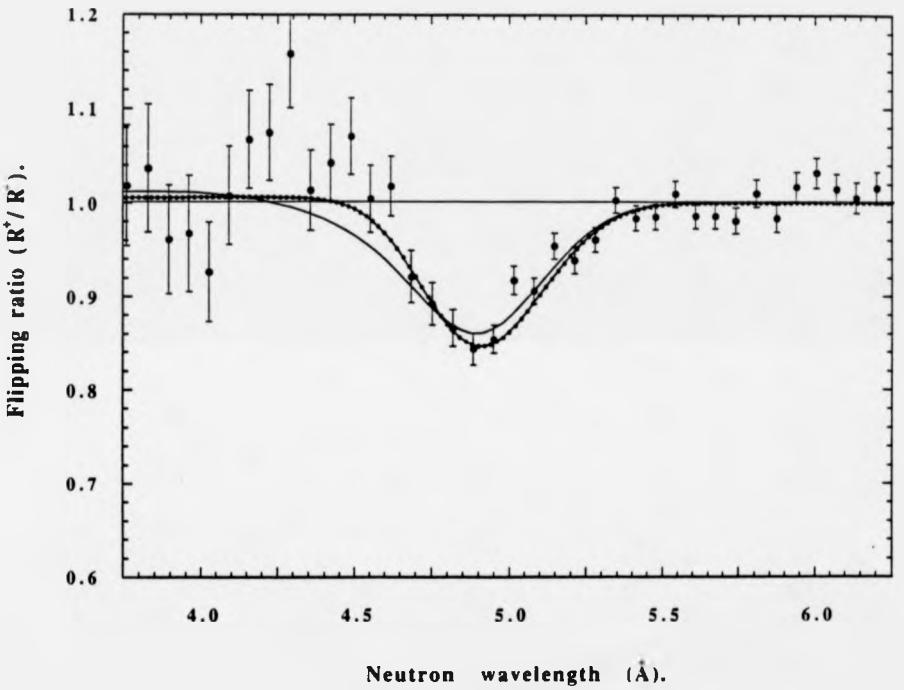

Figure 6.16: The observed flipping ratio for lead at 1.5K in a 7.0 x 10^4 Am^{-1}, (880 Oe), applied field. The continuous line represents the best fit to data using a general empirical form for the field profile. The dotted line represents the calculated flipping ratio from a field profile theoretically calculated from Ginsburg-Landau theory, for a superconductor with κ = 0.502, (H_c = 6.09 x 10^4 Am^{-1}).

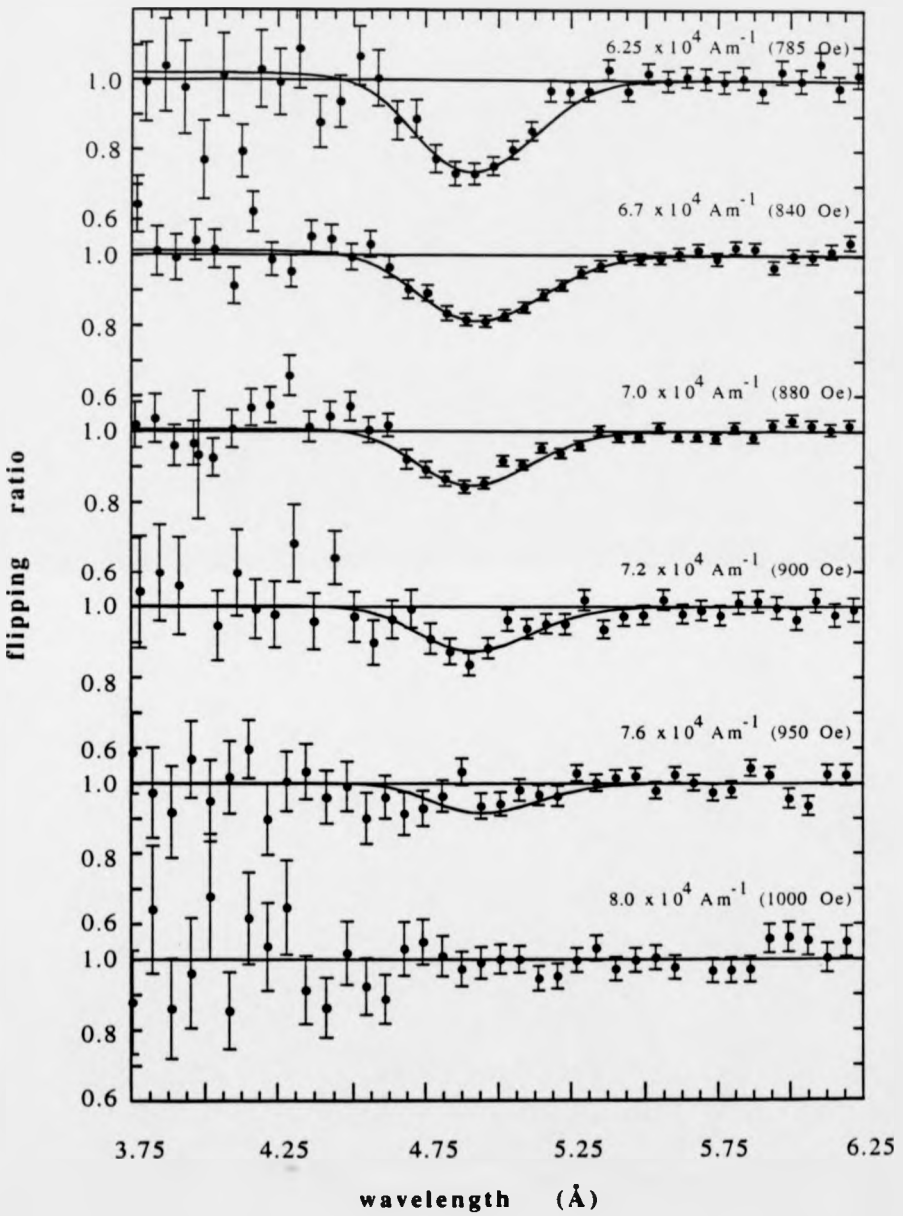

Figure 6.17: The evolution of the flipping ratio with an increasing applied field, in the surface superconducting region. For each applied field the continuous line represents the field profile theoretically calculated from Ginsburg-Landau theory.

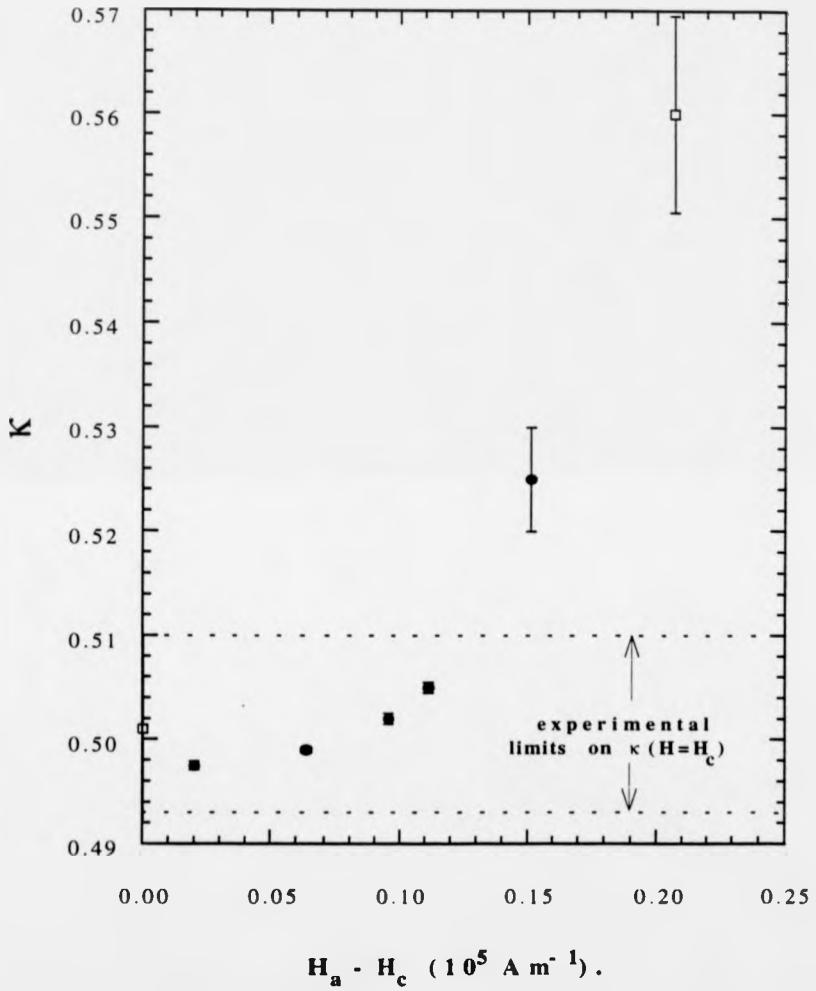

Figure 6.18: The variation of κ with applied field, from fits to the individual flipping-ratio profiles, theoretically calculated from Ginsburg-Landau theory.

The theoretically-modelled flipping ratio, shown in figure 6.14, and calculated from Ginsburg-Landau theory, assuming κ = 0.497 and H_c = 6.09 x 10^4 Am^{-1}, provides a more accurate model of the experimental 6.7 x 10^4 Am^{-1} applied-field profile than was obtained using a purely empirical form of the magnetic induction. A comparison of the two magnetic induction profiles, figure 6.12, appears to suggest the calculated flipping ratio is quite insensitive to the form of the field profiles, contrary to our previous claims. This is largely due to the similarity between the two field profiles near the surface, i.e. a very similar gradient, which is the region which most heavily influences the film`s reflectivity.

6.4.2 Discussion.

For each of the applied fields above H_c we were able to model the measured flipping ratios reasonably accurately with a magnetic induction profile of a purely empirical form. Using a theoretical approach based upon field profiles calculated from the local Ginsburg-Landau theory, and allowing κ to vary, we were able to more accurately model our experimental data.

6.4.2a Superconducting parameters.

Experimentally we obtained H_c = (6.13 ± 0.15) x 10^4 Am^{-1} from the plot of the integrated polarisation against field. In order to compare this to previous results we used the Gorter-Casmir relationship, where $H_c(T) = H_c(0)(1 - (T/T_c)^2)$, to determine $H_c(0)$. This relationship has been experimentally found to describe the temperature dependence of H_c accurately (Rosenblum and Cardona. 1964a). Our calculated value of $H_c(0)$ =(6.41 ± 0.15) x 10^4 Am^{-1} agrees closely with the widely quoted value of $H_c(0)$ = 6.37 x 10^4 Am^{-1} (Tilley and Tilley. 1986).

κ, for type I superconductors, has been previously calculated from the ratio of H_{c3} to H_c obtained during investigations into the surface superconductivity

state. Thermal and electrical conductivity measurements, (Seidel and Meissner. 1965), produced a value of $\kappa = 0.563$ at 1.5K for lead which agreed well with the earlier measured value of 0.56, obtained using a microwave surface-impedance technique (Rosenblum and Cardona. 1964b). A value of κ which is inconsistent with these results was obtained from susceptibility measurements on lead-bismuth alloys at 4.2K where κ for pure lead was extrapolated to be 0.38 from the behaviour of κ for the alloys (Strongin et al. 1964). We may scale this to $\kappa = 0.43$ at 1.5K using the relationship $\kappa(T) = \kappa(0)(1 + T/T_c)^{-1/2}$ which closely models the temperature dependence of κ (Paskin et al. 1964). The inconsistency in this result may be due to fact that one is not able to extrapolate κ for pure lead directly from the behaviour of κ for the alloys. The value for κ we obtained from the ratio of the critical fields, 0.552 ± 0.005 agrees well with the earlier results on pure lead. Additionally, due to the simple interdependence of κ, H_{c3} and H_c,we may also conclude that a H_{c3} of $(8.12 \pm 0.25) \times 10^4$ Am^{-1} agrees well with previously obtained results.

6.4.2b Validity of local Ginsburg-Landau theory.

The analysis of our data within local Ginsburg-Landau theory initially proved difficult due to inconsistencies amongst our experimental results for H_c, H_{c3} and λ_p, $(6.13 \pm 0.15) \times 10^4$ Am^{-1}, $(8.12 \pm 0.25) \times 10^4$ Am^{-1} and (390 ± 10) Å respectively. The simplest solution to this problem appeared to be to neglect λ_p, obtained from the bulk superconducting region, and use the parameters κ, H_c and H_{c3} which were obtained uniquely from the surface superconducting region. Using this approach we were however unable to model accurately the flipping ratios while keeping our parameters within their experimental limits.

Success was obtained in modelling the measured flipping ratios, within the framework of Ginsburg-Landau theory, by simply allowing κ to vary. For applied fields nearer to H_c than H_{c3}, κ was found to increase only slightly

from its value of 0.497 at H_c, with applied field, as illustrated in figure 6.18. Even at an applied field of 7.6 x 10^4 Am^{-1}, κ had increased only to 0.505, a value well inside the experimental error for our calculated κ. If we examine the calculated magnetic induction profiles, corresponding to the calculated flipping ratio profiles, for the four lower applied fields it is clear that above these fields only a small remnant of the characteristic expulsion of the magnetic field from the material surface is present. Therefore we may conclude that for lead the magnetic induction profiles for the majority of the superconducting region are accurately described by Ginsburg-Landau theory, with a $\kappa \approx 0.5$, rather than the conventional κ of 0.56. The variation of κ with applied field, within the surface superconducting phase, is not completely surprising. A similar effect is found within Type II superconductors where the nature of the mixed state, near the upper and lower critical applied fields, is more accurately characterised by two different values of κ.

An additional feature of the surface superconducting region is that the most field exclusion, i.e. the minimum of B(z), occurs approximately one coherence length beneath the surface, as shown in figure 6.19. This illustrates how suitable polarised-neutron reflectometry is for the investigation of the phenomenon of surface superconductivity.

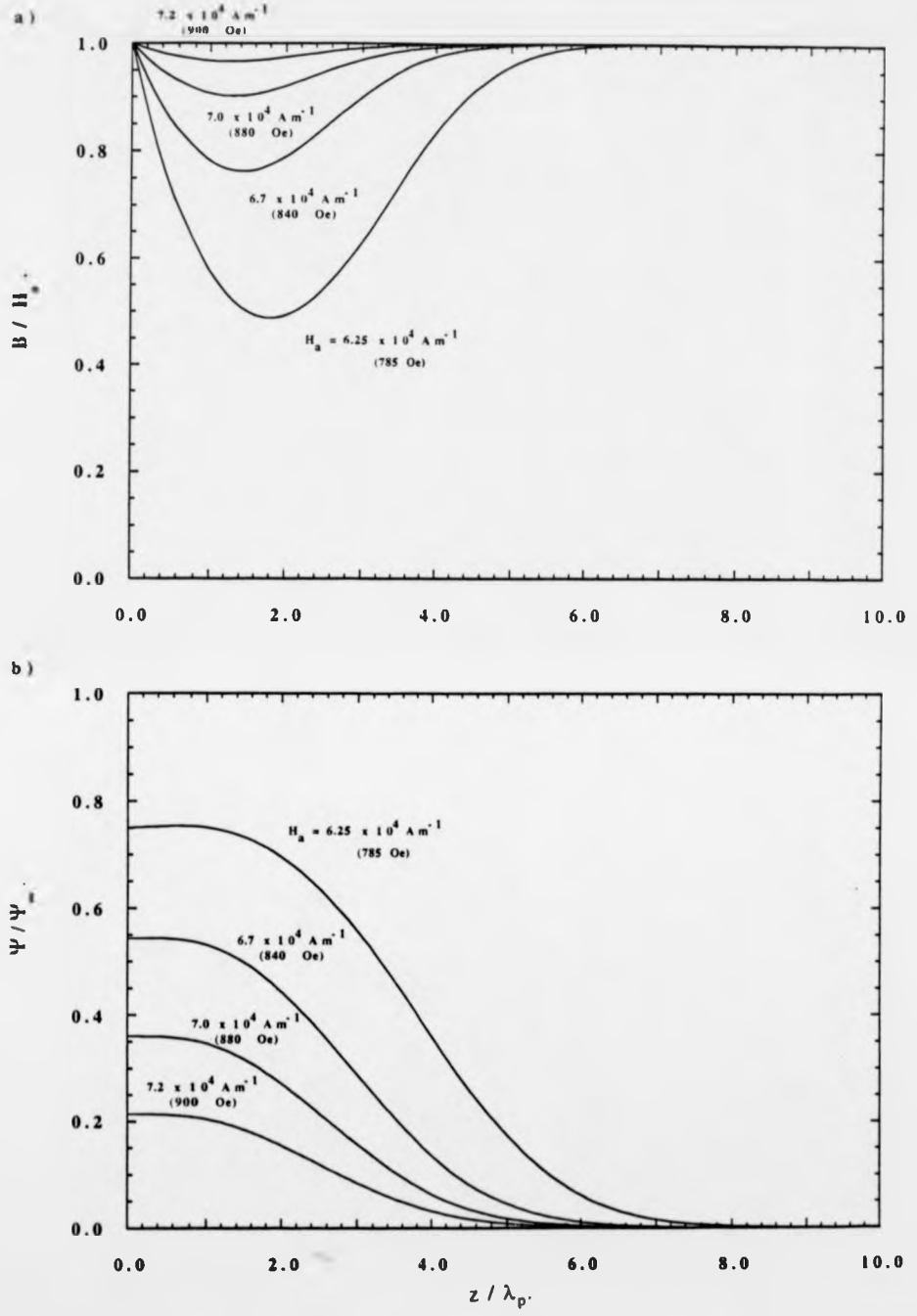

Figure 6.19: a) The theoretical field profiles and b) the superconducting order parameter calculated from Ginsburg-Landau theory for the surface superconducting region and plotted as a function of distance z from the surface, with λ_p = 390 Å.

CONCLUSIONS

Various neutron-scattering techniques have been used to investigate the superconducting and magnetic properties of both conventional and high-T_c superconductors.

In our studies of the magnetic order in a single crystal of non-superconducting $PrBa_2Cu_3O_{7-\delta}$, in three different oxygenation states δ_1, δ_2 and δ_3 (where $\delta_1 < \delta_2 < \delta_3$), the Cu spins in the CuO_2 planes were found to be antiferromagnetically ordered at room temperature with the individual spins lying in the **a - b** plane. For the $\delta_2 = 0.27$ state, the only state which δ was determined precisely, the ordering temperature, T_{N1}, of this high-temperature Cu ordered phase was extrapolated from the temperature dependence of a magnetic Bragg peak to be (400 ± 25) K and the saturated Cu moment was found to be (0.55 ± 0.04) μ_B. Although accurate determination of T_{N1} was not possible due to the upper temperature limit of the cryorefrigerator, T_{N1} appeared to be rather insensitive to changes in the oxygen concentration of the crystal. A similar insensitivity of T_{N1} to the oxygen deficiency δ is observed in the superconducting members of the $ReBa_2Cu_3O_{7-\delta}$ family of compounds.

At a lower temperature, T_{N2}, the Cu magnetic moments also order antiferromagnetically along the Cu chains introducing further complication into the spin configuration. The spin configuration of this low-temperature Cu ordered phase consists of a non-collinear arrangement of spins along the **c** direction. The planar Cu moments either side of a chain Cu ion are each rotated at an angle, the same in magnitude but opposite in sense, to the chain Cu moment. For the $\delta_2 = 0.73$ state, at 2K, the planar and chain Cu moments were found to be (0.54 ± 0.06) μ_B and (0.25 ± 0.03) μ_B respectively and orientated at a relative angle of 23° ± 2°. In contrast to T_{N1}, T_{N2} was found to be strongly dependent on the oxygenation state of the crystal, falling from (40 ± 3) K to

(11 ± 1) K with an increase in oxygen concentration of the crystal from δ_1 to $\delta_2 = 0.73$.

Additionally, at low temperatures, below 20K, diffuse scattering was observed which can be attributed to two-dimensional and three-dimensional short-range correlations of the Pr spins. For the $\delta_2 = 0.73$ crystal at 2K, the Pr spins were found to be antiferromagnetically ordered, with the spin directions along the **c** direction, over a correlation length of ~200 reciprocal lattice spacings in the **a-b** plane and a correlation length of < 2 in the **c** direction. At no temperature, down to the experimental limit of 2K, was any long-range magnetic ordering of the Pr spins observed. The onset of diffuse scattering at such a high temperature coupled with the absence of long range magnetic order is uncharacteristic of typical quasi-two-dimensional magnets and the failure of the Pr spins to order may be explained due to disorder in the crystal. Disorder also provides a mechanism for the failure of the low-temperature Cu ordered phase to form a simple collinear spin configuration at temperatures near OK, unlike the same phase in other $ReBa_2Cu_3O_{7-\delta}$ compounds. Possible sources of disorder may be impurities, e.g. Al present due to the growth of the crystal in an Al_2O_3 crucible, and substitutional defects, e.g. the presence of Pr on the Ba site. If the crystal was of a higher quality and behaved in a similar manner to other quasi-two-dimensional magnets we would expect the Pr spins to order in the vicinity of 10K. This would be an order of magnitude higher than would be expected if one scaled T_N for the other rare earths and would indicate a stronger interaction between the Pr spins. A mechanism for this interaction could be the hybridisation of the Pr 4f electrons with the conduction electrons of the CuO_2 plane.

Analysis of the induced magnetisation density distribution in $PrBa_2Cu_3O_{6.73}$ revealed a strongly aspherical magnetisation density distribution around the Pr site. The magnetisation density was found to be extended towards the Cu

sites in the CuO_2 planes. One cause of this deviation from a spherical free ion distribution may be again the hybridisation of the Pr 4f electrons with the conduction electrons of the CuO_2 plane. The results of this experiment should not be overly interpreted as the magnetisation density distribution may be similar to that for a superconducting compound of the same family. This therefore would mean that our assumption that the magnetisation density surrounding the Re site, in $ReBa_2Cu_3O_7$, would normally be roughly spherical in nature was incorrect. The consequences of the observed magnetisation density distribution around the Pr site could be clarified if a similar experiment was performed on a superconducting compound, e.g. $NdBa_2Cu_3O_7$, which has similar structural parameters to $PrBa_2Cu_3O_7$.

Analysis of the induced magnetisation density distribution also revealed a sizeable moment on the Ba site. This may be explained by the presence of a small percentage of Pr^{3+} ions upon this site. It has been previously shown that the Re^{3+} ions may be deliberately substituted on this site and hence due to the similar radii of Pr^{3+} and Ba^{2+} ions it would seem highly feasible that Pr^{3+} ions may be unintentionally present on the Ba site. If we assume the Pr and Ba sites are similar in respect to the magnetic moment which may be induced upon these sites then from our initial analysis, assuming spherical form factors, (7.8 ± 0.03) % of Pr was found to substituted on to the Ba site. (Note: the presence of this amount of Pr on the Ba site and the subsequent additional positive charge is not thought to play a significant role in the absence of superconductivity in $PrBa_2Cu_3O_7$.) Additionally small magnetic moments were found to be present on the two Cu sites and in our spherical form factor approach to modelling the magnetisation density distribution the induced moments on the Pr, Cu(1) and Cu(2) sites were found to be (0.34 ± 0.01) μ_B, (0.024 ± 0.003) μ_B and (0.006 ± 0.004) μ_B respectively.

Polarised-neutron reflectrometry has proved to be an accurate tool in the investigation of the magnetic induction profiles of Pb films in both the bulk and surface superconducting states. In the bulk superconducting state the observed spin-dependent reflectivity profiles can be accurately described by an exponential magnetic induction decay with a penetration depth of (390 ± 10) Å, as predicted by Londons` theory. No deviations from a purely exponential decay, as predicted to occur at a depth of several penetration depths in type I superconductors due to the non-local relationship between the induced current and field, were observed due to the sensitivity of polarised-neutron reflectrometry to only surface effects. The observed penetration depth and the related Londons` penetration depth, $\lambda_L(0)$, (390 ± 10) Å and (280 ± 10) Å respectively, are relatively small compared to previously reported values but are in very good agreement with theoretical calculations based upon a strong-coupling interaction, (Swilhart and Shaw. 1972).

In the surface superconducting region it was impossible to model all the spin-dependent reflectivity profiles using Ginsburg-Landau theory with a single set of constant parameters the Ginsburg-Landau parameter, the penetration depth and the lower and upper critical applied fields for the surface superconducting state, κ, λ_p, H_c and H_{c3} respectively. By simply allowing κ to increase with the applied field, from 0.497 at H_c to 0.56 at H_{c3}, we were able to accurately model all the magnetic induction profiles between H_c and H_{c3}. Only near to H_{c3} was κ found to increase rapidly and for the majority of the surface superconducting region, away from H_{c3}, the magnetic induction profiles could be accurately described using Ginsburg-Landau theory with $\kappa = 0.501 \pm 0.004$. The observed critical fields H_c and H_{c3}, (6.13 ± 0.15) x 10^4 Am^{-1} and (8.12 ± 0.25) x 10^4 Am^{-1} respectively, agreed well with previously published results for Pb.

APPENDIX

A.1 Propagation of electromagnetic waves in stratified media.

The reflectivity and transmission of a traverse electromagnetic wave through a stratified media can be calculated by solving the second-order differential equations dervived from Maxwell's equations (for a rigorous proof see Born and Wolf. 1975 or Jacobsson. 1975).

Initially we can consider the passage of a wave through a single film. If we consider the plane of incidence to be the y-z plane then the general solutions of the Maxwell equations may be written as

$$E_x = U(z) \exp\{i(k_0 \alpha y - \omega t)\} \tag{A.1}$$

$$H_y = V(z) \exp\{i(k_0 \alpha y - \omega t)\} \tag{A.2}$$

$$H_z = W(z) \exp\{i(k_0 \alpha y - \omega t)\} \tag{A.3}$$

where U(z) and V(z) must satisfy the following second-order differential equations

$$\frac{d^2U}{dz^2} - \frac{d\{\log\varepsilon\}}{dz}\frac{dU}{dz} + k_0^2(n^2 - \alpha^2)U = 0 \tag{A.4}$$

$$\frac{d^2V}{dz^2} - \frac{d\{\log(\mu - \frac{\alpha^2}{\varepsilon})\}}{dz}\frac{dV}{dz} + k_0^2(n^2 - \alpha^2)V = 0 \tag{A.5}$$

where $k_0 = 2\pi/\text{wavelength}$, ε the dielectric constant, μ is the magnetic permeability, n is the refractive index, α is a constant and the $\exp(-\omega t)$ term reflects the time dependence of the solutions. Since U(z) and V(z) each satisfy a second-order linear differential equation they may be expressed as a linear combination of two partial solutions, which in turn, due to their unarbitrary nature, must be coupled by the following first-order differential equations

$$\frac{dU_1(z)}{dz} = ik_0\mu V_1(z), \qquad \frac{dU_2(z)}{dz} = ik_0\mu V_2(z), \tag{A.6,7}$$

$$\frac{dV_1(z)}{dz} = ik_0\left(\varepsilon - \frac{\alpha^2}{\mu}\right)U_1(z), \qquad \frac{dV_2(z)}{dz} = ik_0\left(\varepsilon - \frac{\alpha^2}{\mu}\right)U_2(z). \tag{A.8,9}$$

By representing the solutions as follows

$$U_1 = f(z), \qquad U_2 = F(z), \qquad V_1 = g(z), \qquad V_2 = G(z),$$

where $f(0) = G(0) = 0$ and $F(0) = g(0) = 1$

then U(z) and V(z) may be represented by

$$U(z) = F(z)\,U_0 + f(z)\,V_0 \tag{A.10}$$

$$V(z) = G(z)\,U_0 + g(z)\,V_0 \tag{A.11}$$

where $U_0 = U(0)$ and $V_0 = V(0)$. The solution of these equations may be represented in matrix form, and the more convenient form expressing U_0 and V_0 in terms of U(z) and V(z) can be written as

$$\mathbf{Q_0} = \mathbf{M}\ \mathbf{Q} \tag{A.12}$$

where

$$\mathbf{Q} = \begin{bmatrix} U(z) \\ V(z) \end{bmatrix}, \qquad \mathbf{Q_0} = \begin{bmatrix} U_0 \\ V_0 \end{bmatrix}, \qquad \mathbf{M} = \begin{bmatrix} g(z) & -f(z) \\ -G(z) & F(z) \end{bmatrix}$$

If we now consider the case of two adjacent films where the first one extends from $z=0$ to $z=z_1$ and the second film from $z=z_1$ to $z=z_2$ and $\mathbf{M_1}(z)$ and $\mathbf{M_2}(z)$ are the characteristic matrices of the two films then

$$\mathbf{Q_0} = \mathbf{M_1}(z_1)\ \mathbf{Q}(z_1) \qquad \text{and} \qquad \mathbf{Q}(z_1) = \mathbf{M_2}(z_2 - z_1)\ \mathbf{Q}(z_2) \tag{A.13}$$

so that

$$\mathbf{Q_0} = \mathbf{M_1}(z_2)\ \mathbf{Q}(z_2) \tag{A.14}$$

where

$$\mathbf{M}(z_2) = \mathbf{M_1}(z_1)\ \mathbf{M_2}(z_2 - z_1) \tag{A.15}$$

This result may be generalised for a series of N layers, total thickness z_N where each film is of thickness z_n and has its own characteristic matrix $\mathbf{M_n}$ and therefore

$$\mathbf{Q_0} = \mathbf{M}(z_N)\ \mathbf{Q}(z_N) \tag{A.16}$$

where $$\mathbf{M}(z_N) = \mathbf{M}_1(z_1)\,\mathbf{M}_2(z_2).....\mathbf{M}_N(z_n) \qquad (A.17)$$

If we now consider the case of a wave incident on a film those refractive index varies with depth where θ denotes the angle which the normal to the wave makes with the z axis. By applying Snell's law we may define $\alpha = n \sin\theta$. If we assume the film is equivalent to a number of thin layers, j=1,2 ....N, each of thickness z_j with a constant refractive index n_j, dielectric constant ε_j and magnetic permeability μ_j (Note: $n = \sqrt{\varepsilon\mu}$), then the characteristic matrix for the jth layer becomes

$$\mathbf{M}_j(z_j) = \begin{vmatrix} m_{11} & m_{12} \\ m_{21} & m_{22} \end{vmatrix} = \begin{vmatrix} \cos(k_0 n_j z_j \cos\theta) & -\frac{1}{p_j}\sin(k_0 n_j z_j \cos\theta) \\ -ip_j \sin(k_0 n_j z_j \cos\theta) & \cos(k_0 n_j z_j \cos\theta) \end{vmatrix} \qquad (A.18)$$

where

$$p_j = \sqrt{\frac{\varepsilon_j}{\mu_j}}\cos\theta_j \qquad (A.19)$$

and hence the characteristic matrix of the series of layers can be represented by

$$\mathbf{M} = \prod_j^N \mathbf{M}_j \qquad (A.20)$$

The reflection coefficient for the film may be written as

$$r = \frac{(m_{11} + m_{12}p_N)p_1 - (m_{21} + m_{22}p_N)}{(m_{11} + m_{12}p_N)p_1 + (m_{21} + m_{22}p_N)} \qquad (A.21)$$

where the reflectivity $R = |r|^2$.

REFERENCES

Abrikosov A.A. and Gor'kov L.P.
Sov. Phys. - JETP., **12**, 1243 (1961).

Als-Nielsen J., Bramwell S.T., Hutchings M.T., McIntyre G.J. and Visser D.,
J. Phys.: Condens. Matter., **5**, 7871 (1993).

Anderson P.W.,
Science., **235**, 1196 (1987).

Bacon G.E.,
Neutron Diffraction, Clarendon Press, Oxford, (1975).

Bardeen J., Cooper L.N. and Schrieffer J.R.,
Phys. Rev., **108**, 1175 (1957).

Bardeen J. and Schrieffer J.R.,
Progress in Low-Temperature Physics, vol 3. edited by Gorter C.J. Interscience, New York, (1961).

Barnes L.J and Fink H.J.,
Phys. Rev., **149**, 186 (1966).

Becker P.J. and Coppens P.,
Acta Cryst., A**30**, 129 (1974).

Bednorz J.G. and Müller K.A.,
Z. Phys. B., **64**, 189 (1986).

Birgeneau R.J., Guggenheim H.J. and Shirane G.,
Phys. Rev. B., **1**, 2211 (1970).

Boothroyd A.T., Caves L.W. and Paul D.McK.,
Bull. Mater. Sci., **14**, 613 (1991).

Boothroyd A.T., Doyle S.M. and Osborn R.,
Physica C., **217**, 425 (1993).

Boothroyd A.T.,
Private Communication (1993).

Born M. and Wolf E.,
Principles of Optics, Pergamon Press, Oxford, (1975).

Boucherle J.X., Givord D. and Schweizer J.,
J. de Phys., C**7**, 199 (1982).

Boucherle J.X., Henry J.Y., Papoular R.J., Rossat-Mignod J., Schweizer J., Tasset F. and Uimin G.,
Physica B., **192**, 25 (1993).

Brown P.J.,
International Tables for Crystallography, vol C. edited by Wilson A.J.C. Kluwer Acadamic Publishers, Dordrecht, (1992).

Brown P.J. and Matthewman J.C.,
The Cambridge Crystallography Subroutine Library, Mark 4.
RAL report. RAL-93-009, (1993).

Burlet P., Vettier C., Jurgens M.J., Henry J.Y., Rossat-Mignod J., Noel H., Potel M., Gougeon P. and Levet J.C.,
Physica C., **153&155**, 1115 (1988).

Casalta H.,
Private Communication (1993).

Cava R.J., Batlogg B., Chen C.H., Rietman E.A., Zahurak S.M. and Werder D.,
Phys. Rev. B., **36**, 5717 (1987).

Chaudhuri P., Hoch R.H., Laibowitz R.B., McGuire T.R. and Gambino R.J.,
Phys. Rev. Letts., **58**, 2684 (1987).

Cody G.D and Miller R.E.,
Phys. Rev., **173**, 481 (1968).

Cooke D.W., Kwok R.S., Jahan M.S., Lichti K.L., Adams T.R., Boekema C., Dawson W.K., Kebede A., Schwegler J., Crow J.E. and Mihalisin T.,
J. Appl. Phys., **67**, 5061 (1990).

Dalichaouch Y., Torikachvili M.S., Early E.A., Lee B.W., Seaman C.L., Yang K.N., Zhou H. and Maple M.B.,
Solid State Comm., **65**, 1001 (1988).

Darwin C.T.,
Phil. Mag., **43**, 800 (1922).

Delapalme A.,
Nucleonika., **24**, 723 (1979).

Drangeid K.E. and Sommerhalder R.,
Phys. Rev. Letts., **8**, 467 (1962).

Egloff C., Raychaudhuri A.K, and Rinderer L.,
J Low Temp. Phys., **52**, 163 (1983).

Emery V.J.,
Phys. Rev. Lett., **58**, 2794 (1987).

Felcher G-P.,
Phys. Rev. B., **24**, 1595 (1981).

Felcher G-P., Kampwirth R.T., Gray K.E. and Felici R.,
Phys. Rev. Letts., **52**, 1539 (1984).

Felcher G-P., Felici R., Kampwirth R.T. and Gray K.E.,
J. Appl. Phys., **57**, 3789 (1985).

Felcher G-P., Gray K.E., Kampwirth R.T. and Brodsky M.,
Physica B., **136**, 59 (1986).

Felici R. and Gray K.E.,
Phys. Rev. B., **29**, 6129 (1984).

Felici R., Penfold J., Ward R.C., Olsi E. and Matacotta C.,
Nature., **329**, 523 (1987).

Felner I., Yaron U., Nowik I., Bauminger E.R., Wolfus Y., Yacoby E.R., Hilscher G. and Pillmayr N.,
Phys. Rev. B., **40**, 6739 (1989).

Ferreira J.M., Maple M.B., Zhou H., Hake R.R., Lee B.W. , Seaman C.L. , Kuric M.V. and Guertin R.P.,
Appl. Phys. A., **47**, 1059 (1988).

Fink J., Nucker N., Romberg H., Alexander M., Maple M.B., Neumeier J.J. and Allen J.W.,
Phys. Rev. B., **42**, 4823 (1990).

Finnemore E.E., Mapother R.W. and Shaw R.W.,
Phys. Rev., **118**, 127 (1960).

Gasparovic R.F and McLean W.L.,
Phys. Rev. B., **2**, 2519 (1970).

Gaunt J.G., Miller A.R., Pippard A.B. and Schoenberg D.,
Phys. Rev., **74**, 862 (1948).

Ghamaty S., Lee B.W., Neumeier J.J., Nieva G. and Maple M.B.,
Phys. Rev. B., **43**, 5430 (1991).

Giaever I., Hart H.R. and Megerle K.,
Phys. Rev., **126**, 941 (1962).

Gillon B., Petitgrand D., Delapalme A., Radhakrishna P. and Collin G.,
Physica B., **156&157**, 851 (1989).

Goldman A.I., Yang B.X., Tranquada J., Crow J.E. and Jee C-S.,
Phys. Rev. B., **37**, 7234 (1988).

Goodman G.L. and Soderholm L.
Physica C., **171**, 528 (1990).

Gray K.E.,
Phys. Rev. B., **27**, 4157 (1983).

Gray K.E., Felcher G-P., Kampwirth R.T. and Hilleke R.O.,
Phys. Rev. B., **42**, 3971 (1990).

Guillaume M., Allenspach P., Mesot J., Roessli B., Staub U., Fischer P. and Furrer A.,
Z. Phys. B., **90**, 13 (1993).

Guo G.Y. and Temmerman W.M.,
Phys. Rev. B., **41**, 6372 (1990).

Halbritter J.,
Z. Phys., **243**, 201 (1971).

Han Z.P., Dupree R., Paul D.McK., Howes A.P. and Caves L.W.J.,
Physica C., **181**, 355 (1991).

Hempstead C.F. and Kim B.Y.,
Phys. Rev. Lett., **12**, 145 (1964).

Hewat A.W., Capponi J.J., Chaillout C., Marezio M. and Hewat E.A.,
Solid State Comm., **64**, 301 (1987).

Hirakawa K.,
J. Appl. Phys., **53**, 1893 (1982).

Hirsch J.E.,
Phys. Rev. Lett., **59**, 228 (1987).

Hor P.H., Meng R.L., Wang J.Q., Gao L., Huang Z.J., Bechtold J., Forster K. and Chu C.W.,
Phys. Rev. Letts., **58**, 1891 (1987).

Hughes D.J. and Burgy M.T.,
Phys. Rev., **81**, 498 (1951).

Jacobsson J.,
Progress in Optics, edited by Wolf E, North-Holland, Amsterdam, (1975).

James R.W.,
The Optical Principles of the Diffraction of X-rays. Oxbow Press, Woodbridge CT, (1982).

Jorgensen J.D., Beno M.A., Hinks D.G., Soderholm L., Volin K.J., Hitterman R.L., Grace J.D., Schuller I.K., Segre C.U., Zhang K. and Kleefisch M.S.,
Phys. Rev. B., **36**, 3608 (1987).

Jostarndt H-D., Walter U., Harnischmacher J., Kalenborn J., Severing A. and Holland-Moritz E.,
Phys. Rev. B., **46**, 14872 (1992).

Kadowaki H., Nishi M., Yamada Y., Takeya H., Takei H., Shapiro S.M. and Shirane G.,
Phys. Rev. B., **37**, 7932 (1988).

Kammerlingh Onnes H.,
Leiden Comm., **122b, 124c** (1911).

Kang J-S., Allen J.W., Shen Z-X., Ellis W.P., Yeh J.J., Lee B.W., Maple M.B., Spicer W.E. and Lindau I.,
J. Less-Common Met., **148**, 121 (1989).

Kara M. and Kurki-Suonio K.,
Acta Cryst., **A37**, 201 (1981).

Kebede A., Rodriquez J.P., Perez I., Mihalisin T., Myer G.H., Crow J.E., Wise P.P. and Schlottmann.,
J. Appl. Phys. , **69**, 6739 (1989).

Kebede A, Jee C.S., Schwegler J., Crow J.E., Mihalisin T, Myer G.H., Kuric M.V., Bloom S.H. and Guertin R.P.,
Phys. Rev. B., **40**, 4453 (1989).

Kebede A., Rodriquez J.P., Perez I., Mihalisin T., Myer G., Crow J.E., Wise P.P. and Schlottmann P.,
J. Appl. Phys., **69**, 5376 (1991).

Kennedy S.J., Brown P.J. and Coles B.R.,
J. Phys: Condens. Matter., **5**, 5169 (1993).

Kerchner H.R and Ginsburg D.M.,
Phys. Rev. B., **10**, 1916 (1974).

Lebech B., Rainford B.D,. Brown P.J. and Wedgewood F.A.,
J. Magn. Magn . Mat., **14**, 298 (1979).

Lee B.W., Ferreira J.M., Dalichaouch Y., Torikachvili M.S., Yang K.N. and Maple M.B.,
Phys. Rev. B., **37**, 2368 (1988).

Li W-H., Lynn J.W., Mook H.A., Sales B.C. and Fisk Z.,
Phys. Rev. B., **37**, 9844 (1988).

Li W-H., Lynn J.W., Skanthakumar S., Clinton T.W., Kebede A., Jee C-S., Crow J.E. and Mihalisin T.,
Phys. Rev. B., **40**, 5300 (1989).

Li W-H., Lynn J.W. and Fisk Z.,
Phys. Rev. B., **41**, 4098 (1990).

Li W-H., Chang K.J., Hseih W.T., Lee K.C., Lynn J.W. and Yang H.D.,
Phys. Rev. B., **48**, 519 (1993).

Liang J.K., Xu K.T., Xie S.S., Rao G.H., Shao X.Y. and Duan Z.G.,
Z. Phys. B., **69**, 137 (1987).

Light T.B., Elbridge J.M., Matthews J.W. and Greiner J.H.,
J. Appl. Phys., **46**, 1489 (1975).

Lock J.M.,
Proc. Roy. Soc., **A208**, 391 (1951).

López-Morales M.E, Ríos-Jara D., Tagüeña J., Escudero R., La Placa S., Bezinge A., Lee V.Y., Engler E.M and Grant P.M.,
Phys. Rev. B., **41**, 6655 (1990).

London F and London H.,
Proc. Roy. Soc., **A178**, 560 (1935).

Lovesey S.W.,
Theory of Neutron Scattering from Condensed Matter, vol 1+2.
Clarendon Press, Oxford, (1986).

Lynn J.W., Li W-H., Li Q., Ku H.C., Yang H.D. and Shelton R.N.,
Phys. Rev. B., **36**, 2374 (1987).

Lynn J.W., Li W-H., Mook H.A., Sales B.C. and Fisk Z.,
Phys. Rev. Letts., **36**, 2781 (1988).

Lynn J.W. and Li W-H.,
J. Appl. Phys., **64**, 6065 (1988).

Lynn J.W., Clinton C.J., Li W-H., Erwin R.W., Liu J.Z., Vandervoort K. and Shelton R.N.,
Phys. Rev. B., **48**, 519 (1993).

Lynton E.A.,
Superconductivity, John Wiley & Sons, New York, (1964).

Maletta H., Porschke E., Chattopadhyay T. and Brown P.J,
Physica C., **166**, 9 (1990).

Mansour A., Hilleke R.O., Felcher G-P., Laibowitz R.B., Chaudhari P., and Parkin S.S.P.,
Physica B., **156**, 867 (1989).

Maple M.B.,
Magnetism, vol V chpt 10. edited by Rado G.T and Suhl H.
Acadamic Press, New York, (1973).

Maple M.B., Dalichaouch Y., Ferreira J.M., Hake R.R., Lee B.W., Neumeier J.J., Torikachvili M.S., Yang K.N., Zhou H., Guertin R.P. and Kuric M.V.,
Physica B., **148**, 155 (1987).

Maple M.B., Ferreira J.M., Hake R.R., Lee B.W., Neumeier J.J., Seaman C.L., Yang K.N. and Zhou H.,
J. Less-Common Met., **149**, 405 (1989).

Markert J.T., Dalichaouch Y. and Maple M.B.,
Physical Properties of High Temperature Superconductors, vol I chpt 6. edited by Ginsberg D.M. World Scientific Publishing, Sinapore, (1989).

Marshall W. and Lowde R.D.,
Rep. Prog. Phys., **31**, 705 (1968).

Matthews J.W., Kircher C.J. and Drake R.E.,
Thin Solid Films., **42**, 69 (1977).

Meissner W. and Ochsenfeld R.,
Naturwiss., **21**, 787 (1933).

McIntyre G.J. and Renault A.,
Physica B., **156&157**, 880 (1988).

McIntyre G.J., Renault A. and Collin G.,
Phys. Rev. B., **37**, 5148 (1988).

McIntyre G.J.,
Neutron and Synchrotron Radiation for Condensed Matter Studies. (HERCULES)., vol I. edited by Baruchel J. Springer Verlag, Paris, (1993).

Mende F.F., Raychaudhuri A.K., Tereshchenko N.A. and Rudnev O.E.,
Sov. Phys. Tech. Phys., **22**, 1111 (1977).

Mezei F. and Dagleish P.A.,
Commun. Phys., **2**, 41 (1977).

Miller P.B.,
Phys. Rev., **113**, 1209 (1959).

Muhlschlegel B.,
Z. Phys., **155**, 313 (1959).

Nam S.B.,
Phys. Rev., **156**, 470 (1967).

Nam S.B.,
Phys. Rev., **156**, 478 (1967).

Neumeier J.J., Maple M.B. and Torikachvili M.S.
Physica C., **156**, 574 (1988).

Neumeier J.J., Bjornholm T., Maple M.B. and Schuller I.K.,
Phys. Rev. Letts., **63**, 2519 (1989).

Neumeier J.J., Bjornholm T., Maple M.B., Rhyne J.J. and Gotaas J.A.,
Physica C., **166**, 191 (1990).

Neumeier J.J. and Maple M.B.,
Physica C. **191**, 158 (1992).

Névot L. and Croce P.,
Rev. Phys. Appl., **15**, 761 (1980).

Norton D.P., Lowndes D.H., Sales B.C., Budia J.D., Chakoumakos B.C. and Kerchner H.R.,
Phys. Rev. Letts., **66**, 1537 (1991).

Onuki Y., Suematsu H. and Tanuma J.,
J. Phys. Soc. Jpn., **41**, 1313 (1976).

Orlando T.P., Delin K.A., Foner S., McNiff E.J., Tarascon J.M. , Greene L.H. , McKinnon W.R. and Hill G.W.,
Phys. Rev. B., **36**, 2394 (1987).

Parks R.D.,
Superconductivity, vol 1+2. Marcel Dekker, New York, (1969).

Paskin A., Strongin M., Craig P.P. and Schweitzer D.G.,
Phys. Rev., **137**, 1816 (1965).

Paul D.McK., Mook H.A., Hewat A.W., Sales B.C., Boatner L.A., Thompson J.R. and Mostoller M.,
Phys. Rev. B., **37**, 2341 (1988).

Peabody G.E. and Meservey R.,
Phys. Rev. B., **6**, 2579 (1972).

Peng J.L., Klavins P., Shelton R.N., Radousky H.B., Hahn P.A. and Bernardez L.,
Phys. Rev. B., **40**, 4517 (1989).

Pippard A.B.,
Proc. Roy. Soc., **A216**, 547 (1953).

Radousky H.B.,
J. Mater. Res., **7**, 1917 (1992).

Ramirez A.P., Schneemeyer L.F. and Waszczak J.V.,
Phys. Rev. B., **36**, 7145 (1987).

Reyes A.P, MacLaughlin D.E., Takigawa M., Hammel P.C., Heffner R.H, Thompson J.D., Crow J.E., Kebede A., Mihalisin. and Schweger J.,
Phys. Rev. B., **42**, 2688 (1990).

Reyes A.P, MacLaughlin D.E., Takigawa M., Hammel P.C., Heffner R.H, Thompson J.D. and Crow J.E.,
Phys. Rev. B., **43**, 2989 (1991).

Rosenblum R. and Cardona M.,
Phys. Letts., **9**, 220 (1964).

Rosenblum R. and Cardona M.,
Phys. Letts., **13**, 33 (1964).

Rosov N., Lynn J.W., Cao G, O'Reilly J.W., Pernambuco-Wise P. and Crow J.E.,
Physica. C., **204**, 171 (1992).

Rossat-Mignod J.,
Methods of Experimental Physics, vol 23 part2. edited by Skold K. and Price D.L. Acadamic Press, London, (1982).

Saint-James D. and de Gennes P.G.,
Phys. Letts., **7**, 306 (1963).

Schärpf O.,
Neutron Scattering. edited by Faber J. American Institute of Physics, New York, (1982).

Seidel T. and Meissner H.,
Phys. Letts., **17**, 100 (1965).

Sharma R.J., Rotella F.J., Jorgensen J.D. and Rehn L.E.,
Physica C., **174**, 409 (1991).

Simizi S., Friedberg S.A., Hayri E.A. and Greenblatt M.,
Phys. Rev. B., **36**, 7129 (1987).

Simon I.,
Phys. Rev., **77**, 3841 (1950).

Soderholm L. and Goodman G.L.
J. Solid State Chem., **81**, 121 (1989).

Soderholm L., Goodman G.L. and Loong C-K.,
J. Appl.Phys., **67**, 5067 (1990).

Soderholm L., Loong C-K., Goodman G.L. and Dabrowski B.D.,
Phys. Rev. B., **43**, 7923 (1991).

Soderholm L., Loong C-K., Goodman G.L. and Dabrowski B.D.,
Phys. Rev. B., **43**, 7923 (1991).

Soderholm L., Zhang K., Hinks D.G., Beno A., Jorgensen J.D., Segre C.U. and Schuller I.K.,
Nature., **328**, 604 (1987).

Sommerhalder R. and Thomas H.,
Helv. Phys. Acta., **34**, 29 (1961).

Sommerhalder R. and Thomas H.,
Helv. Phys. Acta., **34**, 265 (1961).

Squires G.L.,
Introduction to the Theory of Thermal Neutron Scattering.
Cambridge University Press, Cambridge, (1978).

Stanley H.E.,
Introduction to Phase Transitions and Critical Phenomena.
Oxford University Press, Oxford, (1987).

Strongin M., Paskin A., Schweitzer D.G., Kammerer O.F. and Graig P.P.,
Phys. Rev. Lett., **12**, 442 (1964).

Swihart J.C. and Shaw W.,
Physica., **55** 678 (1971).

Swihart J.C., Scalapino D.J. and Wada Y.,
Phys. Rev. Letts., **14**, 106 (1965).

Tasset F.,
ILL Internal Report., 91B (1991).

Tasset F.,
Physica B., **174**, 506 (1991).

Tilley D.R. and Tilley J.,
Superfluidity and Superconductivity (2nd ed), Adam Hilger Ltd,
Bristol, (1986).

Tinkham M.,
Introduction to Superconductivity, McGraw-Hill, New York, (1975).

Tomasch W.J. and Joseph A.S.,
Phys. Rev. Lett., **12**, 148 (1964).

Torrance J.B. and Metzger R.M.,
Phys. Rev. Letts., **63**, 1515 (1989).

Tranquada J.M., Cox D.E., Kunnmann W., Moudden H., Shirane G., Suenaga M., Zolliker P., Vaknin D., Sinha S.K., Alvarez M.S., Jacobson A.J. and Johnston D.C.,
Phys. Rev. Lett., **60**, 156 (1988).

Van den Berg J., Van der Beek C.J., Kes P.H. and Mydosh J.A.,
Solid State Comm., **64**, 699 (1987).

Warren P., Forsyth J.B., McIntyre G.J. and Bernhoeft N.,
J. Phys: Condens. Matter., **4**, 5795 (1992).

Williams W.G.,
Polarised Neutrons, Clarendon Press, Oxford, (1988).

Wood R.F.,
Phys. Rev. Letts., **66**, 829 (1991).

Wortmann G and Felner I.,
Solid State Comm., **75**, 981 (1990).

Wu M.K., Asburn J.R., Torng C.J., Hor P.H., Meng R.L., Gao L., Huang Z.J., Wang W.Q. and Chu C.W.,
Phys. Rev. Letts., **58**, 908 (1987).

Yang K.N., Dalichaouch Y., Ferreira J.M., Lee B.W., Neumeier M.S., Torikachvili M.S., Zhou H., Maple M.B. and Hake R.R.,
Solid State Comm., **63**, 515 (1987).

Yang H.D., Lee B.W., Maple M.B. and Laderman S.S.,
Appl. Phys. A., **46**, 229 (1988).

Yang K.N., Ferreira J.M., Lee B.W., Maple M.B., Li W-H., Lynn J.W. and Erwin R.W.,
Phys. Rev. B., **40**, 10963 (1989).

Zachariasen W.H.,
Acta Cryst., **23**, 558 (1967).

Zachariasen W.H.,
Acta Cryst., **A24**, 421 (1968).

Zhu C., Guo-meng Z. and Ran Q-Z.,
Solid State Comm., **66**, 719 (1988).

Publications arising from the work contained in this thesis.

Nutley M.P., Boothroyd A.T. and McIntyre G.J.,
J. Magn. Magn Mater., **104-107**, 623 (1992).

Nutley M.P., Boothroyd A.T., Gregg J.F., Paul D.McK. and Penfold F.,
submitted to : *Phys Rev B.*, (1993).

VARIABLE PRINT QUALITY

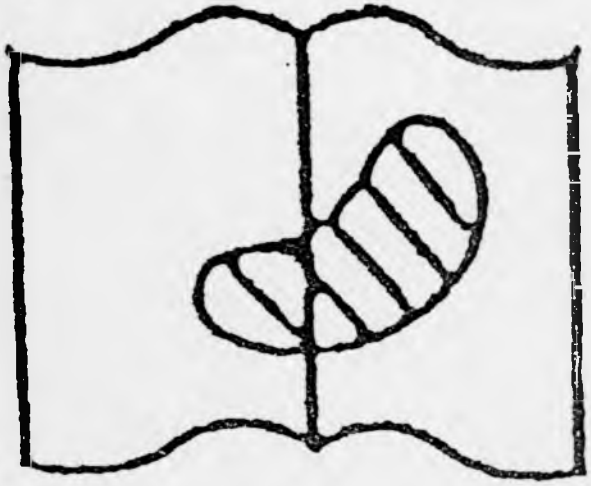

TITLE NEUTRON SCATTERING STUDIES OF MAGNETIC PROPERTIES OF SUPERCONDUCTORS.

AUTHOR Mark Philip
NUTLEY

DEGREE Ph.D

AWARDING BODY Warwick University

DATE 1994

THESIS NUMBER DX182698